EMBEDDED REINFORCEMENT AND BOND-SLIP IN THE NONLINEAR FINITE ELEMENT MODELLING OF REINFORCED CONCRETE

by

ZHENG-PING WU

(BSc, Guizhou Institute of Technology)

A Thesis Submitted for the Degree of

DOCTOR OF PHILOSOPHY

Civil Engineering Department

University of Glasgow

June, 1991

CERTIFICATION OF RESEARCH

This is to certify that, except when specific reference to other investigations is made, the work described in this thesis is the result of the investigation of the candidate

_____CANDIDATE

_____SUPERVISOR

DECLARATION

This is to certify that neither this thesis nor any part of it, has been presented or is being concurrently submitted in candidature for any degree at any other university.

_____CANDIDATE

To

My Parents

and

My Teachers

ACKNOWLEDGEMENTS

The work described in this thesis was carried out in the Department of Civil Engineering at the University of Glasgow. The support of the extensive computer facilities for the research is gratefully appreciated.

I wish to express my indebtedness to my supervisor, Dr. D.V. Phillips, for his valuable guidance, advice and kind help throughout the study.

To Prof. A. Coull, Prof. D.R. Green and Dr. P. Bhatt, I am grateful for their interest, help and general guidance.

Many thanks are also due to Dr. A.C. Chang and Dr. I. McConnochie for their interest of the study and their help.

To the staff members of the Department of Civil Engineering, in particular, Mrs. J. Lawn, Mrs. T.L. Bryden and Mrs. E. Davies, I offer my grateful thanks.

To the former and present colleagues of the Civil Engineering Department at the University of Glasgow with whom I had the privilege to acquire so many friendships, I am grateful for their kind help all the time. They are Prof. C. Zhang, Dr. M. Wei, Dr. B.S. Zhang, Dr. O.A. Awolege, Dr. B. Famiyesin, Dr. A.R. Khan, Ms. X. Leng, Ms. X. Xue, Ms. X. Bai, Mr. H. Wang. Mr. Z.H. Ling, Mr. S.H. Bu, Mr. S.H. Musavi, Mr. S.E. Djellab, Mr. A. Bensalem, Mr. G. Frangopoulos, Mr. L. Jendele and Mr. G. Scilipoti

I extend my grateful thanks to my previous supervisor Prof. Chen DaoZheng of Guizhou Institute of Technology in China, who recruited me as a postgraduate student and encouraged me throughout this study. My acknowlegement is also due to the authorities and staffs of Guizhou Institute of Technology, for their great

assistance and permitting me to take up the doctoral study in the University of Glasgow.

To Prof. Zhu JinQian and Prof. Jiang JianJing of Tsinghua University in China for their encouragement, I offer my thanks.

This study was made possible by an award of the Technical Cooperation Scheme Between China and Britain. I express my thanks to this body and their friendship. Their help throughout project is much grateful.

Finally, my thanks are reserved for my grandmother, my parents and my brother and sisters for their boundless patience, continuous encouragement and moral support in the past years.

SUMMARY

This thesis concentrates on the nonlinear finite element modelling of two dimensional reinforced concrete structures including bond–slip effects. It deals with three aspects of the numerical computation, i. e. modelling techniques, material behaviour and solution techniques.

The modelling techniques concerned the reinforcement and bond–slip. Two embedded reinforcement formulations and one embedded bond–slip model have been developed and implemented, leading to a general model for embedded reinforcement including bond–slip effects. An automatic mesh generation scheme for both concrete and embedded steel bar has been implemented in conjunction with the proposed models.

For the material behaviour of structural concrete, the study reviews concrete, bond–slip and reinforcing steel properties. Particular attention is given to the bond–slip mechanism and its experimental observation. Tension–stiffening and shear retention are also studied along with cracking mechanism. Concrete behaviour is reviewed, including failure rules and constitutive relationships. The constitutive relationships used in this study are summarized.

The cracking behaviour is modelled using smeared approximations. Particularly, fixed cracking model, strain–decomposed cracking model and swing cracking model have been examined and compared.

The nonlinear solution techniques used in this study are modified Newton–Raphson and arc–length procedures along with a line search scheme.

A stock of numerical examples are presented, including studies on both fundamental issues in the modelling techniques, and application to practical

engineering structures.

In this study, it has been shown that finite element representation of structural concrete has become sophisticated. Not only can the reinforcement be modelled properly by using embedded isoparametric reinforced concrete elements including bond–slip effects, but also the material behaviour can be traced properly, usually without great difficulty. The results presented in this study have compared satisfactorily with the experimental results and suggest that the proposed modelling are successful.

TABLE OF CONTENTS

CHAPTER ONE

INTRODUCTION

1.1 Preamble

In the nineteenth century, silicate cement came out as a great development in civil engineering practice. It was immediately used to produce the so-called "man-made rock" together with aggregate and water in a proper ratio. The "rock" was termed concrete and has been widely adopted in both building and construction engineering, from shells, slabs, beams to dams and road/river bridges.

The mechanical properties of concrete are similar to rock. It can be subjected to high pressure but little tension because the adhesive capability of cement is not large. Concrete is hence mainly used in compressive structural regions. If it is used in tension or flexible regions, a quite large cross-section has to be chosen. Alternatively, steel bars/cables are added in the regions of the structure to resist tension deformation and give several advantages. Particularly

1. Concrete provides adhesion and mechanical resistance, and prevents the steel from slipping. The steel is able to carry tension forces transferred to it by shearing mechanisms between the concrete and reinforcement.

2. Since reinforcing steel is buried inside the concrete, it will not be corroded and effected by environmental incursion.

3. Steel bars can resist high tensile stress, which greatly improves the reinforced concrete members' loading-carrying capability.

4. Concrete and steel have almost the same temperature coefficient of expansion (steel: 1.2 x $10^{-5}/^{0}C$, concrete: 1.0 to 1.5 x $10^{-5}/^{0}C$). When a structural member is subjected to temperature change, there will be no internal stress created due to the restriction between the combined materials. Neither will the mechanism between them be destroyed.

5. Due to the close cooperation between these two materials and the wide application of reinforced concrete structures, it has become important to understand the mechanical behaviour of such material when it is subjected to external loading as an engineering structure. This has been carried out both experimentally and theoretically. For theoretical study, principles of mechanics have been applied in the analysis of reinforced concrete structures by assuming that the material is continuous, homogenous and isotropic. The theories of elasticity based on these assumptions have been accepted in engineering design and are still adopted in current design for usual structures.

However, if the mechanism of reinforced concrete is required to be studied in detail, or if the structure is large, a more comprehensive approach must be adopted. This is now possible due to recent numerical approximation developments. Especially due to the appearance of supercomputers, very detailed calculations can be carried out. Among these numerical methods, the finite element method has received a great deal of attention and has gained a prominent niche since the middle of the present century.

In a general sense, the objective of an analysis using this method is: given the joint loading, the geometry of the structure (location of the joints) and the material properties; find the resulting joint displacements, and the internal strains, stresses and other responses in the structural element. The basic procedure for the finite element method is now well established and is given in Appendix I for

completeness.

This method was first applied to aeronautical and marine structural analysis, while application to reinforced concrete structures was later. This was because the former structures are more readily assumed to be homogenous, isotropic and continuous, while the latter structures are anisotropic with complex properties.

For particular situations, the reinforced concrete structure can be represented by large structural elements such as beams, columns or panel type elements taken from an assumed rigid frame structure if the analytical objective is global as shown in Fig.1.1 (a) and (b). When a regional or local analysis is needed the structure will then be discretized as a plane stress, plane strain, plate bending, shell, axisymmetric solid or three dimensional solid system (see Fig.1.1 (c to g)).

Early application of finite element methods to reinforced concrete structures was carried out by the Berkeley group during the 1950's and early 1960's in the analysis of large mass concrete dams designed and built in North America (see [Scordelis 1985]). In their analysis, cracking, time dependent, thermal and sequence of construction effects were traced in the analysis of these plain concrete structures. The earliest published report on the analysis of reinforced concrete was in March 1967 by Ngo and Scordelis[Ngo and Scordelis 1967]. They analysed a beam as a plane stress problem. Cracking were represented by sets of predefined "discrete cracks". Concrete and reinforcement were modelled separately by two–dimensional triangular elements and axial bar elements. Special linkage elements were used to connect concrete and reinforcement. This typical discretisation of a reinforced concrete system is shown in Fig.1.2. The stress concentration at the tip of the cracks was not considered in the analysis.

From there on, it has been clear that when a reinforced concrete structure is

analysed, three aspects need to be considered, i. e. concrete, reinforcement and the interface between them.

For concrete, the standard finite element procedure can be followed assuming that the material is homogeneous, continuous and isotropic within the element. Comprehensive theories are summarized by various researchers, e. g. [Zienkiewicz 1981 and Bathe 1982]. Different types of element can be chosen (e. g. isoparametric triangular elements and quadrilateral elements). However, the investigation of the material properties of structural concrete is still incomplete. In particular, more experimental investigation of concrete properties with reference to the reinforcement influence is still needed for analytical requirements. A systematic description of the material properties of structural concrete can be found in [Chen 1982].

While concrete can be modelled by any appropriate element in the usual manner the representation for reinforcement is often cumbersome. The difficulty arises from the fact that the reinforcement behaves quite differently from the concrete and makes the structure non– homogeneous and non– isotropic. To date, three types of reinforcement approach have been developed and adopted in reinforced concrete structure analysis. These are distributed models, discrete models and embedded models.

In the distributed representation of reinforcement, the steel is assumed to be smeared over the concrete element with reference to the steel bars' angle. The steel is expected to resist stress in the original direction of the bar. In this representation, perfect bond between concrete and reinforcement must be assumed. The steel is modelled by evaluating a concrete– reinforcement constitutive relationship coupled with the concrete element ones, and by assuming that the steel has the same displacement fields as those of concrete.

The discrete representation has the form of either bar elements or beam elements. Bond effects can be take into account by adding some artificial interface or linkage elements along the concrete– steel interface. This however significantly increases the computational effort.

The embedded modelling of reinforcement is usually used in conjunction with higher order isoparametric concrete elements. The reinforcement bar is considered to be an uniaxial member built into the parent concrete element. This approach places less restriction on the layout of reinforcement and the computational cost will not increase much since the stiffness matrix of the reinforcement is assembled into the global system at element level together with the concrete stiffnesses. However, in most models of this type perfect bond is assumed.

The interface between concrete and reinforcing steel is characterised by a complex mechanism. This aspect, along with the concrete cracking behaviour, contributes significantly to the nonlinearity of reinforced concrete structures and hence has been the subject of various research studies in the finite element modelling of reinforced concrete.

There are two main types of interface elements. One is the lumped interface element and the other is the continuous interface element. Both of them are used only with the discrete reinforcement representation. They are hence applicable but not sufficient.

When cracking occurs in a reinforced concrete structure, the behaviour becomes highly nonlinear. Hence the modelling of cracking behaviour has received much attention. Up to now, various simulation techniques have been developed to approximate cracking in a structure. These are discrete cracking models and

smeared cracking models. The first one is used when there exist some dominant cracks known in advance. The main drawbacks are that it suffers from a continuous change in nodal connection and the crack is constrained to follow a predefined path only. This latter objection does not fit the nature of concrete behaviour.

The second approach is widely used and has developed into fixed and swinging subtypes. The fixed crack model assumes orthotropy of the material after cracking, which is not true in some situations, especially where the reinforcement is arranged in a skew direction. In order to overcome this conflict, a strain decomposed approach has been proposed. However, the procedure is complex. The swinging crack allows for changes in the crack direction. This fits the nature of the cracking mechanism but confuses the crack pattern in the loading process.

After the initiation of a crack, aggregate interlock, dowel action and bond–slip mechanisms contribute a lot to the nonlinearity of the structure. Even concrete alone exhibits significant nonlinear stress–strain property. Therefore, in order to closely trace the loading response of a structure, a comprehensive nonlinear solution scheme is needed.

Up to date, various techniques have been proposed. The commonly used Newton–Raphson method is easy to implement into a program but is less effective in critical–stages. When there is snap through or snap back phenomena, the method meets particular difficulty. Recently, improvements have been made in this area, the arc–length method in particular has given effective performance.

This thesis is generally concerned with the modelling of two dimensional reinforced concrete structures including bond–slip effects. It deals with three aspects of the numerical computation, i. e. modelling techniques, material

behaviour and solution techniques. Particular attention is given to the improvement of embedded reinforcement bar modelling. This is because previous embedded bar models still place restrictions on the layout of steel bars as well as assuming perfect bond. On the other hand, the embedded bar approach has advantages over other reinforcement representations (discrete and smeared) in the construction of finite element mesh as well as the computation effort. These become evidently true when a structure with curved reinforcement or prestressing tendons needs to be analysed. In fact, ever since the embedded bar formulation was proposed[Phillips and Zienkiewicz 1976], a general embedded bar model including bond–slip effects has been a potentially powerful development.

1.2 Scope and Aims

In this study, attention is paid to the following aspects of reinforced concrete modelling by finite element methods:

1) To eliminate the restrictions on the embedded bar model and develop a general embedded bar formulation which can be applied to plane structure analysis.

2) To develop a general bond–slip model to be used in conjunction with embedded reinforcement bars within a concrete element.

3) To study bond–slip relationships, and to select a proper constitutive relation for use in bond–slip modelling.

4) To implement strain decomposed crack models and swinging crack models, and compare them with the fixed crack approach.

5) To implement advanced nonlinear solution technique in order to trace post cracking behaviour properly.

6) To develop a method for automatically generating an embedded reinforcement mesh independent of the finite element mesh in order to define the geometry and material properties for each bar element in each concrete element.

7) To examine the implemented modelling techniques, by analysing a stock of numerical examples. Fundamental behaviour is studied by analysing a variety of reinforced concrete panels under different stress states and specimens of bond–slip tests. Perforated deep beams and beam–column junctions are also analysed as examples of more complex engineering structures.

1.3 Layout of Thesis

A literature review on the finite element modelling of structural concrete is given in Chapter two including failure rules and constitutive relationships of concrete. The constitutive relationships used in this study are summarized at the end of the chapter.

Chapter three studies the finite element discretisation of reinforcement. The material properties of structural reinforcing steel are also given. Attention is focused on the embedded reinforcement modelling techniques. Two new models have been developed in this chapter for representing steel bars within a concrete element.

Chapter four deals with cracking behaviour and cracking simulation. In particular, the fixed crack and swinging crack models are studied. The mechanical characteristics of these cracking models are also discussed.

Chapter five focuses on bond–slip behaviour and simulation techniques. Bond–slip mechanisms and bond stress–slip relationships are studied. The discretised modelling of bond–slip behaviour is reviewed. A general embedded bond element is presented at the end of the chapter.

In Chapter six, nonlinear solution techniques are studied. Attention is paid to arc–length procedures and line search schemes.

Having presented the finite element modelling, Chapter seven and eight then lead on to numerical studies of fundamental modelling problems and application to some engineering structures.

Finally, in Chapter nine conclusions have been brought together. Suggestions for further research are also presented.

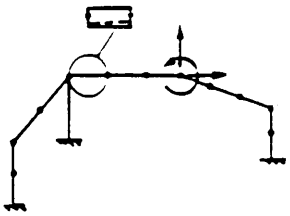

(a) Planar Rigid Frame

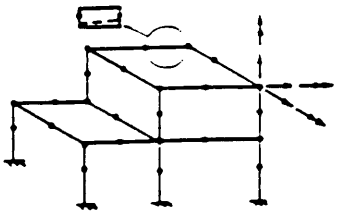

(b) Three-Dimensional Rigid Frame

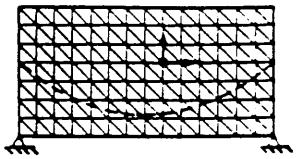

(c) Deep Beam

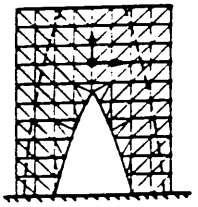

(d) Shear Wall

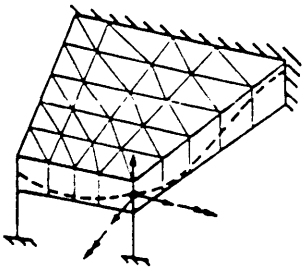

(e) Flat Slab

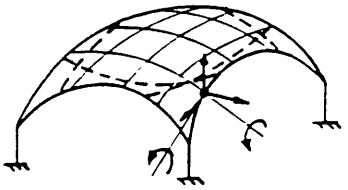

(f) Thin Shell

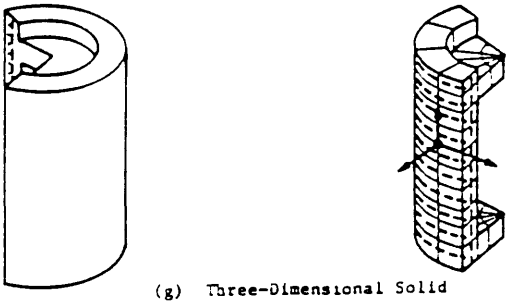

(g) Three-Dimensional Solid

Fig.1.1 Typical Structural Elements

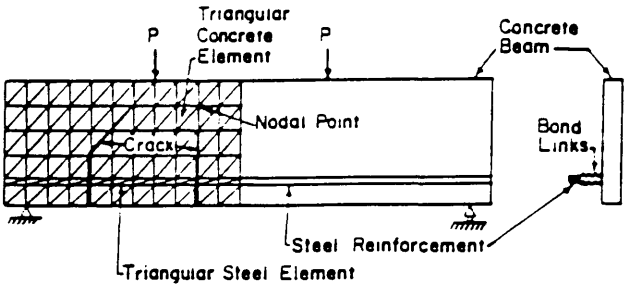

(a) Original Analytical Model of a Beam

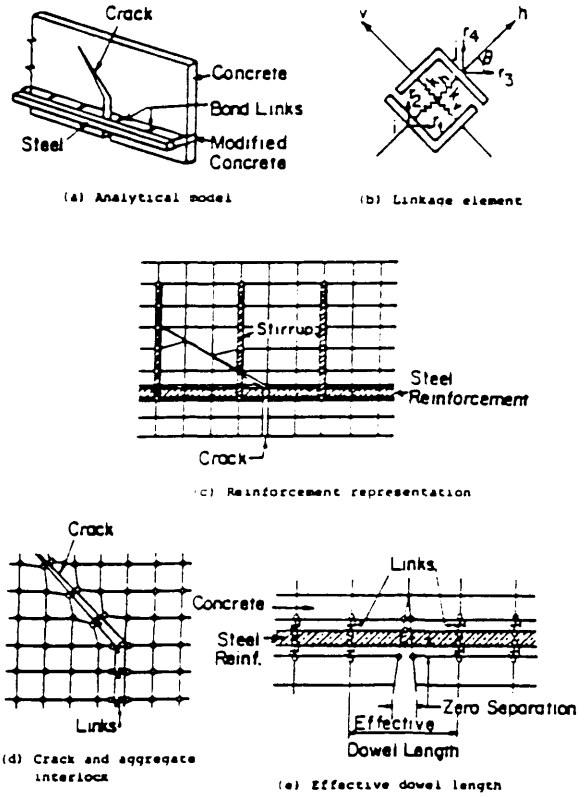

(b) Analytical Models and Linkage Elements

Fig.1.2 A Typical Finite Element Discretisation of RC Structures
(Ngo and Scordelis 1967)

CHAPTER TWO

REVIEW OF CONCRETE BEHAVIOUR AND ITS MODELLING

2.1 Introduction

This Chapter contains a brief review of plain concrete material behaviour and its modelling under multiaxial states of stress. Failure criteria and constitutive relationships under predominantly compressive stress states will be described in fairly general terms since this was not an important aspect of this study. Cracking, however, will be dealt with separately in the next Chapter because this was of major interest.

The main features of the multiaxial constitutive model and compressive failure criteria adopted in this study are explained. This model is straightforward and convenient to use and was selected because it captures the essential aspects of compressive nonlinear behaviour sufficient for the purpose of this investigation.

2.2 Concrete Behaviour

It has been generally observed that concrete can behave as either a linear or a nonlinear material depending on the level and the nature of the stress conditions to which it is subjected. Under low levels of stress, concrete behaves as a linear elastic material. For higher values of stress and for sustained loading it exhibits highly nonlinear properties, which have a considerable effect on the behaviour of reinforced concrete structures. Under multiaxial loading, concrete shows strength and stiffness properties quite different from those displayed under uniaxial loading conditions.

2.2.1 Uniaxial

A typical complete stress–strain relationship under monotonic uniaxial compressive load is shown in Fig.2.1. Up to about 30% of its uniaxial compressive strength f_c', concrete behaves as a linear elastic material. For stresses above $0.3f_c'$, concrete begins to soften until it reaches the peak stress. The curve shows a gradual increase in curvature up to about $0.75f_c'$ to $0.9f_c'$, whereupon it bends more sharply. Concrete microscopic cracks (or microcracks) begin to form at the mortar–coarse aggregate interface. At about $0.7f_c'$ microcracks begin to propagate through the mortar. The onset of mortar cracking occurs at the "discontinuity stress"[Newman 1968] and coincides with an increase in the Poisson's ratio of concrete. Beyond the peak point, damage continues to accumulate and concrete follows a descending curve, i. e. a region marked by the appearance of macroscopic cracks. Finally the concrete crushes at an ultimate strain ϵ_u.

The volumetric strain $\epsilon_v = \epsilon_1 + \epsilon_2 + \epsilon_3$ is plotted against stress in Fig.2.1(b). The volume change is almost linear up to about $0.75f_c'$ to $0.9f_c'$. At this point the direction of the volume change is reversed resulting in a volumetric expansion near or at f_c'. The stress at this point is termed the critical stress[Richart et al 1929].

The shape of the stress–strain curves in Fig.2.1 are closely associated with the mechanism of internal progressive microcracking. For a stress in the region up to about $0.3f_c'$ the micro cracks existing in concrete before loading remain unchanged. This indicates that the available internal energy is less than the energy required to create new microcrack surfaces. The stress level of about $0.3f_c'$ has been termed "onset of localized cracking" and has been proposed as a limit

of elasticity[Kotsovos and Newman 1977].

For a stress between $0.3f_c'$ to $0.5f_c'$, the bond cracks start to extend due to stress concentrations at the crack tips. Mortar cracks remains negligible until a later stress stage. For this stress range, the available internal energy is approximately balanced by the required crack– release energy. At this stage, crack propagation is stable in the sense that crack lengths rapidly reach their final values if the applied stress is kept constant.

When the stress ranges from $0.5f_c'$ to $0.75f_c'$, some cracks at nearby aggregate surfaces start to bridge in the form of mortar cracks. At the same time other bond cracks continue to grow slowly. If the load is kept constant, the cracks continue to propagate with a decreasing rate to their final lengths. For compressive stresses above about $0.75f_c'$, the largest cracks reach their critical lengths. The available internal energy is now larger than the required crack– release energy. Thus, the rate of crack propagation increases and the system is unstable, since complete disruption can occur even if the load is kept constant. The stress level of $0.75f_c'$ is termed "onset of unstable fracture propagation or critical stress" because it corresponds to the minimum value of volumetric strain.

If concrete undergoes cyclic compressive loading, it exhibits some nonlinearities at stress above $0.6f_c'$. It degrades in both stiffness and strength[Karsan and Jirsa 1969, Sinha et al 1964] (see Fig.2.2). If reloading takes place, a small characteristic hysteresis loop is formed. On the average, the unloading– reloading curve is almost parallel to the initial tangent of the initial curve. However, for unloading from stresses about $0.75f_c'$, the unloading– reloading curves show strong nonlinearities, and a significant degradation of stiffness can also be observed. Reloading shows that the material stiffness properties have changed drastically.

Experimental work also indicates that the monotonic uniaxial stress–strain curve serves as a reasonable envelope for the peak values of stress for concrete under cyclic loading. The area enclosed by each unloading–reloading curve represents the energy dissipated during that cycle.

2.2.2 Biaxial

Early attempts on tests of concrete under biaxial loading was focused on the strength of concrete. Later, experimental work turned to study strength, deformation characteristics and microcracking behaviour. Comprehensive reviews were given by Neilissen[Neilissen 1972] and Tasuji et al[Tasuji et al 1978] and the state–of–the–art by Nilson and others[Nilson1982].

The typical experimental stress–strain curves for concrete under biaxial compression, combined tension and compression, and biaxial tension are shown in Fig.2.3 to 2.5. From these curves, the following characteristics can be seen.

1. the maximum compressive strength increases for the biaxial–compression state. A maximum strength increase of approximately 25% is achieved at a stress ratio of $\sigma_2/\sigma_1 = 0.5$, reducing to about 16% at equal biaxial compression state. Under biaxial compression–tension, the compressive strength decreases almost linearly as the applied tensile stress is increased. Under biaxial tension, the strength is almost the same as that of uniaxial tensile strength.

2. Concrete ductility under biaxial stresses has different values depending on whether the stress states are compressive or tensile. For uniaxial and biaxial compression, the average maximum compressive microstrain is about 3000 and the average maximum tensile microstrain varies from approximately 2000 to 4000. The tensile ductility is greater under biaxial compression than under uniaxial

compression. In biaxial compression– tension, the magnitude at failure of both the principal compressive strain and the principal tensile strain decreases as the tensile stress increases. In uniaxial and biaxial tension, the average value of the maximum principal tensile microstrain is about 80. Although the existence of a descending branch under biaxial stress states has not generally been observed, by using a constant rate of straining, Nelissen[Nelissen 1972] was able to achieve the descending portions of stress– strain curves in biaxial– loading tests.

3. As the failure point is approached, an increase in volume occurs as the compressive stress continues to increase as shown in Fig.2.6. This inelastic volume increase termed "dilatancy" is usually attributed to progressive growth of major microcracks in concrete.

4. Failure of concrete occurs by tensile splitting with the fractured surface orthogonal to the direction of the maximum tensile stress or strain. Tensile strains are of crucial importance in the failure criterion and failure mechanism of concrete. Failure modes of biaxially loaded concrete are shown in Fig.2.7.

5. The maximum strength envelope seems to be largely independent of the load path[Nelissen 1972] although there is some indication that nonproportional loading produces a lower strength than proportional loading for lightweight concrete[Taylor et al 1972]. For proportional loading, the failure of concrete under all combinations of biaxial loading appears to be based on a maximum tensile– strain criterion[Newman 1968 and Tasuji et al 1978].

2.2.3 Triaxial

As shown in Fig.2.8, concrete can act as a quasi– brittle, plastic– softening or plastic– hardening material under triaxial loading. This is because the possibility of

bond cracking is greatly reduced and the failure mode shifts from cleavage to crushing of cement paste. Fig.2.8 and Fig.2.9 show that the axial strength increases with increasing confining pressure. Under very high confining stresses, extremely high strengths have been recorded (see Fig.2.9).

Contrary to popular belief, concrete shows nonlinear stress–strain behaviour under hydrostatic compressive loading. The hydrostatic pressure versus volumetric strain curve in Fig.2.10 shows a reversal in curvature on loading. On unloading, the slope is almost constant and is very close to the slope during initial loading, except for a sharp tail in the low–stress range, which is similar to that of the uniaxial case (Fig.2.2). Analysis of test data by Kotsovos and Newman (1977) indicates that when it is subjected to a constant hydrostatic stress (or constant σ_{oct}) and an increasing shear or deviatoric stress (or τ_{oct}), concrete undergoes not only octahedral shear strain γ_{oct} but also consolidation in the form of compressive octahedral normal strain ϵ_{oct}.

Under triaxial loading, experiments indicate that concrete has a fairly consistent failure surface which is a function of the three principal stresses. If isotropy is assumed, the elastic limit (onset of crack propagation), onset of unstable crack propagation, and the failure limit can all be represented as surfaces in three–dimensional principal stress space. Figs.2.11 and 2.12 shows systematically the elastic–limit surface and failure. For large hydrostatic compressions (along the $\sigma_1 = \sigma_2 = \sigma_3$ axis), the deviatoric sections (planes perpendicular to the axis $\sigma_1 = \sigma_2 = \sigma_3$) of the failure surface are more or less circular, which indicates that the failure in this region is independent of the third stress invariant. For smaller hydrostatic pressures, these deviatoric cross sections are curved but more triangular in shape with 3–way symmetry about the principal axes. The failure surface can be represented by three stress invariants. Within the present limits of reported experimental work, this failure surface appears to be independent of load

path[Gerstle et al 1978 and Kotsovos 1979].

2.3 Failure Criteria

In defining failure for concrete under combined states of stress, criteria such as yielding, load–capacity, initiation of crack and extent of deformation have been used. In this study, failure is represented by the stress and/or strain states at which concrete cannot maintain its load carrying capacity. Increasing increments of strain result in a decrease in the stress carried by the concrete after peak stress.

In general, the failure of concrete can be divided into two types: cleavage–type tensile failure and shear–type compressive failure. These are characterized by brittleness and ductility, respectively. Tensile types of failure are caused by the formation of major cracks and the concrete loses its tensile strength normal to the direction of the crack. Compressive failure occurs when many small cracks develop with a loss in strength of concrete in all directions. Tensile failure criteria will be discussed in the next Chapter on cracking.

Under multiaxial compression, two types of peak stress failure criteria have been widely accepted: i) Mohr's theory and ii) octahedral shearing stress theory.

Mohr's theory is based on the concept that failure takes place as sliding along planes of least resistance. The theory states that the shearing stress τ_n on the most vulnerable plane is a function of the normal stress σ_n on this plane at failure, i.e.

$$\tau_n \geqslant f(\sigma_n) \qquad (2.1)$$

It is illustrated in Fig.2.13(a). This is expressed in terms of principal stresses as

$$(\sigma_1 - \sigma_3) \geqslant f(\sigma_1 + \sigma_3) \qquad (2.2)$$

where it is apparent that the failure criteria is independent of the intermediate principal stress σ_2. This further implies that the biaxial strength equals the uniaxial strength. Moreover, this theory assumes that there is a unique failure envelope for any material. These points conflict with experimental evidence. However, the error is not great and the theory is quite commonly accepted. Several works[Cowan 1953, Goode and Helmy 1967] have been used to support Mohr's theory.

The most common form of Mohr's theory is Coulomb's internal friction theory. It approximates eq.(2.1) by a straight line. Failure is assumed to occur when the shear stress on the failure plane exceeds the sum of a constant shearing strength, termed cohesion, and a frictional resistance which is proportional to the normal stress on the plane, i. e.

$$\tau_n \geqslant c - \sigma_n \tan\varphi \qquad (2.3)$$

where c is the cohesion factor, and φ is the angle of internal friction, and tension is positive. Fig.2.13(b) illustrates this law.

In Fig.2.14, the above law can be expressed in terms of principal stresses as

$$(\sigma_1 - \sigma_3) \geqslant 2\, c \cos\varphi - (\sigma_1 + \sigma_3) \sin\varphi \qquad (2.4)$$

If the law is only applied in the pure compressive zones i. e. $I_1 < -f_c'$ (I_1 is the first stress invariant, see Appendix II), then Coulomb's failure surface is a right hexagonal pyramid with an axis $\sigma_1 = \sigma_2 = \sigma_3$, truncated at the plane σ_1

$+ \sigma_2 + \sigma_3 = -f_c'$ in principal stress space. This is shown against a typical failure envelope in Fig.2.15, where it can seen that it under-estimates failure. A disadvantage of this law is that c and φ have to be estimated in some manner.

If failure is based on the octahedral shearing stress, τ_{oct} (see Appendix II) is a function of the octahedral normal stress σ_{oct}[Bresler and Pister 1958, Mills and Zimmerman 1970], such that

$$\tau_{oct} \geq f(\sigma_{oct}) \qquad (2.5)$$

Good fits have been found by assuming a linear relationship. If the law is only applicable in pure compressive zones, the linear form of the above equation is given by

$$\tau_{oct} + n\sigma_{oct} + c \geq 0 \qquad (2.6)$$

where n and c are evaluated directly from a plot of τ_{oct} against σ_{oct} of available test data.

Alternatively n and c can be determined by substituting known compressive strength data in above equation (2.6). As shown in Fig.2.16, for uniaxial compressive tests:

$$\sigma_1 = \sigma_2 = 0 \qquad (2.7a)$$

$$\sigma_3 = -f_c' \qquad (2.7b)$$

$$f_c' > 0 \qquad (2.7c)$$

for biaxial compressive tests:

$$\sigma_1 = 0 \tag{2.8a}$$

$$\sigma_2 = \sigma_3 = -mf_c' \tag{2.8b}$$

$$m \searrow 0 \tag{2.8c}$$

which gives

$$\tau_{oct} + \frac{\sqrt{2}\,(m-1)\,\sigma_{oct}}{(2m-1)}\,\sigma_{oct} - \frac{\sqrt{2}\,m}{3(2m-1)}\,f_c' \geqslant 0 \tag{2.9a}$$

$$\sigma_{oct} < -f_c'/3 \tag{2.9b}$$

In principal stress space, this equation represents a circular cone with axis $\sigma_1 = \sigma_2 = \sigma_3$ and truncated at the plane $\sigma_1 + \sigma_2 + \sigma_3 = -f_c'$. The cone intersects the biaxial plane to give an ellipse which passes through the uniaxial and equal biaxial compressive strength points as shown in Fig.2.17. The ellipse is a very reasonable fit to the actual failure envelope.

However, there are objections to the use of this theory. One is that it is apparently insensitive to large changes in the third principal stress, which can have significant influence on the mode of behaviour. Another is that different relationships are obtained for biaxial compressive stress states and triaxial compressive states. To overcome this latter objection[Bresler and Pister 1958], the third stress invariant, i. e.

$$I_3 = \sigma_1\sigma_2\sigma_3 \tag{2.10}$$

can be included into the failure law, noticing I_3 is equal to zero in biaxial situations.

The octahedral shearing stress criteria has been interpreted as a natural

extension of Mohr's criterion. On the other hand, as the octahedral quantities are directly related to the stress invariants, it is a particular case of the general invariant law

$$f(I_1, I_2, I_3) \geqslant 0 \qquad (2.11)$$

On the whole, both octahedral theory and Mohr's theory approximately agree with experimental evidence, even though both have various weaknesses.

Apart from the simple models described above, there are various more sophisticated ones. The generalized Drucker–Prager surface proposed by Bresler and Pister[Bresler and Pister 1958] assumes a parabolic relation between τ_{oct} and σ_{oct} and the deviatoric sections are independent of θ (θ is a angle of similarity), whilst Willam and Warnke[Willam and Warnke 1975] used a linear $\tau_{oct}-\sigma_{oct}$ relation with deviatoric sections exhibiting θ independence. Ottosen[Ottosen 1975 and 1977] proposed a parabolic $\tau_{oct}-\sigma_{oct}$ relation and θ dependent surface. These refined models contain all the stress invariants, reflect all the required characteristics concerning smoothness, convexity, symmetry, curved meridians and include the simple models as special cases. They hence give a closer estimate of relevant experimental data. However they often require more material parameters for their definition which is a definite disadvantage in many practical situations.

2.4 Constitutive Relationships

Constitutive laws for concrete are the analytical formulations to approximate numerically the complicated stress–strain behaviour of concrete. A large number of numerical models have been developed and the literature abounds with their descriptions. Most of the constitutive models can be classified into one of the following models[Nilson 1982].

(a) Elasticity based models

(b) Plasticity based models

(c) Plastic– Fracturing models, and

(d) Endochronic models

In the following, these models will be briefly described. The model used in this study will then be explained in detail.

2.4.1 Elasticity Based Models

The elasticity based model is the simplest one deduced directly by intuition or approximate considerations which avoid the use of more sophisticated concepts such as loading functions (surface), flow rules and intrinsic time. The elasticity based models can be subdivided into uniaxial, biaxial and triaxial models in terms of stress state or subdivided into incremental and total stress– strain models in terms of the constitutive relationships. These are usually of the nonlinear elastic type and are used primarily to represent concrete behaviour under monotonic or proportional loading only. However, there are some uniaxial and biaxial models developed to represent the behaviour of concrete under cyclic loading.

In general, two different approaches are employed:

i) Finite (or total) description, and

ii) Incremental (differential) description

The former is in the form of secant stress– strain formulation while the latter is used in the form of tangential stress– strain models. These are usually in the form of Hookean formulation, i. e.

$$\{\sigma\} = [D]\{\epsilon\} \tag{2.12}$$

or

$$\{d\sigma\} = [D]\{d\epsilon\} \tag{2.13}$$

where $[D]$ represents either the secant or tangential constitutive matrix. $\{\sigma\}$ and $\{\epsilon\}$ are the stress and strain vectors, respectively.

In the total (secant) stress–strain models, the current state of stress $\{\sigma\}$ is assumed to be uniquely determined as a function of the current state of strain $\{\epsilon\}$, or vice versa. Clearly, this behaviour description is path–independent, which is not true in general for concrete. Thus, the application of such a model is restricted to monotonic or proportional loading regimes, and difficulty arises if it is extended to include general stress histories involving unloading. However, this model has been extensively utilized in describing the nonlinear deformation of concrete under biaxial and triaxial compressive stresses due to its simplicity. In general, most of the secant constitutive models for concrete have been formulated basically as a simple extension of isotropic linear elastic stress–strain relations by replacing two constant modulii (Young' modulus E and Poisson's ratio ν, or bulk modulus K and shear modulus G) with secant modulii (E_S and ν_S, or K_S and G_S), which are assumed to be functions of the stress and/or strain invariants.

The incremental elasticity based formulations are hypoelastic, i. e. they can describe the path–dependent stress–strain state. In this material model, the stress–strain is related linearly by material response modulii given in terms of either $\{\sigma\}$ or $\{\epsilon\}$ or both, i. e. the tangential material matrix $[D]$ depends on the current stress and/or strain state.

Due to their path–dependent behaviour characteristic, incremental (hypoelastic)

models provide a more realistic description for concrete than the total stress– strain models. However, under general stress histories involving reloading from unloading, the formulation fails at or near neutral loading[Nelson and Baron 1971]

Various simplified forms of the tangential formulations have been used in the finite element analysis of concrete material. In the simplest one, the constitutive relations are restricted to be incremental isotropic and the tangential stiffness matrix [D] is then expressed in an isotropic form in which the tangential modulii are taken as functions of the stress and strain invariants.

2.4.2 Plasticity Based Models

From experimental results, it is clear that the concrete nonlinear deformations are basically inelastic. Upon unloading, only a portion of the total strain can be recovered. The total strain of concrete can hence be separated into recoverable and irrecoverable components. Plasticity based models attempt to treat each component individually. In general, models based on the theory of plasticity describe concrete as an elastic– perfectly plastic material or account for some hardening as an elasto– plastic hardening material. The former assumes that under triaxial compression, concrete can flow like a ductile material on the yield or failure surface before reaching its crushing strains. After crushing, the concrete is assumed to lose its resistance completely against further deformations and the current stresses (upon crushing) decrease to zero. The stress– strain relationships include three parts: i) before yielding; ii) during plastic flow; iii) after crushing (failure).

For the elastic– perfectly plastic models, the plastic stress– strain relations can be formulated by defining the yield condition that marks the beginning of plastic

flow and the failure condition that marks the beginning of crushing.

Elastic– plastic hardening models make use of the strain– hardening theory of plasticity in establishing the constitutive relationships for concrete[Buyukoztur 1977, Chen 1981]. The primary characteristic of this model is the introduction of the pressure sensitivity of inelastic behaviour. The initial discontinuity surface is defined as the limiting surface for elastic and is located at a certain distance from the crushing (failure) surface.

To form constitutive relations for a strain– hardening plastic material, three fundamental assumptions have to be made. These are:

i) a shape of the initial yield surface,

ii) a subsequent loading surface (i. e. hardening rule), and

iii) an appropriate flow rule.

The yield condition specifies the state of multiaxial stress corresponding to the start of plastic flow. It is assumed that yielding occurs only if the stress $\{ \sigma \}$ satisfies the general yield criterion of the form:

$$F(\{\sigma\}, k) = 0 \qquad (2.14)$$

where k is a hardening parameter.

During an infinitesimal increment of stress, changes of strain are assumed to be divisible into elastic recoverable and plastic irrecoverable components, thus:

$$\{d\epsilon\} = \{d\epsilon_p\} + \{d\epsilon_e\} \qquad (2.15)$$

A flow rule is assumed to relate the plastic strain increments $\{d\epsilon_p\}$ to the stress subsequent to yielding through a plastic potential function Q ($\{\sigma\}$, k) as follows:

$$\{d\epsilon_p\} = \{\partial Q / \partial\{\sigma\}\} \qquad (2.16)$$

The elastic strain and stress increments are related by the elasticity matrix [D]

$$\{d\epsilon_e\} = [D]^{-1} \{d\sigma\} \qquad (2.17)$$

Substituting eqs.(2.16) and (2.17) into eq.(2.15), the total incremental strains are given by

$$\{d\epsilon\} = [D]^{-1} \{d\sigma\} + \{\partial Q / \partial\{\sigma\}\} \qquad (2.18)$$

When plastic yield is occurring, the stresses are on the yield surface given by eq.(2.14). Differentiating this equation gives:

$$dF = \{\partial F/\partial\{\sigma\}\} \{d\sigma\} + \partial F/\partial k \; dk = 0 \qquad (2.19)$$

The work hardening material parameter k is taken to be represented by the amount of work done during plastic deformation, thus:

$$dk = \{\sigma\}^T \{d\epsilon_p\} \qquad (2.20)$$

The theory of plasticity with an associated flow rule (F = Q) has been used extensively in early studies to describe the behaviour of concrete. Cervenka and Gerstle[Cervenka and Gerstle 1972] used Von– Mises criterion to study reinforced concrete panels, Suidan and Shnobrich[Suidan and Shnobrich 1973] used the same criterion for beams.

In the field of concrete research in relation to the theory of plasticity, attempts have been made to alter some of the classical failure theories such as Von– Mises, in order to overcome some disadvantages or otherwise improve their agreement with the phenomenological behaviour of concrete. New failure theories were therefore developed with specific application to concrete. Buyukozturk[Buyukozturk 1977] generalized Mohr– Coulomb theory based on the biaxial experimental data of Kupfer et al[Kupfer et al 1969] and Liu et al [Liu et al 1972]. However, the need for a non associated flow rule ($F \neq Q$), i. e. formulation based on the plastic potential function Q, has been demonstrated by Vermeer and de Borst[Vermeer and de Borst 1984] in order to take into account the plastic deformation in a direction different from that of loading. The application of a non associated flow rule has been introduced by Han and Chen[Han and Chen 1986] which has succeeded in controlling the major deviations observed in the volumetric strains using an associated flow rule. Recently, Famiyesin proposed a non– associated flow rule, which was applied to material and geometric nonlinear analysis[Famiyesin 1990]. However, much more computational effort is required due to the lack of symmetry in the stiffness matrices

2.4.3 Plastic– Fracturing Models

The study of Andernaes[Andernaes, Gerstle and Ko 1977] on the post fracture behaviour of concrete under biaxial compression indicated that the normality flow rule used for plastic flow of concrete is not strictly observed in the case of fractured concrete. The inelastic behaviour was attributed to two sources: plastic slip and micro cracking. This led to the development of constitutive models based on the plastic– fracturing theory[Bazant and Kim 1979]. In contrast to plastic phenomena characterized in terms of loading surfaces that depend on stresses,

$\{\sigma\}$, the fracturing phenomena are better described in terms of loading surfaces or potential functions[Dougill 1975 and 1976] that depend on strains, $\{\epsilon\}$. Thus, the plastic–fracturing theory requires two loading surfaces[Bazant and Kim 1979]

$$F(\{\sigma\}, H) = 0 \tag{2.21}$$

$$\Phi(\{\epsilon\}, H') = 0 \tag{2.22}$$

where, H and H', are some hardening and fracturing parameters, respectively. The functions F and Φ are chosen to depend on the first and second invariants and take into account both plastic and fracturing deformations. In this theory the incremental stress–strain relations are given by:

$$d\{\sigma\} = [D]\, d\{\epsilon\} \tag{2.23a}$$

where

$$[D] = [D^{el}] - [D^{pl}] - [D^{fr}] \tag{2.23b}$$

in which $[D^{el}]$ is the elastic stiffness matrix, and $[D^{pl}]$ and $[D^{fr}]$, introduce the decrease is the stiffness $[D]$ due to plastic strain increments and fracturing stress decrements respectively. $[D]$ is non–symmetric and generally not orthotropic.

The theory combines plastic stress increments and fracturing stress decrements, which reflect microcracking and takes account of internal friction, inelastic dilatancy due to microcracking, strain softening, degradation of elastic modulii, etc. The model requires six inelastic material parameters which have been obtained by Bazant and Kim by fitting a large set of various types of test data for concrete, available from the literature.

The plastic fracturing model was originally evolved for modelling the behaviour of metals based on the mechanisms of plastic slip in crystals (and dislocation theory). It is therefore less effective for describing concrete. An advantage of this model is that it gives an inelastic response for stress increments tangent to the current loading surface, whereas the classical plasticity theory gives a perfect elastic response for such stress increments, which is not true for concrete.

2.4.4 Endochronic Based Models

The models described so far are incrementally linear. The endochronic based models are not, which makes little difference for proportional loading, but a great difference for significantly nonproportional loading with rotating principal stress directions.

The endochronic based models[Bazant and Bhat 1976] represent a special type of viscoplasticity. The material behaviour is defined in terms of several internal state parameters. The central key in the endochronic theory is that the stress state is considered to be a function of the strain rate and the strain history, defined with respect to an intrinsic time measure, which is an internal state variable of the material. This intrinsic time is a non-decreasing scalar variable used to measure the extent of the irreversible damage of the internal structure of the concrete material when subjected to deformation histories. A simple form of the theory was suggested by Schapery[Schapery 1968] and later was called endochronic by Valanis[Valanis 1971].

The most extensive developments for concrete have been carried out by Bazant and his coworkers[Bazant 1978 and 1980, Bazant and Shieh 1980] who extended the theory, originally developed for metals, to concrete. This extension comprises

several important nonlinear effects expressed analytically with an extensive set of functions which fit experimentally observed behaviour of plain concrete; inelastic volume dilatancy, strain softening range, strain rate effects..etc. It should be mentioned that this increase of scope is achieved at the expense of greater complexity and several material parameters. In general this type of formulation appears to have remarkable potential for special practical applications. However, further research is needed in order to simplify and reduce the number of material constants without sacrificing accuracy.

Due to the complexity of the model and that many parameters are needed for its application, the endochronic based models are not widely used in the finite element analysis of reinforced concrete structures. More details of this model can be found elsewhere, e. g. [Nilson 1982] and [Chen and Yamaguchi 1985].

2.5 Constitutive Model Used In This Study

The model adopted in this study is an incremental elasticity based formulation, (i. e. hypoelastic type) developed by Phillips[Phillips 1972]. This is summarized in the following.

Before any nonlinearity has occurred (including cracking) the concrete is assumed to be an isotropic, homogeneous material, so that the incremental constitutive relationships are given in the global directions by the following well known expression:

$$\{\Delta\epsilon\} = [D]\ \{\Delta\epsilon\} \qquad (2.24)$$

For plane stress

$$\begin{Bmatrix} \Delta\sigma_x \\ \Delta\sigma_y \\ \Delta\tau_{xy} \end{Bmatrix} = \frac{E}{1-\nu^2} \begin{bmatrix} 1 & \nu & 0 \\ \nu & 1 & 0 \\ 0 & 0 & G(1-\nu^2)/E \end{bmatrix} \begin{Bmatrix} \Delta\epsilon_x \\ \Delta\epsilon_y \\ \Delta\gamma_{xy} \end{Bmatrix} \qquad (2.25a)$$

and

$$\Delta\epsilon_z = -\nu\,(\Delta\sigma_x + \Delta\sigma_y)/E \qquad (2.26b)$$

For plane strain

$$\begin{Bmatrix} \Delta\sigma_x \\ \Delta\sigma_y \\ \Delta\tau_{xy} \end{Bmatrix} = \frac{E}{(1-\nu)(1-2\nu)} \begin{bmatrix} (1-\nu) & \nu & 0 \\ \nu & (1-\nu) & 0 \\ 0 & 0 & G(1+\nu)(1-2\nu)/E \end{bmatrix} \begin{Bmatrix} \Delta\epsilon_x \\ \Delta\epsilon_y \\ \Delta\gamma_{xy} \end{Bmatrix} \qquad (2.26a)$$

and

$$\Delta\sigma_z = \nu\,(\Delta\sigma_x + \Delta\sigma_y) \qquad (2.26b)$$

where E, ν and G are the initial elasticity modulus, Poisson's ratio and shear modulus, respectively.

Once nonlinear behaviour starts to develop, the elasticity matrix $[D]$ becomes a tangential material matrix $[D_T]$ so that

$$\{\Delta\sigma\} = [D_T]\,\{\Delta\epsilon\} \qquad (2.27)$$

in which E, ν and G become functions of the state of stress.

If cracks occur, several options are applicable and $[D_T]$ is modified accordingly, to be discussed in Chapter 3.

The model simulates nonlinear behaviour in compressive regions and was developed on the basis of deviatoric and hydrostatic components of stress and strain. Experimental evidence suggests that for monotonically increasing load approximately unique relationships exist between hydrostatic stress σ_m and volumetric strain ϵ_θ, and between deviatoric stress and strain (conveniently represented by octahedral stress and strain τ_{oct}, γ_{oct}) until fairly close to ultimate/peak stress conditions. The deformation response can then be represented by unique relationships up to peak stresses. Using an incremental formulation, the bulk modulus K_T and the tangent shear modulus G_T are assumed to be functions of the first and the second stress invariants I_1 and J_2, respectively, i. e.

$$K_T = f_1(I_1) \tag{2.28a}$$

$$G_T = f_2(J_2) \tag{2.28b}$$

The above assumptions imply that the concrete remains isotropic under multiaxial stress, in the absence of cracking, up to ultimate conditions.

The invariant relationships can be obtained directly from experimental curves of σ_m against ϵ_θ, and τ_{oct} against γ_{oct}. In cases where the data is insufficient, it can be reasonably assumed that K_T is constant and the deviatoric relationship obtained from this starting point. In this study, K_T was always assumed to be constant such that

$$K_T = \frac{E_c}{3\ (1-2\nu)} \tag{2.29}$$

where E_c is the initial elastic modulus of concrete and ν is Poisson's ratio.

Using this assumption, the tangent shear modulus G_T was derived[Phillips 1972]

from experimental curves[Kupfer 1969 and Richart 1928] as shown in Fig.2.18. A permanent table of constants defining this curve is used in this study, which is accessed in a linear piecewise manner. An alternative relationship can be used as follows:

$$\frac{G_T}{G_0} = 0.0536 \left(\frac{\sqrt{J_2}}{f_c'}\right)^{-1.8446} \qquad (2.30)$$

where G_0 is the initial elastic shear modulus.

Ultimate stress conditions are predicted by the octahedral shear stress theory, described earlier in section 2.3 and defined by equations (2.6) to (2.9). The equal biaxial strength to uniaxial strength ratio, $m = f_{bc}'/f_c'$, was normally set to 1.2 unless experimental data for a specific concrete was otherwise available (which is very rare).

After peak stress, the material disintegrates considerably because of internal microcracking. The existence of a stress–strain curve beyond peak stress allows the load to be redistributed to adjacent material after maximum strength is exceeded. This is modelled in a fairly crude manner. The values of G_T and K_T are simultaneously reduced to relatively small values and the state of stress is held constant at a proportion of its peak values $\{\sigma_p\}$ for increasing strain, i. e.

$$\{\sigma\} = c \{\sigma_p\} \qquad (2.31)$$

where $0 < c < 1.0$.

This allows local stress redistribution to occur until a maximum strain condition is reached indicating crushing, after which all stress is reduced to zero. This is given by an octahedral shear strain criterion

$$\gamma_{oct} + n\,\epsilon_{oct} + c \geq 0 \qquad (2.32)$$

where γ_{oct} and ϵ_{oct} are octahedral shear strain and octahedral normal strain (see definition in Appendix II). a and c are constants evaluated directly from the experimental uniaxial crushing strain ϵ_{cu} and biaxial crushing strain $m\epsilon_{cu}$ in a similar manner to that for the octahedral shear stress criterion, eq.(2.7) to (2.9).

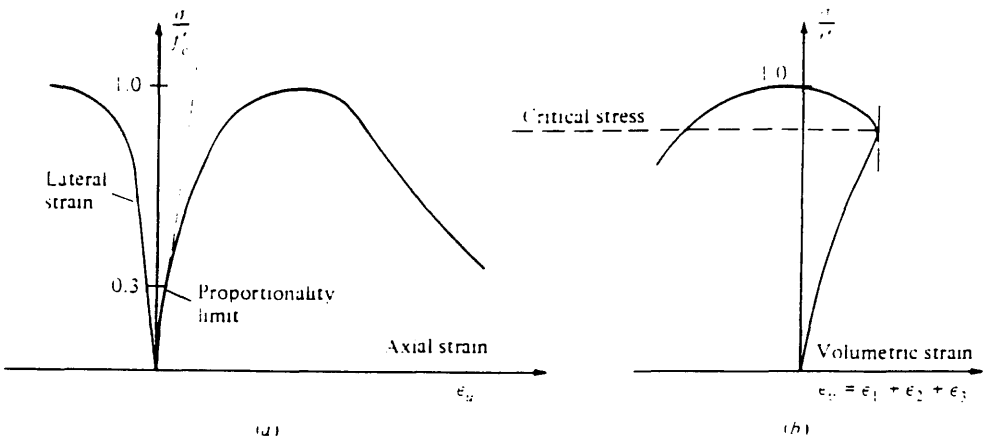

Fig.2.1 Typical Stress– strain Curves Under Monotonic Loading

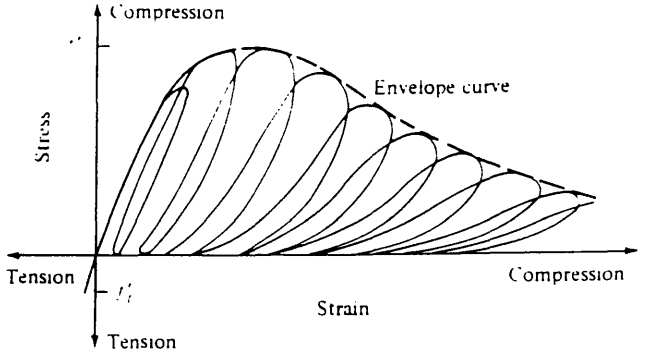

Fig.2.2 Uniaxial Compressive Cyclic Loading

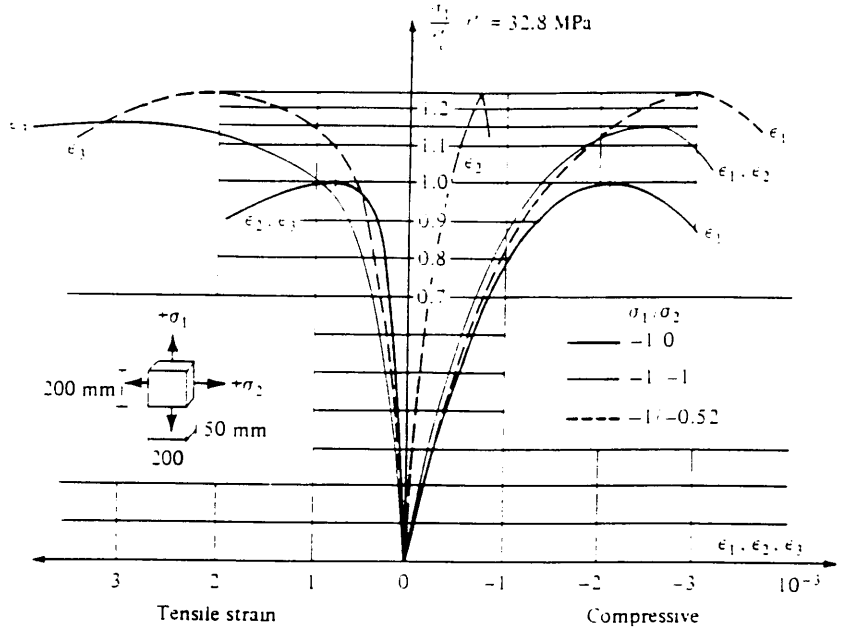

Fig.2.3 Stress– strain Curves Under Biaxial– compression (Kupfer et al 1969)

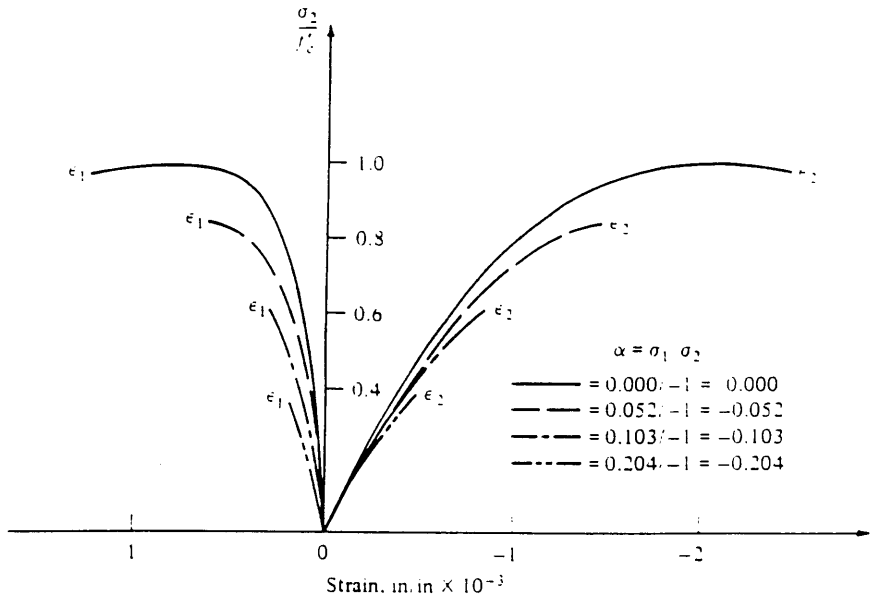

Fig.2.4 Stress– strain Curves for Biaxial Tension– compression (Kupfer et al 1969)

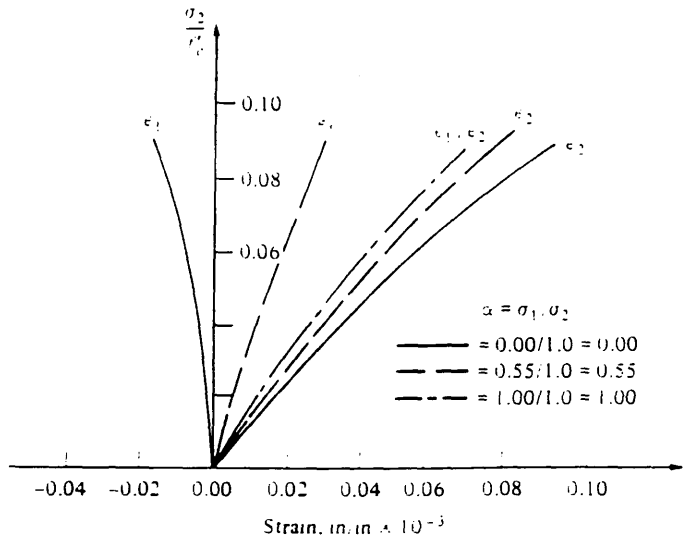

Fig.2.5 Stress– strain Curves for Biaxial Tension (Kupfer 1969)

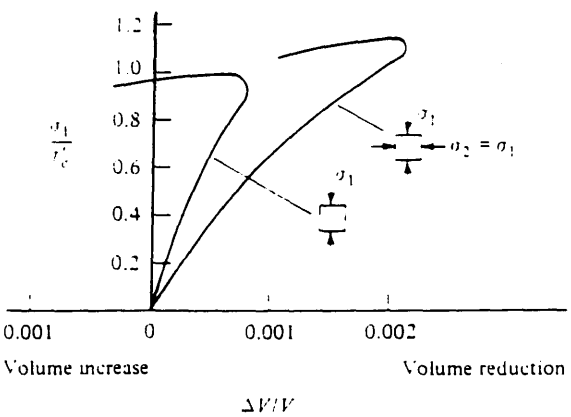

Fig.2.6 Volume Change Under Biaxial Compression

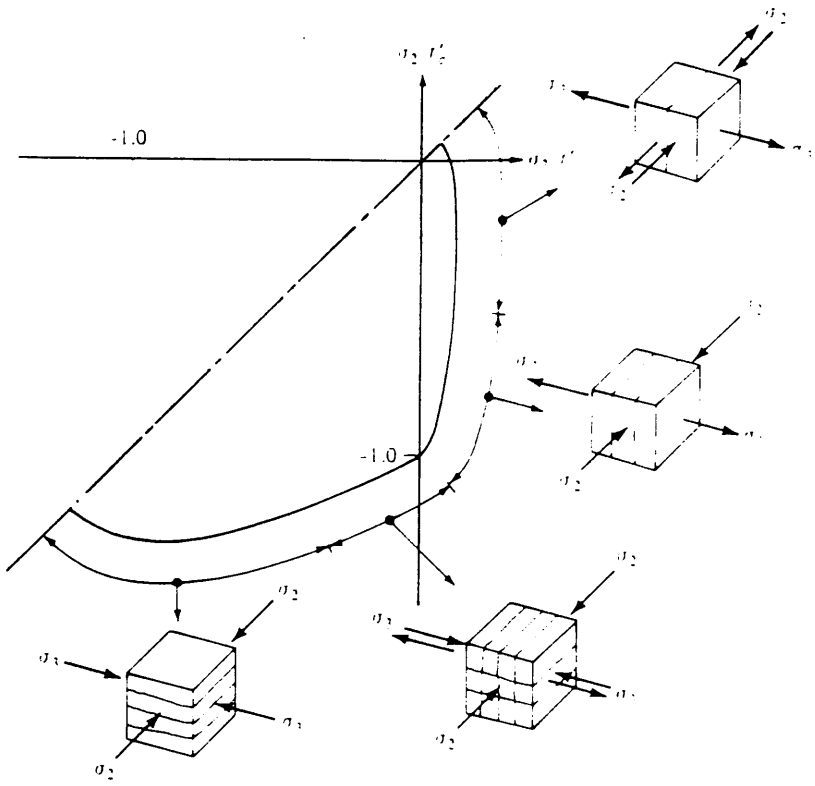

Fig.2.7 Failure Modes of Concrete Under Biaxial Loading (Nelissen 1972)

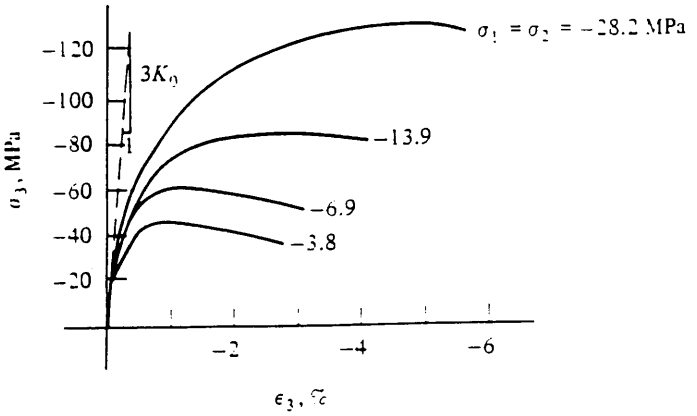

Fig.2.8 Triaxial Compression Test (Richart et al 1928)

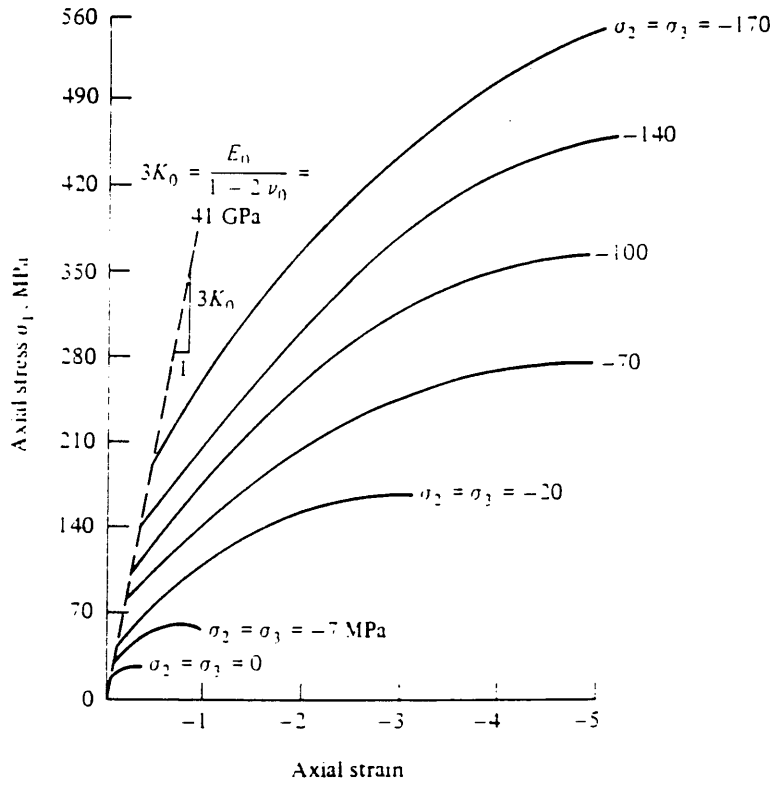

Fig.2.9 Triaxial Stress– strain Curves (Balmer 1949)

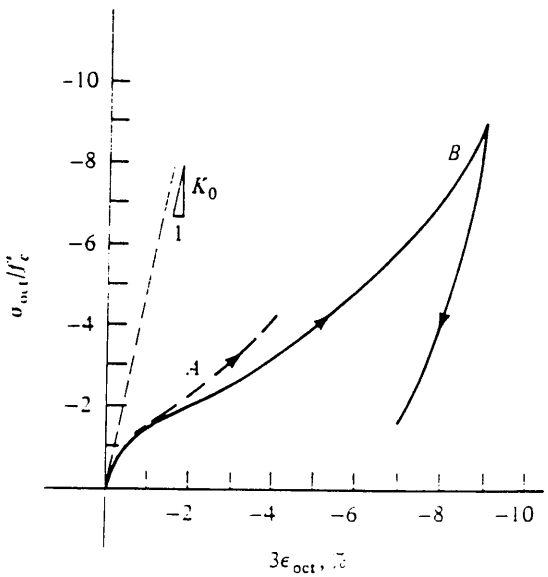

Fig.2.10 Behaviour of Concrete in Hydrostatic Compression

(A= Palaniswamy 1973; B= Green and Swanson 1973)

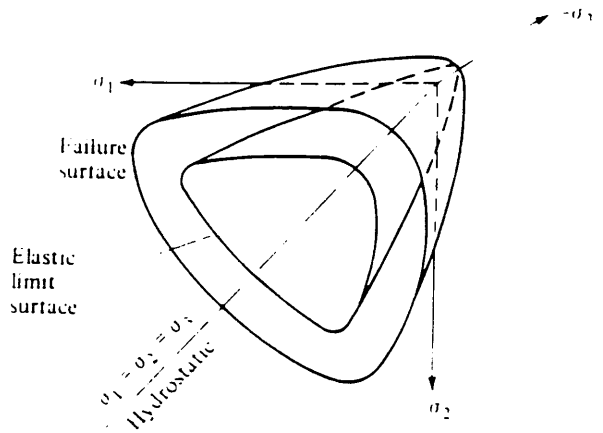

Fig.2.11 Failure Surface of Concrete in 3− D Stress Space

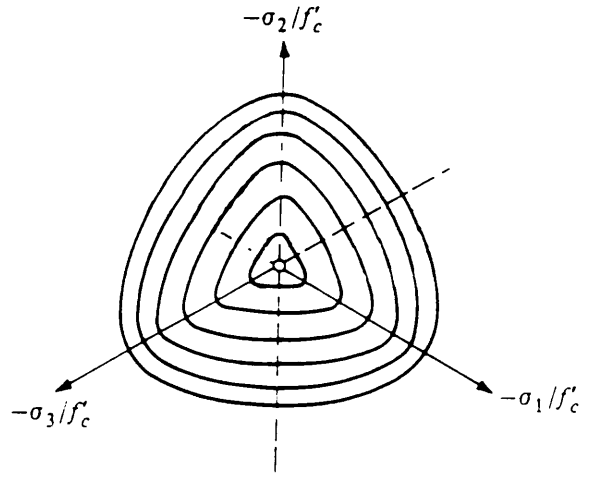

Fig.2.12 Failure Surface for Concrete on Deviatoric Planes

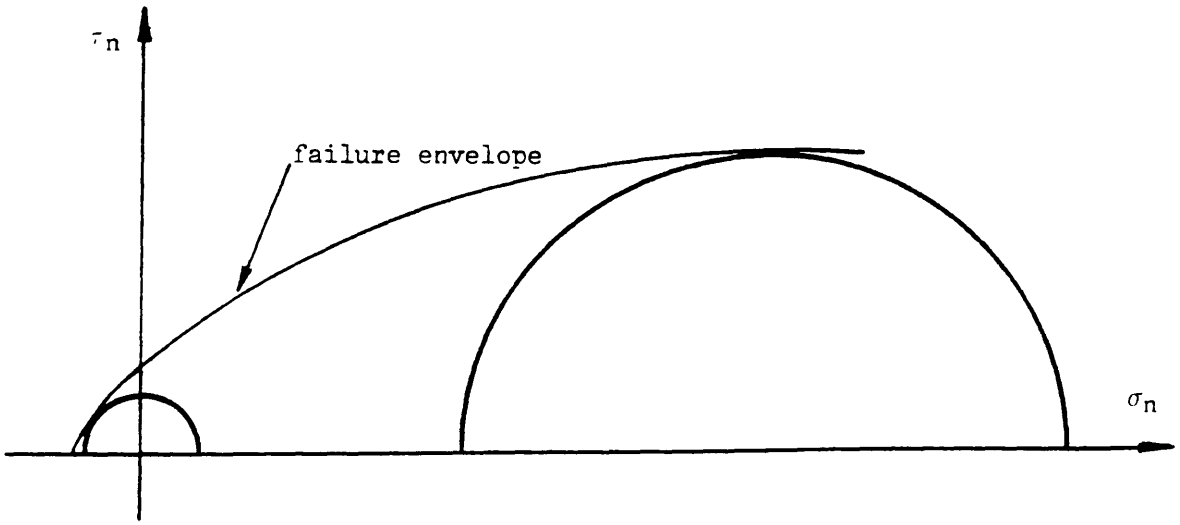

(a) Generalised Mohr's Failure Envelope

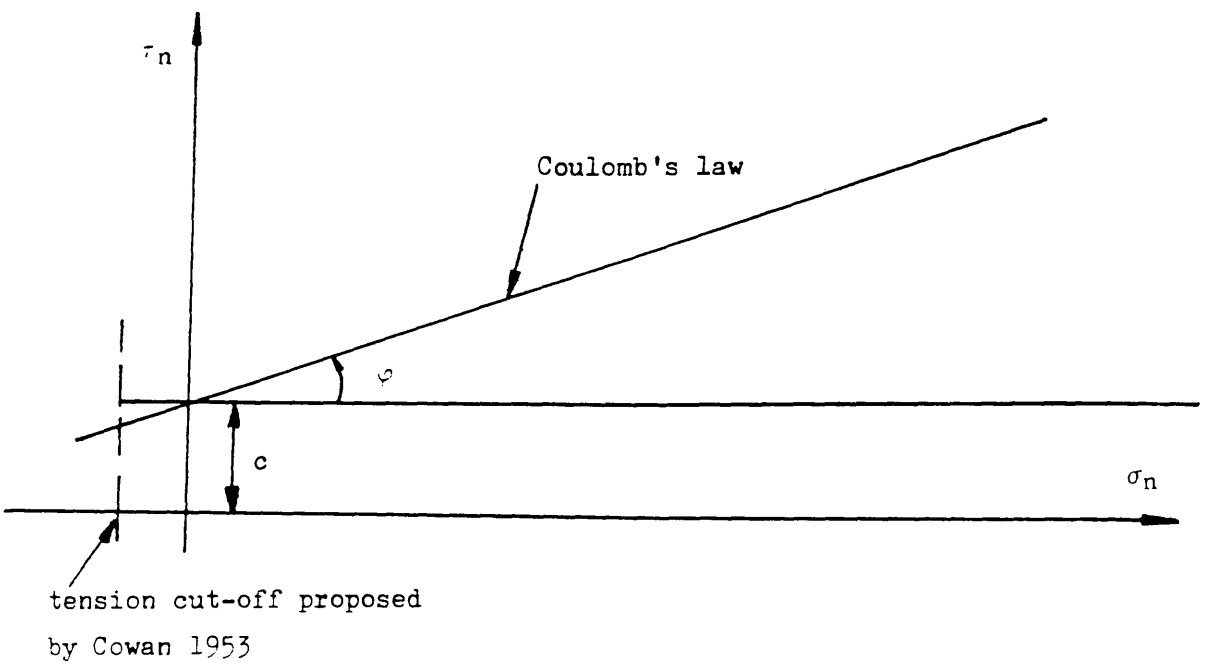

(b) Internal Friction Theories

Fig.2.13 Mohr– Coulomb Failure Theories

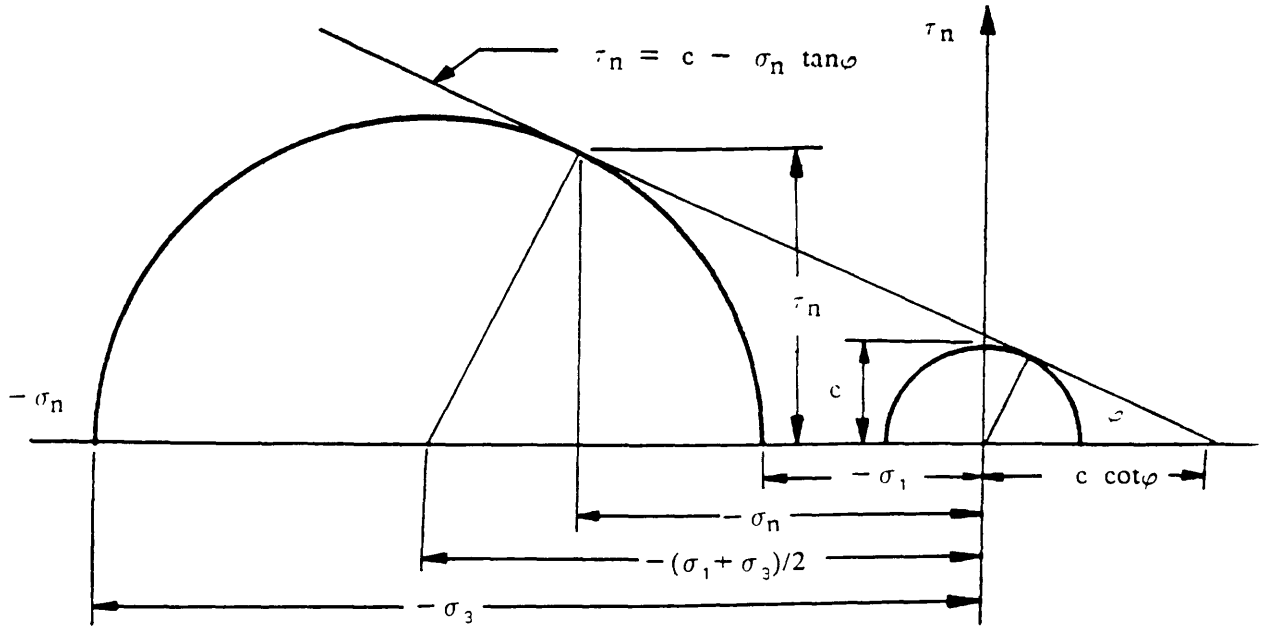

Fig.2.14 Coulomb Failure Envelope

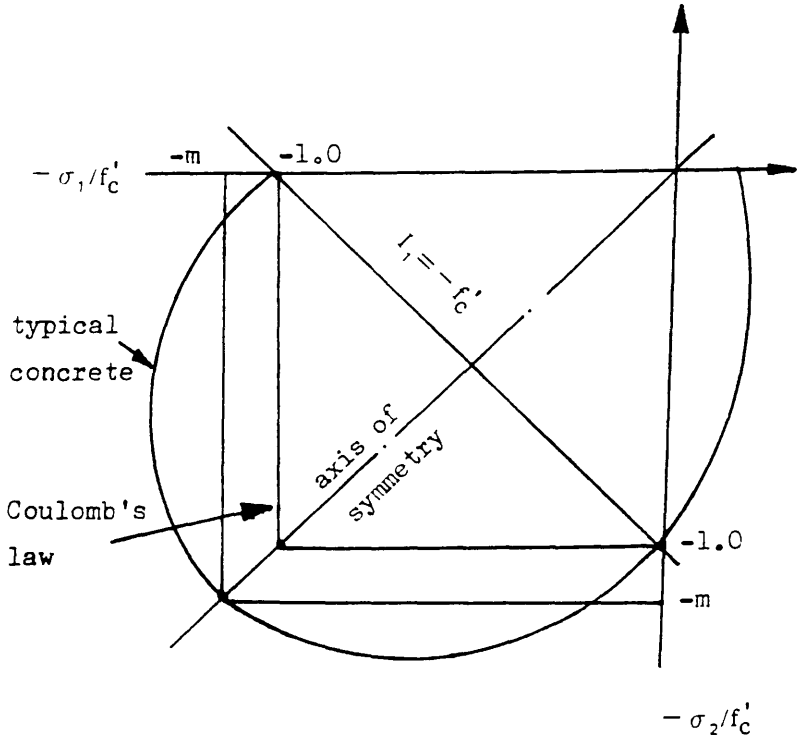

Fig.2.15 Coulomb Biaxial Failure Envelope

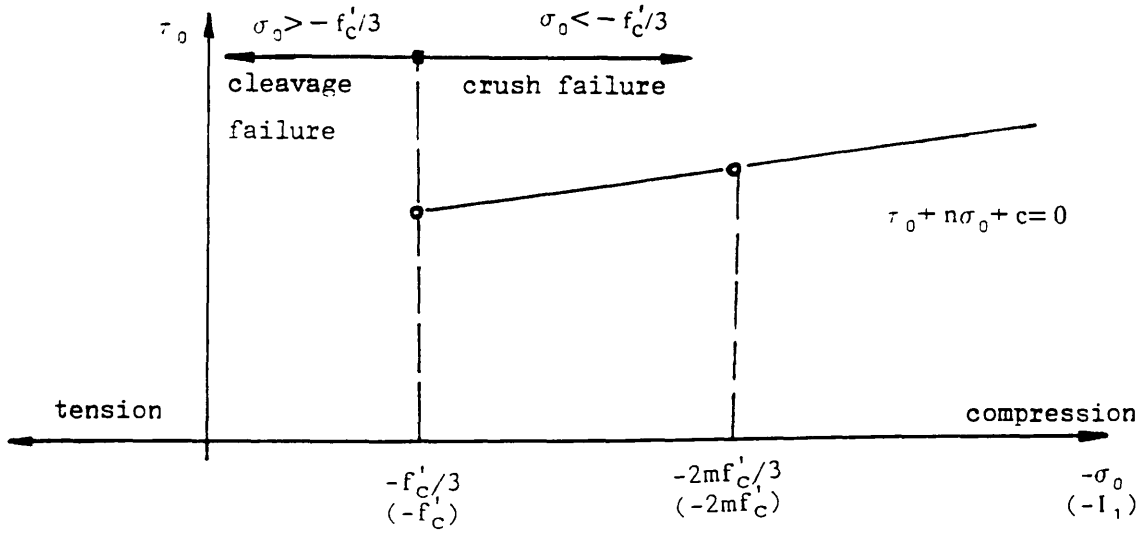

Fig.2.16 Linear Octahedral Shear Stress Law

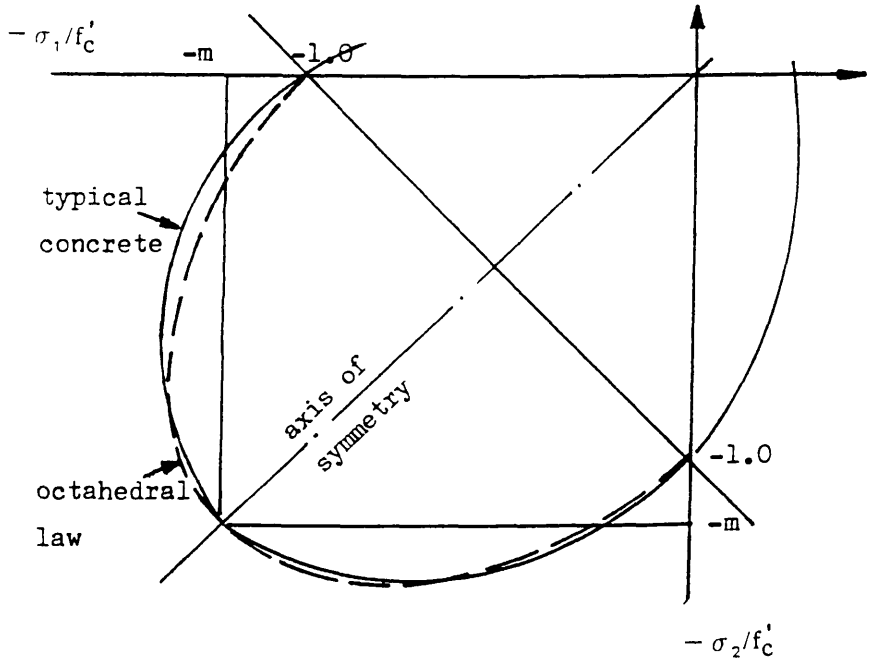

Fig.2.17 Biaxial Octahedral Failure Envelope

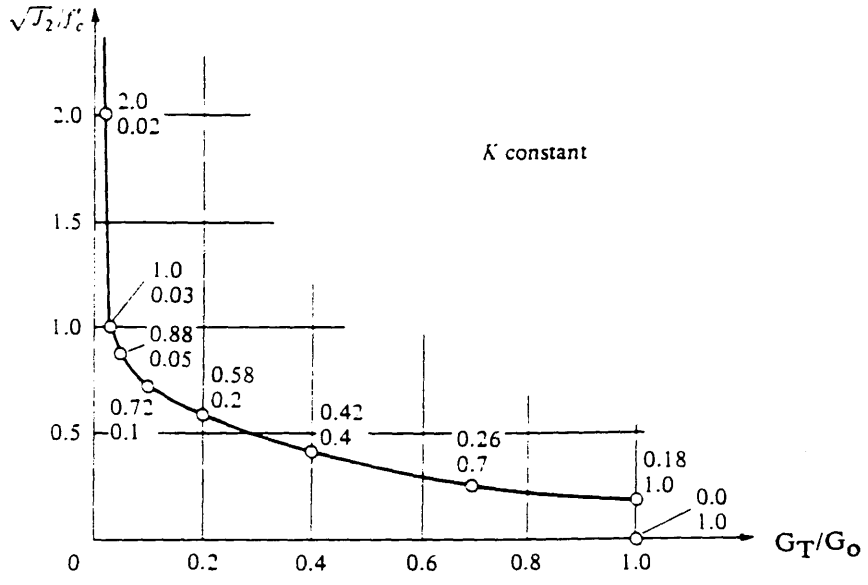

Fig.2.18 Variation of G_T as a function of J_2 (Phillips and Zienkeiwicz 1976)

CHAPTER THREE

CRACKING BEHAVIOUR AND NUMERICAL MODELLING OF CRACKS IN REINFORCED CONCRETE

3.1. Introduction

Due to the tensile weakness of concrete, concrete behaves in a brittle manner. When the tensile stress of the concrete exceeds its strength a crack will occur, after which the mechanism becomes complicated. In the presence of reinforcement, force transfer at and between cracks is effected not only by aggregate interlock, but also by dowel action, bond–slip interaction, and tension stiffening. In the concrete itself, some tensile capability still exists due to softening behaviour.

There is no doubt that the formation of cracks is one of the most important nonlinear phenomena which govern the behaviour of reinforced concrete structures. Consequently, any numerical approach used for the analysis of such structures should embody a sound numerical procedure for dealing with the formation of cracks, including not only opening but also closing and reopening. The force transfer between cracks and at the crack surface also needs to be taken into account. In fact, ever since the finite element method has been applied to reinforced concrete structures, the formation of cracks and post cracking behaviour have received much attention.

Ngo and Scordelis[Ngo and Scordelis 1967] presented the first published procedure to allow cracks to form in a finite element mesh, in which cracks propagate along predefined inter–element boundaries. This became well–known as

the discrete crack model. An alternative approach known the smeared crack concept was introduced by Rashid[Rashid 1968]. This simulates the formation of cracks by replacing the isotropic stiffness matrix by an orthotropic or non-orthotropic stiffness matrix upon crack initiation. This approach effectively smears cracked concrete properties over an appropriate zone of interest (usually an element or volume represented by an integration point). Since these works, there have been numerous developments which are comprehensively summarized elsewhere[Nilson(ed.) 1982 and Chen 1982]. However, of the two approaches, the smeared crack concept has become by far the most popular because it can be readily incorporated into finite element procedures.

In this chapter, cracking behaviour will be firstly reviewed. Secondly, crack simulation techniques are discussed with smeared crack approaches being examined in detail, including the fixed orthogonal crack model, the multi-directional strain decomposed crack model and the rotating crack model. Finally, discussion on the relation between these crack models will be given.

3.2. Behaviour of Cracked Concrete

In a reinforced concrete element, when a crack occurs at a point where the tension stress exceeds the tensile strength of the concrete, the behaviour of the cracked reinforced concrete will depend not only on the overall state of the stress but also on the direction of the reinforcement in relation to that of cracking. Phenomena such as tension stiffening, dowel action and aggregate interlock across the crack surface will arise therefrom. These accumulated factors will characterise the nonlinearity of the structure locally and on the whole.

In finite element analysis, the concrete in tension is usually considered to be a linear-elastic and isotropic material before cracking. In the two dimensional plane

stress configuration, the incremental constitutive relationship is simply given by

$$\begin{bmatrix} \Delta\sigma_{xx} \\ \Delta\sigma_{yy} \\ \Delta\sigma_{xy} \end{bmatrix} = \frac{E_c}{1-\nu^2} \begin{bmatrix} 1 & \nu & 0 \\ \nu & 1 & 0 \\ 0 & 0 & (1-\nu)/2 \end{bmatrix} \begin{bmatrix} \Delta\epsilon_{xx} \\ \Delta\epsilon_{yy} \\ \Delta\epsilon_{xy} \end{bmatrix} \quad (3.1)$$

where E_c is Young's modulus, ν is Poisson ratio.

After cracking has occurred, the material constitutive relationship must be modified. In the "smeared crack approach", the elastic modulus associated with the direction of the maximum principal tensile stress σ_1 is reduced. In the local crack system, a common stress–strain relationship is given by

$$\begin{bmatrix} \Delta\sigma_1 \\ \Delta\sigma_2 \\ \Delta\tau_{12} \end{bmatrix} = \begin{bmatrix} \frac{\mu E_c}{1-\mu\nu^2} & \frac{\nu\mu E_c}{1-\mu\nu^2} & 0 \\ \frac{\nu\mu E_c}{1-\mu\nu^2} & \frac{E_c}{1-\mu\nu^2} & 0 \\ 0 & 0 & \beta G \end{bmatrix} \begin{bmatrix} \Delta\epsilon_1 \\ \Delta\epsilon_2 \\ \Delta\gamma_{12} \end{bmatrix} \quad (3.2)$$

where μ is elastic modulus reduction factor depending on the tension stiffening law, β is a shear retention factor, and where it is assumed no interaction exists between normal and shear stresses and strains.

3.2.1 Tension Stiffening/Strain Softening

Up to cracking, the strain–stress response of concrete in tension is practically linear. Soon after cracking, plain concrete's ability to resist tension drops to zero. Gopalaratnam and Shah[Gopalaratnam and Shah 1985] were able to obtain the post peak response of plain concrete in tension. In their rectangular prism specimen, they obtained the local strains and average crack widths using optical measurements. They proposed an expression in which the tensile stress in concrete decreases asymptotically to zero as the width of the crack increases. The

post–cracking resistance of concrete was attributed to the hypothesis that the cracked surface is connected and/or bridged by aggregates or crystals and the observed crack width is only a measure of the average separation of these surfaces.

In reinforced concrete structures, the cracked concrete can resist average tensile stresses by virtue of the tensile strength capacity of the uncracked portions of concrete between two adjacent cracks, and between which the bond transfers the forces from concrete to reinforcement. This phenomenon is termed tension stiffening. Many researchers have proposed expressions to model the tension stiffening effect which relate the average tensile stress in cracked concrete to the average tensile strain.

As shown in Fig.3.1, when the concrete reaches its tensile strength, primary cracks form. The number and extent of the cracks are controlled by the size and the placement of the reinforcing steel. The concrete stress does not drop to zero but remains at a certain amount due to the tension stiffening effect. The change of the stress distribution in concrete and reinforcement is related to the bond effect.

In order to improve the numerical representation of cracking and to some extent ensure the numerical stability of the solution, tension stiffening[Scanlon 1971] needs to be added.

In this study, the following tension stiffening laws have been examined.

— the stiffness of the concrete is neglected after cracking, i. e. the tension stress drops to nearly zero right after cracking, see Fig.3.2(a);

— the concrete modulus is reduced gradually in a bilinear manner with a discontinuity upon crack initiation, see Fig.3.2(b)[Yamaguchi 1985], in which α and ϵ_t are assumed to be 0.5 and $20\epsilon_{cr}$, respectively. This type of curve is commonly used in the finite element analysis of reinforced concrete structures.

— a recent experimental study on plain concrete by Phillips and Zhang[1990], indicating a steep portion in the strain softening curve at cracking. Afterwards, the concrete stiffness reduces gradually. Therefore, concrete behaves in a trilinear manner, as shown in Fig.3.2(c). Based on their experimental results, a derivation using fracture energy theory gave the relationship

$$\delta_{ssc} = 6\delta_f - 5\delta_{cr} \qquad (3.3a)$$

where $\delta_{cr} = f_t/E_c$, E_c is the concrete modulus,

f_t is the concrete tension strength,

δ_f, δ_{ssc} and δ_{cr} are denoted in Fig.3.2(c).

This curve overcomes the sudden discontinuity at the crack point, which is preferable in computation. However, since it was obtained from pure concrete specimens it dose not include the influence of tension stiffening effects.

— based on a systematic experimental study of the cracking mechanism, Bhide and Collins[Bhide and Collins 1987] considered that tension stiffening is affected to a certain extent by the angle between the cracking direction and the reinforcing direction, and proposed the following equation:

$$\sigma_1 = E_c \epsilon_1 \qquad (\epsilon_1 \leq \epsilon_{cr}) \qquad (3.3b)$$

$$\sigma_1 = \frac{f_t}{1 + 1000\epsilon_1/\alpha} \quad (\epsilon_1 \succ \epsilon_{cr}) \tag{3.3c}$$

where E_c is the initial Young's modulus of concrete, and ϵ_{cr} and f_t are the cracking strain and stress, respectively. The factor α accounts for the influence of the reinforcing bar orientation and is given by

$$\alpha = (90/|\ \theta\ |)^{1.5} \tag{3.3d}$$

where θ is the angle between the crack direction and the reinforcement, measured in degrees. If a radian measure is used, the term 90 should be replaced by $\pi/2$. In the case of unequal reinforcement in two orthogonal directions, the direction of the stronger reinforcement is taken as the axis of reinforcement. Fig.3.2(d) shows the strain–stress relations for different values of θ ranging from 90 degrees to 20 degrees.

According to the results of Bhide and Collins, good agreement was obtained when comparing their own experimental data with those of Kollegger et al[Kollegger1986]. In fact, this relation has quite often been adopted in recent research studies.

With tension stiffening introduced into the finite element modelling of reinforced concrete, the analysis becomes more close to the real behavior. However, the inclusion of tension stiffening in the material constitutive relationship means that such modified stress–strain relations do not any more match the properties of plain concrete or steel. The resulting constitutive matrix is actually an anistropic relationship. Furthermore, the steep descending part of the tension stiffening curve can sometimes cause computational divergence.

A further difficulty is that softening behaviour is related to the energy release

rate over a given area or crack length. This means that it will depend on the volume of material represented by a finite element or integration point, thus causing mesh dependency. This can be partially overcome by noting that the fracture energy of concrete G_F is related to a characteristic length l_c of the crack which in turn can be related to the volume of material. The fracture energy G_F can be deduced from the area under the softening branch of the prescribed stress– strain curve. This allows the parameters defining the curve (e. g. α, δ_{SSG}, δ_F, ϵ_t in Fig.3.2) to be determined according to element size. However, this concept dose not account for tension stiffening, only softening, and therefore it is difficult in practice to set realistic values to the parameters involved. Furthermore G_F is not usually available, nor easy to measure.

3.2.2 Shear Retention

In general, cracks in concrete are rough. Shear force can then be transferred on the faces of the crack due to the aggregate interlock. The amount of the shear stress transmitted by the interlock is dependent upon the average width of the crack, compressive strength of the concrete, maximum aggregate size and local compressive stress due to riding of one face of the crack over the other. The mechanism is shown in Fig.3.3.

The shear stress and normal stresses transmitted by reinforcing steel due to dowel action across the crack is dependent upon the crack width, diameter of the reinforcing bar and the relative displacement of one face of the crack with respect to the other in the direction at right angles to the reinforcing bar, see Fig. 3.4.

In reinforced concrete, the mechanism of dowel action is in fact an interaction between reinforcement and concrete. Many experimental investigations[Fenwick

1966 and Millard and Johnson 1985] have been carried out since late 1960's. Park and Paulay[Park and Paulay 1975] have identified the three mechanisms of dowel action, i. e. the direct shear, kinking and flexure of the reinforcing bar. A formulation to calculate the maximum dowel shear for a reinforcing bar was derived as well. They concluded that if the concrete supporting the reinforcing bar is considered to be rigid, the first two mechanisms would predominate. However, Mills[Mills 1975] recognized that significant deformation does occur in the concrete supporting the reinforcing bar, so that flexure of the steel is a principle action.

Recently, in the study of Bhide and Collins[Bhide and Collins 1987], a beam model was suggested for the dowel action and interlock simulation, in which the effective length of the beam was assumed to be the component of the crack width in the direction of the reinforcing bar plus four times the diameter of the bar under consideration. If the concrete layer in the direction of the dowel displacement is weakened, the effective length of the dowel action will be longer.

In finite element analysis, the overall shear transfer effects are represented by a shear retention factor, β. This was first introduced independently by Phillips[Phillips 1972] and Suidan and Schnobrich[Suidan and Schnobrich 1973]. Normally one of the following methods is adopted.

— the shear stiffness of the uncracked state is kept unchanged after the first crack appears (i. e. the shear retention factor $\beta = 1.0$);

— the shear stiffness is set to a constant value after cracking (for instance $\beta = 0.5$ as shown in Fig.3.5(a));

— the shear modulus is reduced linearly (Cedolin/Dei Poli[1977]) or hyperbolically

(Al– Mahaidi[1979]) as a function of the actual strain normal to the crack, see Fig.3.5(b) and (c).

— recently, Mehlhorn[Mehlhorn 1990] proposed a approximation based on their experimental investigation, which takes account of the reinforcement ratio ρ, i. e.

$$\beta = \frac{\ln(\epsilon_{cr}/c_1)}{c_2} \qquad (3.4a)$$

where

$$c_1 = 7 + 5 \cdot (\rho - 0.005)/0.015 \quad (\rho \leq 0.02) \qquad (3.4b)$$

$$c_2 = 10 - 2.5 \cdot (\rho - 0.005)/0.015 \qquad (3.4c)$$

If the reinforcement ratio is greater than 0.02, $\rho = 0.02$ is suggested.

If two directions are cracked, the reciprocal of the retention factor β is given by the addition of reciprocals β_1 and β_2 determined separately from both directions using the above equation.

$$\frac{1}{\beta} = \frac{1}{\beta_1} + \frac{1}{\beta_2} \qquad (3.4d)$$

All these alternative relationships are have been examined and compared in this study.

A more comprehensive scheme for calculating the shear modulus of cracked reinforced concrete has been suggested by Bazant and Gambarova[1980] and Walraven[1980] based on experimental data. They decomposed the average strains of the cracked reinforced concrete element into the strains of the uncracked concrete between the cracks and the strains due to the cracks. Each of these

obeys different constitutive laws obtained from experiments. The incremental material law of cracked reinforced concrete is given by combining the constitutive relations of reinforcement with that of concrete which includes the cracking effects. The resulting equation describes the relation between stresses and strains in a cracked reinforced concrete element in the 'smeared manner'.

If a crack closes during unloading or reloading, the shear retention factor is usually set back to 1.0, which in fact implies that the crack closes perfectly which is an approximation to real behaviour, although the error is reasonable.

3.3. Simulation Techniques of Reinforced Concrete Cracking

As mentioned earlier, crack representation in reinforced concrete can be classified into discrete and smeared models in finite element analysis. The former approach simulates a crack as a geometrical discontinuity, whereas the latter imagines a cracked solid to be a continuum. In the following sections, the discrete crack model will be briefly described and the smeared crack model will be discussed in detail. In particular, the orthogonal fixed crack, non−orthogonal strain decomposed fixed crack and rotating crack models are derived and examined. The smeared models have all been programmed and compared numerically, some results of which are reported later.

3.3.1 Discrete Crack Model

As shown in Fig.3.6 Ngo and Scordelis[Ngo 1967] and Nilson[Nilson 1968] analysed a particular crack configuration of the beam. The cracks were modelled by the separation of the predetermined nodal points. Special spring or linkage elements were placed across the crack to simulate aggregate interlock (see Fig.3.7). Nilson allowed the finite element model to generate the location of the

cracks. In this representation, cracking is based on the average stress in two adjacent elements. When the average stress exceeds the tensile strength of the concrete, the elements were disconnected.

Later, this method of representing discrete cracks was further improved by partially automating the generation of crack patterns by Mufti et al[Mufti 1970 and 1972] and Al-Mahaidi[Al-Mahaidi 1979]. The former author incorporated a predefined crack utilizing two nodes at one point connected by a linkage element which had no physical dimension before cracking. When the stress in the adjacent elements exceeded the concrete strength, the linkage element was softened to allow the crack to open. The remaining stiffness represented interlock. The latter author followed a similar routine by defining either two or four nodes at a single point, tied together by stiff linkage elements until cracking occurs. In his model, aggregate interlock was also represented by varying the stiffness of the linkage elements. Two nodal points allow cracking in one direction while four nodal points at each boundary intersection allow cracking in two directions (Fig.3.7).

However, all the approaches above suffer from two drawbacks. First, it implies a continuous change in nodal connection, which dose not fit the nature of the finite element method. Second, the the crack is constrained to follow a predefined path along the element edges, which puts doubts on the fidelity of the approach compared to reality.

The drawbacks are generally considered to be serious and attempts to eliminate them have been reported only sporadically. Prominent amongst these are the introduction of graphics-aided algorithms of automatic remeshing and of techniques which permit discrete cracks to extend through finite elements[Blaauwendraad 1981 and 1985].

On the other hand, a class of problems do exist where the exact orientation of the discrete crack is not necessarily the prime subject of interest, for example mode I fracture at a crack tip in the form of a straight separation band, the location of which is known in advance, or in some engineering problems in which cracking is dominant in a particular position only. For such cases, the above drawbacks vanish and a simple form of discrete cracks with a predefined orientation can be used.

3.3.2 Smeared Crack Models

The smeared crack modelling is based on the assumption that the concrete element is a continuum. The approach, introduced by Rashid[Rashid 1968], starts from the notion of stress and the strain permitting a description of cracking in terms of a stress–strain relationship. It is sufficient to switch from the initial isotropic stress–strain law to an orthotropic law upon crack formation, with the axes of orthotropy being determined according to the condition of crack initiation. The procedure is attractive not only because it preserves the topology of the finite element mesh, but also because it does not impose restrictions with respect to the orientation of crack directions. It is for these two reasons that smeared models quickly replaced the early discrete ones and came into widespread use during the 1970s.

In fact, ever since cracking has been modelled, the discrete concept and the smeared concept have been the subject of much controversy. The discrete concept fits our natural conception of fracture since we generally accept fracture as a true geometrical discontinuity. Conversely, it has been stated that a smeared representation might be a more realistic consideration for the "band of micro–cracks" that blunt fracture in matrix–aggregate composites like concrete. The width of such a band which occurs at the tip of a visible crack has even

been claimed to be a material property. At present, however, it is difficult to judge these arguments since experimental detections are scarce and contradictory as far as whether these processes occur in a discrete manner or not[Diam 85, Tait 86]. Furthermore, it is indeed correct that the cracking distributions vary from structure to structure due to the arrangement of the reinforcement and the steel– concrete ratio.

The arguments change when a distributed fracture is considered. Examples are the diffuse crack patterns in large– scale shear walls or panels due to the presence of densely distributed reinforcement. Such cases provide a true physical basis for the smeared concept, at least if the scale of the representative continuum is large compared to the crack spacing. Therefore, the smeared concept is a rational approach towards distributed fracture while the use of the discrete concept, which considers each individual crack as if "under a magnifying glass", clearly becomes unwieldy.

3.3.3 Failure Criteria

The cracking failure criteria to predict crack initiation can be used with any crack modelling concept. Two types of cracking critera are commonly employed. In maximum stress theory, it is assumed that cracking occurs when the maximum tensile stress in a direction exceeds the limiting value of tensile stress, while the maximum strain theory assumes that the crack appears when a maximum tensile strain reaches a limiting value. These two criteria are in fact the same if ν = 0.0. A crack is normally assumed to occur in a plane normal to the direction of the principal stress or strain.

The two criteria are compared against a typical two dimensional failure envelope of concrete in tensile regions in Fig.3.8. The stress theory overestimates

the fracture stress whilst the strain theory underestimates it.

In this study, the maximum stress criterion is used.

3.4 Smeared Crack Models

Smeared crack concepts can be categorized into fixed and rotating crack concepts. With a fixed concept, the orientation of the crack is fixed during the entire computation process, whereas a rotating concept allows the orientation of the crack to co-rotate with the axes of principal strain and stress.

In all methods, the initial crack at a point is determined by the appropriate failure criteria. However, if this crack is caused by stresses or strains higher than the allowed maximum stress/strain value due to the increment step size, the resulting crack angle will be different from that if sufficient incremental quantities had been added. Therefore, the effect of increment size can be minimized by calculating the correct angle. The formulation used in this study is

$$\alpha_c = \frac{1}{2} \tan^{-1} \left[\frac{\tau_{xy} + \Delta\tau''_{xy}}{(\sigma_x + \Delta\sigma''_x) - (\sigma_y + \Delta\sigma''_y)} \right] \qquad (3.5a)$$

where $\{\Delta\sigma''\} = F \cdot \{\Delta\sigma\}$, F is a correction factor, $\{\Delta\sigma\}$ is the stress incremental vector obtained in the solution and $\{\Delta\sigma''\}$ is the proportion of incremental stress sufficient to cause cracking.

F is calculated on the assumption of proportionality of stress and is given by

$$F = \frac{-\beta + \sqrt{(\beta^2 - 4\,\alpha\,\lambda)}}{2\alpha} \qquad (3.5b)$$

where

$$\alpha = (\Delta\tau^2_{xy} - 4\,\Delta\sigma_x\,\Delta\sigma_y)$$

$$\beta = 2\,[\tau_{xy}\,\Delta\tau_{xy} + 2(\sigma_{cr} - \sigma_y)\Delta\sigma_x + 2(\sigma_{cr} - \sigma_x)\Delta\sigma_y]$$

$$\lambda = [\tau^2_{xy} - 4(\sigma_{cr} - \sigma_x)(\sigma_{cr} - \sigma_y)]$$

For maximum strain criterion, a similar procedure can be followed by replacing $\{\sigma\}$ with $\{\epsilon\}$, and $\{\Delta\sigma\}$ with $\{\Delta\epsilon\}$.

3.4.1 Fixed Crack Models

In fixed crack models, the crack direction is fixed during subsequent loading and the next crack can only occur at a right angle or at a predefined angle to the previous one. These are modelled by orthogonal and non–orthogonal strain–decomposed crack models, respectively.

3.4.1.1 Orthogonal Fixed Crack Model

When the first crack occurs, the material properties associated with σ_1 are modified. In the local crack system, the adopted relationship adopted in this study is given by

$$\begin{bmatrix} \Delta\sigma_1 \\ \Delta\sigma_2 \\ \Delta\tau_{12} \end{bmatrix} = \begin{bmatrix} E_c' & 0 & 0 \\ 0 & E_c & 0 \\ 0 & 0 & \beta G \end{bmatrix} \begin{bmatrix} \Delta\epsilon_1 \\ \Delta\epsilon_2 \\ \Delta\gamma_{12} \end{bmatrix} \qquad (3.6)$$

where E_c' denotes the reduced elastic modulus and β is a shear retention factor. This is a special case of eq.(3.2) in which the Poisson effect is ignored after cracking.

A second crack is allowed to form at a right angle to the first one and the constitutive relationship in the local crack system is then modified accordingly. Crack closing and reopening are checked by examing the normal strain ϵ_{cr} across the crack, i. e. a crack closes if

$$\epsilon_{cr} \leqslant \epsilon_R \tag{3.7a}$$

and re– opens if

$$\epsilon_{cr} \geqslant \epsilon_R \tag{3.7b}$$

where ϵ_R is a residual strain. In this study $\epsilon_R = 0$.

3.4.1.2 Strain Decomposed Model

Basic Concept

The strains in the above equations represent an overall incremental strain of the cracked concrete which includes the strain due to cracking as well as the strain of the concrete between the cracks which represents uncracked concrete. Consequently, the stress– strain laws correspond to a smeared– out relation for the cracked concrete, without making any distinction between the crack and the solid material between cracks. However, a particular crack law usually starts from the notion of crack strain rather than total strain, which can not be incorporated in a transparent manner. A disadvantage therefore arises. Indeed, a gap has tended to develop between the sophisticated crack models developed by material scientists and the coarse smeared crack concepts employed by structural analysts. For instance, the choice of the shear retention factors was often made arbitrarily

without reference to aggregate–interlock models, and the stress–strain relations were employed regardless to the coincidence of their directions.

A solution to this deficiency is to decompose the total strain $\Delta\epsilon$ of the cracked concrete into a part $\Delta\epsilon^{cr}$ of the crack and a part $\Delta\epsilon^{co}$ of the solid material between the cracks (superscript ^{cr} and ^{co} refer to the crack and solid concrete respectively), i.e.

$$\Delta\epsilon = \Delta\epsilon^{cr} + \Delta\epsilon^{co} \qquad (3.8a)$$

The importance of the decomposition has been recognized by a number of researchers[Litton 1974, Bazant 1980, de Borst 1985, Rots 1985a, Riggs 1986]. It is in essence an attempt to come closer to the discrete crack concept which completely separates the solid material from the crack by using separate finite elements, and in which the concrete element and the linkage element models the cracking mechanism using different constitutive laws.

The strain vectors in eq.(3.7) relate to the global axes and for a three dimensional configuration they have six components. The global crack strain vector is given by

$$\Delta\epsilon^{cr} = [\ \Delta\epsilon_{xx}^{cr}\ \ \Delta\epsilon_{yy}^{cr}\ \ \Delta\epsilon_{zz}^{cr}\ \ \Delta\gamma_{xy}^{cr}\ \ \Delta\gamma_{yz}^{cr}\ \ \Delta\gamma_{zx}^{cr}\ ]^T \qquad (3.8b)$$

where x, y and z refer to the global coordinate axes and the superscript T indicates a transpose. When incorporating crack traction–crack strain laws it is convenient to set up a local n, s, t–coordinate system which is aligned with the crack, as shown in Fig.3.9. In the local system, a local crack strain Δe^{cr} is defined as

$$\Delta e^{cr} = [\ \Delta\epsilon_{nn}^{cr} \quad \Delta\gamma_{ns}^{cr} \quad \Delta\gamma_{nt}^{cr}\ ]^T \tag{3.9}$$

where the components in the brackets are the mode I crack normal strain and the mode II and III shear strains respectively. The other three remaining crack components in the local system do not have a physical meaning and can be omitted.

The relation between local and the global crack strain is then obtained by

$$\Delta\epsilon^{cr} = T\ \Delta e^{cr} \tag{3.10}$$

where T is a transformation matrix reflecting the orientation of the crack.

A fundamental feature of the present concept is that the orientation of the crack is assumed to be fixed upon crack formation, so that the concept belongs to the class of fixed crack concepts. For a three dimensional configuration T is given by

$$T = \begin{bmatrix} l_x^2 & l_x\, l_y & l_z\, l_x \\ m_x^2 & m_x\, m_y & m_z\, m_x \\ n_x^2 & n_x\, n_y & n_z\, n_x \\ 2l_x m_x & l_x m_y + l_y m_x & l_z m_x + l_x m_z \\ 2m_x n_x & m_x n_y + m_y n_x & m_z n_x + m_x n_z \\ 2n_x l_x & n_x l_y + n_y l_x & n_z l_x + n_x l_z \end{bmatrix} \tag{3.11}$$

where l_x, m_x and n_x form a vector which indicates the direction of the local normal axis expressed in global coordinates. In accordance with this convention, the direction cosines with subscript y indicates the local s– axis and those with

subscript z indicate the local t− axis. For a plane stress configuration the third column and third, fifth and sixth rows of eq(3.11) vanish, rendering a 3 by 2 matrix, while for axi− symmetric and plane strain configurations the third column and the fifth and sixth rows of eq.(3.11) vanish, leading to a 4 by 2 matrix. In other words, the reduced number of rows corresponds to the reduced number of global strain components, while the reduction from three to two columns arises from the fact that the mode II component vanishes.

In the local coordinate system, we define a vector Δt^{cr} of incremental tractions across the crack

$$\Delta t^{cr} = [\ \Delta t_n^{cr} \quad \Delta t_s^{cr} \quad \Delta t_t^{cr}\ ]^T \tag{3.12}$$

where Δt_n^{cr} in the mode I normal traction and Δt_s^{cr} and Δt_t^{cr} are mode II and mode III shear traction increments as shown in Fig.3.9. The relation between stress increment $\Delta\sigma$ and the local traction increment can be derived as

$$\Delta t^{cr} = T^T \ \Delta\sigma \tag{3.13}$$

In order to complete the system of equations, a constitutive model for intact concrete and a traction− strain relation for the smeared cracks is needed. For the concrete between the cracks a relationship is given by

$$\Delta\sigma = D^{co} \ \Delta\epsilon^{co} \tag{3.14}$$

where the matrix D^{co} contains the instantaneous modulus of the uncracked concrete. In a similar way, a relation is inserted between the local crack strain and the local tractions

$$\Delta t^{cr} = D^{r} \ \Delta e^{cr} \tag{3.15}$$

where D^{cr} is a constitutive matrix incorporating the crack properties of the mode I, the mode II and the mode III. This will be discussed in detail later.

The overall stress– strain relation for the cracked concrete with respect to the global coordinate system can now be developed. Substituting eq.(3.8) into (3.7), and subsequently (3.7) into (3.14), yields

$$\Delta\sigma = D^{co} [\Delta\epsilon - T \Delta e^{cr}] \qquad (3.16)$$

Pre– multiplying eq.(3.16) by T^T and substituting eq.(3.15) and (3.13) into the resulting left side of eq.(3.16) gives the relation between the local crack strain and the global strain, i. e.

$$\Delta e^{cr} = [D^{cr} + T^T D^{co} T]^{-1} T^T D^{co} \Delta\epsilon \qquad (3.17)$$

The overall relation between global stress and global strain is therefore obtained by substituting eq.(3.17) into eq.(3.16),

$$\begin{aligned} \Delta\sigma &= [D^{co} - D^{co} T [D^{cr} + T^T D^{co} T]^{-1} T^T D^{co}] \Delta\epsilon \\ &= D^{crco} \Delta\epsilon \end{aligned} \qquad (3.18)$$

where D^{crco} indicates the expression between the brackets, referring to the cracked concrete.

In this relation, it is noticed that as long as the the constitutive matrices D^{co} and D^{cr} remain symmetric, symmetry is also preserved with regard to the constitutive relation eq.(3.18) for the cracked concrete.

In the incremental expression of eq.(3.18) two points need to be addressed for proper cracked concrete modelling. First, the relation implies a linearization around the current state, which means that the stress increment computed holds

exactly only if D^{co} and D^{cr} remain constant during the current strain increment. If either of these matrices is not constant, which occurs for instance if the concrete model involves plasticity or if the crack model involves nonlinear fracture functions, eq.(3.18) serves as a first order approximation. A corrective procedure is then provided by an inner iteration loop that repeatedly evaluates eq.(3.17) and eq.(3.16). However, in the case of strong discontinuities (e. g. very steep softening), the method may sometimes fail, as pointed out by Rots[Rots 1986].

Secondly, in this incremental expression the state change of the concrete stress due to crack initiation, closing and re-opening should be involved. The criteria are generally defined in terms of total local crack stress or crack strain, which can be obtained from the global stress or strain at the sampling point. In this study, strains are used as described for the orthogonal fixed crack model.

3.4.1.3 Multi-directional Fixed Crack Model

An advantage of the decomposition of the total strain into the concrete strain and crack strain is that it allows for a sub-decomposition of the concrete strain and crack strain individually. In this study, a sub-decomposition of the concrete strain[de Borst 1986] will not be considered, only a sub-decomposition of the crack strain. This then will allow for the separate contributions from a number of multi-directional cracks which occur at a sampling point simultaneously. The crack strain is given by

$$\Delta\epsilon^{cr} = \Delta\epsilon_1^{cr} + \Delta\epsilon_2^{cr} + \ldots \qquad (3.19)$$

where $\Delta\epsilon_1^{cr}$ is the global crack strain increment owing to a primary crack, $\Delta\epsilon_2^{cr}$ is the global crack strain increment owing to a secondary crack and so on.

In fact, the idea of such sub-decomposition of the crack strain is not new. It was advocated by Litton[Litton 1974]. The essence of the approach is that each fixed crack is assigned its own local crack strain vector e_i^{cr} and its own traction vector t_i^{cr} and its own transformation matrix T_i, according to eqs.(3.9), (3.12) and (3.11), respectively. Furthermore, it is convenient to assemble these single-crack vectors and matrices into

$$\Delta\hat{e}^{cr} = [\ \Delta e_1^{cr} \quad \Delta e_2^{cr} \quad \dots\ ]^T \tag{3.20}$$

$$\Delta\hat{t}^{cr} = [\ \Delta t_1^{cr} \quad \Delta t_2^{cr} \quad \dots\ ]^T \tag{3.21}$$

$$\Delta\hat{T}^{cr} = [\ \Delta T_1^{cr} \quad \Delta T_2^{cr} \quad \dots\ ] \tag{3.22}$$

In these formulae above, $\hat{}$ indicates an assembly of multi-directional cracks. Similar to eq.(3.10), eq.(3.19) becomes

$$\Delta\hat{\epsilon}^{cr} = \hat{T}^{cr}\Delta\hat{e}^{cr} \tag{3.23}$$

In a similar way, the single-crack traction-strain relations can be expanded into a multi-crack equivalent of eq.(3.15)

$$\Delta\hat{t}^{cr} = \hat{D}^{cr}\,\Delta\hat{e}^{cr} \tag{3.24a}$$

or in matrix form

$$\begin{bmatrix} \Delta t_1^{cr} \\ \Delta t_2 \\ \dots \end{bmatrix} = \begin{bmatrix} D_{11}^{cr} & D_{12}^{cr} & \dots \\ D_{21} & D_{22} & \dots \\ \dots & \dots & \dots \end{bmatrix} \begin{bmatrix} \Delta e_1 \\ \Delta e_2 \\ \dots \end{bmatrix} \tag{3.24b}$$

From this expression, it is seen that the relation is very general since it allows for interaction between the cracks via the off-diagonal submatrices.

In the similar way to the single crack strain decomposition concept described in the previous section, an analogous expression for multi–directionally cracked concrete is obtained.

$$\Delta\sigma = [\ D^{co} - D^{co}\ \hat{T}\ [\ \hat{D}^{cr} + \hat{T}^{T}\ D^{co}\ \hat{T}\ ]^{-1}\ \hat{T}^{T}\ D^{co}\ ]\ \Delta\epsilon \tag{3.25}$$

in which the assembled matrices $\hat{T}$ and $\hat{D}^{cr}$ are inserted instead of the single crack matrices T and D^{cr}. By using eq.(3.25), the cracking state at a point can be represented by cracks in different directions at the same time, i. e. a multi–directional cracking state. However, if this occurs it does cause some difficulties in computation.

After an initial crack direction has been established potential subsequent crack directions are defined by a 'threshold angle' α_{th} in relation to the original crack direction. These are checked in turn through 180°. e. g. if $\alpha_{th} = 30.0$, then 5 directions are examined for potential cracks.

Cracking States

A state change for one of the cracks promotes state changes in the others. For instance, the initiation of a new crack encourages existing cracks to close. If such multiple state changes occur during the current strain increment, the 'most critical' state changes should be traced and handled first, while subsequent state changes should be treated by splitting $\Delta\epsilon^{cr}$ in its turn. Depending on the particular crack closing condition, this procedure may become elusive and it may be more convenient to allow only one crack to change its state during the incremental simulation. In the latter case, inconsistencies can not entirely be avoided, since postponing crack closing involves the crack normal strain to

temporarily become negative, which is physically meaningless.

Constitutive Relationships

As pointed out above, the material constitutive relationship D^{co} are the properties of the uncracked concrete, in which the initial value of the Young's modulus E is used. But the structure of the material matrix D^{cr} is slightly more complicated than that of the stress–strain matrix D^{co} due to that the size D^{cr} is dependent on the number of the opening cracks in an integration point. For one crack, it is a 2 x 2 matrix while for two cracks it is a 4 x 4 matrix and so on. For n open cracks, a reasonable approximation is given by

$$D^{cr} = \left[\begin{array}{cc|c} D_1^{cr} & 0 & 0 \\ 0 & D_2^{cr} & 0 \\ \hline 0 & 0 & D_n^{cr} \end{array}\right] \qquad (3.26)$$

where all the off–diagonal terms are zero. This indicates that no coupling effects between different cracks are considered. The stress increment in crack n is assumed to depend on the crack strain increment of the same crack only. The relation is given by the two by two submatrix D_n^{cr}. This is actually a simplification of reality since the amount of damage which has already been done in an existing crack reduces the energy that can be released in subsequent cracks. Furthermore, the off–diagonal terms of the submatrices in the constitutive matrix D_n^{cr} are zero. This assumption implies that no coupling is taken into account between the normal stress increment in a crack and the shear strain increment.

Based on the above assumptions, we can put simple material models into practice. From Fig.3.10, it is seen that in the case of one crack the relation

between the normal stress increment Δt_n^{cr} and the normal strain increment Δe_n of the cracked concrete is given by E_t, the modulus of the descending portion. By the virtue of the decomposition of eq.(3.7), the concrete and crack act like springs connected in series, which gives

$$\frac{1}{E^{cr}} = \frac{1}{E} + \frac{1}{E_t} \tag{3.27}$$

where E^{cr} represents the modulus of the cracked concrete.

E is the Young's modulus of the uncracked concrete.

The relation between the normal stress Δt_n^{cr} of the cracked concrete and the normal strain of crack Δe_n^{cr} can be worked out to be

$$E^{cr} = EE_t/(E-E_t) \tag{3.28}$$

For shear stress–strain relation, it is assumed that the shear strain increment $\Delta\epsilon_{12}$ of the crack and the shear increment $\Delta\sigma_{12}$ of that crack are related through $\frac{1}{2}\ \beta E/[(1-\beta)(1+\nu)]$, where ν is Poisson's ratio and β is the shear retention factor. This derives from the decomposition of the total shear strain increment into a concrete and into a crack shear strain increment.

With the above relations, the decomposed crack approach can be connected with the more traditional approaches which assume the relation $\frac{1}{2}\ \beta E/(1+\nu)$ between the total shear strain increment and the shear stress increment. The following expression can therefore be obtained for a crack:

$$D_n^{cr} = \begin{bmatrix} \frac{\mu E}{1-\mu} & 0 \\ 0 & \frac{\beta}{1-\beta}\frac{E}{2(1+\nu)} \end{bmatrix} \tag{3.29}$$

where $\mu = E_t/E$, indicates the reduction of Young's modulus.

The magnitude of E_t mainly depends on the ultimate normal strain ϵ_u of the descending portion, which has to be adjusted in accordance with the element size as to obtain objective results with regards to the finite element mesh. The fundamental parameter which governs crack propagation is then the fracture energy.

In the decomposed multi–directional cracking model, a simple descending portion of the concrete stress–strain curve is usually adopted for cracking strain since more complex relations (for example trilinear or curved) will make the procedure difficult. However, it is noticed that the existing strain–stress law governs overall behaviour with regard to total strain and stress while the crack strain should be distinguished from overall concrete strain since these two strain concepts are physically not the same. In order to obtain a better understanding, more experimental investigation is needed regarding the two different strain concepts.

3.4.1.4 Relation Between Different Fixed Crack Models

Having studied the strain decomposition concepts for both single crack and multi–directional cracks, it is important to investigate the relation between the multi–directional decomposed crack model and other crack models which are usually employed in the finite element analysis of reinforced concrete structures. Particularly, the relation with the fixed single crack model and fixed two directional orthogonal cracking models are of primary interest.

Single Directional Crack

If there is a crack in the y– direction with its normal aligned with the x–axis, the transformation matrix T is then given by

$$T = \begin{bmatrix} 1 & 0 \\ 0 & 0 \\ 0 & 1 \end{bmatrix} \tag{3.30}$$

The constitutive relation of the concrete is well known and is given by the following equation

$$D^{co} = \frac{E}{1 - \nu^2} \begin{bmatrix} 1 & \nu & 0 \\ \nu & 1 & 0 \\ 0 & 0 & (1 - \nu)/2 \end{bmatrix} \tag{3.31}$$

for the plane stress problem. Then

$$T^T D^{co} T = \frac{E}{1 - \nu^2} \begin{bmatrix} 1 & 0 \\ 0 & (1 - \nu)/2 \end{bmatrix} \tag{3.32}$$

Adding the stress–strain matrix D^{cr} for the crack and inverting the resulting matrix yields:

$$[\, D^{cr} - T^T D^{co} T \,]^{-1} = \frac{E}{1 - \nu^2} \begin{bmatrix} \dfrac{1 - \mu}{1 - \mu \nu^2} & 0 \\ & \dfrac{2 (1 - \beta)}{1 - \nu} \end{bmatrix} \tag{3.33}$$

Premultiplying with $D^{co} T$ and postmultiplying with $T^T D^{co}$ and subtracting from D^{co} gives

$$D^{co} - D^{co}\, T \left[D^{cr} + T^{T} D^{co} T \right]^{-1} T^{T} D^{co} =$$

$$\begin{bmatrix} \dfrac{E_t}{1-\mu\nu^2} & \dfrac{\nu\mu E_t}{1-\mu\nu^2} & 0 \\ \dfrac{\nu\mu E_t}{1-\mu\nu^2} & \dfrac{E}{1-\mu\nu^2} & 0 \\ 0 & 0 & \beta G \end{bmatrix} \qquad (3.34)$$

where $G = \dfrac{E}{2\,(1+\nu)}$, the shear modulus of the concrete.

This was obtained by Bazant and Oh[1983] when they investigated cracked concrete. The only difference is that the shear term is included in the above equation, while Bazant and Oh expressed their equation in terms of the principal stress directions, i. e. in the local system.

If a crack is at an arbitrary inclined angle, exactly the same conclusion will be reached.

Two–directional Orthogonal Cracks

If two cracks open in two directions x– and y– at a point, the transformation matrix will be

$$T = \begin{bmatrix} 1 & 0 & 0 & 0 \\ 0 & 0 & 1 & 0 \\ 0 & 1 & 0 & -1 \end{bmatrix} \qquad (3.35)$$

Following a similiar procedure to that of the single crack gives:

$$D^{co} - D^{co}\, T \left[D^{cr} + T^{T} D^{co} T \right]^{-1} T^{T} D^{co} =$$

$$\begin{bmatrix} 0 & 0 & 0 \\ 0 & 0 & 0 \\ 0 & 0 & \dfrac{\beta}{(2-\beta)}G \end{bmatrix} \qquad (3.36)$$

again $G = \dfrac{E}{2(1+\nu)}$, the shear modulus of the concrete.

From this expression, it is noticed that the shear retention factor is not the commonly used value β but $\beta/(2-\beta)$. This is because the factor which has been adopted in the constitutive relation $\mathbf{D}^{cr}$ for the crack is $\beta/(1-\beta)$, which is derived on the assumption that there is only one crack existing. Indeed, if two direction cracks are taken into account, it may assumed that the total strain is composed of the concrete strain and strain of the two cracks, and the reduction factor should be equal to $2\beta/(1-\beta)$ for each crack. Having assumed this, the shear retention factor would be β, which becomes exactly the same as that in the conventional two-direction orthogonal crack model. However, there is not much difference whether or not the above assumption is made, as shown in Fig.3.11.

Using the same procedure, the relation with other non-orthogonal models can be derived although the algebraic manipulation is more tedious and cumbersome[Litton 1976 and de Borst and Nauta 1985].

3.4.2 Rotating Crack Model

Basic Concept

In order to overcome the misalignment of principal stress and strain directions and crack directions in fixed crack modelling, Cope et al[Cope 1980] co-rotated the axes of material orthotropy with the axes of principal strain. The approach immediately led to the concept of the "rotating crack". The concept is attractive

from an engineering point of view, since the nonlinear stress– strain relationship for the principal direction can be specified without having to set up complex theories.

In fact, Bazant[Bazant 1983b] raised a number of objections to the earliest versions of the concept. One of them relates to the fact that the assumption of material orthotropy generally implies that the rotation of principal stress deviates from the rotation of principal strain. Consequently, when the axes of material orthotropy co– rotate with the axes of principal strain, they will cease to coincide with the axes of principal stress. The direct use of principal stress– strain curves then becomes inconsistent, unless transformation rules are included in the derivation of the tangential stiffness modulii.

Procedures

To illustrate the concept, consider a two– dimensional configuration of initial coaxiality, with the principal 1 and 2 directions of stress, strain and material orthotropy being aligned. By virtue of Mohr's strain circle, a small increment of shear strain causes the direction of principal strain to rotate by an angle $\Delta\theta_\epsilon$ according to

$$\tan 2\Delta\theta_\epsilon = \frac{\Delta\gamma_{12}}{2\,(\epsilon_{11} - \epsilon_{22})} \qquad (3.37)$$

if $|\Delta\gamma_{12}| << |\,\epsilon_{11} - \epsilon_{22}\,|$. $\Delta\gamma_{12}$ is the shear strain increment in the 1, 2 reference axes. ϵ_{11} and ϵ_{22} are the initial principal strains. In a similar manner, Mohr's stress circle indicates that a small increment of shear stress causes a principal stress rotation by an angle $\Delta\theta_\sigma$ according to

$$\tan 2\Delta\theta_{\sigma} = \frac{\Delta\sigma_{12}}{(\sigma_{11} - \sigma_{22})} \tag{3.38}$$

if $|\Delta\sigma_{12}| << |\sigma_{11} - \sigma_{22}|$. $\Delta\sigma_{12}$ is the shear increment in the reference axes 1 and 2, σ_{11} and σ_{22} are initial principal stresses.

Preserving coaxiality between principal stress and strain requires

$$\Delta\theta_{\epsilon} = \Delta\theta_{\sigma} \tag{3.39}$$

Using the orthotropic law of the principal stress–strain in reference axes 1 and 2, this condition is satisfied if and only if the tangential shear modulus G_{12} is given by

$$G_{12} = \frac{\sigma_{11} - \sigma_{22}}{2(\epsilon_{11} - \epsilon_{22})} \tag{3.40}$$

The linearized form of the tangential stress–strain law for a consistent rotating crack then becomes

$$[\ \Delta\sigma_{11}\quad \Delta\sigma_{22}\quad \Delta\sigma_{33}\quad \Delta\sigma_{12}\quad \Delta\sigma_{23}\quad \Delta\sigma_{31}\ ]^{T} =$$

$$
\begin{bmatrix}
\frac{\partial\sigma_{11}}{\partial\epsilon_{11}} & \frac{\partial\sigma_{11}}{\partial\epsilon_{22}} & \frac{\partial\sigma_{11}}{\partial\epsilon_{33}} & 0 & 0 & 0 \\
\frac{\partial\sigma_{22}}{\partial\epsilon_{11}} & \frac{\partial\sigma_{22}}{\partial\epsilon_{22}} & \frac{\partial\sigma_{22}}{\partial\epsilon_{33}} & 0 & 0 & 0 \\
\frac{\partial\sigma_{33}}{\partial\epsilon_{11}} & \frac{\partial\sigma_{33}}{\partial\epsilon_{22}} & \frac{\partial\sigma_{33}}{\partial\epsilon_{33}} & 0 & 0 & 0 \\
0 & 0 & 0 & \frac{\sigma_{11}-\sigma_{22}}{2(\epsilon_{11}-\epsilon_{22})} & 0 & 0 \\
0 & 0 & 0 & 0 & \frac{\sigma_{11}-\sigma_{22}}{2(\epsilon_{11}-\epsilon_{22})} & 0 \\
0 & 0 & 0 & 0 & 0 & \frac{\sigma_{11}-\sigma_{22}}{2(\epsilon_{11}-\epsilon_{22})}
\end{bmatrix}
\begin{bmatrix}
\Delta\epsilon_{11} \\ \Delta\epsilon_{22} \\ \Delta\epsilon_{33} \\ \Delta\gamma_{12} \\ \Delta\gamma_{23} \\ \Delta\gamma_{31}
\end{bmatrix}
\tag{3.41}
$$

where the derivatives $\partial\sigma_{11}/\partial\sigma_{11}$ etc. can be inserted directly since the shear terms guarantee coaxiality between principal stress and strain.

Eq.(3.41) was developed in a more elegant way by Willam et al[Willam 1987]. An alternative formulation was derived by Gupta and Akbar[Gupta 1984] and Crisfield[Crisfield 1987]. They started from a description in a fixed x and y coordinate system.

Since eq.(3.41) is given in incremental form, a corrective procedure must be added in order to suppress drifting from the coaxiality condition. To do so, a inner iteration loop is employed in which eq.(3.40) is repeatedly evaluated using the initial tangential shear term in the first iteration (predictor) and updated tangential shear terms in subsequent iterations (corrector).

As far as the concrete constitutive relationship for the rotating crack approach

is concerned, all the tension stiffening laws can be used directly. The shear modulus is no longer reduced by the retention factor but determined using eq.(3.40). Crack closing and re-opening procedures are identical to those described primarily in Section 3.4.1.1.

It is intriguing to examine the parallels between the fixed smeared multi-directional crack concept and the rotating crack concept. While the fixed multi-directionally decomposed concept controls the formulation of subsequent cracks using the threshold angle, the rotating concept assumes the crack orientation to change continuously. Assuming the threshold angle for multi-directional cracks to vanish, a new fixed crack arises at the beginning of each stage of the incremental process. In doing so, it is observed that the fixed multi-directional concept reduces to the rotating concept, provided that

— the condition of a vanishing threshold angle is the only condition which controls the orientation of subsequent cracks, i. e. it is not supplemental by a maximum stress state as was done in a previous study done by de Borst and Nauta[de Borst and Nauta 85].

— in smeared rotating crack modelling, previous cracks are rigorously made inactive and erased from memory upon activation of the new crack, so that we invariably have only one active crack which is unique to the loading condition.

— the local traction-strain law eq.(3.41) of the active crack is filled in such a way that the memory of the previous effects is accounted for, and the overall shear modulus ensures coaxiality according to eq(3.40), which is iterated in its inner loop.

To be strict, the term "rotating crack" swings the crack direction continuously

while the load increases. When the swinging angle exceeds the "threshold angle" in the fixed crack model, a new fixed crack occurs. This means that the fixed cracks occurs always later than in a continuing rotating crack model. The larger the threshold angle, the later will the crack occur. From this point of view the rotating crack has an advantage over the fixed crack concept since it does not postpone the appearance of the crack corresponding to a certain loading level. Furthermore, the rotating crack uses a shear modulus to enforce the stress and strain directions to coincide with each other. This avoids defects which would otherwise exist in the rotating model, which are unacceptable from a physical point of view due to the tensorially invariant condition of the material[Bazant 1983]. For these reasons, the rotating crack concept gives an acceptable approach to reinforced concrete structural response after cracking.

In addition, it is necessary to point out that in the swinging crack approach, the shear modulus is no longer dependent upon the force transfer mechanism but is determined by the normal strains and stresses in the crack normal surface and its tangential surface in order to force the stress and strain directions to rotate together.

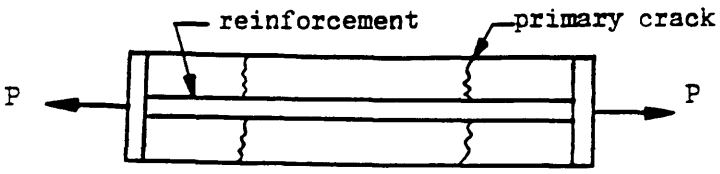

(a) A Freebody of Cracked Reinforced Concrete

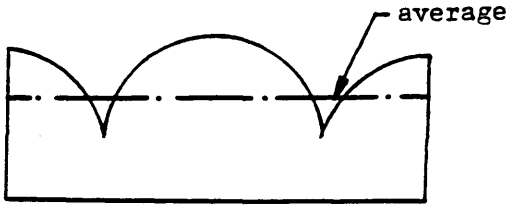

(b) Stress in Concrete

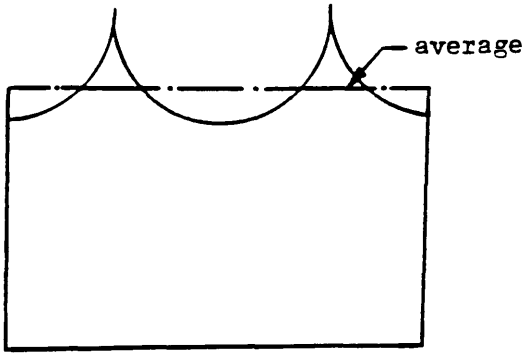

(c) Stress in Reinforcement

Fig.3.1 Stress Distribution in a Cracked Reinforced Concrete Element

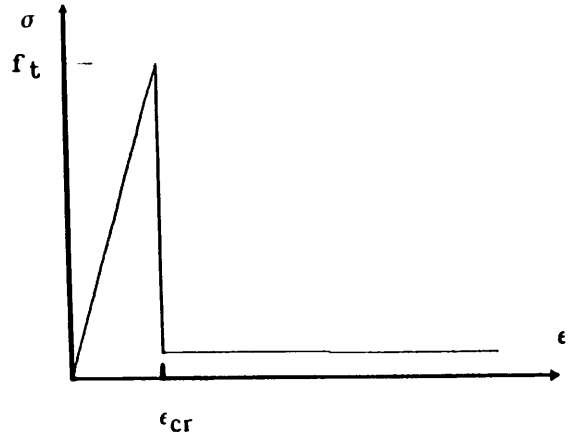

(a) Sudden Drop

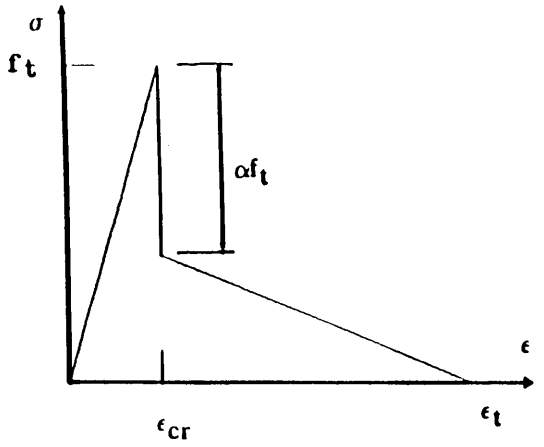

(b) Yamaguchi (1985)

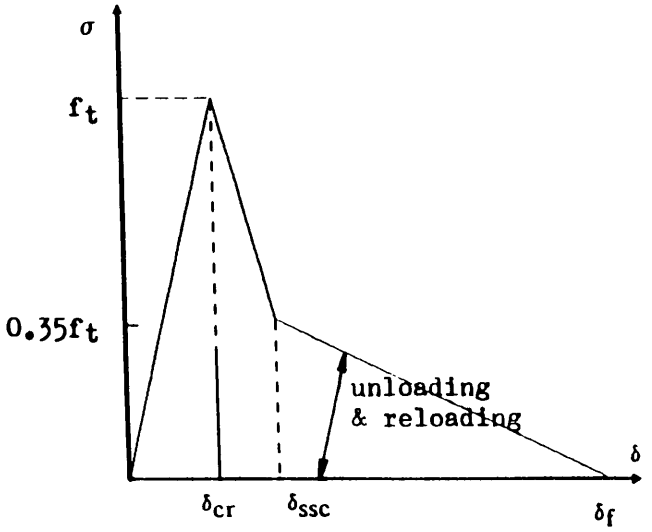

(c) Phillips-Zhang (1990)

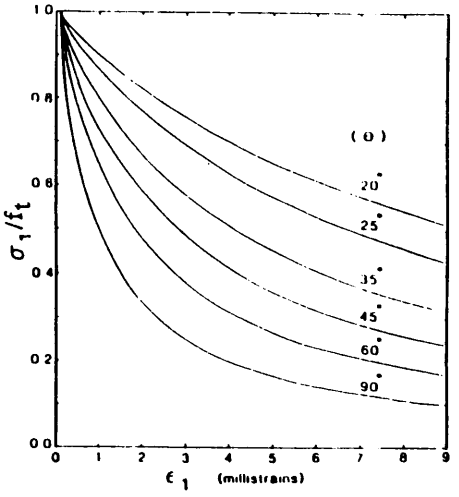

(d) Bhide-Collins (1987)

Fig.3.2 Tension Stiffening Laws

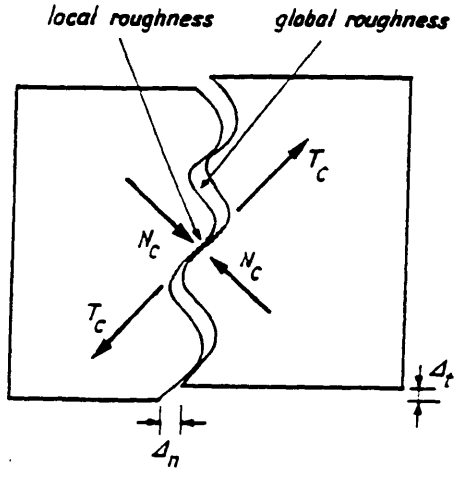

Fig.3.3 Transfer of Shear Forces Cross a Crack by Aggregate Interlock

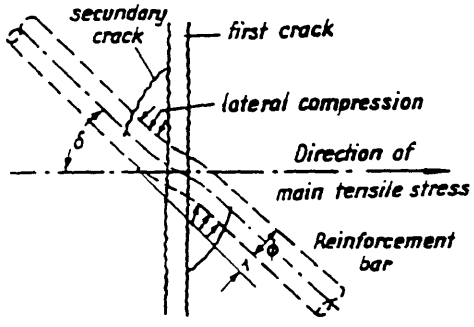

Fig.3.4 Dowel Action of Reinforcement

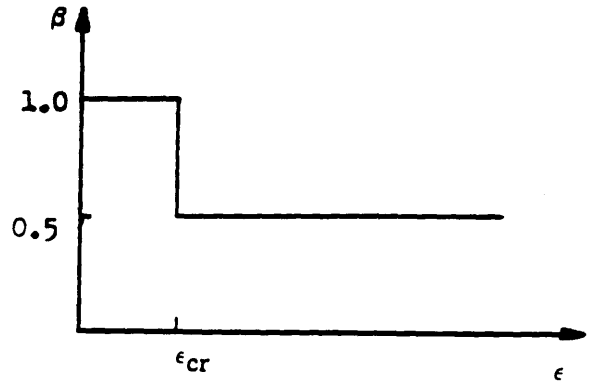

(a) Reduced to a Constant

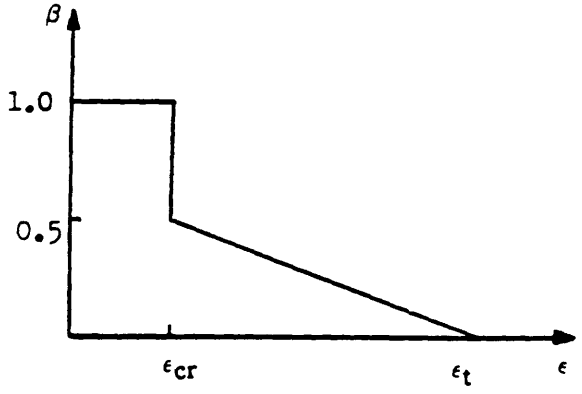

(b) A Linear Reduction

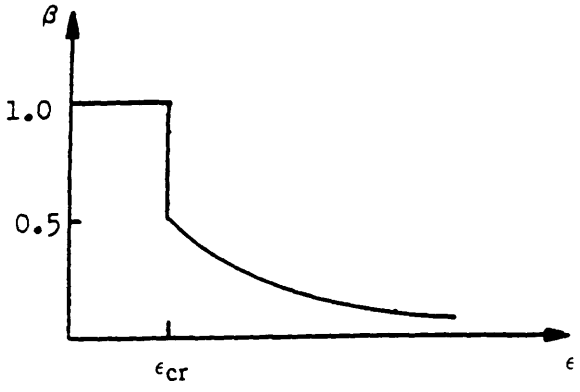

(c) Hyperbolic Reduction

Fig.3.5 Shear Retention Laws

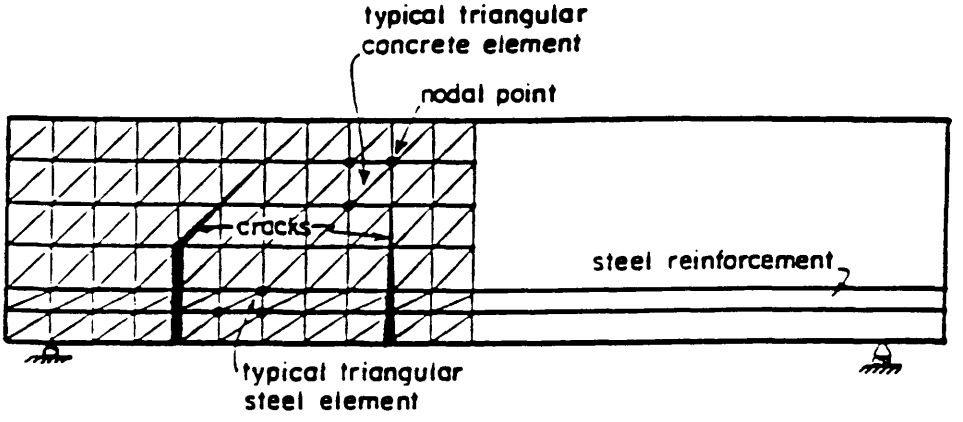

Fig.3.6 Finite Element Model Used by Ngo and Scordelis (1967)

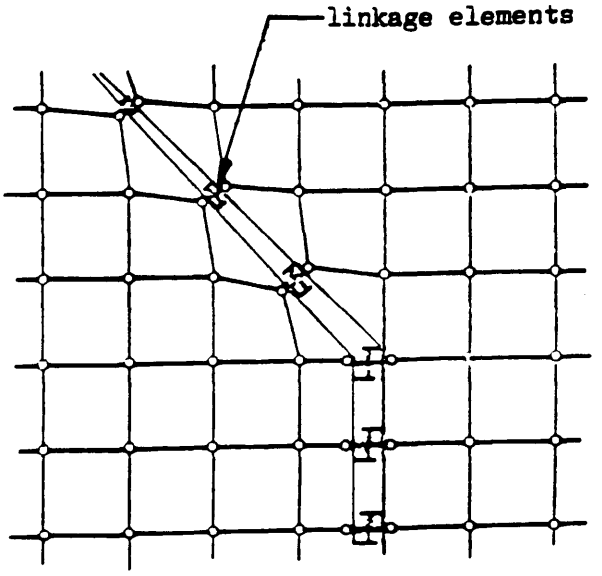

(a) Aggregate Interlock Using Linkage Elements

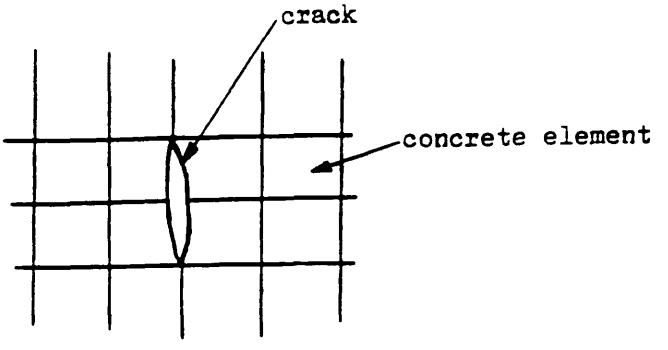

(b) Cracking in One Direction

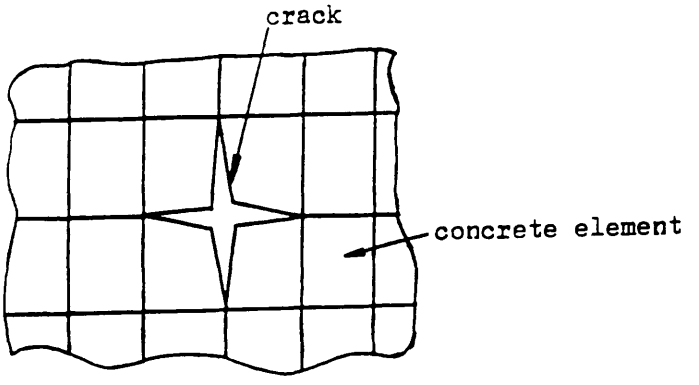

(c) Cracking in Two Directions

Fig.3.7 Discrete Representation of Cracking

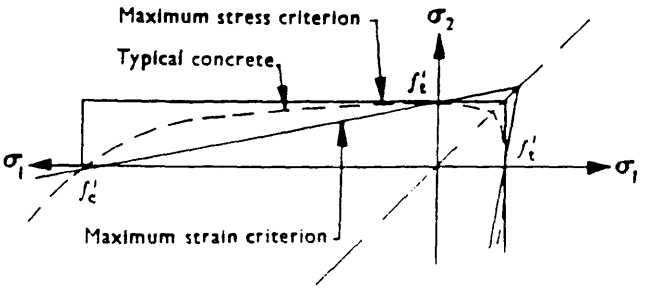

Fig.3.8 Cracking Failure Criteria in Tension

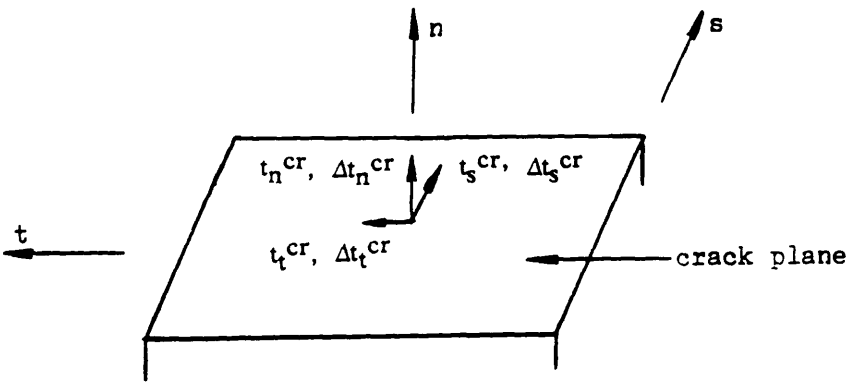

Fig.3.9 Local Coordinates and Tractions Across a Crack

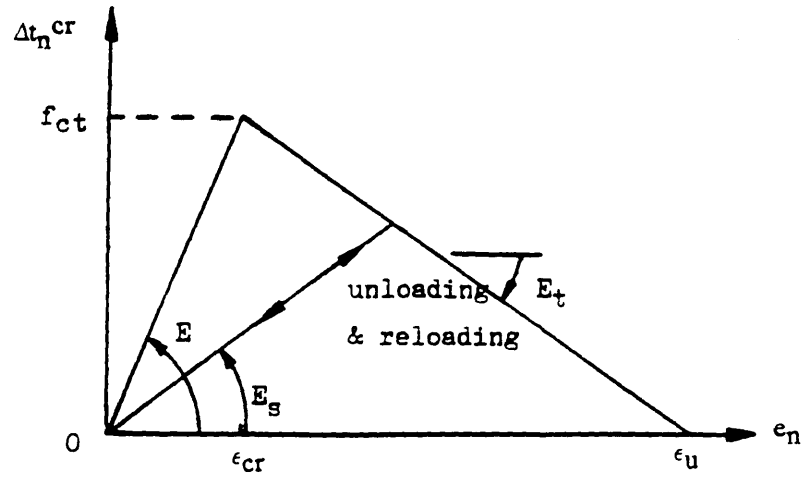

Fig.3.10 Normal Stress V. S. Normal Strain Relationship of Cracked Concrete

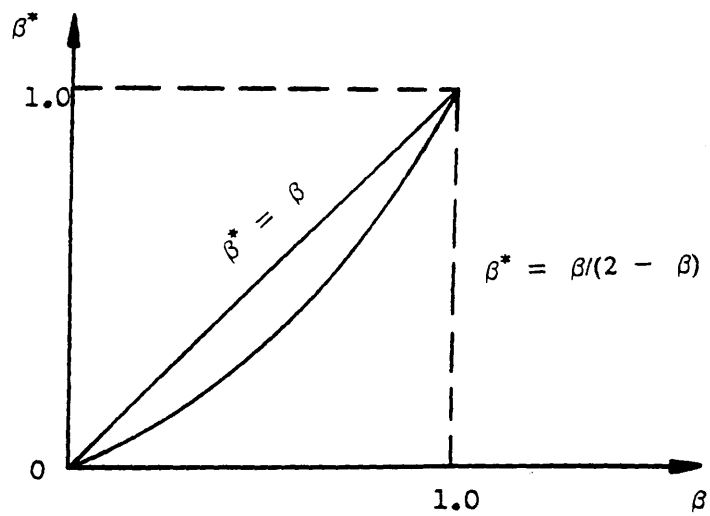

Fig.3.11 Shear Retention in Decomposed Approach

CHAPTER FOUR

FINITE ELEMENT DISCRETISATION OF REINFORCEMENT

4.1 Introduction

Special problems are introduced when the finite element method is applied to reinforced concrete members and structures. These difficulties are mainly due to the combination of the materials, concrete and reinforcement. Acting together they do not satisfy isotropic conditions because they have vastly different material properties, nor do they satisfy compatibility conditions due to bond–slip phenomena. From a mechanical point of view, concrete is generally in a biaxial or even triaxial state of stress while the reinforcement is usually considered to carry uniaxial stress only.

Since the late 1960's, some general agreement has been reached in the modelling techniques of concrete and reinforcement. The concrete can be well represented by selecting a suitable conventional finite element while the reinforcement can be discretised in various alternative ways, depending on the purpose of a particular analysis. Bond–slip effects between concrete and reinforcement can be taken into account if proper choice of reinforcement representation is made.

In this chapter, finite element constitutive relationships for reinforcement are described after briefly presenting the basic characteristics of engineering steel reinforcing bars. Finite element discretisation of reinforcement is also discussed and two new embedded bar models are proposed. Bond–slip modelling is discussed in Chapter 5. Finally, a mesh generation scheme for both concrete and reinforcement is presented. This scheme allows the finite element mesh to be

constructed independently of the reinforcement layout, removing a restriction which has often hindered finite element modelling of reinforced concrete structures.

4.2 Characteristic Properties of Reinforcing Steel

Reinforcing or prestressing steel in a reinforced concrete structure is usually in the form of slender bars or cables. They are, therefore, usually considered to be direct tension or compression members. Behaviour can be adequately approximated by uniaxial stress– strain curves. However, in some cases, especially where a crack occurs and dowel action arises, the steel is not only subjected to uniaxial forces but also to shear and bending forces, behaving like a beam. This effect needs to be taken into account in the detailed analysis of reinforced concrete structures where crack directions are inclined to the reinforcement. However these shear effects are outside the scope of this study, and only the uniaxial behaviour of reinforcing steel bars will be discussed in the following.

Protrusions or deformations, called ribs or lugs, are commonly rolled onto the surface of a reinforcing bar. The deformed lugs restrict the relative longitudinal movement and establish better bond characteristics between the bar and the surrounding concrete. For a smooth bar, a curved anchorage is usually required in the end of the bar in order to properly transfer force from concrete to steel.

The commonly used carbon steel bars[BS 4449] in the U. K. are plain round steel bars in grade 250 and deformed high yield steel bars in grade 460. The nominal sizes of bars in both grades range from 6mm to 50mm. If a bar smaller than 8mm is required the recommended size is 6mm while 50mm is recommended for the use of a bar larger than 40mm.

Typical stress–strain curves for steel reinforcing bars subjected to monotonic loading in tension are shown in Fig.4.1. These are characterized by the following features:

(i) an initial elastic region up the yield strain, ϵ_y;

(ii) a yield plateau from ϵ_y to the strain hardening strain, ϵ_h;

(iii) a strain hardening region from ϵ_h to the ultimate strain ϵ_u and a softening region to the fracture strain ϵ_f;

(iv) Corresponding yield and ultimate stresses are σ_y and σ_u, respectively.

The mechanical properties of reinforcing steel bars vary in a probabilistic manner[ASCE 1982]. The variations in measured mechanical characteristics result from the variability of the steel, variability in the cross–section area of the bar, the rate of loading, and the definition used to specify the property.

As the strength of the reinforcement increases, the capacity to undertake inelastic deformation, or its ductility, decreases. In engineering, ductility is however a most important attribute of reinforcement since it is necessary to ensure the ductile behaviour of concrete structures and hence prevent brittle failure. The steel strength may be increased by changing the chemical composition of the steel, cold working, heat treating, or some combination of such techniques.

For simplicity in design calculations, it is often necessary to idealize the steel stress–strain curve. Three types of idealizations are commonly adopted, as shown in Fig.4.2. For each idealization, it is necessary experimentally to determine the stresses and strains at the onset of the yield, strain hardening and/or ultimate

tensile strength.

If the load is released before failure, the response curve for unloading from any stress state is approximately a straight line parallel to the initial elastic response. Reloading results in a response path approximately the same as the original elastic shape, with perhaps a small hysteresis and/or a strain hardening effect. Then it continues closely on the remainder of the virgin stress– strain curve as if unloading had not occurred. When subjected to stress reversal after initial yielding the reloading retraces the unloading path with very minor deviation until the previous initial yielding point is reached again, where plastic flow occurs again. The previous initial yielding point is then interpreted as a subsequent yield point in a strain hardened material. However, if the material first hardened in tension, and is subsequently loaded in compression, the yield point in compression will be less than in tension. This is the well known "Bauschinger Effect". It complicates practical application a lot and is often neglected.

A typical stress– strain response curve with reversed loading is illustrated in Fig.4.3

4.3 Constitutive Relationships for Reinforcement

In the implementation of the steel constitutive relationship into a finite element program, the degree of the sophistication is dependent to a large extent on the special purposes of the program. The most general relationship should include stress, strain, temperature and time for arbitrary histories of these quantities. However, it is usually true that only some of these variables are involved. For instance, for seismic response, loading is rapid, therefore it is essential to cover inelastic strain reversal effects, while temperature and time dependent characteristics are generally not significant. On the other hand, for primary

nuclear containments subjected to severe thermal cycling, it may be necessary to include time and temperature dependent stress relations for the prestressing tendons, but stress reversal will not occur. Generally, it is advantageous to use the simplest constitutive relationship which models the essential behaviour for the particular application.

Since the steel in concrete construction is mainly one-dimensional and although it can be subjected to shear force due to the dowel action, it is rarely necessary to introduce the complexities of a multiaxial constitutive relationship. In finite element modelling, therefore, a uniaxial relationship is widely adopted.

In the purely elastic region, the steel stress is determined by the standard linear-elastic relation.

$$\sigma_s = E_o \ (\epsilon_s - \epsilon_t) \qquad (4.1)$$

where ϵ_s if the total strain, ϵ_t is the thermal strain and E_o is the initial modulus of steel.

For the consideration of plastic deformation, it is common to idealize the behaviour into a bilinear or trilinear stress-strain curve. In this study, a bilinear curve with simple isotropic strain hardening rules has been adopted, based on the following simplifications:

i) The actual stress-strain curve is approximated by an elastic-linear strain hardening curve, as shown in Fig.4.4. Elastic-perfect plastic behaviour is represented by the hardening angle $E_h = 0$.

ii) Unloading after yielding follows a path parallel to the initial elastic slope. The

Bauschinger effect is ignored.

iii) The total strain ϵ_s is decomposed into elastic and inelastic components and the stress σ_s is given by

$$\sigma_s = E_o (\epsilon_s - \epsilon_p - \epsilon_t) \qquad (4.2)$$

in which ϵ_p represents the plastic strain.

In this study, strain and stress calculations are carried out using an incremental–interation procedure. In particular, the following operations are made:

1. Enter with initial stress σ_i, initial strain ϵ_i and current yield stress σ_{yi} and the incremental strain $\Delta\epsilon_i$.

2. Calculate the total strain

$$\epsilon_{i+1} = \epsilon_i + \Delta\epsilon_i \qquad (4.3)$$

3. Calculate the first approximation to the total stress.

$$\sigma_{i+1} = \sigma_i + E_o \Delta\epsilon_i \qquad (4.4)$$

where E_0 is the initial elasticity modulus of steel

4. If the magnitude of the stress is less than the current yield stress $|\sigma_{yi}|$

$$\sigma_{i+1} \leqslant |\sigma_{yi}| \qquad (4.5)$$

then the plastic flow does not occur. The value of the stress is correct and the procedure is terminated.

5. If the stress is greater than the current yield stress, the stress needs to be corrected by

$$|\sigma^{c}_{i+1}| = |\sigma_{iy}| + \frac{E_h}{E_0} [\ |\sigma_{i+1}| - |\sigma_{iy}|\ ] \quad (4.6)$$

where E_h is the strain hardening modulus of the steel, and σ^{c}_{i+1} is the corrected value of the stress. This procedure is shown in Fig.4.5.

6. The current yield stress is then updated by

$$\sigma_{i+1} = |\sigma^{c}_{i+1}| \quad (4.7)$$

The modulus is consequently set to E_h in the calculation of the stiffness.

7. If $\Delta\epsilon_i \prec 0.0$, i. e. the steel is unloading, the stress should be

$$\sigma^{c}_{i+1} = -|\sigma^{c}_{i+1}| \quad (4.8)$$

8. Updated values σ_{i+1}, ϵ_{i+1}, σ_{i+1} are stored into memory for use in the next cycle, in which the steps 1 to 8 are repeated.

When using variable stiffness nonlinear solution algorithms (see Chapter 6), this procedure can encounter difficulties if unloading from the yield surface occurs. If a solution is based on a stiffness using E_h, then it is probable that $\Delta\epsilon_i$ will be considerably larger than that based on the elastic unloading curve. This large reversal of strain could possibly cause a reversal in sign of the yield surface that should not occur. Furthermore, a new modulus would then be selected on the

basis that plastic flow was still occurring, causing automatic reversals of load which increase in size as iterations continue. This is illustrated in Fig.4.6.

Thus it is necessary to suppress the yielding routine so that the correct level of stress and strain can be obtained by normal iteration with the correct modulus as shown in Fig.4.7. This is accomplished by checking whether the sign of the yielding surface should actually occur within one iteration. If the stress given by

$$\sigma_R = \sigma_o + E_h \Delta\epsilon_i \qquad (4.9)$$

is less than the current yield stress then reverse yielding should not occur. Then, steps 5 to 7 are suppressed and the elastic modulus is retained for the subsequent stiffness calculation.

Clearly, this problem does not arise with a constant stiffness algorithm, as incremental strains are always calculated on the basis of the initial elastic modulus. However, this solution procedure does not satisfy cyclic loading conditions.

4.4 Finite Element Representations for Reinforcement

In the past, at least three types of finite element model have been developed for reinforcement in the analysis of reinforced concrete structures. These are (see Fig.4.8):

i) Distributed

ii) Discrete

and iii) Embedded

4.4.1 Distributed Layer Approach

In the distributed representation, as shown in Fig.4.8(a), the steel is assumed to be distributed over the concrete element, with a particular orientation angle θ. The steel is expected to resist stress in the original direction of the bar. In this representation, perfect bond must be assumed between the concrete and steel in order to derive a composite concrete– reinforcement constitutive relationship and to obtain the displacement field of reinforcement. Sometimes, bond– slip is represented by reducing the modulus of steel[Sinisalo, Tuomala and Mikkola 1979] or increasing it when load is transferred from steel to concrete. The distributed reinforcement model can be further classified into smeared representation and layered representation.

Layered representation is widely used in reinforced concrete plate and shell structures, in which the plate or shell element is divided into layers. This approach was first adopted by Wegmuller[Wegmuller 1974]. He used a rectangular element with three degrees of freedom (θ_x, θ_y and w). The element ignores in– plane effects, and thus assumes a fixed position for the middle plane of the plate. This assumption would be restricted only to problems in which membrane forces are negligible or there is little shift in the neutral axis position. In order to overcome this difficulty, the layered approach has been improved by Wegmuller himself[Wegmuller 1974] and others[Johanarry 1979, Cope and Rao 1977]. In the improved procedure, the effect of membrane stresses was taken into consideration for bending problems where the neutral axis shifts from its initial position towards the compressive face as the cracking progresses deeper into the slab depth. Consequently, it is possible to reduce computational effort. This has been achieved by Rahman[Rahman1981] by using a selective integration rule.

In plane stress type problems, the distributed representation is used as a special

case of this approach, in which the displacement (u,v) at any point in the plane with coordinates (x,y) can be expressed as:

$$\begin{bmatrix} u(x,y) \\ \\ v(x,y) \end{bmatrix} = [N] \begin{bmatrix} u_i \\ \\ v_i \end{bmatrix} \qquad (4.10)$$

where u_i, v_i are the nodal displacements of the concrete element and $[N]$ is the shape function matrix.

Using the standard finite element procedure, the strain expression is therefore given by

$$\begin{bmatrix} \epsilon_x \\ \\ \epsilon_x \\ \\ \epsilon_{xy} \end{bmatrix} = \sum_{i=1}^{n} \begin{bmatrix} \frac{\partial N_i}{\partial x} & 0 \\ \\ 0 & \frac{\partial N_i}{\partial y} \\ \\ \frac{\partial N_i}{\partial y} & \frac{\partial N_i}{\partial x} \end{bmatrix} \begin{bmatrix} u_i \\ \\ \\ \\ v_i \end{bmatrix} \qquad (4.11)$$

where n is the number of the nodes. ϵ_x, ϵ_y and γ_{xy} are the normal and shear strains, see Fig.4.9.

Rewriting the equation gives

$$\{ \epsilon \} = \sum_{i=1}^{n} [B_i] \{ \delta_i \} \qquad (4.12)$$

where

$$\{ \delta_i \} = \begin{bmatrix} u_i \\ \\ v_i \end{bmatrix} \qquad (4.13)$$

Consequently, the stress–strain relationship for each layer is given by

$$\{ \sigma \} = [D'] \{ \epsilon \} \qquad (4.14)$$

where D' is the constitutive relationship. For the steel layer, the behaviour is first described in the local coordinate direction of the steel so that the bar can be orientated at any angle to the global x–y axes. Then the constitutive relationship is transferred from the local to the global. The transformation matrix is derived in terms of the angle θ between the local axes ($\bar{x}$, $\bar{y}$) and the global axes (x,y)

$$[D'] = E_s [T] \qquad (4.15)$$

where E_s is Young's modulus of elasticity of steel and [T] is a transformation matrix.

Noticing that steel reinforcement is uniaxial in contrast to concrete, the transformation matrix reads

$$[T] = \begin{bmatrix} c^2 & c\,s & c\,s \\ & s^2 & c\;\; s \\ \text{sym.} & & c\;\; s \end{bmatrix} \qquad (4.16)$$

where $c = \cos\theta$, $s = \sin\theta$ and θ is the inclination angle shown in Fig.4.10

After the stiffness matrix is calculated for each steel and concrete layer, the summation for all the layers is given by

$$K = \sum_{i=1}^{n} \left\{ \int_{l_x} \int_{l_y} [B]^T D' [B] \, dx \, dy \right\} dz_i \qquad (4.17)$$

where dz_i is the thickness of the i−th layer, n is the total number of the layers, [B] is the strain matrix and [D'] is the constitutive matix depending on the type of the material and the state of the stress in respect to each layer.

4.4.2 Discrete

The discrete representation uses one−dimensional bar elements and beam elements. The bar element model has been widely used due to the fact that it is easy to incorporate it into a usual finite element program. In this representation, it is assumed that the bar is pin connected with two degrees of freedom at nodal points. Only an uniaxial force will be carried by the element. Alternatively, discrete beam elements can be used, in which the steel is assumed to be capable of resisting axial force, shear force and bending moment. Three degrees of freedom are hence assigned at each node of the element. The beam element representation is also simple and easily superimposed on a two−dimensional finite element mesh such as those employed for concrete. Furthermore, another significant advantage is that they can take account of possible displacement of reinforcement with respect to the surrounding concrete, i.e. the possible bond−slip is allowed between reinforcement and concrete by using linkage elements. However, the computation cost of doing this is usually large. The discrete representation of reinforcement is illustrated in Fig.4.8(b) and 4.11

The discrete reinforcement model was first used by Ngo and Scordelis[Ngo and Scordelis 1968] in the analysis of a beam. In their analysis, the reinforcement steel in the bottom of the beam was simulated by a number of bar elements. The stiffness of the bar was calculated at the element level and then assembled into the structural system. The connection between the bar and concrete elements is made by linkage elements at each nodes, which was used to take into account

dowel action and bond slip.

As shown in Fig.4.11, a local coordinate system ζ is set up for the bar. Let x_i and y_i be the nodal coordinates, while u_i and v_i be the nodal displacements. Following the standard finite element procedure, the coordinate and displacement for an arbitrary point are given by

$$x = \sum_{i=1}^{n} N_i \, x_i \tag{4.18a}$$

$$y = \sum_{i=1}^{n} N_i \, y_i \tag{4.18b}$$

$$u = \sum_{i=1}^{n} N_i \, u_i \tag{4.19a}$$

$$v = \sum_{i=1}^{n} N_i \, v_i \tag{4.19b}$$

where i = 1, 2, ..., n, the total number of the nodes for each bar.

The strain is given by

$$\epsilon_r = \begin{bmatrix} \cos^2\theta & \sin^2\theta \end{bmatrix} \begin{bmatrix} \frac{\partial \zeta}{\partial x} & 0 \\ 0 & \frac{\partial \zeta}{\partial y} \end{bmatrix} \begin{bmatrix} \frac{\partial u}{\partial \zeta} \\ \frac{\partial v}{\partial \zeta} \end{bmatrix}$$

$$= \begin{bmatrix} \cos^2\theta & \sin^2\theta \end{bmatrix} \begin{bmatrix} \frac{\partial \zeta}{\partial x} & 0 \\ 0 & \frac{\partial \zeta}{\partial y} \end{bmatrix} \begin{bmatrix} \frac{\partial N_i}{\partial \zeta} & 0 & \cdots \\ 0 & \frac{\partial N_i}{\partial \zeta} & \cdots \end{bmatrix} \begin{bmatrix} u_i & v_i & \cdots \end{bmatrix}^T$$

$$= \begin{bmatrix} J \end{bmatrix} \begin{bmatrix} \frac{\partial N_i}{\partial \zeta} & 0 \\ 0 & \frac{\partial N_i}{\partial \zeta} \end{bmatrix} \begin{bmatrix} u_i \\ v_i \end{bmatrix}$$

$$= \begin{bmatrix} B_i \end{bmatrix} \begin{bmatrix} u_i \\ v_i \end{bmatrix} \tag{4.20}$$

where $[J]$ is the Jacobian matrix and $[B_i]$ is the strain matrix.

Following the standard finite element procedure, the stiffness matrix of the bar is given by

$$K = \int_V [B]^T [D] [B] \, dv \qquad (4.21)$$

where $[D] = E_s$, the elastic Young's modulus of the reinforcement. Integration is carried out over the volume of the bar. The stiffness matrix of the bar is assembled into the global system at the structural level after it is formed.

4.4.3 Embedded

Embedded modelling of reinforcement is usually used in conjunction with higher order isoparametric concrete elements. The reinforcement bar is considered to be a uniaxial member built into the parent concrete element. The displacement field is assumed to be consistent with those of its parent element. Normally perfect bond is assumed. The embedded representation of reinforcement is shown in Fig.4.8(c). Recently, Balakrishnan and Murray[Balakrishnan and Murray 1985] have developed a method of simulating the relative displacement between reinforcement and concrete using the embedded representation. This thesis addresses this problem further, as discussed in Chapter 5.

The embedded model was first proposed by Phillips and Zienkiewicz[Phillips and Zienkiewicz 1976]. In their formulation, the element was restricted to lie along the local coordinate axes, ξ or η of the basic element of concrete. As shown in Fig.4.12, a bar lying along a direction of constant $\eta = \eta_c$ is considered. The position of the bar was then defined using the same shape function as its parent element. The compatibility between the bar and the concrete was obtained by

assuming full bond between them.

Based on the above assumption, the displacement field of the bar is given by

$$\{f\} = \begin{Bmatrix} u \\ v \end{Bmatrix} = [\ N(\xi)\ ]\,[\,\delta\,]^e \qquad (4.22)$$

The uniaxial strain, which is the only component contributing to the strain energy, is given in the local system by

$$\epsilon_p{}' = \partial u'/\partial x' \qquad (4.23)$$

where x' and y' are the local coordinate system at point P with y' being normal to the line of the bar while u' and v' are the corresponding displacements.

The distortion matrix of the bar strain is defined as

$$[\,j\,] = \begin{bmatrix} \frac{\partial u}{\partial x} & \frac{\partial v}{\partial x} \\ \\ \frac{\partial u}{\partial y} & \frac{\partial v}{\partial y} \end{bmatrix} = \begin{bmatrix} \frac{\partial N}{\partial x} \\ \\ \frac{\partial N}{\partial y} \end{bmatrix} \begin{bmatrix} u_i & v_i \\ \\ u_j & v_j \\ \\ .. & .. \end{bmatrix} \qquad (4.24)$$

and the Jacobian matrix $[\,J\,]$ by

$$[\,J\,] = \begin{bmatrix} \frac{\partial x}{\partial \xi} & \frac{\partial y}{\partial \xi} \\ \\ \frac{\partial x}{\partial \eta} & \frac{\partial y}{\partial \eta} \end{bmatrix} = \begin{bmatrix} \frac{\partial N}{\partial \xi} \\ \\ \frac{\partial N}{\partial \xi} \end{bmatrix} \begin{bmatrix} u_i & v_i \\ \\ u_j & v_j \\ \\ .. & .. \end{bmatrix} \qquad (4.25)$$

Therefore, from the relation

$$\begin{bmatrix} \frac{\partial N}{\partial \xi} \\ \\ \frac{\partial N}{\partial \eta} \end{bmatrix} = [\,J\,] \begin{bmatrix} \frac{\partial N}{\partial x} \\ \\ \frac{\partial N}{\partial y} \end{bmatrix} \qquad (4.26)$$

it follows that

$$[j] = [J]^{-1} \begin{bmatrix} \frac{\partial N}{\partial \xi} \\ \\ \frac{\partial N}{\partial \eta} \end{bmatrix} \begin{bmatrix} u_i & v_i \\ u_j & v_j \\ .. & .. \end{bmatrix} \qquad (4.27)$$

$[j]$ is a second order tensor and transforms on coordinate rotation from x, y to x', y' according to

$$[j'] = \begin{bmatrix} \frac{\partial u'}{\partial x'} & \frac{\partial v'}{\partial x'} \\ \\ \frac{\partial u'}{\partial y'} & \frac{\partial v'}{\partial y'} \end{bmatrix} = [R][j][R]^T \qquad (4.28)$$

where $[R]$ is the rotation matrix of direction cosines at point P.

Since x' and ξ' coincide and differ only in magnitude, we have

$$[R] = \begin{bmatrix} \frac{\partial x}{\partial x'} & \frac{\partial y}{\partial x'} \\ \\ \frac{\partial y}{\partial y'} & \frac{\partial y}{\partial y'} \end{bmatrix} = \frac{1}{\left[\left(\frac{\partial x}{\partial \xi}\right)^2 + \left(\frac{\partial y}{\partial \xi}\right)^2 \right]^{\frac{1}{2}}} \begin{bmatrix} \frac{\partial x}{\partial \xi} & \frac{\partial y}{\partial \xi} \\ \\ \frac{\partial y}{\partial \xi} & \frac{\partial x}{\partial \xi} \end{bmatrix} \qquad (4.29)$$

From eqs.(4.23, 28 and 29), it follows that

$$\epsilon_p = \frac{1}{h^2} \left[\left(c_1 \frac{\partial N_i}{\partial x} + c_2 \frac{\partial N_i}{\partial y}\right), \left(c_2 \frac{\partial N_i}{\partial x} + c_3 \frac{\partial N_i}{\partial y}\right), \cdots \right] \begin{Bmatrix} u_i \\ v_i \\ u_j \\ v_j \\ \vdots \end{Bmatrix}$$

$$= [B] \begin{Bmatrix} u \\ v \end{Bmatrix} \qquad (4.30)$$

where

$$c_1 = \left(\frac{\partial x}{\partial \xi}\right)^2 \qquad c_2 = \frac{\partial x}{\partial \xi}\,\frac{\partial y}{\partial \xi}$$

$$c_3 = \left(\frac{\partial y}{\partial \xi}\right)^2 \qquad h = \left[\left(\frac{\partial x}{\partial \xi}\right)^2 + \left(\frac{\partial y}{\partial \xi}\right)^2\right]^{\frac{1}{2}}$$

Again following the standard finite element procedure, the element stiffness matrix can be set up as

$$K = \int_V [B]^T [D_s][B]\, dv \qquad (4.31)$$

The integration is carried out over the volume of the bar.

Matix [D_s] is given by [D_s] = E_s, the elastic Young's modulus of steel.

In the application of the above equations, inconvenience is caused by the restriction that the bar has to coincide with the coordinate system of the basic element, which limits the direction of the bars. In a typical analysis, mesh generation is restricted by the direction of the reinforcement.

In order to remove the above restrictions, two new embedded models have been developed in this study.

4.5. Two New Embedded Bar Models

4.5.1 Introduction

The previous embedded reinforcement formulation does not expand the bandwidth of the stiffness matrix due to existence of the steel bar. This means that if the restriction on the bar's position can be removed the embedded model would become a more powerful approach for finite element analysis of reinforced concrete structures.

In this section, two computational formulations will be presented. The first model developed allows a straight bar to be generally orientated across the element, the sides of which are also assumed to be straight. This is a very common situation and consequently it was thought worthwhile to develop the formulation which represents this situation, reducing computational effort. The second reinforcement formulation is a general embedded reinforcement approach. This allows a bar layout at any arbitrary position within the parent element or along the sides. Both the reinforcement element and the sides of the concrete element can be either straight or curved.

In these two derivations, the basic assumptions made are:

i) The reinforcement is a uniaxial member so that only the strain component in the direction of the bar contributes to the strain energy;

ii) Perfect bond exists so that the strain in the bar at an arbitary point is similar to that of the concrete at that point. Extension for bond–slip effects will be considered in detail in Chapter 5.

4.5.2 An Orientated Embedded Straight Bar Model

In order to derive this formulation, two more assumptions are made in addition to the above basic assumptions: i) the reinforcement bar is straight across opposite sides of the concrete element and, ii) the concrete element sides are also straight, see Fig.4.13.

Since there is no slip between reinforcement and concrete, the position of the bar can be defined by the same shape functions as those used for the main

element. The displacement field of the reinforcement can then be given by a function of the nodal displacements of the main element.

Thus the coordinates are given by:

$$\begin{bmatrix} x \\ y \end{bmatrix} = [\ N(\xi,\eta)\ ] \begin{bmatrix} x_i \\ y_i \end{bmatrix} \qquad (4.32)$$

and the displacement field by:

$$\{\ f_s\ \} = \begin{bmatrix} u \\ v \end{bmatrix} = [\ N(\xi,\eta)\ ]\ \{\delta^e\} \qquad (4.33)$$

In the bar direction, the strain is given by

$$\vec{\epsilon}_s = \vec{\epsilon}_x\, e_{sx} + \vec{\epsilon}_y\, e_{sy}$$

$$= (\epsilon_{xx}\, \vec{e}_x + \epsilon_{xy}\, \vec{e}_y)\, e_{sx} + (\epsilon_{yx}\, \vec{e}_x + \epsilon_{yy}\vec{e}_y)e_{sy} \qquad (4.34)$$

where $\vec{\epsilon}_x$ and $\vec{\epsilon}_y$ are the strain vectors in x- and y- directions, respectively, and

$\vec{e}_x$ and $\vec{e}_x$ are the unit strain vectors in x- and y- directions, respectively.

Therefore the steel strain is given by

$$\epsilon_s = \epsilon_{xx}\, e_{sx}^2 + 2\, \epsilon_{xy}\, e_{sx}\, e_{sy} + \epsilon_{yy}\, e_{sy}^2$$

$$= \epsilon_{xx} \cos^2\alpha + 2\, \epsilon_{xy} \cos\alpha \sin\alpha + \epsilon_{yy} \sin^2\alpha$$

$$= \frac{\partial u}{\partial x} \cos^2\alpha + \frac{\partial v}{\partial y} \sin^2\alpha + \left[\frac{\partial v}{\partial x} + \frac{\partial u}{\partial y} \right] \sin\alpha \cos\alpha$$

$$= \left[\sum_{i=1}^{n} \frac{\partial N_i}{\partial \xi} \frac{\partial \xi}{\partial x} u_i + \sum_{i=1}^{n} \frac{\partial N_i}{\partial \eta} \frac{\partial \eta}{\partial x} u_i \right] \cos^2\alpha +$$

$$\left[\sum_{i=1}^{n} \frac{\partial N_i}{\partial \xi} \frac{\partial \xi}{\partial y} v_i + \sum_{i=1}^{n} \frac{\partial N_i}{\partial \eta} \frac{\partial \eta}{\partial y} v_i \right] \sin^2\alpha +$$

$$\left[\sum_{i=1}^{n} \frac{\partial N_i}{\partial \xi} \frac{\partial \xi}{\partial x} v_i + \sum_{i=1}^{n} \frac{\partial N_i}{\partial \eta} \frac{\partial \eta}{\partial x} v_i + \right.$$

$$\left. \sum_{i=1}^{n} \frac{\partial N_i}{\partial \xi} \frac{\partial \xi}{\partial y} u_i + \sum_{i=1}^{n} \frac{\partial N_i}{\partial \eta} \frac{\partial \eta}{\partial y} u_i \right] \sin\alpha \cos\alpha$$

(4.35)

where n is the total number of the parent element nodes and α is the angle between the global x– axis and the bar direction.

In matrix form

$$\epsilon_s =$$

$$\sum_{i}^{n} \begin{bmatrix} \left[\frac{\partial N_i}{\partial \xi} \frac{\partial \xi}{\partial x} + \frac{\partial N_i}{\partial \xi} \frac{\partial \xi}{\partial x} \right] \cos^2\alpha & \left[\frac{\partial N_i}{\partial \xi} \frac{\partial \xi}{\partial x} + \frac{\partial N_i}{\partial \eta} \frac{\partial \eta}{\partial x} \right] \sin\alpha\cos\alpha \\ \left[\frac{\partial N_i}{\partial \xi} \frac{\partial \xi}{\partial y} + \frac{\partial N_i}{\partial \eta} \frac{\partial \eta}{\partial y} \right] \sin\alpha\cos\alpha & \left[\frac{\partial N_i}{\partial \eta} \frac{\partial \eta}{\partial y} + \frac{\partial N_i}{\partial \eta} \frac{\partial \eta}{\partial y} \right] \sin^2\alpha \end{bmatrix} \begin{Bmatrix} u_i \\ v_i \end{Bmatrix}$$

(4.36)

Since the bar is subject only to uniaxial forces, only uniaxial deformation contributes to the strain energy and the shear deformation at the point has no effect on the bar's elongation (which only rotates the bar). Therefore, the subdiagonal terms are then equal to zero (see Ref. [Timoshenko and Goodier 1951]).

Equation (4.36) then becomes

$$\sum_{i}^{n} \begin{bmatrix} A_1 & & & & & & \\ & B_1 & & & & & \\ & & A_2 & & & & \\ & & & B_2 & & & \\ & & & & \ddots & & \\ & & & & & A_n & \\ & & & & & & B_n \end{bmatrix} \begin{Bmatrix} u_i \\ \\ \\ v_i \end{Bmatrix} = [B_s]\{\delta^e\} \tag{4.37}$$

where A_i and B_i read

$$A_i = \left[\frac{\partial N_i}{\partial \xi} \frac{\partial \xi}{\partial x} + \frac{\partial N_i}{\partial \xi} \frac{\partial \xi}{\partial x} \right] \cos^2\alpha$$

$$B_i = \left[\frac{\partial N_i}{\partial \eta} \frac{\partial \eta}{\partial y} + \frac{\partial N_i}{\partial \eta} \frac{\partial \eta}{\partial y} \right] \sin^2\alpha$$

Following the standard finite element method, the stiffness matrix is then given by:

$$\begin{aligned} K_s &= \int_V [B]^T [D]_s [B] dv \\ &= \int_V [B]^T E_s [B] dv \text{ (due to the uniaxial assumption)} \\ &= E_s \int_V [B]^T [B] dv \\ &= E_s A_s \int_l [B]^T [B] dr \end{aligned} \tag{4.38}$$

where E_s is the elasticity modulus of the reinforcement bar

A_s is cross-section area of the bar.

Moreover, since the reinforcement bar is assumed to be straight across the

sides of the concrete element whose sides are also straight, the terms in the diagonal positions are therefore only functions of either ξ or η, which makes the integration over the volume of the bar easy to carry out using a conventional Gauss integration rule.

Integration is carried out along the bar's direction in the local system of the concrete element. If the bar crosses the element from sides $\xi = \pm 1$ of the concrete element local coordinate system, the integration is carried out over the ξ direction from -1 to $+1$, otherwise, the integration is over η direction from -1 to $+1$.

As shown in Fig.4.13, the position of the bar can be defined by a function of ξ and η, by

$$\frac{\xi - \xi_1}{\eta - \eta_1} = \frac{\xi_2 - \xi_1}{\eta_2 - \eta_1} \qquad (4.39a)$$

i.e.

$$\xi = \xi_1 + (\eta - \eta_1)\cdot(\xi_2 - \xi_1)]\cdot \frac{1}{\eta_2 - \eta_1} \qquad (4.39b)$$

where (ξ_1, η_1) and (ξ_2, η_2) are the local coordinates at the end of the bar on each side of the concrete element.

Therefore, the expression for dr is given by

$$dr = \left[1+ \left(\frac{d\xi}{d\eta} \right)^2 \right]^{\frac{1}{2}} d\eta = \left[1+ \left(\frac{\xi_2 - \xi_1}{\eta_2 - \eta_1} \right)^2 \right]^{\frac{1}{2}} d\eta \qquad (4.40)$$

In the other case where the bar is arranged across the concrete element in the

direction of ξ, the expression of dr should be given by $d\xi$ in order to integrate over ξ:$(-1, +1)$.

Finally, the stiffness K_s is assembled into the stiffness of the parent element.

4.5.3 A General Embedded Model

A fully general reinforcing or prestressing embedded bar element is presented in the following. The displacement field of the bar is obtained using the displacements at a set of 'characteristic' points of the concrete element (these concrete points are termed 'characteristic' because they are attributed to the bar element nodes), and a local system for bar is then employed to achieve the strain expression and to integrate the virtual work of the bar element.

Displacement Field

In terms of the nodal displacements of the reinforcements bar, the reinforcement displacement field is obtained using shape functions, see Fig.4.14, as

$$\{f_s\} = u \cos\alpha + v \sin\alpha \qquad (4.41)$$

or in matrix form

$$\{f_s\} = \begin{bmatrix} \cos\alpha & \sin\alpha \end{bmatrix} \begin{bmatrix} u \\ v \end{bmatrix} \qquad (4.42)$$

and

$$\begin{bmatrix} u \\ v \end{bmatrix} = \begin{bmatrix} H_j \end{bmatrix} \begin{bmatrix} u_{jb} \\ v_{jb} \end{bmatrix} \qquad (4.43)$$

where

H_j are the shape functions of the bar element,

u_{jb} and v_{jb} are the nodal displacements of the bar element,

and j = 1, 2, ... p, the total number of bar element nodes.

The bar nodal displacements can be expressed in terms of the nodal displacements of the parent concrete by

$$\begin{bmatrix} u_{jb} \\ \\ v_{jb} \end{bmatrix} = \begin{bmatrix} N_i(\xi_j, \eta_j) \end{bmatrix} \begin{bmatrix} u_{ic} \\ \\ v_{ic} \end{bmatrix} \qquad (4.44)$$

where (ξ_j, η_j) are the nodal coordinates of the bar element in the local system of the parent element, u_{ic} and v_{ic} are the displacements of the parent element nodes. N_i are the shape functions of the parent element, i= 1, 2, ..., n, the total number of the parent element nodes.

Therefore, substituting eq.(4.44) into eq.(4.43), the displacement field of the bar is expressed as,

$$\begin{bmatrix} u \\ \\ v \end{bmatrix} = [H_j][N_i(\xi_j, \eta_j)] \begin{bmatrix} u_{ic} \\ \\ v_{ic} \end{bmatrix} \qquad (4.45a)$$

In detail, this can be written as

$$\begin{bmatrix} u \\ \\ v \end{bmatrix} = \begin{bmatrix} H_1 & 0 \\ 0 & H_1 \\ \vdots & \vdots \\ H_p & 0 \\ 0 & H_p \end{bmatrix}^T \begin{bmatrix} N_i(\xi_1, \eta_1) & 0 & \cdots \\ 0 & N_i(\xi_1, \eta_1) & \cdots \\ \vdots & \vdots & \\ N_i(\xi_p, \eta_p) & 0 & \cdots \\ 0 & N_i(\xi_p, \eta_p) & \cdots \end{bmatrix} \{\delta\}^e \qquad (4.45b)$$

where

$$\{\delta\} = \begin{bmatrix} u_{ic} \\ \\ v_{ic} \end{bmatrix} \qquad (4.46)$$

The Steel Strain

The only steel strain contributing to the virtual work is the component in the steel's direction, i. e.

$$\epsilon_s = \frac{df_s}{dr} \tag{4.47}$$

Substituting eq.(4.42) and eq.(4.45) into eq.(4.47)

$$\{\epsilon_s\} = [\ \cos^2\alpha \quad \sin^2\alpha\ ] \begin{bmatrix} \frac{d\zeta}{dx} & 0 \\ 0 & \frac{d\zeta}{dy} \end{bmatrix} \cdot \begin{bmatrix} \frac{dH_1}{d\zeta} & 0 \\ \vdots & \vdots \\ 0 & \frac{dHp}{d\zeta} \end{bmatrix}^T [\ Ni(\xi_j, \eta_j)\ ] \{\delta\}^e$$

$$= [B_s]\{\delta\}^e \tag{4.48}$$

The virtual work done by steel is

$$V.W_{steel} = [\delta]^* [\ \int_1 [B_s]^T [D_s][B_s] A_s\, dr\ ] \{\delta\}^e \tag{4.49}$$

in which $[D_s]$ is the constitutive matrix of steel. In this case $[D_s] = E_s$, the Young's modulus of steel. A_s is the cross section area of the steel bar, and dr is expressed as

$$dr = \sqrt{[(\frac{dx}{d\zeta})^2 + (\frac{dy}{d\zeta})^2]}\, d\zeta \tag{4.50}$$

The term in the square bracket in eq.(4.49) is the stiffness matrix of the steel bar. It is assembled into the global stiffness matrix in the conventional manner.

The shape functions H_j and N_i in the above equations are used for the bar

element and the parent element, respectively. Mathematically, they are independent of each other; however from physical considerations the two element systems should be kept compatible and hence be related. In this study, a parabolic bar function H_j is assumed in the parabolic concrete element.

To set up the relation between the displacement fields of a bar and the main element, it is necessary to determine the local coordinates of an arbitrary global–system's point in the local system of the parent element, and this requires inverse mapping procedures.

Local Coordinates of an Arbitrary Point in the Parent Element

In the derivation, it is shown that after the centre point of the parent element is defined, the local coordinates of an arbitrary point in the element can be obtained linearly with reference to the local coordinates of a point on the boundary, and that the solution is singular.

Linearity

In Fig.4.15(a), P is an arbitrary point in the element. In order to define its local coordinates, a straight line in global coordinates is drawn from the centre point, C, to the boundary through point P. The coordinates of point Q are (ξ_0, η_0) and the coordinate ξ (or η) for a point on this line changes from zero to ξ_0 (or η_0). Fig.4.15(b) describes the relation between the local coordinate ξ and the distance l from the central point C, in which l_0 is the global length CQ. It is seen that the relation between ξ and l can be either linear, along OPQ, or nonlinear, along OP'Q.

Now consider a situation where the element is under a constant stress–strain

(σ_0, ϵ_0) state and then calculate the potential work done on a infinitesimal area dxdy at two adjacent points P_1 and P_2 on the line CQ, see Fig.4.15(c). If local coordinates ξ and η change nonlinearly (along curve OP'Q) the same area dxdy will map onto a different amount of $d\xi d\eta$. As a result, the potential work would be denser at one point than that at another point, which is not true. Therefore, the relation between the distance from the central point and the local coordinates is linear.

Singularity

Singularity exists when a pair of global coordinates has only one unique pair of local coordinates corresponding to it both within the element and on the boundary.

On the boundary, using the linear relation and basing the centre in the middle of the side, the singularity is easily proved.

Investigating within the element, let points P_1 and P_2 be in the parent element and Q_1 and Q_2 be points on the boundary crossed by the lines OP_1 and OP_2, respectively, See Fig.4.16.

The local coordinates are given by

$$Q_1(\xi_1, \eta_1) \qquad Q_2(\xi_2, \eta_2)$$

$$P_1(\xi_{i1}, \eta_{i1}) \qquad P_2(\xi_{i2}, \eta_{i2})$$

The length from the central point is given by

$$OP_1 = l_1 \qquad OQ_1 = l_{01}$$

$$OP_2 = l_2 \qquad OQ_2 = l_{02}$$

The expressions of the local coordinates of the two points are, using the linearity relationship,

$$\xi_{i1} = \frac{l_1}{l_{01}} \xi_1 \qquad \eta_{i1} = \frac{l_1}{l_{01}} \eta_1 \qquad (4.51a)$$

$$\xi_{i2} = \frac{l_2}{l_{02}} \xi_2 \qquad \eta_{i2} = \frac{l_2}{l_{02}} \eta_2 \qquad (4.51b)$$

If not singular, i. e. one pair of the local coordinates correspond to two points in the global system, or one point in global system corresponds to two pairs of local coordinates, then referring to Fig.4.16

$$\xi_{i1} = \xi_{i2} \qquad \text{and} \qquad \eta_{i1} = \eta_{i2} \qquad (4.52)$$

and

$$\frac{l_1}{l_{01}} \xi_1 - \frac{l_2}{l_{02}} \xi_2 = 0 \qquad (4.53a)$$

$$\frac{l_1}{l_{01}} \eta_1 - \frac{l_2}{l_{02}} \eta_2 = 0 \qquad (4.53b)$$

or in matrix form

$$\begin{bmatrix} \xi_1 & -\xi_2 \\ \eta_1 & -\eta_2 \end{bmatrix} \begin{bmatrix} \frac{l_1}{l_{01}} \\ \frac{l_2}{l_{02}} \end{bmatrix} = \begin{bmatrix} 0 \\ 0 \end{bmatrix} \qquad (4.53c)$$

A solution of these equations is given by

$$\frac{l_1}{l_{01}} - \frac{l_2}{l_{02}} = 0 \qquad (4.54)$$

This violates eq.(4.52) and therefore, the relation from the global system to the local system is singular.

4.6 Mesh Generation of Isoparametric Concrete Element and Embedded Bar

Introduction

The basic philosophy for mesh generation is that a mesh should be established by the computer from a minimum amount of input. Schemes for such automatic generation range from simple but effective ones[Bridge...1968] based on the structure geometry to ones based on mapping between local curvi−linear and global Cartesian coordinates. The former is straightforward but specific for a given structure whilst the latter is designed with flexibility and is capable of generating general meshes. Zienkiewicz and Phillips[Zienkiewicz and Phillips 1971] have fully described a theory employed to generate meshes for both plane and curved surfaces defined in three dimensions (shells). Since then, many developments have taken place, see [Baldwin (ed.) 1986].

For finite element analysis of reinforced concrete structures, the mesh for both concrete and reinforcement needs to be taken into account. If the reinforcement is considered as a smeared layer over concrete then separate reinforcement mesh generation is not necessary. If bars are bar placed along the concrete sides (e. g. discrete bar model), a bar element generating scheme would reduce mesh preparation, but is rarely used. However one of the advantages of the embedded reinforcement model is that the finite element mesh and the reinforcement layout can be independent of each other. To make full use of this advantage, it is desirable to include a reinforcement generation scheme which allocates reinforcing

bars to each element through which it passes and to correctly apportion each bar and its fictitious nodes within the concrete element. In such a scheme, only a minimum definition of each reinforcing bar is necessary, thereby reducing tedious data preparation.

In this study, a simple geometric based mesh generation scheme is adopted for concrete, emphasis being placed on the mesh generation of reinforcement elements for the embedded formulation.

However, it is straightforward to include the reinforcement generating scheme into a more sophisticated concrete element mesh generation procedure.

Concrete Mesh Generation

A program generating a mesh for eight nodal elements has been implemented. The input data consists of specifying a total number of generating lines. For each generating line the total number of intervals n, together with the coordinates of the two terminal points (X_a, Y_a, X_b, Y_b) and a weighting factor k are also defined.

The number of divisions in adjacent generating lines need not be equal to each other, as shown in Fig.4.17.

For banded solution schemes, the generating lines should cross the shorter direction of the structure to minimize the bandwidth.

The weighting factor k is based on a geometric progression so that intervals along a generating line can be progressively shorter ($0 < k < 1.0$), equal ($k = 1.0$) or progressively longer ($k > 1.0$). Referring to Fig.4.18, the coordinates of

point i along a generating line ab are given by

$$X_i = (X_b - X_a) \frac{\sum_{j=1}^{i} K^{j-1}}{\sum_{j=1}^{n} K^{j-1}} + X_a \qquad (4.55)$$

i.e.

$$X_i = (X_b - Xa) \frac{K^i - 1}{K^n - 1} + X_a \qquad (4.56)$$

with similar definitions for Y_i

For K=1.0

$$X_i = X_a + (X_b - X_a) \frac{i}{n} \qquad (4.57)$$

In addition, when k = 1.0, the line can be further divided into sublines where the intervals are equal in each subline

The nodal numbers are labelled in increasing sequence from line to line. Element definitions are then established afterwards.

Reinforcement Mesh Generation

The mesh for reinforcement bars is automatically generated by specifying the total number of steel bars and their terminal coordinates. In addition, the concrete elements through which a particular steel bar passes also need to be specified although this restriction could be removed if necessary by employing a searching scheme to define mutual element boundaries. For a curved bar, a circular arc is employed to approximate the curvature. This requires the two end points of the arc to be defined, with an additional point on the arc or the

centre of the circle.

Straight Reinforcement Bars

In the simplest situation where the bar is contained within one element only, the bar element nodal coordinates, nodal number and element number are straight forward, i. e. the bar fictitious nodal coordinates are simply equal to the bar's terminal ones and the nodal numbers and the bar element numbers are set without any difficulty.

If a bar crosses more than one concrete element, as shown in Fig.4.19(a), the intersection points for each concrete element are given by solving the line function of the bar with the line function of the concrete element side. Each side is considered in turn until a solution is obtained. It is then necessary to decide whether or not the solution is true. For instance, in Fig.4.19(b), solution giving P_1 and P_4 are false whilst P_2 and P_3 are not. This is checked by ensuring the point lies within the interval of the element side. To reduce computational effort, only those concrete elements through which a particular bar crosses are used to search for intersection points, e. g. elements 1, 2, 5, 6, 9 in Fig.4.20. Concrete element numbers need to be specified in sequential order along the bar, for example, in Fig.4.20, the elements can be specified either as 9, 6, 5, 2, 1 or 1, 2, 5, 6, 9.

If one or two ends of bar are terminated inside the concrete element, only one true solution can be found during the intersection point calculation, as shown in Fig.4.21. The terminal of the bar will then be automatically used as a intersection point. In this situation, the concrete element specification needs to be in an order which begins with the one containing the beginning point of the steel bar, or ends with the one containing the end point.

Curved Reinforcement Bars

For a curved steel bar, three points are used to define a circular curve function. The intersections of the bar with the sides of a concrete element are then easily calculated in the same way as for straight bars. Now, however, there are two roots in solving these functions. True or false solution checks are therefore needed twice.

Connection Between the Reinforcement Bars

Often reinforcing bars are not purely straight or curved over its whole length, and made of different curved parts and different straight parts. The scheme allows for this situation by considering each portion of the bar as a separate bar with its own terminal coordinates.

The connection between the bars is then automatic because the coordinates of the first point of the bar under computation will be the same as the coordinates of the last point of the bar previously calculated. However, this needs to borne in mind when constructing the data for such 'connected' bars.

A flow chart of the above scheme is given in the following, in which k is the weighting factor used in concrete mesh generation.

Concrete Mesh

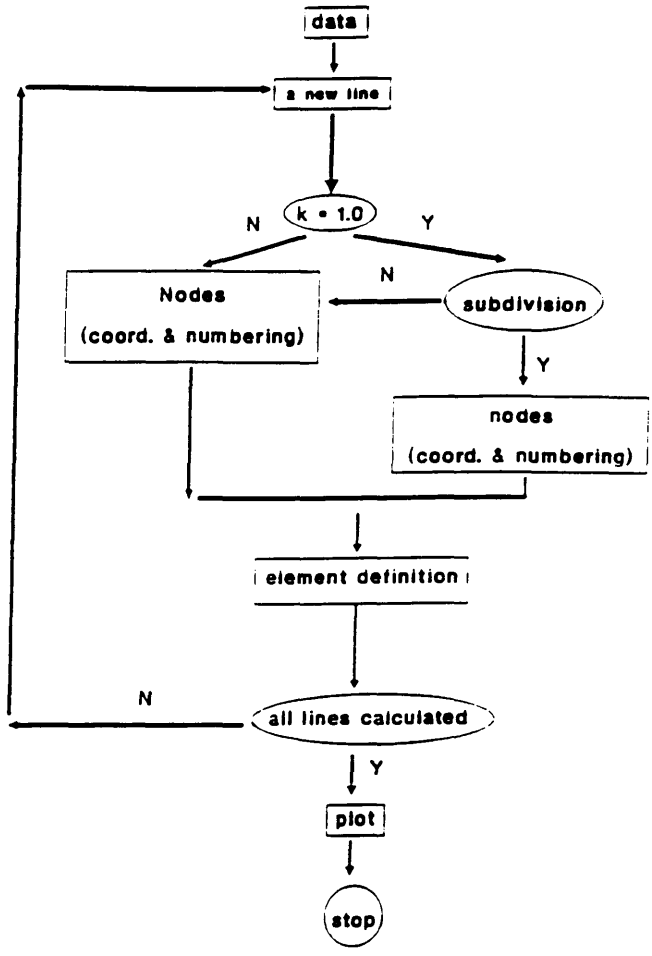

Reinforcement Mesh

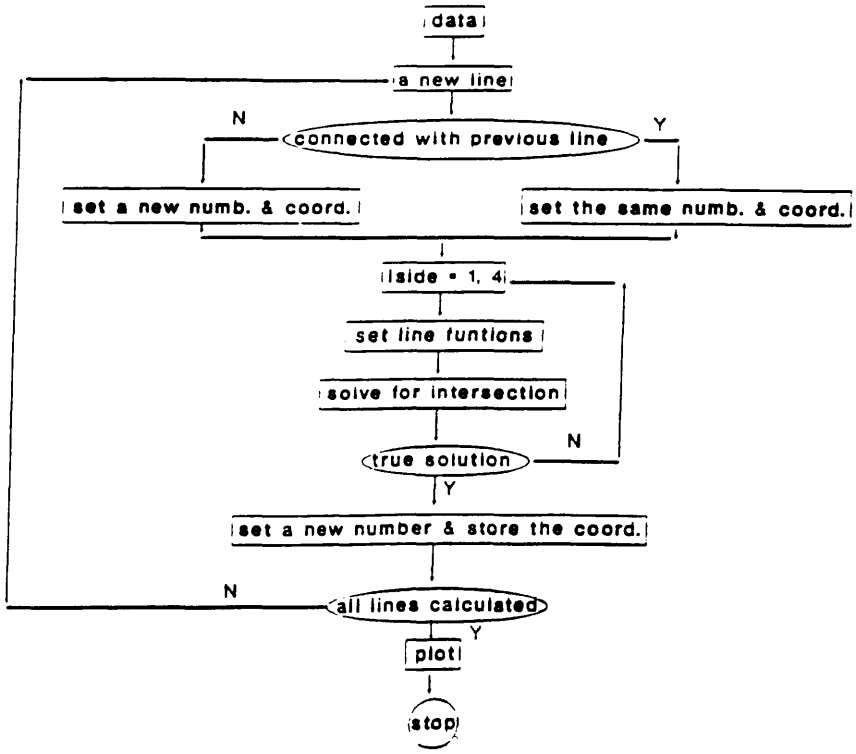

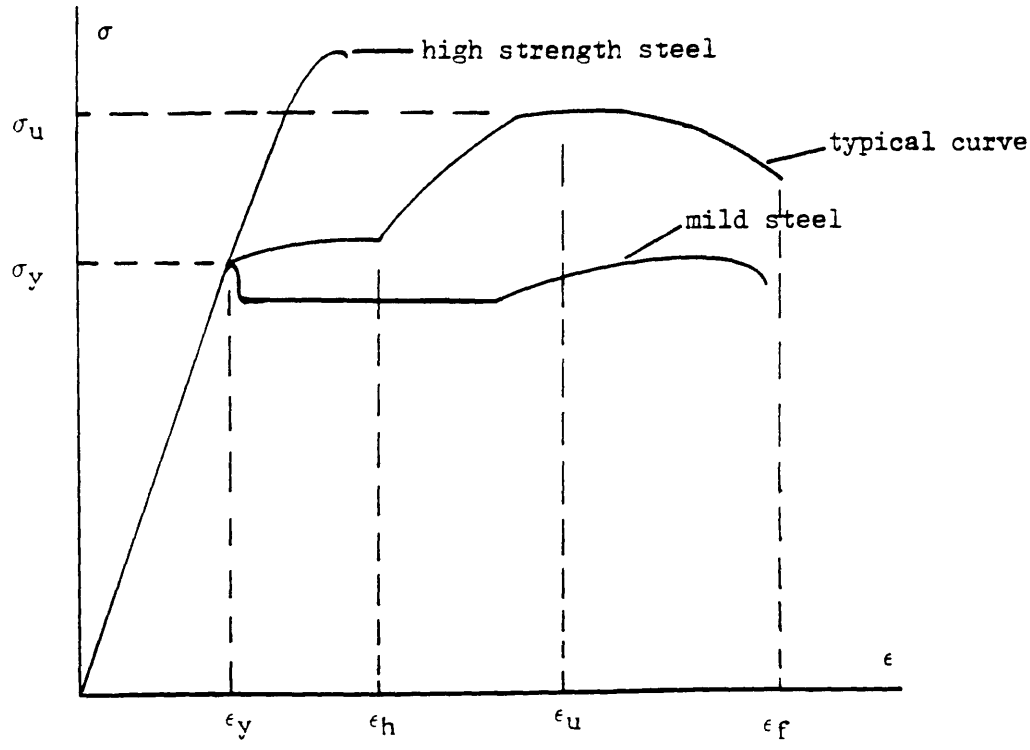

Fig.4.1 Typical Steel Stress– strain Curves

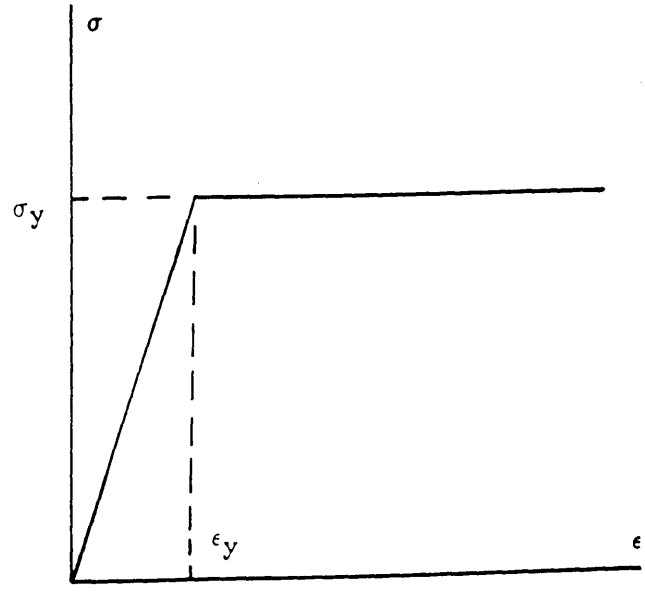

(a) Elastic-perfect Plastic

Fig.4.2 Idealization of Steel Stress– strain Curves

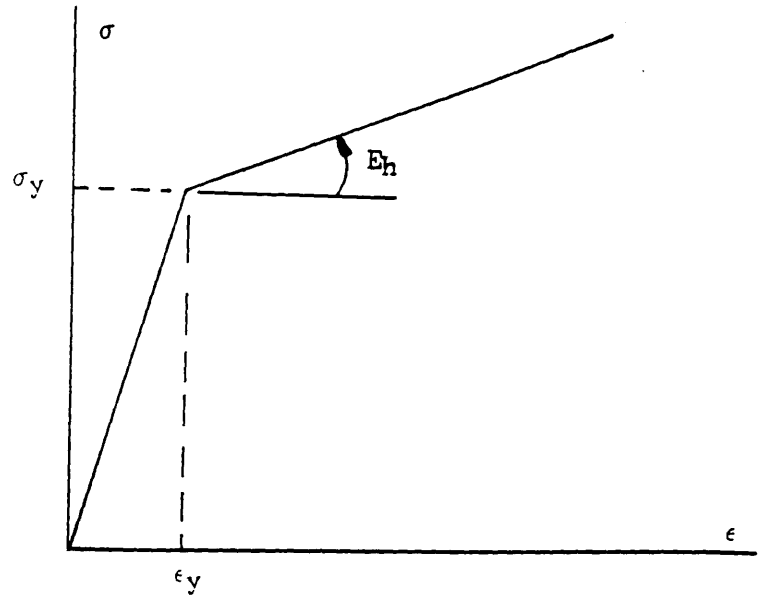

(b) Bilinear Approximation

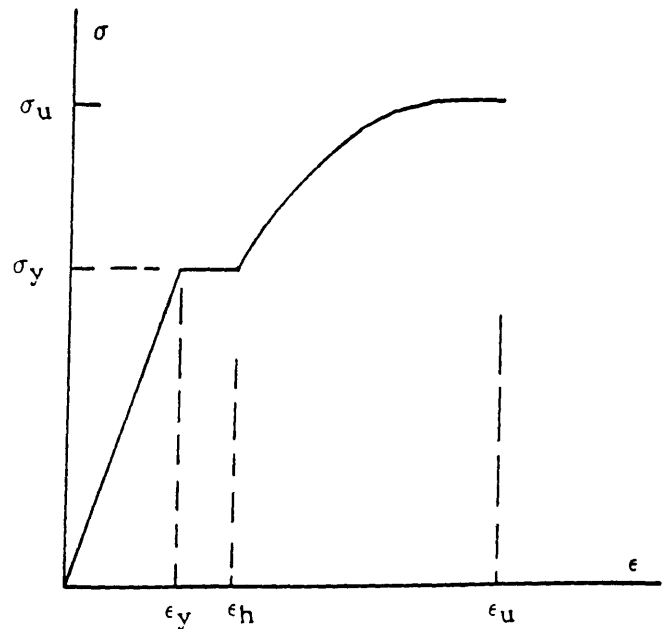

(c) Complete Curve

Fig.4.2 Idealization of Steel Stress– strain Curves (continued)

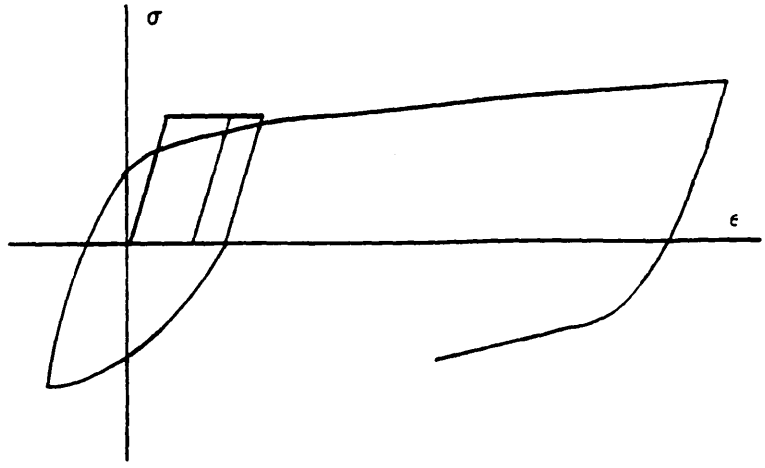

Fig.4.3 Stress– strain Curve With Reversed Loading

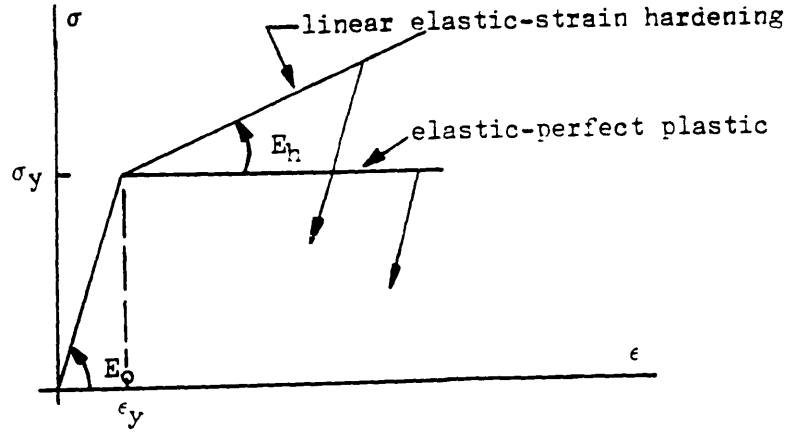

Fig.4.4 Simplified Steel Law

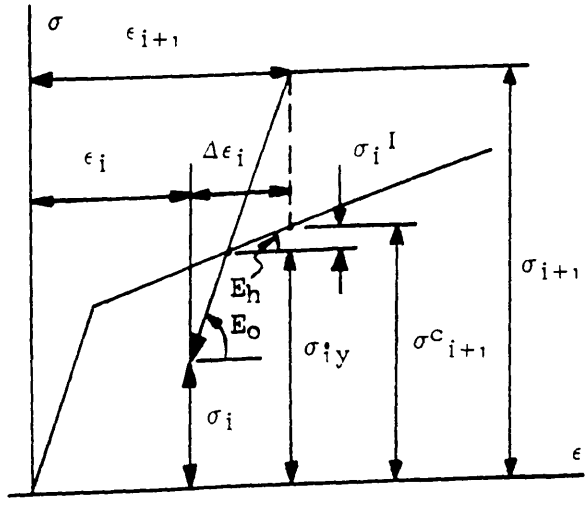

Fig.4.5 Stress Calculation After Yielding

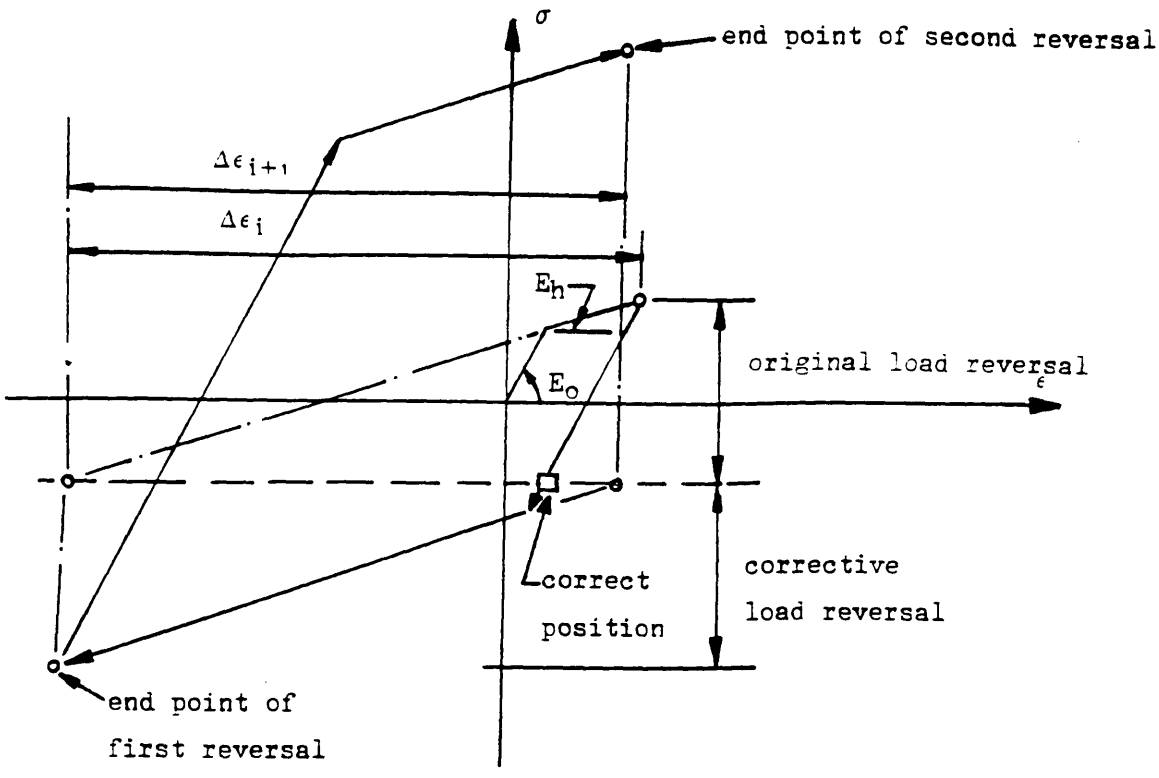

Fig.4.6 Unstable Load Reversals

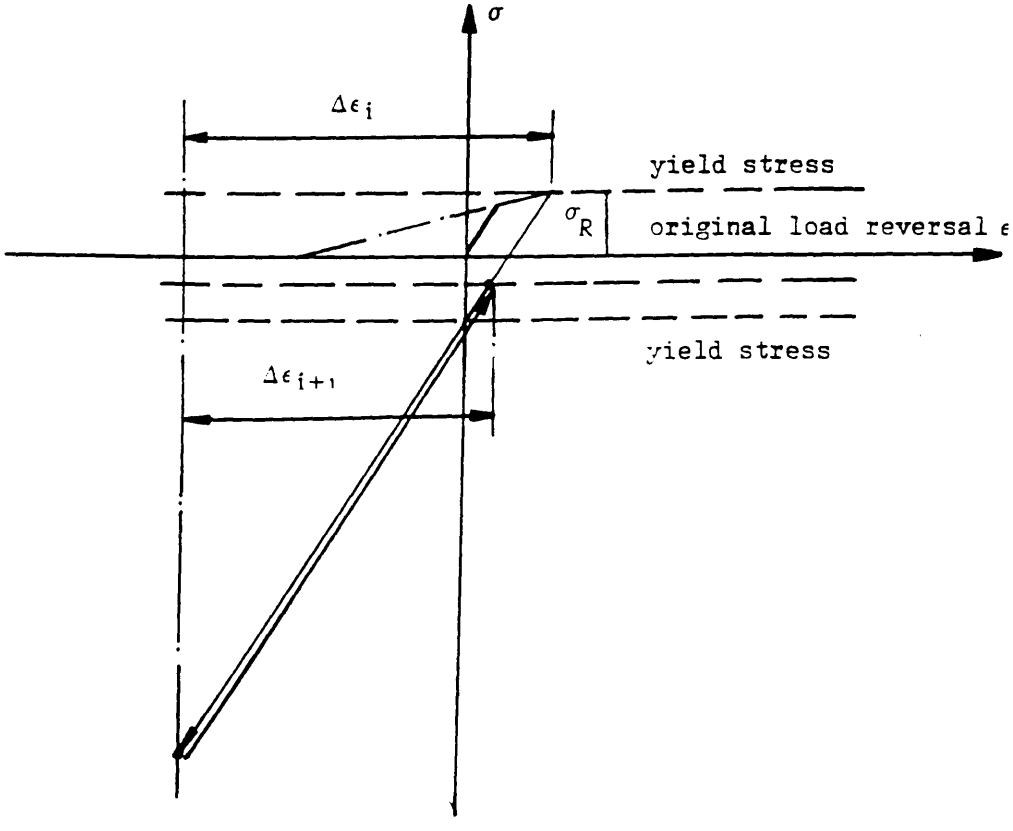

Fig.4.7 Suppressed Yielding Routine

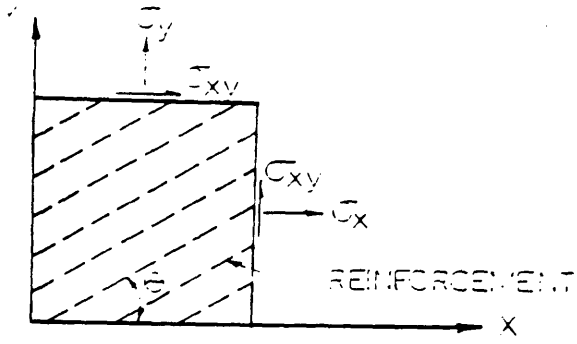

(a) Distributed

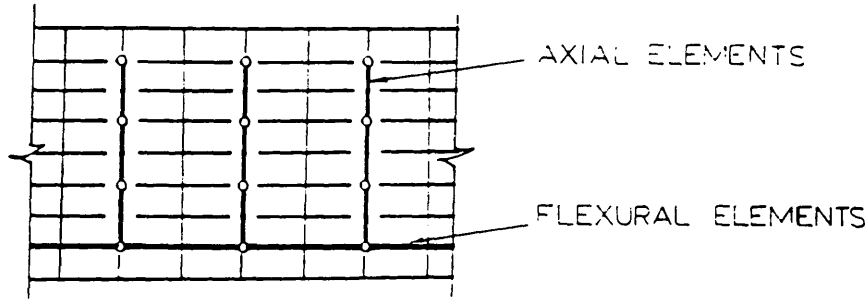

(b) Discrete

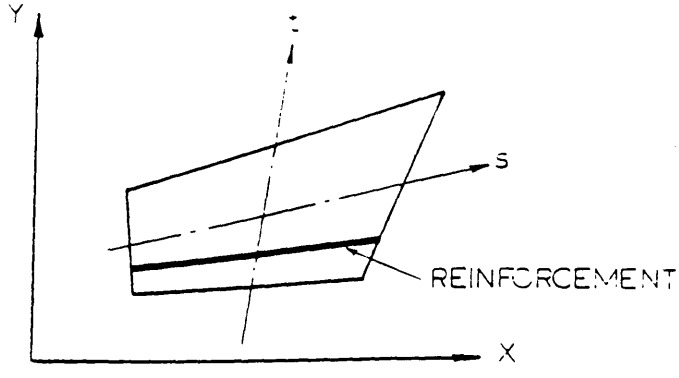

(c) Embedded

Fig.4.8 Alternative Representations

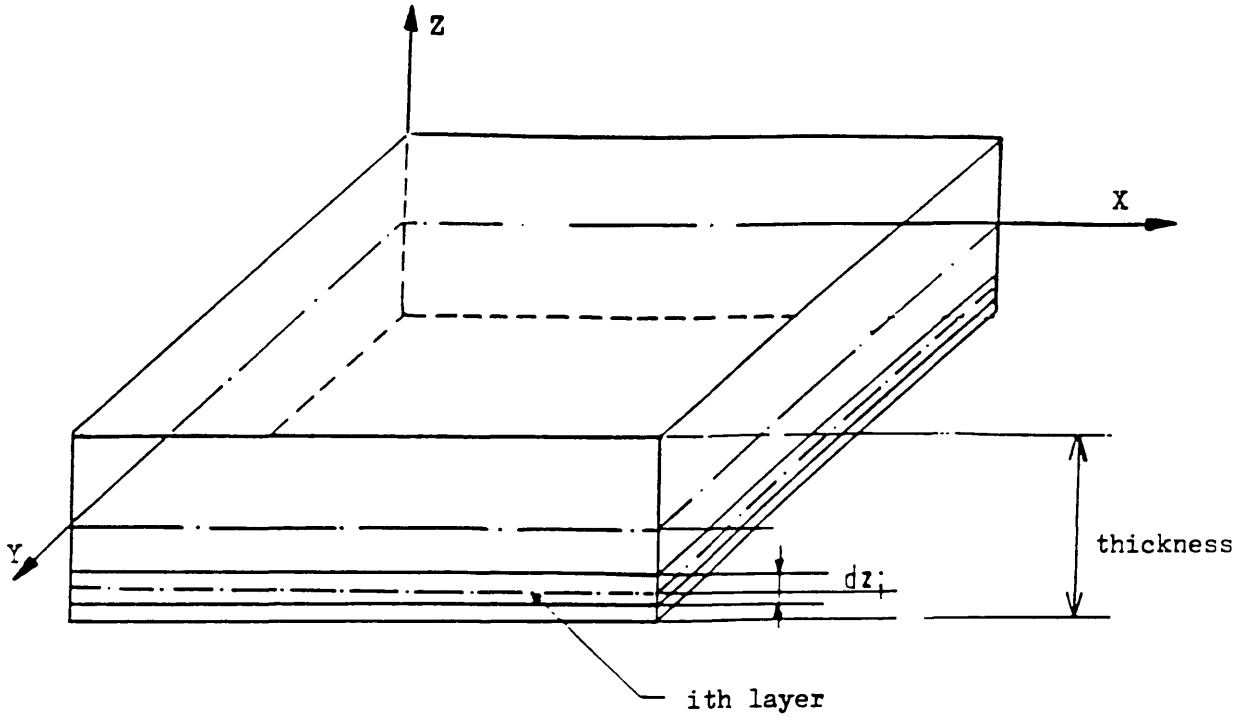

Fig.4.9 Layer Idealization

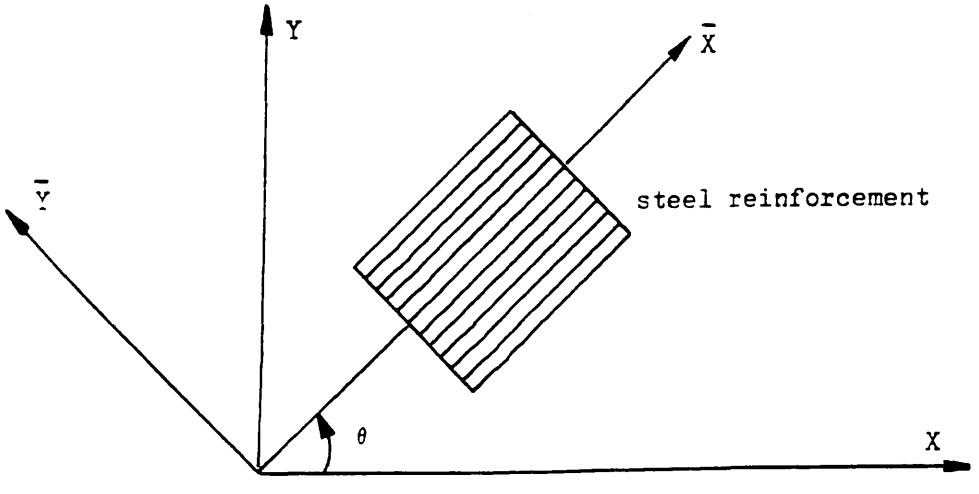

Fig.4.10 Steel in a General Direction

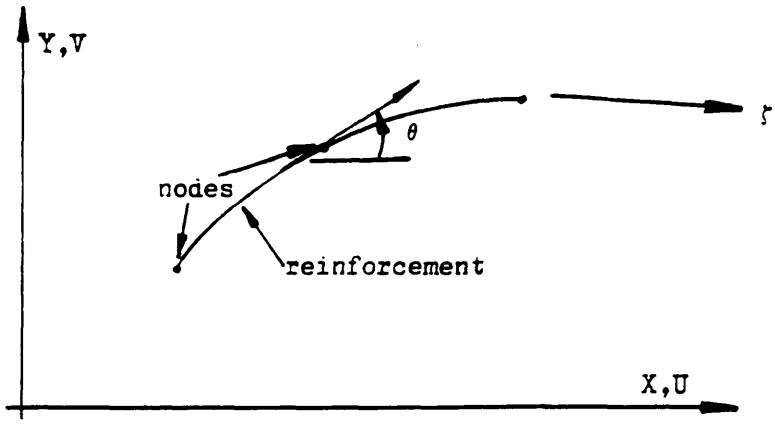

Fig.4.11 A Discrete Reinforcement Bar Element

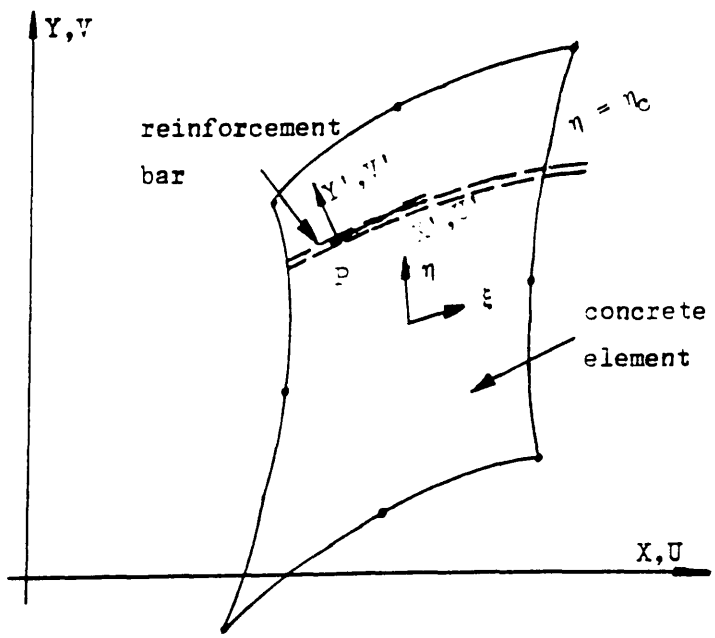

Fig.4.12 Phillips– Zienkiewicz Embedded Bar Model

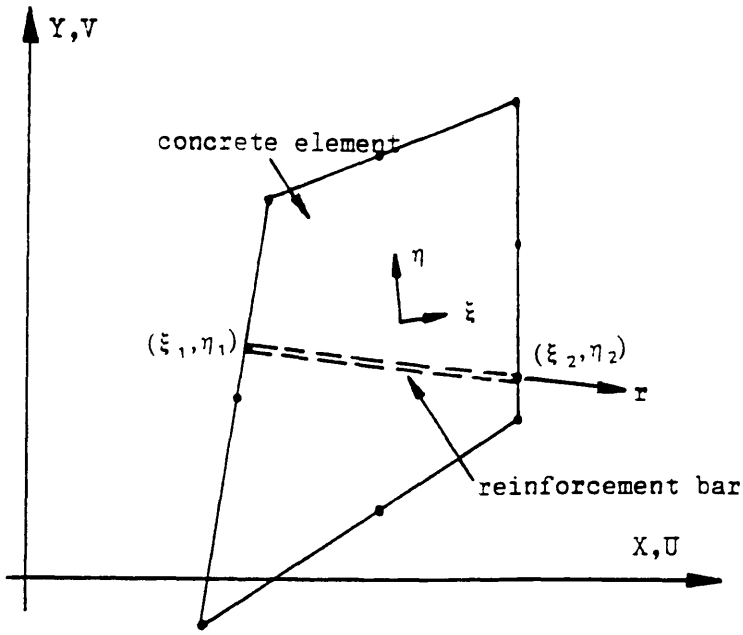

Fig.4.13 An Orientated Embedded Bar Model — formulation I

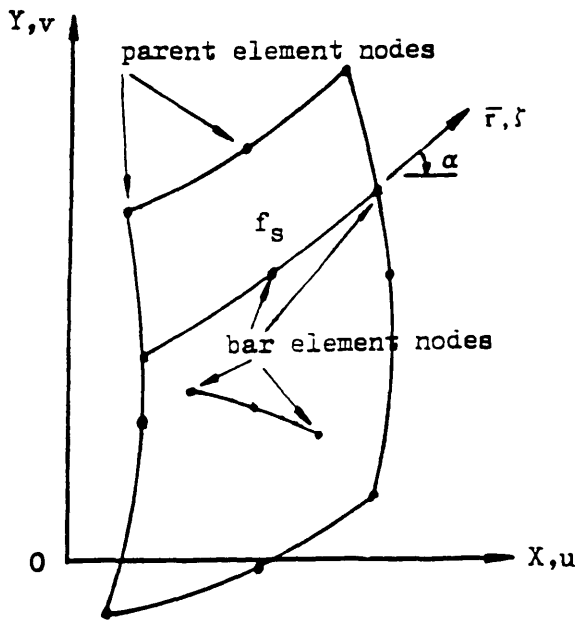

Fig.4.14 A General Embedded Bar Model — formulation II

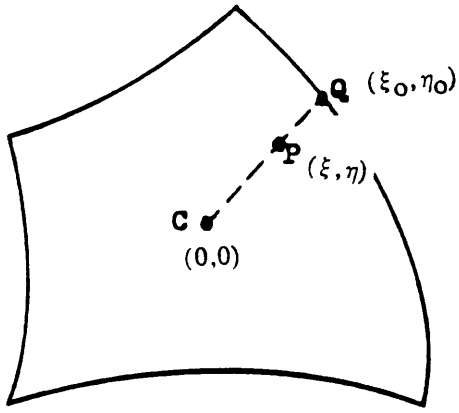

(a)

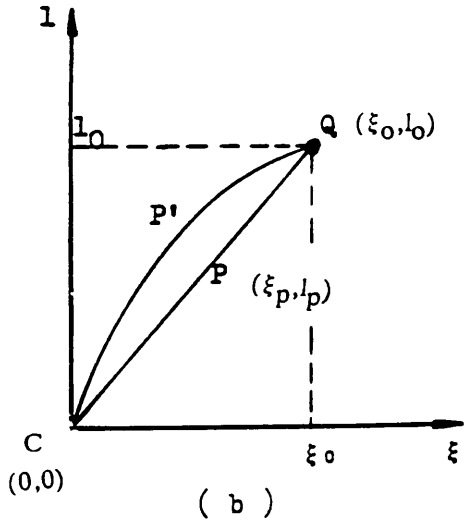

(b)

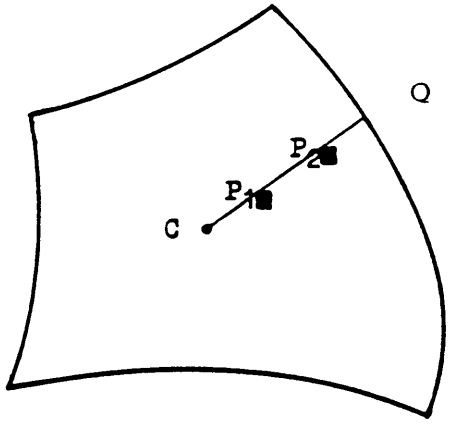

(c)

Fig.4.15 Linearity Verification

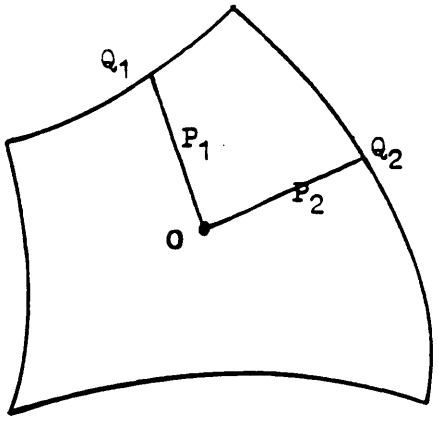

Fig.4.16 Singularity Verfication

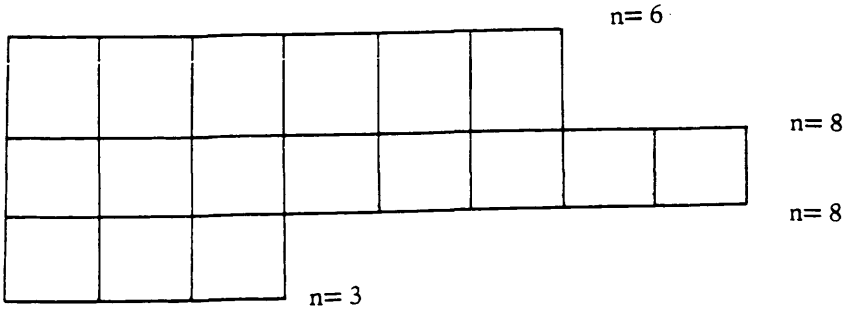

Fig.4.17 Different Situations in Adjacent Lines

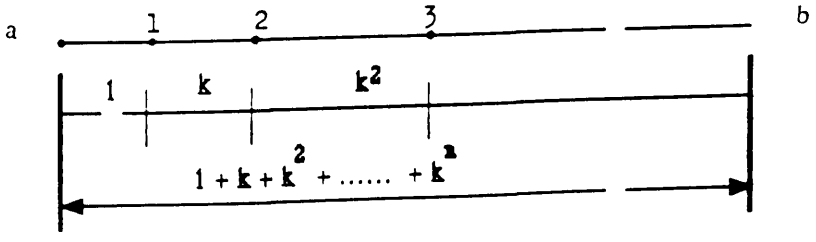

Fig.4.18 Effect of Weighting Factor

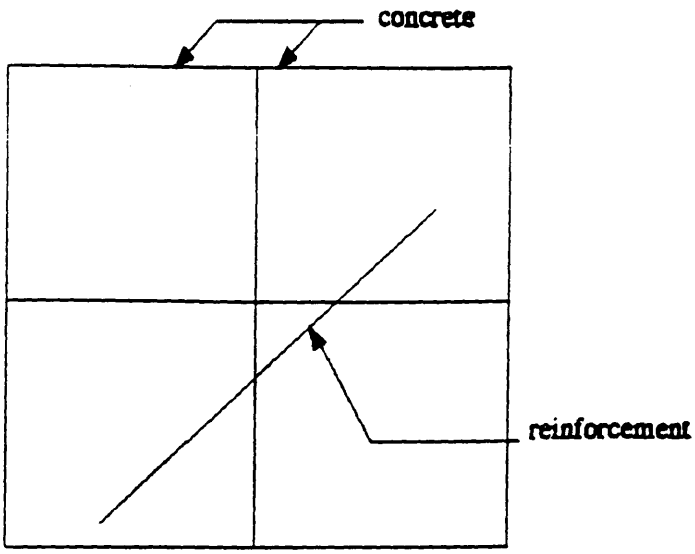

(a)

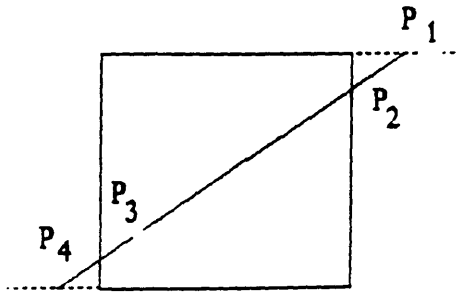

(b)

Fig.4.19 Intersections of a Bar With Concrete Element Sides

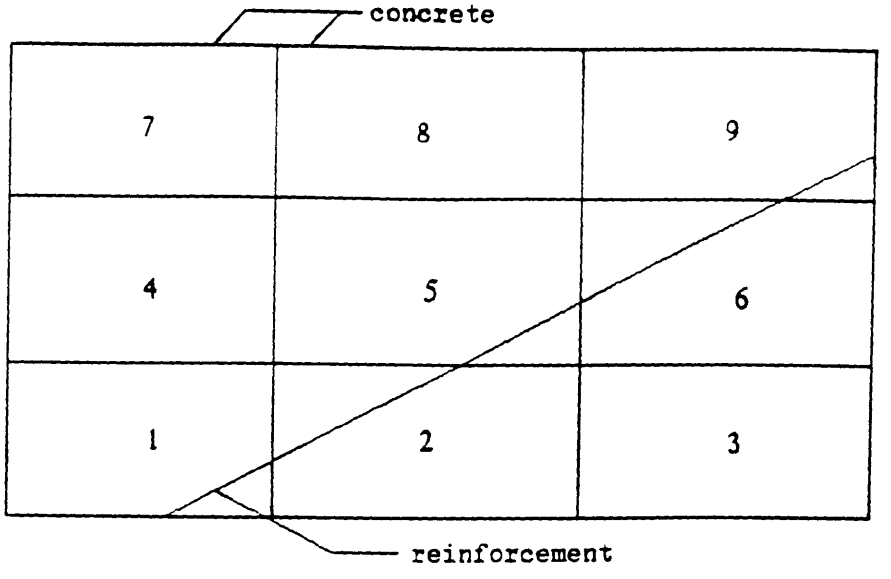

Fig.4.20 Efficient Computation Over Concrete Elements

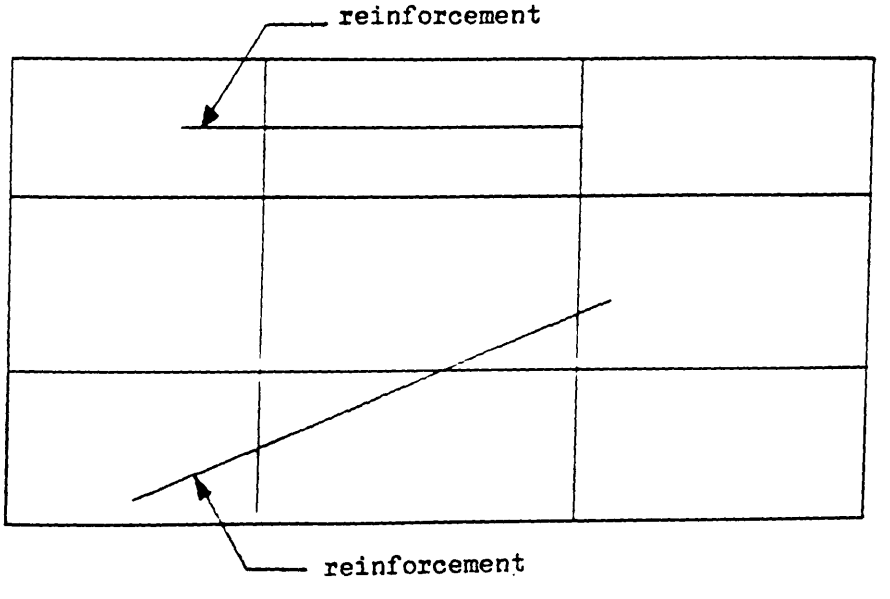

Fig.4.21 A Bar Terminlated Inside Concrete Element

CHAPTER FIVE

BOND–SLIP BEHAVIOUR

AND

SIMULATION TECHNIQUES

5.1. Introduction

It has been recognized for some time that there is a close relationship between bond behaviour and crack formation in reinforced concrete. Therefore, much interest has been shown in the mechanism of stress transfer between steel and concrete, and it has been found that the carrying capacity of reinforced concrete structures depends on this bond between steel reinforcement and concrete. Over the years, both numerical and experimental investigations have been done in this field. For example, Watstein[Watstein 1941] measured the distribution of bond stress by using mechanical gauges, Mains[Mains 1951] and Bresler and Bertero[Bresler and Bertero 1968] by using electrical strain gauges. Broms[Broms 1965] studied the relationships between bond slip, crack spacing and width, and Rehm[Rehm 1961] and Lutz and Gergely[Lutz and Gergely 1967] investigated the mechanics of bond, bond–slip and bond splitting of deformed reinforcing bars.

In the early application of the finite element method to reinforced concrete structures, Ngo and Scordelis[Ngo Scordelis 1967] used a idealized linear–elastic bond–slip relationship to model bond behaviour in 1967. Their pioneering work confirmed the degree to which member behaviour is affected by bond–slip, giving impetus to a surge of studies to formulate reasonable bond–slip relationships for use in finite element analysis.

In 1968, Nilson[Nilson 1968] used the results of Bresler and Bertero to

formulate a high-order polynomial bond-slip relationship for use with bond links. Later, various experimental techniques were developed for measuring local bond stress and bond-slip in order to construct a constitutive relationship, for example, Nilson and Tanner[Nilson and Tanner 1971], Dorr[Dorr 1978], Nies[Nies 1979] and others. In the 1970's, Mirz and Houde[Houde 1973, Mirz and Houde 1973] derived an empirical bond stress-slip relationship from the results of tests on sixty two axial reinforced tension specimens and thirty two beam end specimens.

Khouzam[Khouzam 1977] analyzed four of Houde's tension test specimens using a nonlinear finite element program and an incremental load approach. It was seen that the load-displacement response could be predicted with reasonable accuracy by using the bond-slip relation derived by Houde.

Studies have also focused on the effects of concrete cover and end distances[Hungspreug 1981] and load history effects[Morita 1973]. But there is still no general agreement. Some researchers[Nilson 1972, Pochanart and Harmon 1989] believe that the shear stress-slip relationship is of a local nature, i. e the relationship is not unique but depends on the location. Edwards and Yannopoulos[Edwards and Yannopoulos 1979] and Nammur and Naaman[Nammur and Naaman 1989] however concluded that the bond-slip relationship is a material property and hence location-independent.

Currently, Pochanart and Harmon[Pochanart and Harmon 1989] interpreted general behaviour of bond-slip under monotonic and cyclic loading, and presented a model for the local bond-slip relationship in well-confined concrete (i.e. no splitting effect considered). The model was suggested as applicable to monotonic, cyclic and fatigue-type loading conditions. The model's parameters are all related to the bar deformation pattern quantified directly from the physical

dimensions of the bar, and the concrete strength. Further work is needed to generalize the model for it to be applicable to any scale.

In finite element analysis, two types of bond element models have been developed, i. e.

i). Interface element, and
ii). Embedded bond element.

The first type of bond elements can be further divided into a lumped form and a continuous form. The former was proposed by Ngo and Scodelis[Ngo and Scodelis 1967] in the discretization of a beam. The latter was proposed by Goodman, Taylor and Brekke[Goodman, Taylor and Brekke 1968] in solving problems in rock mechanics. The continuous form was based on the notion of a continuous relative displacement field, while the lumped interface element lumps the relative displacement to the nodes. Both of these elements connect one node of a concrete element with one node of an adjacent steel element. They have no physical dimension so that the two nodes have the same coordinates before loading. The two elements are used in finite element analysis usually in conjunction with discrete reinforcement elements.

The continuous interface element is potentially more powerful and has been further investigated. Hoshino[Hoshino 1974] introduced the continuous interface element into modelling bond problems by utilizing a linear bond– slip relationship. It was then developed and generalized by Schafer[Schafer 1975]. In their contributions, the relative displacement between concrete and reinforcement was considered only in the direction of reinforcing bar, whereas in the direction normal to the bar complete compatibility was assumed.

It has been suggested[Nilson 1982] that the continuous interface element is superior to the lumped form, but this was not accompanied by a comparative study. It is still questionable which type of element is preferable.

More recently, a modified and more general version of the continuous interface element has been developed by Mehlhorn and Keuser[Mehlhorn and Keuser 1985] in two and three dimensional structural analysis and shell structure analysis using layered shell elements, which takes into account the normal stress between concrete and reinforcement. Application of this continuous element to pull-out test analysis showed satisfactory agreement with their experimental results.

A variation of the interface element is the so-called "bonds zone element", proposed by de Groot, Kusters and Monnier[Groot, Kusters and Monnier 1981]. In their model, not only was the contact surface between the steel and concrete modelled, but also the concrete in the immediate vicinity of reinforcing bar was modelled by an adopted material law which considered the special properties of the bond zone. Since these properties are difficult to obtain, this bond zone element is not often adopted.

An embedded bond element was proposed by Balakrishnan and Murry[Balakrishana and Murry 1987] using the embedded reinforcing bar model[Phillips and Zienkiewicz 1976] by introducing artificial "nodes" along the reinforcing bar. These authors intended to utilize the independence of the steel mesh layout from that of concrete finite element mesh. The virtual work of the bond element was taken into account and the stiffness matrix of the bond-slip element was assembled with its parent concrete element's stiffness matrix and embedded reinforcement bar matrix in a standard manner. However, this increases the total number of degrees of freedom and hence increases the computational cost in solving the consequent equations for the whole structure. Phillips and

Wu[Phillips and Wu 1990] also proposed an embedded bond element for straight bars generally orientated across opposite sides of the concrete element. This approach also utilised artificial "bond" nodes along the steel bar, but the extra degrees of freedom associated with the bond–slip at these nodes were condensed out so that there was no increase in the global stiffness matrix. This will be described in more detail later, along with several enhancements which improve its performance and make it applicable to curved bars in a generally curved side parent element.

Allwood and Bajarwan[Allwood and Bajarwan 1989] proposed a different approach which required a separate analysis of the steel and concrete. The combined response was obtained by using the concept of "interforces" to represent bond forces between the concrete and steel. The technique requires an iterative procedure to avoid any additional increase in the number of equations to be solved. However, their method did not take advantage of the embedded formulation, the reinforcing bars being discretized separately.

In the remainder of this chapter, bond–slip behaviour and its constitutive relationships under monotonic and repeated/cyclic loading will be first discussed. Attention will then be focused on the bond–slip modelling techniques. Finally the new general embedded bond element will be presented with detailed derivation and interpretation.

5.2. Bond–Slip Behaviour

5.2.1 Bond Mechanism and Basic Concepts

Bond can be thought of as the shear stress or force between a bar and the surrounding concrete. It comprises i) chemical adhesion, ii) friction and, iii)

mechanical interaction between concrete and steel. The force in the bar is transmitted to the concrete by this bond, or vice versa.

As shown in Fig.5.1, assuming the effects of the discrete ribs and internal cracks are "smeared" so as to cause continuous action along the bar, the longitudinal force equilibrium of an infinitesimal bar element requires that the bond stress is proportional to the change of the bar tension, which gives

$$F_b \, dr = \frac{\partial F_s}{\partial r} \, dr \qquad (5.1)$$

where F_b is the bond force distribution, F_s is the steel force distribution, and r represents the bar direction.

Letting τ_b be the bond stress and Φ the bar perimeter, we obtain

$$\tau_b = \frac{E_s \, A_s \, d\epsilon_s}{\Phi \, dr} \qquad (5.2)$$

where E_s is the elasticity modulus of steel A_s is the bar's cross section, and $d\epsilon_s$ is the strain change rate of the steel.

This indicates that the bond stress is proportional to the slope of the bar force distribution, and that the area between any two points of the bond stress curves is equal to the change of bar force between these two points.

In order to determine bond stress, the average bond force over a length Δr is calculated first based on the difference of the forces in a steel bar between two successive gauges I and II, i. e.

$$\Delta F_s = F_{IIs} - F_{Is} \qquad (5.3)$$

where ΔF_s is the difference in steel force between cross sections I and II,

and F_{Is} and F_{IIs} are the steel forces at section I and II, respectively.

The average bond stress is then given by

$$\tau_{ave} = \frac{F_{IIs} - F_{Is}}{\Phi \, \Delta l} \qquad (5.4)$$

Bond–slip is defined as a relative displacement between concrete and steel along their interface. Early attempts[Mains 1951] to obtain bond–slip made use of miniaturized differential transducer gauges, and specially–adapted electrical resistance strain gauges. A practical method is to calculate the displacement difference between concrete and steel at specific locations along the interface. The steel displacement is found by numerical integration of steel strains, as given by the interval gauges. The concrete displacement is obtained by integrating the concrete displacements measured by special electrical resistance strain gauges embedded in concrete a short distance from the steel–concrete interface (see Fig.5.2). The technique is imperfect since concrete strain is obtained not at the interface, but a short distance from it, and the effect of concrete cracking is averaged out over the length of each concrete gauge. However, analyses based on stress–slip curves found in this way indicate that results are quite good.

Referring to the measurement, it should be pointed out that the bond slip obtained is a total slip over the length between the two adjacent strain gauges rather than the local bond–slip, which contrasts to the constitutive relationship used for "slip" in finite element analysis. The former is the displacement of the bar relative to an imaginary cross section of concrete over which the transferred stress is distributed. The slip in this sense is denoted as "apparent slip". The latter is the total slip at a particular position.

5.2.2 Under Monotonic Increasing Loading

Many investigations have been carried out to determine the bond stress– slip relationship under monotonic increasing loading[Mains 1951, Somayaji and Shah 1979 and Houde 1973]. Most of them used one bar size while Houde reinforced the specimens with #8, #6 and #4 bars. The tests conducted are usually anchorage tests and force transfer tests as shown in Fig.5.3. The former simluates the anchorage effect of a reinforcement bar end while the latter models the condition in the tension zone of a concrete beam between flexural cracks.

From the experimental results presented so far, the following points can be concluded.

1). Deformed bars develop relatively higher bond stress over a shorter length of bar than plain bars.

2). Plain straight– bar specimens fail mostly by slip, while deformed bar specimens fail by yielding of the bar with no bond failures.

3). The maximum local bond stress of a plain straight bar occurs near the unloaded end. The maximum value is not reached until maximum total load is applied. The maximum local bond stress occurs near the loaded end at relatively low loads. It then moves towards the unloaded end as the load is increased.

4). For a deformed straight bar, the maximum local bond stress occurs near the loaded end of the bar, while the part of the bar near the unloaded end never develops a large bond stress.

5). A hook on a deformed bar increases the bond effectiveness along the parts of the bar ahead of the hook. A hook on a plain bar changes the failure mode from slip failure to fracture failure of the bar.

8). Local cracks govern the magnitude and distribution of both tensile stress in the reinforcing bar and bond stresses. Crack locations are coincident with lumps of the bar force curve and the positive and negative peaks of the bond–stress curve.

5.2.3 Under Repeated and Cyclic Loading

For repeated and cyclic loading behaviour, the bond at any stress level is influenced by the previous loading history. The effectiveness depends mainly on the given stress level and previous peak stress and less on the number of the cycles. The bond stress–slip curves are characterized by residual slip at zero load level and hysteresis loops. Particularly, the following experimental phenomena have been observed[Shipman and Gerstle1979 and Rehm and Eligeausen 1979].

1). There is no evidence of a significant difference between the curves of small and those of large specimens subjected to the same amplitude of cycles.

2). Under repeated and cyclic loading, a residual slip exists at zero load level, the loading and unloading paths are not coincident, and thereby form hysteresis loops.

3). Under very low amplitude of applied load, no residual slip or significant hysteresis loop occurs, which indicates that there is a linear elastic region in the bond stress–slip relation curve.

4). As loading is applied, the hystersis loops shift by a small amount to the right, producing additional residual slip at zero load, as well as additional slip at any other load level. These additional bond stress and slip tend to diminish as the number of load cycles is increased, and the hystersis loops become congested.

5). The amount of the bond destruction in the first repeated loading increases with increasing load. The trend is that the higher the load amplitude, the larger the additional slip, i.e. the rate of bond deterioration is larger at higher load amplitudes than at lower ones

6). Although every subsequent loading produces additional slip at all load levels in a repeating cycle, this slip is small in comparison with the slip produced during the first cycle.

5.3 Bond–slip Constitutive Relationships

General Remarks

When the constitutive relationship is derived, the bond slip is defined as a local slip, rather than a total interface slip. The bond stress represents the force transfer from concrete to reinforcement or the decreasing/increasing ratio of concrete force and steel force.

Under Monotonic Increasing Loading

Various formulations have been derived from experimental results to represent the bond stress–slip relationships. An early formula was obtained by Nilson[Nilson 1968] using the results of Bresler and Bertero. He obtained the third–order polynomial,

$$\tau_b = 3606\ (10^3\ s) - 5356\ (10^3\ s)^2 + 1986\ (10^3\ s)^3 \qquad (5.5)$$

in which τ_b is the bond stress in psi and s is the slip in inches.

Based on the experimental results from tests on sixty two tension specimens reinforced with a #8, #6 or #4 deformed bar, and thirty two pull–out tests on beam end specimens reinforced with #8 deformed bars, Houde[Houde 1973] derived the following general fourth order relationship:

$$\tau_b = 1.95 \times 10^6\ s - 2.35 \times 10^9\ s^2 + 1.39 \times 10^{12}\ s^3 - 0.33 \times 10^{15} s^4 \qquad (5.6a)$$

where τ_b and s are the same as defined above. In this derivation, the author considered the load level, the thickness of the concrete cover and the concrete strength.

In contrast to the early studies, Nilson[Nilson 1972] investigated the end distance effects on the bond–slip constitutive relationships. He concluded that the end distance effect was significant, as shown in Fig.5.4, with the initial modulus of all these bond–slip curves being 2×10^6 psi/inch. However, there is some doubt since his bond slip was the total slip at a particular point, rather than a local slip at that point. Therefore, it is reasonable that the slip could be larger under a lower bond stress at a position nearer to the loaded end, i.e. no matter where the point is taken into consideration, bond stress may have a unique relation with local bond slip.

In fact, in selecting a bond stress–slip curve in finite element analysis it is usually best to keep it as simple as possible based on reasonable agreements with

experimental phenomena. The relationship derived by Houde in 1973 (eq.5.6) has been examined in this study with appropriate conversion to S.I. units, because it is generally accepted as being reliable. Thus the relationship is given by

$$\tau_b = 5.29 \times 10^2 \, s - 6.38 \times 10^5 \, s^2 + 3.77 \times 10^8 \, s^3 - 8.96 \times 10^{10} s^4 \qquad (5.6b)$$

in which τ_b is in N/mm^2 and s is in mm, and is shown in Fig.5.5.

Under Repeated and Cyclic Loading

As far as repeated and cyclic loading is concerned, the bond stress–slip relationship becomes very complex. Not only does the bar geometry and concrete confinement need to be considered, but also the loading history should be taken into account, which produces a hysteresis response. Due to bond deterioration effects, the bond–slip increases in subsequent loading cycles. An empirical formulation to deal with this situation was given by Rehm and Eligehausen[Rehm and Eligehausen 1979] who tested 308 pull–out specimens. The parameters studied were the loading amplitude, bar diameter, concrete quality and bond length. They calculated the slip S_n from the initial slip S_0 after a certain number of load reversals n by the equation

$$S_n = S_0 \, (1 + K_n) \qquad (5.7)$$

where K_n is the deterioration coefficient determined from the experimental data by

$$K_n = (1+ n)^{0.107} - 1 \qquad (5.8)$$

It was also concluded that the relation eq.(5.8) was not significantly influenced by the various other parameters.

Recently, Pochanart and Hatmon[Pochanart and Harmon 1989] presented bond–slip relationships for well–confined concrete based on a damage rule (see appendix III). The parameters studied could be determined directly from the bar's deformation pattern and concrete strength. They related the bond stress–slip curve of repeated/cyclic loading with monotonic response by a reduction factor, and termed the curve a "reduced monotonic envelope".

As shown in Fig.5.6, four parameters are needed to define the monotonic curve as follows

$$\tau_1 = 4.2 - 0.06 \left(l_s/l_h \right) \tag{5.9}$$

$$s_1 = 0.003\ \sigma_b \tag{5.10}$$

$$\tau_3 = 0.80 - 0.01 \left(l_s/l_h \right) \tag{5.11}$$

$$s_3 \simeq l_s \tag{5.12}$$

where l_s is the spacing between steel lugs, l_h is the lug height, and σ_b is the lug bearing pressure at maximum bond strength, i. e. splitting strength of concrete.

The ascending branch follows the cubic relationship given in the figure. The descending branch follows a straight line to a point defined by the frictional bond stress τ_3 and the corresponding slip s_3. The horizontal frictional branch represents the remaining frictional stress after the bond strength is eliminated.

Having obtained the monotonic bond stress–slip curve, the reduced monotonic envelope can be constructed as shown in Fig.5.7. It is defined by (τ_1', s_1', τ_3', s_3'

and τ_f'), where

τ_1' and s_1' are new peak bond stress and corresponding slip.

τ_3' is the new residual frictional stress.

$s_3' = l_3' = l_s - ex$, is the undamaged length of the concrete key.

τ_f' is the current value of the developed frictional stress.

In addition, an offset value of 1/4 ex is suggested which identifies where the strength component of the reduced envelope begins.

These relationships can be extended to include hysteresis rules for bond behaviour. Referring to Fig.5.8, these can be summarized as follows:

1. Under monotonic loading, the bond stress–slip relationship follows the monotonic envelope.

2. The unloading path is very stiff.

3. As long as there is no slip in the opposite direction, reloading will be on the same path as unloading. When the stress reaches the point where the unloading took place, the bond stress–slip relation will follow the previous envelope.

4. If the reversed load is higher than the developed frictional bond stress, there will be slip in the opposite direction, and the reduced envelope based on the remaining concrete key will be used for the new envelope.

5. If loading takes place after there is slip in the opposite direction, the reloading path follows the unloading stiffness relationship until either a reduced envelope or frictional envelope is crossed.

6. If loading continues in the opposite direction, the loading path will follow the frictional stress path until it crosses the new envelope and then will follow the new envelope.

The monotonic version of this relationship has also been examined in this study.

5.4 Bond–Slip Modelling Techniques

5.4.1 Lumped Interface Element

The so–called "lumped element" shown in Fig.5.9 is a lumped interface element and in concept consists of two linear springs K_t and K_n parallel to a set of orthogonal axes. It has mechanical properties but no physical dimensions. The element stiffness of the bond link, K_b, is then given in its local coordinate system by

$$\underline{F}^b = \underline{K}_b \cdot \underline{s} \qquad (5.13)$$

i.e.

$$\begin{bmatrix} F_t^b \\ F_n^b \end{bmatrix} = \begin{bmatrix} K_t & 0 \\ 0 & K_n \end{bmatrix} \begin{bmatrix} s_t \\ s_n \end{bmatrix}$$

where $K_t = \pi \Phi l_e E_t$, l_e is the length of the bond element,

Φ is the diameter of the reinforcement bar,

E_t is the bond modulus in direction t, and

F_t^b is the bond force in direction t.

Similar definitions apply in direction η.

This linkage element can be used to connect steel with concrete, or connect steel with steel if such necessity arises.

The element stiffness matrix is then transformed from local to global coordinates and the relative displacements are related to the nodal displacements, which gives

$$\underline{F}^b = \underline{K} \cdot \underline{\delta} \tag{5.14}$$

i.e.

$$\begin{bmatrix} F_y^i \\ F_z^i \\ F_y^k \\ F_z^k \end{bmatrix} = \begin{bmatrix} k_{11} & k_{12} & -k_{11} & -k_{12} \\ k_{12} & k_{22} & -k_{12} & -k_{22} \\ -k_{11} & -k_{12} & k_{11} & k_{12} \\ -k_{12} & -k_{22} & k_{12} & k_{22} \end{bmatrix} \begin{bmatrix} \delta_y^i \\ \delta_z^i \\ \delta_y^k \\ \delta_z^k \end{bmatrix}$$

where

$k_{11} = K_t \cos^2\alpha + K_n \sin^2\alpha$

$k_{12} = (K_t - K_n) \sin\alpha \cos\alpha$

$k_{22} = K_t \sin^2\alpha + K_n \cos^2\alpha$

F_y^i is the nodal force in the global system, at node i in direction y.

δ_y^i is the nodal displacement in the global system, at node i in direction y,

α is the angle between the local t-axis and the global y-axis, as shown in Fig.5.9.

Having obtained this final form, the element stiffness matrix $\underline{K}$ can be inserted into the global stiffness matrix.

The stiffness K_t known as a "slip modulus" can be estimated based on experimental results. The stiffness K_n in the normal direction to the reinforcing bar represents the normal force causing dowel action or a "press down" effect of reinforcement in resisting shear. It is needed when large crack openings take place. In this situation, the bond depends not only on the chemical adhesion and mechanical interlocking between the steel and concrete, but also on how well the surrounding concrete holds the steel from vertical separation. This is, of course, a three dimensional problem. Despite these complexities, it is reasonable that in the range when dowel action can be neglected, a very large value of K_n can be chosen, thereby assuming that steel and concrete are nearly rigidly connected. However, if the movement of the steel is needed to be considered to represent the dowel action in the calculation, a realistic value of the spring stiffness, K_n, is demanded. At present, it is open to question and requires further investigation on how to find out a realistic calculation of K_n to simulate the dowel action.

The lumped interface bond element has been extended to three dimensional structural analysis by Ahmad and Bangah in 1987[Ahmad and Bangah 1987]. The authors adopted three idealized forms of the bond stress– slip relationships for the modulii in the three directions.

5.4.2 Continuous Interface Elements

1. 1– D Continuous Interface Element

The one dimensional continuous interface element has no physical dimension in the transverse direction when undeformed. It has two or three double nodes as shown in Fig.5.10, using linear, parabolic or cubic interpolation functions, respectively. The number of nodes should be compatible with that of the concrete and reinforcement elements. For example, the connection between a three– node

parabolic element with three nodes along each side of a concrete is accomplished by a contact element with three double– nodes.

In the unloaded stage, two opposite nodes i and k have identical coordinates, these nodes combining into a so– called double node ik, as shown in Fig.5.10(a).

The local coordinates of any point $\underline{x}$ are related to the global coordinates of the nodal points $\underline{x}_i$, which gives

$$\underline{x} = \underline{N} \cdot \underline{u}_i \tag{5.15a}$$

i. e. $$x(\xi) = \sum_{i=1}^{n} N_i(\xi)\, x_i \tag{5.15b}$$

and $$y(\xi) = \sum_{i=1}^{n} N_i(\xi)\, y_i \tag{5.15c}$$

When the load is applied the displacements $\underline{u}$ at an arbitrary point along the element are related to the nodal displacements $\underline{u}_i$ by the shape functions, which are given by

$$\underline{u} = \underline{N} \cdot \underline{u}_i \tag{5.16a}$$

i. e. $$u(\xi) = \sum_{i=1}^{n} N_i(\xi)\, u_i \tag{5.16b}$$

and $$v(\xi) = \sum_{i=1}^{n} N_i(\xi)\, v_i \tag{5.16c}$$

where N_i are interpolation functions, and n is the number of nodes along the contact element.

The relative displacements $\underline{\delta}$ between the two connected points will occur, as

shown in Fig.5.11, given by

$$\underline{\delta} = \underline{A} \cdot \underline{u} \tag{5.17}$$

i.e.

$$\begin{bmatrix} \delta_x \\ \delta_y \\ \delta_z \end{bmatrix} = \begin{bmatrix} -1 & 0 & 0 & 1 & 0 & 0 \\ 0 & -1 & 0 & 0 & 1 & 0 \\ 0 & 0 & -1 & 0 & 0 & 1 \end{bmatrix} \begin{bmatrix} u_i \\ v_i \\ w_i \\ u_k \\ v_k \\ w_k \end{bmatrix}$$

Substituting eq.(5.16) into eq.(5.17) leads to eq.(5.18), which relates the relative displacements $\underline{\delta}$ at any point of an element to the nodal displacements $\underline{u}_i$.

$$\underline{\delta} = \underline{A} \cdot \underline{N} \cdot \underline{u}_i = \underline{B} \cdot \underline{u}_i \tag{5.18}$$

Analogous to eq.(5.17), the stress $\underline{\sigma}$ at points i and k are related in eq.(5.19) to the contact stresses $\underline{\tau}$ between two elements (see Fig.5.12), i.e.

$$\underline{\sigma} = \underline{A}^T \cdot \underline{\tau} \tag{5.19}$$

i. e.

$$\begin{bmatrix} \sigma_{xi} \\ \sigma_{yi} \\ \sigma_{zi} \\ \sigma_{xk} \\ \sigma_{yk} \\ \sigma_{zk} \end{bmatrix} = \begin{bmatrix} -1 & 0 & 0 \\ 0 & -1 & 0 \\ 0 & 0 & -1 \\ 1 & 0 & 0 \\ 0 & 1 & 0 \\ 0 & 0 & 1 \end{bmatrix} \begin{bmatrix} \tau_x \\ \tau_y \\ \tau_z \end{bmatrix}$$

The relationship between contact stresses and relative displacements in the contact interface is defined in the local coordinate system by

$$\underline{\tau}^{L} = \underline{C}^{L} \cdot \underline{\delta}^{L} + \underline{\tau}^{oL} \tag{5.20}$$

i. e.

$$\begin{bmatrix} \tau_r \\ \tau_t \\ \tau_s \end{bmatrix} = \begin{bmatrix} C_{rr} & C_{rt} & C_{rs} \\ C_{tr} & C_{tt} & C_{ts} \\ C_{sr} & C_{st} & C_{ss} \end{bmatrix} \begin{bmatrix} \delta_r \\ \delta_t \\ \delta_s \end{bmatrix} + \begin{bmatrix} \tau_r^o \\ \tau_t^o \\ \tau_s^o \end{bmatrix}$$

where L indicates the local system. τ^{oL} is the initial stress, and r, s and t are tangential and normal directions at the double node ik. C^{L} is a material matrix.

In the special case when the contact behaviour in the coordinate directions are independent from each other, we obtain the material matrix C^{L*} as

$$[C^{L*}] = \begin{bmatrix} C_{rr} & 0 & 0 \\ 0 & C_{tt} & 0 \\ 0 & 0 & C_{ss} \end{bmatrix} \tag{5.21}$$

where C_{rr}, C_{tt} and C_{ss} are the bond–modulii in the r–, t– and s–directions.

To build up the element stiffness matrix and the vector of nodal forces, the material matrix has to be transformed from the local to the global coordinate system. Then the element stiffness matrix $[\underline{K}^{m}]$ and the vector of element nodal forces $\underline{F}^{m}$ are obtained in the global system, which can be assembled into the structural force vector directly without any additional effect. These transformations and integrals are

$$[\underline{C}] = [\underline{T}]^{T} [\underline{C}^{L}] [\underline{T}] \tag{5.22}$$

$$[\underline{K}^{m}] = \int [\underline{B}]^{T} [\underline{C}] [\underline{B}] \, dA \tag{5.23}$$

$$F^{m} = \int [\underline{B}]^{T} \underline{\tau} \, dA \tag{5.24}$$

and

$$\underline{\tau} = [\ \underline{C}\ ]\ \underline{\delta} \qquad (5.25)$$

where

$$[\underline{T}] = \begin{bmatrix} \underline{t}_r \\ \underline{t}_n \\ \underline{t}_s \end{bmatrix}$$

is a transformation matrix, consisting of unit direction vectors parallel and normal to the contact interface at the double node ik, see Fig.5.12.

The integrations above are carried out numerically over the contact surface, usually with a Gauss numerical integration procedure.

The differential area dA for the one–dimensional contact element is

$$dA = b\ \det|J|\ d\xi \qquad (5.26)$$

where b is the width of the contact surface and $\det|J|$ is the determinant of the Jacobian matrix. In particular, for the one–dimensional contact problem considered here, $\det|J|$ is equal to the real length of the element, L.

2. 2–D Continuous Interface Element

As shown in Fig.5.13, the 2D contact element is used to connect 3D elements as well as layered shell elements.

In principle, the procedure developed for the one–dimensional contact element can be directly used for the two–dimensional element, except that the second coordinate η is employed. The coordinates ξ, and η form an orthogonal natural coordinate system.

Furthermore, the differential area dA is now

$$dA = \det|J|\, d\xi\, d\eta \tag{5.27}$$

where $\det|J|$ is related to the two coordinates. Therefore, for the two dimensional contact element $\det|J|$ is equal to the real surface area of the element, which is obtained from

$$\frac{\partial}{\partial \underline{r}} = [\underline{J}] \cdot \frac{\partial}{\partial x} \tag{5.28}$$

i.e.

$$\begin{bmatrix} \frac{\partial}{\partial r} \\ \frac{\partial}{\partial s} \\ \frac{\partial}{\partial t} \end{bmatrix} = \begin{bmatrix} \frac{\partial x}{\partial r} & \frac{\partial y}{\partial r} & \frac{\partial z}{\partial r} \\ \frac{\partial x}{\partial s} & \frac{\partial y}{\partial s} & \frac{\partial z}{\partial s} \\ \frac{\partial x}{\partial t} & \frac{\partial y}{\partial t} & \frac{\partial z}{\partial t} \end{bmatrix} \begin{bmatrix} \frac{\partial}{\partial x} \\ \frac{\partial}{\partial y} \\ \frac{\partial}{\partial z} \end{bmatrix}$$

5.4.3 Embedded Bond Element

Fig.5.14 shows the embedded bond element of Balakrishnan and Murray[Balakrisknan and Murray 1987]. They assumed that the bar and element sides are straight. Bond nodes are added along the embedded reinforcement bar. The reinforcement displacement field is then given by

$$f_s = f_c + f_b \tag{5.29a}$$

where f_c and f_b are the displacement of the concrete and bond slip at that point. They are defined as

$$f_c = u \cos\theta + v \sin\theta \tag{5.29b}$$

where u and v are the displacements of concrete in x— and y— direction,

respectively, and θ is the tangential angle of the bar at a particular point.

and $$f_b = \sum_{j=1}^{p} H_j \, U_{bj} \qquad (5.29c)$$

in which H_j is the shape function of the embedded the bond element, U_{bj} are the nodal bond displacements and p is the number of slip nodes along the bar.

The virtual work of the embedded bond element is given by

$$\delta[U_{bj}]^T \left\{ \sum_{m} \int_{-1}^{1} [H_j]\,[D_b]\,[H_j]^T A_p \, J_s \, d\zeta \right\} [U_{bj}] \qquad (5.30)$$

where D_b is the bond stress producing unit slip; m is the number of bond elements in the concrete element; A_p is the contact area per unit length of reinforcing steel; and $J_s = [(dx/d\zeta)^2 + (dy/d\zeta)^2]^{\frac{1}{2}}$. The factor in the curly bracket is the stiffness matrix for the bond element.

Because the bar is straight θ does not change along the element, and therefore the reinforcement strain can be obtained by

$$\epsilon_s = \frac{du}{dr}\cos\theta + \frac{dv}{dr}\sin\theta + \frac{df_b}{dr}$$

$$= \frac{1}{J_s}[\cos\theta \ \sin\theta] \begin{bmatrix} \left[\frac{\partial N_i}{\partial \zeta}\right] & [0] \\ [0] & \left[\frac{\partial N_i}{\partial \zeta}\right] \end{bmatrix} \begin{Bmatrix} u_i \\ v_i \end{Bmatrix} + \frac{1}{J_s}\left[\frac{dH_j}{d\xi}\right] \{U_{bj}\}$$

$$= [B_{cs} \ B_{bs}] \begin{Bmatrix} [u_i] \\ [v_i] \\ U_{bj} \end{Bmatrix} \qquad (5.31)$$

where i = 1, 2, ..., q are the total number of the concrete nodes; j = 1, 2, ..., p the total number of the bond nodes; and N_i are the shape functions of the concrete element.

The stiffness matrix for the concrete parent element is expanded to include stiffness coefficients related to the reinforcement and bond, the increase in size depending on the number of additional bond nodes. The expanded stiffness matrix is then assembled into the global stiffness in the standard manner.

However, this will expand the bandwidth significantly when bandwidth solution procedures are adopted. On the other hand, it will be difficult to use a front solution technique in the conventional manner. These disadvantages are overcome using the general embedded bond element derived in the next section.

5.4.4 A General Embedded Bond Element

This general formation follows a procedure similar to that used by Balakrishnan and Murray[Balakrishnan and Murray 1987]. However the bar element and the parent concrete element are now generally curved finite elements.

The displacement of steel bar consists of the displacements of the concrete and the bond– slip between the two components, as shown in Fig.5.15.

Consider a point P on the original undeformed bar. After deformation, the reinforcement at this point moves to P_s whilst the concrete has moved to P_c, a point which lies along the deformed reinforcing bar. The distance P_c to P_s represents the bond slip f_b between concrete and steel during deformation. The reinforcement displacement along the deformed bar is then given by

$$f_s = f_c + f_b \tag{5.32}$$

where f_c is the concrete displacement in the direction of the deformed bar. This is obtained by interpolating the nodal displacement of the parent concrete element using the derivation given in Chapter 4 for the embedded element when perfect bond was assumed.

Let U_{b1}, U_{b2}, ..., U_{bp} be p slip degrees of freedom of p bond nodes located on the reinforcement within the element. Then

$$f_b = \sum_{i=1}^{p} H_j \, U_{bj} \tag{5.33}$$

where H_j are the shape functions used to interpolate the bond slip at an arbitrary point along the bar.

The uniaxial strain in the reinforcing steel is then given by

$$\epsilon_s = \frac{df_s}{dr} \tag{5.34}$$

where r is the local direction along the reinforcement.

From eqs.(5.32), (5.33) and (5.34), the steel strain is given by

$$\epsilon_s = [B_{cs}] \{\delta^e\} + \frac{df_b}{dr} \tag{5.35}$$

where $[B_{cs}]$ is a reinforcement strain matrix due to concrete displacement assuming full bond and $\{\delta^e\}$ is the nodal displacements of the concrete element. Note that $[B_{cs}]$ is identical to $[B_s]$ derived in Chapter 4 (eq.(4.52)).

Using eq.(5.33), eq.(5.35) becomes

$$\epsilon_s = [B_{cs}]\{\delta^e\} + \frac{1}{J_s}\left[\frac{\partial H_j}{\partial \xi}\right]\{U_b\} - \left[[B_{cs}] \quad \frac{1}{J_s}\left[\frac{\partial H_j}{\partial \xi}\right]\right]\begin{Bmatrix}\delta^e \\ U_b\end{Bmatrix}$$

$$= [B_{cs}\ B_{bs}]\begin{Bmatrix}\delta^e \\ U_b\end{Bmatrix} \tag{5.36}$$

where $\delta^e = [u_i, v_i]^T$ are the nodal displacements of the concrete element; ξ is the local curvilinear coordinate along the reinforcing bar;

and $$J_s = \left[\left(\frac{dx}{d\xi}\right)^2 + \left(\frac{dy}{d\xi}\right)^2\right]^{\frac{1}{2}}$$

Now the strain energy in the concrete element is

$$\pi_c = \frac{1}{2}\int_{v_e}\{\delta^e\}^T [B_c]^T [D_c] [B_c] \{\delta^e\}\, dv_e \tag{5.37}$$

the strain energy in the steel bar is

$$\pi_s = \frac{1}{2}\int_{v_s}\begin{bmatrix}\delta^e \\ u_b\end{bmatrix}^T [B_{cs}\ B_{bs}]^T [D_s] [B_{cs}\ B_{bs}] \begin{bmatrix}\delta^e \\ U_b\end{bmatrix} dv_s \tag{5.38}$$

the strain energy absorbed by the bond is

$$\pi_{bond} = -\frac{1}{2}[U_b]^T \int_{\substack{bond \\ surface}} [H_b]^T [D_b] [H_b]\, dv_b\, [U_b] \tag{5.39}$$

and the work done by the nodal forces $\{F_e\}$ is

$$\pi_F = -\{\delta^e\}^T [F_e] \qquad (5.40)$$

and the work done by "self-equilibrating external force pairs" ψ_a applied on bond nodes is

$$\pi_{\psi_a} = -\{U_b\}^T \cdot [\psi_a] \qquad (5.40)$$

where all terms have been previously defined.

Minimizing the total potential energy ($\pi_c + \pi_s + \pi_{bond} + \pi_F + \pi_{\psi_a}$), we obtain

$$[K_e] \cdot \begin{Bmatrix} \delta^e \\ U_b \end{Bmatrix} = \begin{Bmatrix} F^e \\ \psi_a \end{Bmatrix} \qquad (5.41a)$$

where $$K_e = \begin{bmatrix} K_c + K_s & K_{bs1} \\ K_{bs1}^T & K_{bs} - K_b \end{bmatrix} \qquad (5.41b)$$

$K_c = \int_{ve} [B_c]^T [D_c][B_c] dv_e$ is the concrete stiffness matrix;

$K_s = \int_{vs} [B_{cs}]^T [D_s][B_{cs}]\, dv_s$ is the reinforcement stiffness matrix, excluding bond effects;

$K_{bs} = \int_{vs} [B_{bs}]^T [D_s][B_{bs}]\, dv_s$, and

$K_{bs1} = \int_{vs} [B_{cs}]^T [D_s][B_{bs}]\, dv_s$ are stiffness matrices due to bond effects;

$K_b = \int_{bond\ surface} [H_b]^T [D_b] [H_b]\, dv_b$ is the bond stiffness matrix.

For K_s, K_{bs} and K_{bs1}, the matrix $[D_s] = E_s$, the modulus of elasticity for steel and $dv_s = A_s dr$ where A_s is the cross-sectional area of the bar, and dr is the differential length. $dv_b = \Phi_s\, dr$, where Φ_s is the perimeter of the reinforcing bar.

Expanding the partitioned matrix gives

$$(K_c + K_s) \cdot \delta^e + K_{bs1} \cdot U_b = \{F^e\} \qquad (5.42a)$$

and $$K_{bs1}^T \cdot \delta^e + (K_{bs} - K_b) \cdot U_b = \psi_a \qquad (5.42b)$$

At a bond degree of freedom, the force can be interpreted of

consisting of two parts

$$\psi_e = \psi_a + \psi_b$$

where ψ_a has been defined already, and ψ_b is the internal self-equilibrating bond force representing the action and reaction between reinforcement and concrete. In Appendices IV and V, it has been explained, in which

$$\psi_b = K_b \cdot U_b \qquad (5.42d)$$

actually appears on the left hand side of the equation and consequently ψ_a is the only force left on the right hand side.

In order to maintain compatiblity at the boundary and only the internal bond-slip can be condensed out, and assuming no external force pair ψ_a act on internal nodes then eq.(5.41) can be re-arranged to give

$$\left[\begin{array}{cccc:c} K_c+K_s & (K_{bs1})_1 & (K_{bs1})_p & & (K_{bs1})_m \\ (K_{bs1}^T)_1 & (K_{bs}-K_b)_{11} & (K_{bs}-K_b)_{1p} & & (K_{bs}-K_b)_{1m} \\ (K_{bs1}^T)_p & (K_{bs}-K_b)_{p1} & (K_{bs}-K_b)_{pp} & & (K_{bs}-K_b)_{pm} \\ \hdashline (K_{bs1}^T)_m & (K_{bs}-K_b)_{m1} & (K_{bs}-K_b)_{mp} & & (K_{bs}-K_b)_{mm} \end{array}\right] \left[\begin{array}{c} \delta^e \\ U_{b1} \\ U_{bp} \\ \hdashline [U_{bm}] \end{array}\right] = \left[\begin{array}{c} F^e \\ \psi_{a1} \\ \psi_{ap} \\ \hdashline [0] \end{array}\right] \qquad (5.43a)$$

i.e.

$$\left[\begin{array}{cc} K_{csb} & K_{sbm} \\ K_{sbm}^T & K_{sbmm} \end{array}\right] \left[\begin{array}{c} \left[\begin{array}{c} \delta^e \\ U_{b1} \\ U_{bp} \end{array}\right] \\ [U_{bm}] \end{array}\right] = \left[\begin{array}{c} \left[\begin{array}{c} F^e \\ \psi_{a1} \\ \psi_{ap} \end{array}\right] \\ [0] \end{array}\right] \qquad (5.43b)$$

where m indicates the middle nodes of the bond element.

$[U_{bm}]$ is hence given by

$$[U_{bm}] = -K_{sbmm}^{-1} \cdot K_{sbm}^{T} \begin{bmatrix} \delta^e \\ U_1 \\ U_p \end{bmatrix} \qquad (5.44a)$$

and

$$[K_{csb} - K_{sbm} \cdot K_{sbmm}^{-1} \cdot K_{sbm}^{T}] \cdot \begin{bmatrix} \delta^e \\ U_1 \\ U_p \end{bmatrix} = \begin{bmatrix} F^e \\ \psi_{a1} \\ \psi_{ap} \end{bmatrix} \qquad (5.44b)$$

$$\text{i.e.} \quad [K_{rec}] \cdot \begin{Bmatrix} \delta^e \\ U_1 \\ U_p \end{Bmatrix} = \begin{Bmatrix} F^e \\ \psi_{a1} \\ \psi_{ap} \end{Bmatrix} \qquad (5.44c)$$

where K_{rec} is a general embedded stiffness matrix for the reinforced concrete element including bond-slip effects. Notice that in the most normal situations ψ_{a1} and ψ_{ap} would be equal to zero. However, ψ_a could be applied in computation as an external self-equilibrating force pair associated with the slip degree of freedom, but the physical interpretation of doing this needs further clarification (see bond examples later).

5.5 Summary

The above described formulation has been implemented into a program used in this study. The sequence for each embedded bar element is summarized as follows:

1. Calculate B_{cs}, B_{bs} and H_b.
2. Calculate K_s and assemble into the concrete element.
3. Calculate K_{bs1}, K_{bs} and K_b
4. Inverse $(K_{bs} - K_b)_{mm}$
5. Multiply $- K_{sbm} \cdot K_{sbmm}^{-1} \cdot K_{sbm}^{T}$ and assemble the resulting matrix at structural level.
6. $[U_{bm}]$ is obtained from the element nodal displacements using eq.(5.44a).

This procedure is repeated for all the bars in a concrete element.

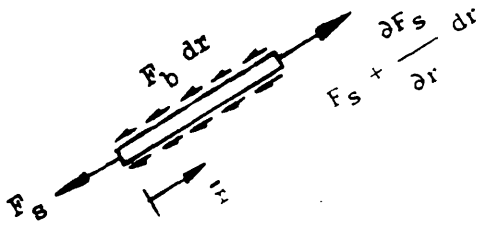

Fig.5.1 Force Transfer

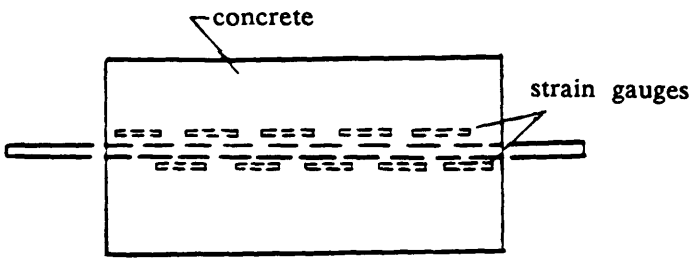

(a) Concrete Strain Gauges

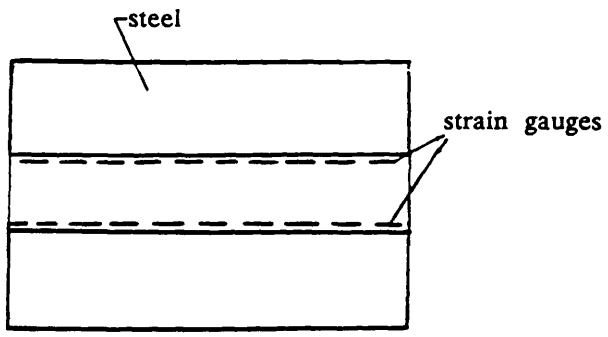

(b) Steel Strain Gauges

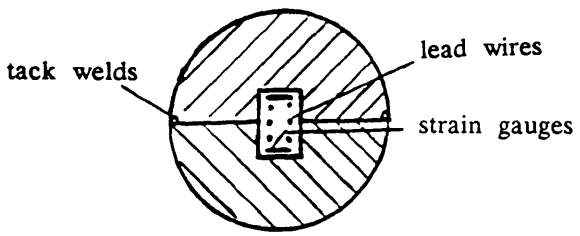

(c) Details of Bar Section

Fig.5.2 Details of Strain Gauges in Bond Tests

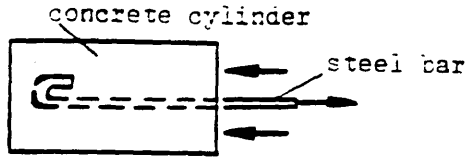

(a) Anchorage Test

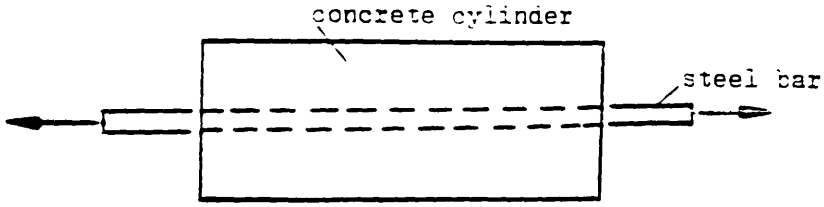

(b) Transfer Test

Fig.5.3 Basic Bond Tests

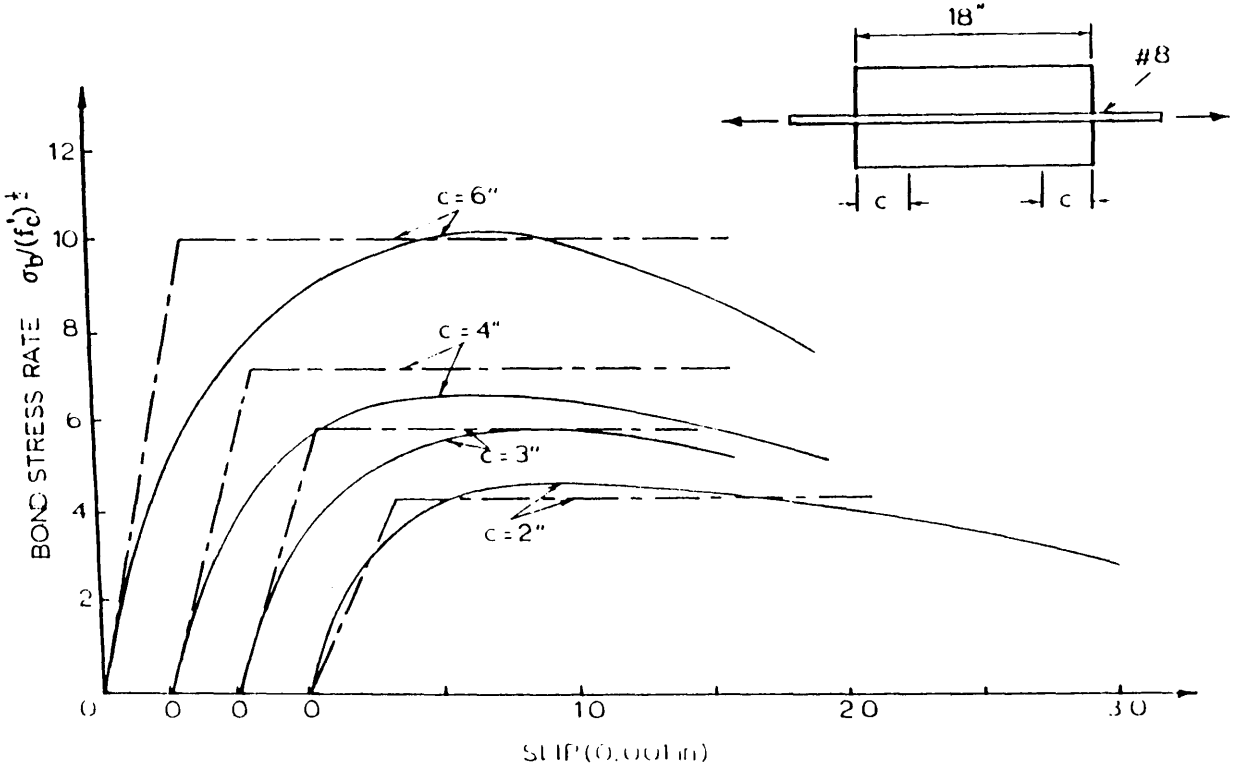

Fig.5.4 Nilson's Experimental Bond–Slip Curves (1972)

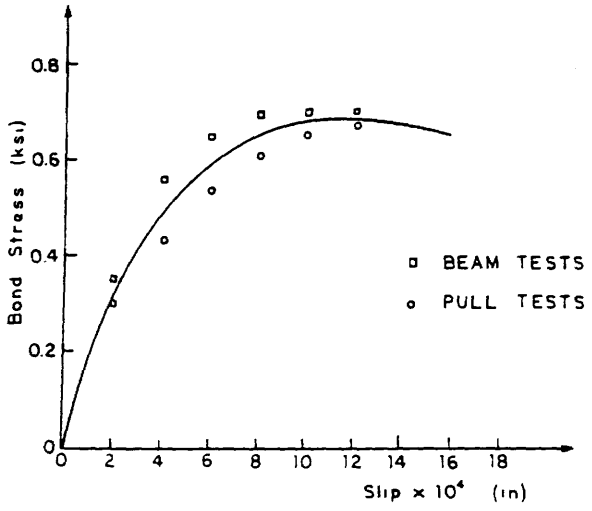

Fig.5.5 Houde's Bond– slip Law (1973)

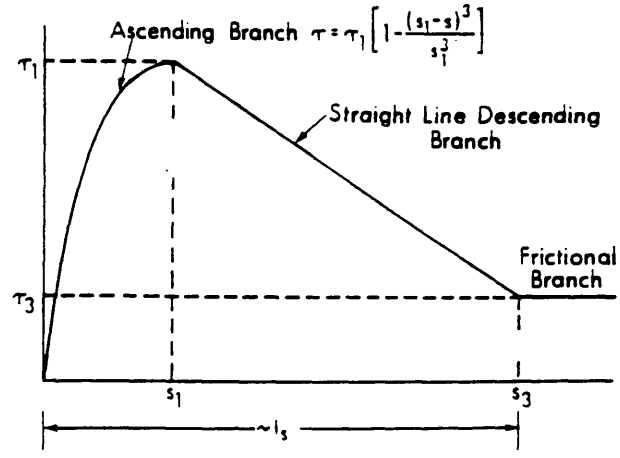

Fig.5.6 Idealization of Bond Stress– Slip Curve

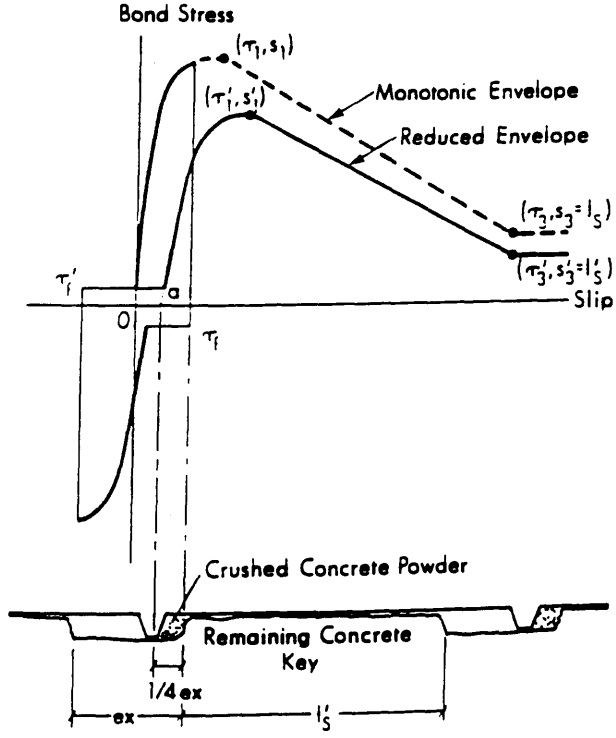

Fig.5.7 Reduced Monotonic Envelope

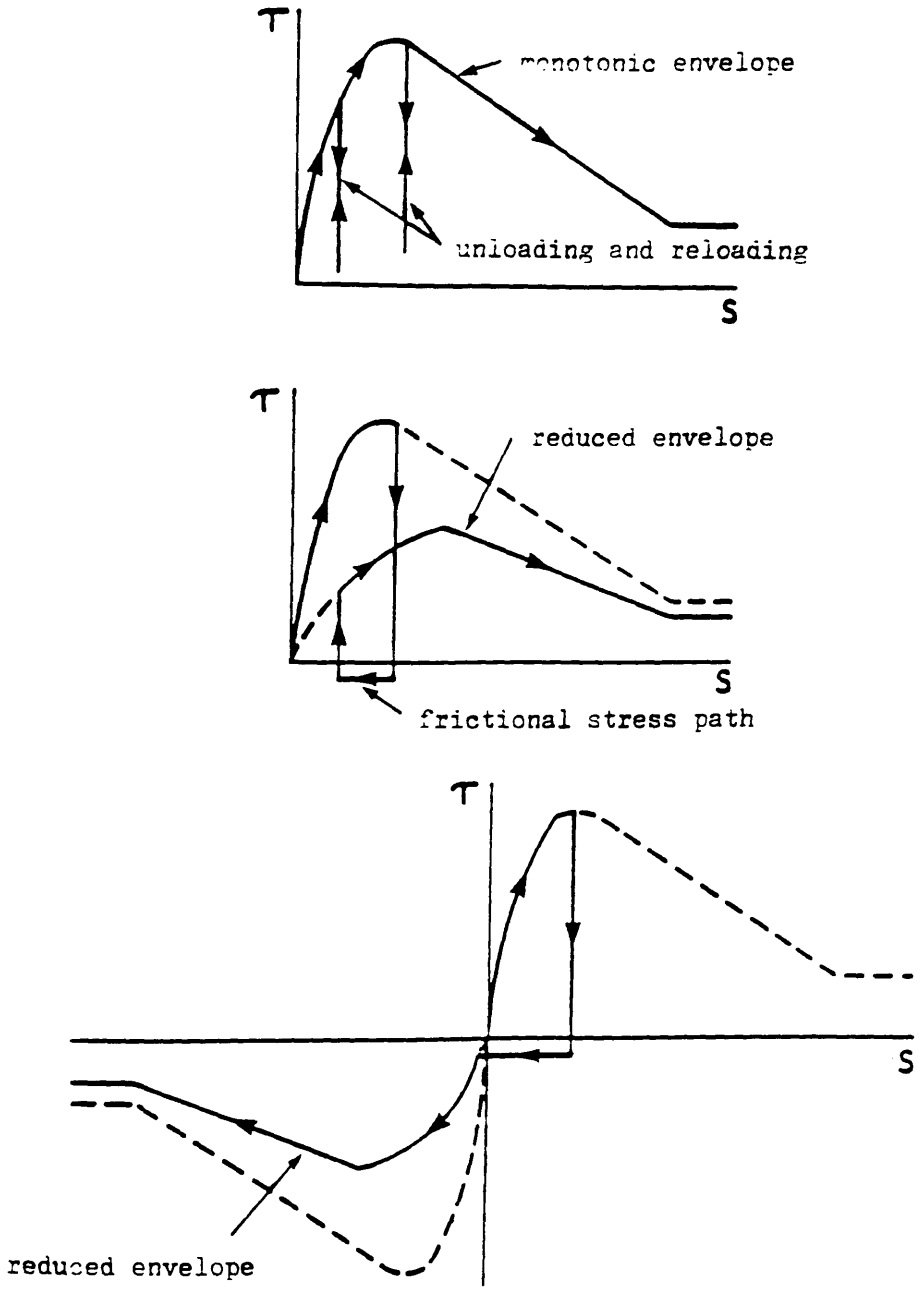

Fig.5.8 Generalized Bond Stress–Slip Rules

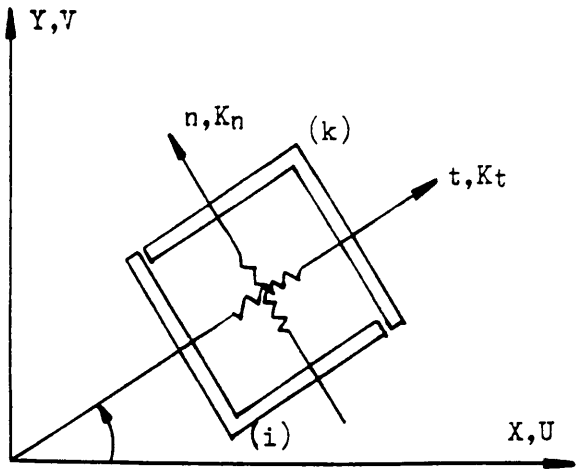

Fig.5.9 Linkage Element

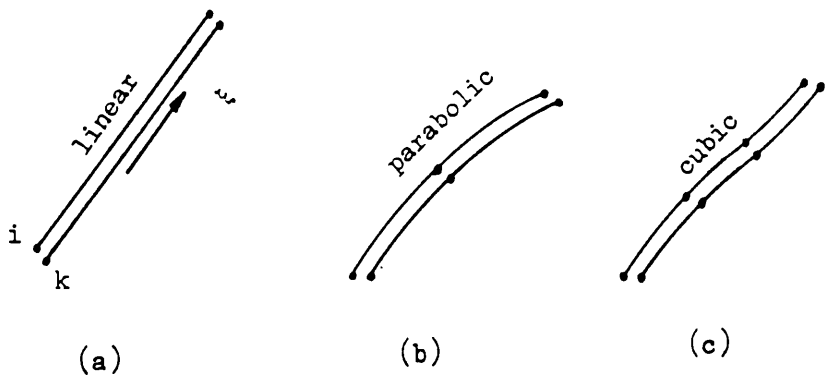

Fig.5.10 1− D Continuous Interface Elements

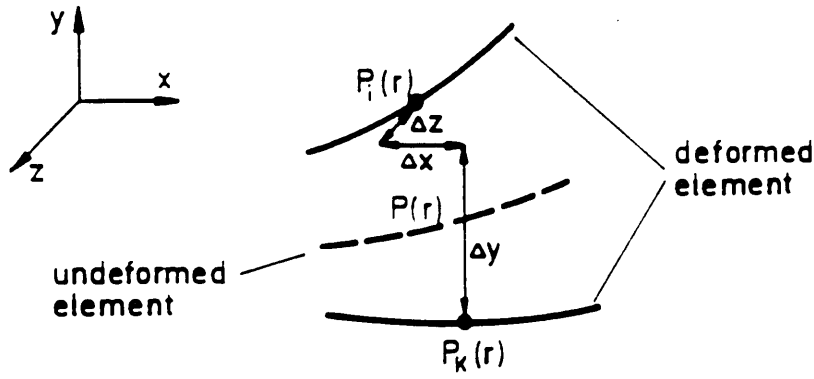

Fig.5.11 Relative Displacements

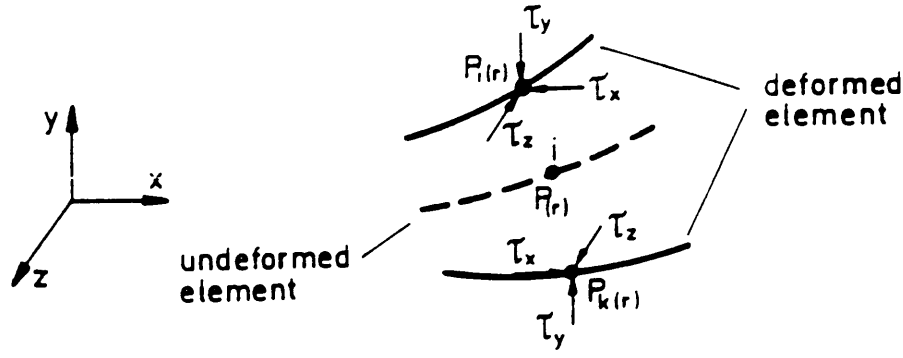

Fig.5.12 Stresses in the Double Node ik

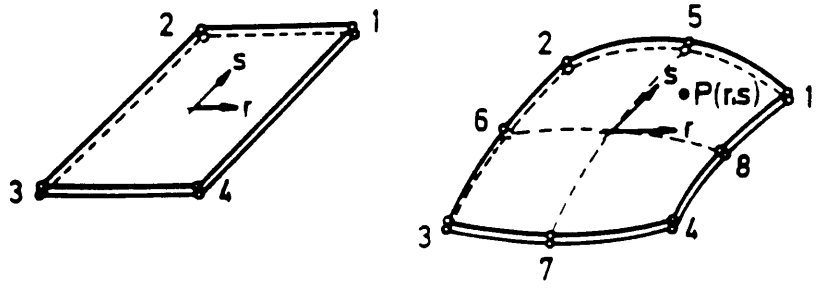

Fig.5.13 2– D Continuous Interface Elements

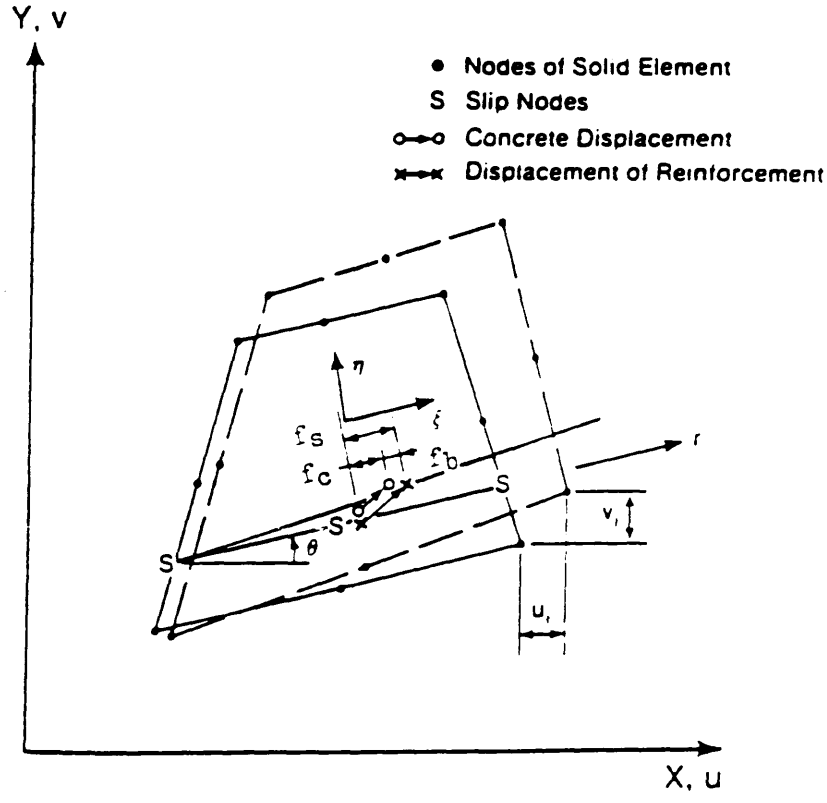

Fig.5.14 An Embedded Bond Element (Balakrishana– Murray 1987)

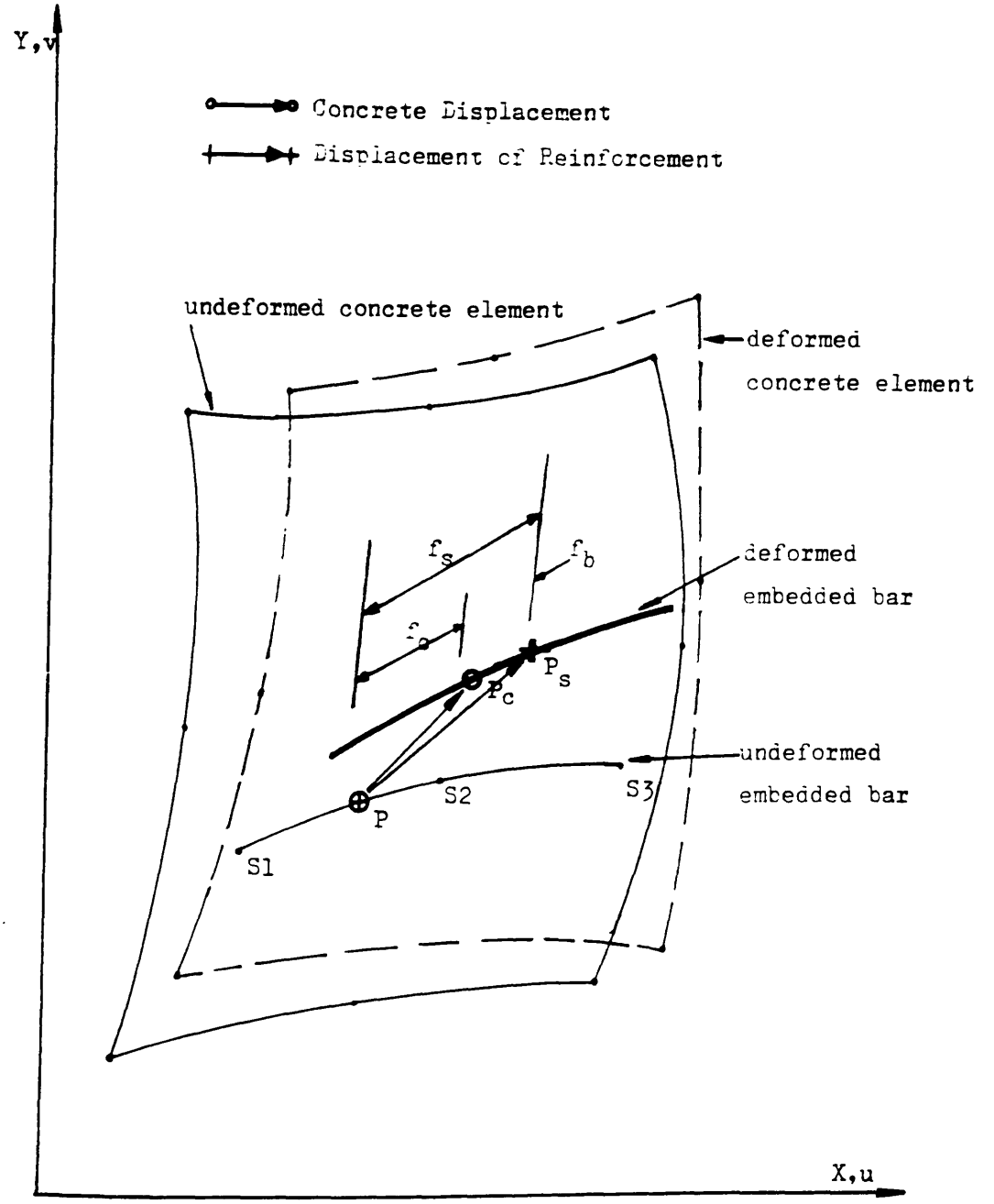

Fig.5.15 A General Embedded Bond Element

CHAPTER SIX

NONLINEAR SOLUTION TECHNIQUES

6.1 Introduction

The finite element method has been applied successfully to a wide range of linear structural problems, and has been extended to geometric and material nonlinearities. While the analysis of linear problems is relatively straightforward, a nonlinear analysis is considerably more difficult. A crucial factor is that the nonlinear problem, in general, requires solving a set of nonlinear algebraic equations, which in itself, is a formidable task. In addition, the nonlinear problems encountered in structural mechanics may be path–dependent (e.g. plasticity), or they may possess multiple solutions (e.g. snap–through buckling). A typical example is the imperfection sensitivity of certain structures which in general is directly related to the postcritical response. The prediction of postcritical response can be of great value, particularly for structures exhibiting a decreasing post–limit characteristic, such as cracking in reinforced concrete. Therefore, the quest for reliable solutions to nonlinear structural analysis is indeed a necessary though difficult task.

In order to overcome the difficulties encountered in solving nonlinear algebraic equations, a stepwise linearization technique is usually adopted. Of these the Newton–Raphson incremental iteration method is the most popular. This procedure can be summarized as follows:

$$K(u)\Delta u = q - f(u) \qquad (6.1a)$$

$$= \varphi(u)$$

where q is a vector of the total external applied forces.

f(u) is a vector of internal forces which is the sum of equivalent nodal forces of each element.

Δu is a vector of incremental deformation.

u is a vector of total deformation.

K(u) is the stiffness matrix, which is a function of deformation state.

$\varphi(u)$ is residual force vector.

This is sketched in Fig.6.1 for a one dimensional problem. In this procedure, the incremental displacement Δu for an increment of load Δq is obtained by

$$\Delta u = K^{-1}(u)\,\Delta q \qquad (6.1b)$$

Th residual forces φ are found using eq.(6.1a). If φ is not within the prescribed tolerances, iteration is required under constant load level q until the convergence criteria are satisfied.

In its conventional form, the stiffness matrix is changed at every iteration. This is quite time consuming and not necessary in many cases. The modified Newton–Raphson method (Fig.6.2) does not change the stiffness matrix at each iteration. Usually one change per increment, at the first or second iteration, is adopted, although schemes exist which allow a change after several iterations. While requiring more iterations, modified Newton–Raphson is usually more efficient computationally.

Using load increments, the Newton–Raphson method can fail to calculate equilibrium states near to, at the point of, and beyond critical points. In other words, the convergence of the numerical procedure can be lost within a certain

neighborhood of a critical state of equilibrium. However, the failure of the direct application of the Newton– Raphson method does not necessarily imply that the procedure can not be used at all. In most engineering problems, the determination of the first critical state of equilibrium and load corresponding to it is the objective of the analysis. When this is the case, it is possible to define the critical point configuration as the equilibrium state beyond which the convergence of the method is lost. But, it should be borne in mind that an unwelcome increase in computational effort may result.

In order to extend analysis beyond the critical point, displacement control schemes are often adopted in many finite element programs. This method interchanges the dependent and independent values in solving the equilibrium equations to avoid the singularity at the critical point. i. e. the displacement level is kept constant while adjusting the load vector. The simplest form of this is to impose a displacement at a load application point and to calculate the reactive forces corresponding to this displacement at the point of application.

Another displacement control method[Ramm 1980] is to take a single displacement component as a controlling parameter during the iterations. But this requires a proper selection of the controlling parameter. It also fails in some situations, for example in snap– back phenomena.

To provide an efficient iterative performance beyond the limit point, arc– length solution methods were proposed in the early 1980s, and have been increasingly used in nonlinear analysis since then. This method controls the iterations in the numerical approximation by using restrictions on the loading parameter $\Delta\lambda$ to trace equilibrium. These restrictions, known as constraint equations, can be a sphere, an updated normal plane or some other alternative form. This iterative technique was independently introduced by Riks[Riks 1972 and

1979], Wempner[Wempner 1971] and Wessels[Wessel 1977] in the 1970's. Later, it was improved by Ramm[Ramm 1980] and Crisfield[Crisfield 1980], who made it much more suitable for finite element analysis.

In the remainder of this Chapter, the displacement control method is first described, after which the arc–length method will be discussed in detail together with line search techniques. Line searches are methods of accelerating the iteration procedure and can be most beneficial for problems involving sudden nonlinearities such as occurs in reinforced concrete with significant strain softening in the constitutive relationships. Both arc–length and line search procedures have been implemented into the programs developed in this study.

6.2 Starting Point and Notation

The solution of eq.(6.1) for nonlinear finite element analysis is based on an incremental–iterative procedure, i. e. the nonlinear problem is stepwise linearized and the linearization error is corrected by additional equilibrium iterations. If loading is assumed to be proportional, a load vector q can be expressed as

$$q = \lambda\, q_0 \tag{6.2}$$

where q_0 is a vector of reference loads.

Eq.6.1 can then be rewritten as

$$K(u)\ \Delta u = \lambda q_0 - f(u) \tag{6.3}$$

Within one increment from configuration m to m+1, the load and displacement states at positions i and j, before and after an arbitrary iteration cycle are shown in Fig.6.3. The total increments between positions m and i are denoted by u_i, q_i and λ_i while the changes in a iteration from i to j are denoted by Δu_i, Δq_i

and $\Delta\lambda_i$, respectively. Thus

$$^{i}u = {}^{m}u + u_i \tag{6.4}$$

$$u_j = u_i + \Delta u_i \tag{6.5}$$

$$^{i}\lambda = {}^{m}\lambda + \lambda_i \tag{6.6}$$

$$\lambda_j = \lambda_i + \Delta\lambda_i \tag{6.7}$$

in which the left superscript refers to the 'total' displacement or loading configuration, the right subscript refers to 'incremental', while Δ refers to iterative.

This notation was devised by Ramm[Ramm1980] and is illustrated in Fig.6.3.

The load level is then expressed as

$$^{i}q = {}^{m}q + q_i \tag{6.8}$$

$$q_j = q_i + \Delta q_i \tag{6.9}$$

In order to progress from i to j on a constrained load–displacement path, both the load and displacement have to change. However, incremental displacement at i, denoted δ_i, is calculated linearly on the basis of the current residual force ψ_i and some appropriate stiffness matrix ^{i}K existing at i. This then takes the solution to an intermediate point j' at the some load level $^{i}\lambda = {}^{j'}\lambda$. Hence the state at j' is governed by the equation,

$$^{i}K\ \delta_i = {}^{i}q - f(^{i}u) = {}^{i}\lambda q_0 - f(^{i}u) \tag{6.10}$$

$$= {}^{i}\varphi$$

In order to reach point j, a load factor $\Delta\lambda_i$, defined by $\Delta q_i = \Delta\lambda_i\, q_o$, is calculated by some means which allows the iterative equilibrium equations to be expressed by,

$$
\begin{aligned}
{}^{i}K\,\Delta u_i &= \Delta q_i + {}^{i}q - f({}^{i}u) \\
&= \Delta q_i + {}^{i}\varphi = \Delta\lambda_i\, q_0 + {}^{i}\varphi
\end{aligned}
\qquad (6.11)
$$

where $f({}^{i}u)$ are the internal forces and ${}^{i}\varphi$ are the out-of-balance forces. q_0 is the same as in eq.(6.2)

The stiffness matrix ${}^{i}K$ at state i takes account of all possible nonlinear effects. It can change at every iteration or be occasionally updated as in the modified Newton-Raphson method.

The singularity of the stiffness is usually checked by the determinant

$$|\mathrm{Det}({}^{i}K)| = 0 \qquad (6.12)$$

This determinant can easily be calculated as the product of all diagonal terms in the triangularized matrix during Gaussian elimination. In the usual finite element computation, it is very rare to get a zero determinant. But it is necessary to find out whether or not it is a negative. When it is negative, unloading should be applied.

Since the linearized error is corrected by equilibrium iterations it is necessary to check when equilibrium has been achieved so that iteration can cease. This is done by making use of convergence criteria. In this study, the following criteria are employed.

1)
$$\frac{|\varphi_i|}{|q_i|} \leq C_{F1} \tag{6.13}$$

2).
$$\frac{|\varphi_i^{max}|}{|q_i|} \leq C_{F2} \tag{6.14}$$

3).
$$\frac{|\varphi_i|}{|\varphi_1|} \leq C_{F3} \tag{6.15}$$

where $|\varphi_i|$ is the norm of the residual forces,

$|q_i|$ is the norm of the applied forces,

$|\varphi_1|$ is the norm of the residual forces at start of an increment.

and $|\varphi_i^{max}|$ the maximum component of the residual forces.

C_{F1}, C_{F2} and C_{F3} are prescribed tolerances.

The first criteria ensures that the convergence should be satisfied within a reasonable range. The second criteria is for the situation where the first may not be the best indication of convergence because it represents an 'average' assessment of overall equilibrium of the structure. If the magnitude of the total applied loads is large and the nonlinearity small, the ratios in the first criteria would be small. On other hand, the reverse situation will produce ratios of large values. In order to guard against these, the final convergence criteria should be applied.

In all convergence checks, the total stresses are used in calculating the unbalanced forces in order to avoid the residuals accumulating.

6.3 Displacement Control Scheme

In order to obtain convergence at a critical point, a primary task of solution techniques is to avoid any singularities. Many displacement control schemes attempt to do this by selecting a single displacement component as a controlling parameter and taking the corresponding loading level as unknown.

If eq.(6.11) is reordered, so that the prescribed component Δu_{2i} is the last in the displacement vector $\Delta \underline{u}_i$, equilibrium can be expressed as

$$ {}^{i}\begin{bmatrix} \underline{K}_{11} & \underline{K}_{12} \\ \underline{K}_{21} & K_{22} \end{bmatrix} \begin{bmatrix} \Delta \underline{u}_1 \\ \Delta u_2 \end{bmatrix}_i - \Delta\lambda_i \cdot \begin{bmatrix} \underline{q}_1 \\ q_2 \end{bmatrix} + {}^{i}\begin{bmatrix} \underline{\varphi}_1 \\ \varphi_2 \end{bmatrix} \qquad (6.16) $$

where the underline _ denotes submatrices or vectors.

Then interchanging variables

$$ {}^{i}\begin{bmatrix} \underline{K}_{11} & -\underline{q}_1 \\ \underline{K}_{21} & -q_2 \end{bmatrix} \begin{bmatrix} \Delta \underline{u}_1 \\ \Delta\lambda \end{bmatrix}_i = {}^{i}\begin{bmatrix} \underline{\varphi}_1 \\ \varphi_2 \end{bmatrix} - {}^{i}\begin{bmatrix} \underline{K}_{12} \\ K_{22} \end{bmatrix} \Delta u_{2i} \qquad (6.17) $$

In this equation, it is seen that the symmetry and the banded structure of the stiffness matrix is lost. However, if it is formed in two parts, a solution can be obtained. The first line of the equation gives

$$ {}^{i}\underline{K}_{11}\ \Delta u_{1i} = \Delta\lambda_i\ {}^{i}\underline{q}_1 + {}^{i}\underline{\varphi}_1 - {}^{i}\underline{K}_{12}\ \Delta u_{2i} \qquad (6.18) $$

This is a linear equation in the unknown increment of the load parameter $\Delta\lambda_i$. Therefore, the solution can be decomposed into two parts as

$$\Delta \underline{u}_{1\,i} = \Delta\lambda_i \; \Delta \underline{u}_{1\,i\,I\!I} + \Delta \underline{u}_{1\,i\,I\!I\!I} \qquad (6.19)$$

corresponding to the two parts of the right hand side of eq.(6.18). Hence, both solutions are obtained simultaneously using two different 'load' vectors:

$$^{i}\underline{K}_{1\,1} \; \Delta \underline{u}_{1\,i\,I\!I} = \underline{q}_1 \qquad (6.20\ a)$$

$$^{i}\underline{K}_{1\,1} \Delta \underline{u}_{1\,i\,I\!I\!I} = {}^{i}\underline{\varphi} - \underline{{}^{i}K_{1\,2} \Delta u_{2\,i}} \qquad (6.20\ b)$$

Substituting the displacement increment $\Delta \underline{u}_{1i}$ in eq(6.19) into the second part of eq.(6.17), the load factor $\Delta\lambda_i$ can be obtained as

$$\Delta\lambda_i = \frac{{}^{i}\varphi_2 - \underline{{}^{i}K_{2\,2} \; \Delta u_{2\,i}} - {}^{i}\underline{K}_{2\,1} \Delta \underline{u}_{1\,i\;I\!I}}{-{}^{i}q_2 + {}^{i}\underline{K}_{2\,1} \; \Delta \underline{u}_{1\,i\,I\!I}} \qquad (6.21)$$

Instead of solving an unsymmetrical system equation, the modified stiffness expression eq.(6.17) is analysed for two right hand sides provided that $^{i}\underline{K}_{1\,1}$ is not singular. Since the displacement Δu_{2i} is fixed during iterations the underlined terms in eqs.(6.20) and (6.21) are omitted in all further iteration cycles.

However, the technique described above requires a modification of the stiffness matrix ($^{i}\underline{K}$ to $^{i}\underline{K}_{1\,1}$). Since it is not very likely that the solution will be exactly at a singular point, the original matrix $^{i}\underline{K}$ may still be used and eq.(6.20) replaced by

$$^{i}\underline{K} \; \Delta \underline{u}_{i\,I} = \underline{q} \qquad (6.22\ a)$$

$$^{i}\underline{K} \; \Delta \underline{u}_{i\,I\!I\!I} = {}^{i}\underline{\varphi} \qquad (6.22\ b)$$

where the underlined term in eq.(6.20) is not required to be formed. Similar to eq.(6.19), both solutions are added together, thus

$$\Delta \underline{u}_i = \Delta\lambda_i \, \Delta \underline{u}_{iI} + \Delta \underline{u}_{iII} \qquad (6.23)$$

in which the component Δu_{2i} is also included. i. e.

$$\Delta u_{2i} = \Delta\lambda_i \, \Delta u_{2iI} + \Delta u_{2iII} \qquad (6.24)$$

This, in fact, is a constraint equation. In the first iteration cycle, it is used to determine the load factor $\Delta\lambda_1$ given by

$$\Delta\lambda_1 = \frac{\Delta u_{2i} - \Delta u_{21II}}{\Delta u_{2iI}} \qquad (6.25a)$$

For all further cycles Δu_{2i} does not change, i. e. Δu_{2i} is zero, and $\Delta\lambda_i$ is given by

$$\Delta\lambda_i = \frac{- \Delta u_{2iII}}{\Delta u_{2iI}} \qquad (6.25b)$$

Applying the modified Newton– Raphson technique, eqs.(6.22) need to be solved simultaneously. This additional store for $\Delta \underline{u}_{2iI}$ is required. Iterations are continued until all other displacement components are adjusted and the new equilibrium position is found.

The displacement control method is usually used only in the neighborhood of the critical point although it may be applied throughout the entire load range. Obviously, the method fails when the structure snaps back from one displacement level to a lesser level, and some knowledge of the failure mode is desirable for a proper choice of the controlling displacement. It might even be necessary to change the prescribed displacement parameter during the solution. An effective modification is to relate the procedure to a measure including the effect of all displacements rather than to a single displacement component. However, the

arc– length method is much more effective in solving this type of nonlinear problem.

6.4 Arc– length Solution Technique

In contrast to the normal Newton– Raphson procedure under load control, the arc– length technique treats the load level as a variable in the governing equilibrium equations to bring the load– displacement state from j' to j (Fig.6.3). An extra governing equation is then needed to calculate the load factor, $\Delta\lambda_i$.

Decomposing eq(6.11) into two parts, it is assumed that:

$$ {}^{i}K\ \delta_T = q_0 \qquad (6.26a) $$

$$ {}^{i}K\ \delta_i = {}^{i}\varphi \qquad (6.26b) $$

The iterative and incremental displacements are given by

$$ \Delta u_i = \Delta\lambda_i\ \delta_T + \delta_i \qquad (6.27a) $$

$$ u_j = u_i + \Delta u_i \eta \qquad (6.27b) $$

where η is an artificial factor used to accelerate the convergence speed in an analysis. This will be discussed in detail in section 6.5. For the moment, it is assumed to be 1.0 (i. e. the solution is not accelerated).

Since eq.(6.26) is an n– dimensional problem, then eq.(6.27) represents a (n+1) dimensional problem. In this case, $\underline{\delta}_T$, $\underline{\delta}_i$ and $\Delta\underline{u}_i$ are of order (n+1) with their (n+1)th coordinate set to zero, while $\Delta\underline{\lambda}_i$ is a vector with its (n+1)th coordinate being $\Delta\lambda_i$ and others being zero. Viewing the load– displacement space in terms of vectors, as shown in Fig.6.4, then vectors $\underline{t}_i$ and $\underline{n}_i$ are defined as

$$\underline{t}_i = \underline{u}_i + \underline{\lambda}_i \tag{6.28}$$

$$\underline{n}_i = \eta \, \Delta\underline{u}_i + \Delta \, \underline{\lambda}_i \tag{6.29}$$

where $\underline{u}_i$ is the incremental displacement vector in which the (n+1)th coordinate equals zero, $\underline{\lambda}_i$ is a vector of incremental load factors with only the (n+1)th coordinate not zero. Therefore vector $\underline{t}_j$ is given by

$$\underline{t}_j = \underline{t}_i + \underline{n}_i \qquad j = i + 1 \tag{6.30}$$

In order to find $\underline{t}_j$, a constraint R_i is placed on $\underline{t}_i$ and $\underline{n}_i$, such that

$$R_i = \underline{t}_i \cdot \underline{n}_i \tag{6.31}$$

Substituting eqs.(6.27a), (6.28) and (6.29) into eq.(6.31), the scalar factor $\Delta\lambda_i$ is determined as

$$\Delta\lambda_i = \frac{-\underline{u}_i^T \, \underline{\delta}_i + R_i}{\eta \, \underline{u}_i^T \, \underline{\delta}_T + \lambda_i} \tag{6.32}$$

Obviously, if the constraint expression eq.(6.31) were added into the incremental stiffness matrix equation, the symmetric and banded structure of the matrix would be destroyed, as was the case in the displacement controlling scheme. This was the situation in the original arc–length method; however Wessels[Wessels 1977] realized, using geometrical considerations, that the difficulties could be removed by a two step technique similar to that used to improve the displacement control solution procedure.

The constraint R_i can be chosen in various ways. Two common, but effective, ones are updated normal plane tracing and spherical tracing.

6.4.1 Iterating Along an Updated Normal Plane

If the iteration path is restricted to a 'plane' normal to the updated tangent $\underline{t}_i$, see Fig.6.5, the scalar product of the tangent $\underline{t}_i$ and vector $\underline{n}_i$, which contains the unknown load factor $\Delta\lambda_i$, vanishes. Thus

$$\underline{t}_i \cdot \underline{n}_i = 0 \tag{6.33}$$

i. e.

$$R_i = 0 \tag{6.34}$$

Therefore, eq.(6.32) becomes

$$\Delta\lambda_i = - \frac{\Delta\underline{u}_i^T \underline{\delta}_i}{\eta \underline{u}_i^T \underline{\delta} + \lambda_i} \tag{6.35}$$

Instead of the updated tangent $\underline{t}_i$, the 'plane' normal to the first tangent $\underline{t}_1$ can also be used. In this case the load factor $\Delta\lambda_i$ is then expressed as

$$\Delta\lambda_i = - \frac{\Delta\underline{u}_1^T \underline{\delta}_i}{\eta \underline{u}_1^T \underline{\delta} + \lambda_1} \tag{6.36}$$

6.4.2 Tracing on a 'Sphere'

Instead of following the updated normal plane, the so—called 'sphere' tracing iterates along a sphere with the centre at m and the radius ds of the initial tangent vector vector $\underline{t}_1$, as shown in Fig.6.6, i. e.

$$|\underline{t}_1| = |\underline{t}_2| = \ldots = |\underline{t}_i| = ds \tag{6.37}$$

This restriction is defined by

$$\underline{t}_i \cdot \underline{t}_i - (ds)^2 = 0 \tag{6.38}$$

The radius ds is also given by

$$|ds| = |\underline{t}_j| = |\underline{t}_i + \underline{n}_i| \tag{6.39}$$

Hence

$$\underline{n}_i \cdot (\underline{n}_i + 2\underline{t}_i) = 0 \tag{6.40}$$

Substituting eqs.(6.28) and (6.29) into eq.(6.40), and writing in matrix form results in

$$\eta \, \Delta\underline{u}_i^T \; (\eta \, \Delta\underline{u}_i + 2 \, \underline{u}_i) + \Delta\lambda_i \, (\Delta\lambda_i + 2 \, \lambda_i) = 0 \tag{6.41}$$

in which $\Delta\underline{u}_i$ is expressed in eq.(6.27a). Eq.(6.41) then leads to a quadratic constraint equation for the load parameter $\Delta\lambda_i$.

$$a \, (\Delta\lambda)^2 + 2b \, \Delta\lambda_i + c = 0 \tag{6.42}$$

where

$$a = 1 + \underline{\delta}_T^T \; \underline{\delta}_T \; \eta^2 \tag{6.43a}$$

$$b = \lambda_i + \eta^2 \; \underline{\delta}_T^T \; \underline{\delta}_i + \eta \; \underline{\delta}_T^T \; \underline{u}_i \tag{6.43b}$$

$$c = 2\eta \; \underline{\delta}_i^T \; \underline{u}_i + \eta^2 \; \underline{\delta}_i^T \; \underline{\delta}_i \tag{6.43c}$$

Eq.(6.42) generally has two roots, $\Delta\lambda_{i_1}$ and $\Delta\lambda_{i_2}$, which means there are two intersections with the sphere as shown in Fig.6.7. Therefore, it is necessary to select the correct one to trace convergence properties and the forward structural

behaviour.

The two roots $\Delta\lambda_{i_1}$ and $\Delta\lambda_{i_2}$ give two values for angle θ between the previous tangent vector $\underline{t}_i$ and the new one $\underline{t}_{i+1}$. The appropriate root is chosen by ensuring an acute 'angle' θ, i. e.

$$\cos\theta = \frac{\underline{t}_i \cdot \underline{t}_{i+1}}{|\underline{t}_i| \cdot |\underline{t}_{i+1}|} \tag{6.44}$$

where $\underline{t}_i$ and $\underline{t}_{i+1}$ are defined in eqs.(6.28) and (6.30).

Usually, one of these roots will give a positive $\cos\theta$ and the other negative, so that there should be no problem in choosing the loading factor, $\Delta\lambda_i$, which gives an acute 'angle' θ. However, some situations do exist where both values of $\cos\theta$ are positive. In this case, the appropriate $\Delta\lambda_i$ may be chosen as the root closest to the linear solution of the eq.(6.42) which is

$$\Delta\lambda_{i,lin} = -\frac{c}{b} \tag{6.45}$$

This situation happens rarely. But if it is encountered in the solution procedure, it must be dealt with very carefully, because it could mean that there is something wrong such as divergence, violation of the solution etc. A way to avoid this is to reduce the step length. If this does not help, increasing the length can be tried, since reducing the step length is not always on the safe side.

Step Length ds

So far it has been assumed that the step length ds is known. For the initial increment, some guessed load factor $\Delta\lambda_0$ can be applied and, having obtained a solution from eq.(6.26a), the step length is given by

$$ds = \Delta\lambda_0 \sqrt{\left(\delta_T^T \quad \delta_T \right)} \tag{6.46}$$

which is then used in the following iterations. In the constant arc-length method of Riks/Wempner, this step length ds is held constant in the rest of the increments. In variable step length procedures, the step length ds is adjusted from one increment to another to account for the different degree of nonlinearity throughout the load-displacement path. This change can be accomplished in various ways. The followings are commonly used ones:

$$ds_i = (I_d/I_{i-1})^{\frac{1}{2}} ds_{i-1} \tag{6.47a}$$

or

$$ds_i = (I_d/I_{i-1})^{\frac{1}{4}} ds_{i-1} \tag{6.47b}$$

where ds_{i-1} is the incremental length at the previous increment, I_d is the desired number of iterations, usually assumed to be 2 or 4 and I_{i-1} is the number of iterations needed at the (i-1)th increment.

If I_{i-1} is zero, ds_i is then chosen as

$$ds_i = 2\, ds_{i-1} \tag{6.48a}$$

or

$$ds_i = 1.5\, ds_{i-1} \tag{6.48b}$$

From numerical experience, it is not good enough to just simply use the step length adjustments given by eqs.(6.47) and (6.48), because before and after cracking occurs in a reinforced concrete structure, the nonlinearities are very different. It is better to set the step length before cracking and to load the structure very carefully after cracking using the equations described above.

6.4.3 Intermediate Process in Arc– length Iteration

As described in eqs.(6.10) and (6.11), before the final position j is reached in an iteration, the load– displacement state has to be brought to the so– called 'intermediate point', j'. The procedure is actually an iteration in the Newton– Raphson method in load– displacement space. However, in this process the reactions at prescribed boundary points are redistributed in order to follow the nonlinearities of the structure. This phenomenon is significant in the nonlinear analysis of reinforced concrete structures. Furthermore, when the structure traces the arc– length path (along an updated normal or a sphere or others) from j' to j, the reactions in the load vector are also dependent on the updated stiffness matrix. If the stiffness matrix is different from the previous one, the load vector needs to be reformed in terms of the changes occurring when the reference load is added onto the structure. In particular, the displacements corresponding to the reaction forces need to be reformed. This will effect the final load configuration through the factor $\Delta\lambda_i$.

From this point of view, the 'proportional' assumption in eq.(6.2) can not be simply used, we must deal with it cautiously through an iteration procedure to trace the nonlinearities. In programming, when eq.(6.26b) is employed for δ_i the reactions should be allowed to redistribute in reaching j'. Furthermore, the external force vector in eq.(6.2) should be reconstructed when using eq.(6.26a). Finally, the external forces are iterated to obtain

$$\Delta \underline{q}_i = \Delta \underline{q}_i' + \Delta\lambda_i \underline{q}_0 \qquad (6.49)$$

where $\Delta \underline{q}_i'$ represents the iterative load vector due to the residual forces ${}^i\varphi$, obtained from eq.(6.26b), and $\underline{q}_0$ is the iterative load after calculation of δ_T.

Computational experience has shown that, if this intermediate process is neglected and eq.(6.2) is incorporated directly, there will be large difference in the reaction forces for a slight nonlinearity. Sometimes, this is such that numerical convergence can not be obtained, especially in the nonlinear analysis of reinforced concrete structures.

6.4.4 Iteration in the Descending Part of Load– Displacement Space

If tracing the descending part of the load– displacement space (i.e. the stiffness matrix exhibits a negative determinant), nonlinear analysis falls into a difficult stage. In the increasing part, either the tangent or secant stiffness matrix can be used and usually there is no problem in obtaining convergence. The only significant point is that the tangent matrix usually converges faster than the secant one. But for the descending part, it is difficult to a find solution if the secant stiffness matrix is adopted because it is always positive and it is necessary to use the tangent stiffness matrix to escape from this problem and reach convergence. These phenomena for an iteration is illustrated in Figs.(6.8) and (6.9).

6.5 Line Search Scheme

In eq.(6.27) the accelerating parameter η was assumed to be a constant 1.0. This section will discuss η in more detail, with particular reference to the line search scheme.

Basically, the line search concept attempts to find parameter η such that the energy Φ done by the out– off– balance forces on the incremental displacement u_i is stationary in the direction η. The energy Φ at iteration j is defined by

$$\Phi(^{j}\underline{u}) = \Phi(^{i}\underline{u}) + \int_{\underline{u}}^{^{j}\underline{u}} [\,\underline{\varphi}(\underline{u})\,]^{T}\, d\underline{u} \qquad (6.50)$$

Now minimizing the energy with respect to η and using eq.(6.27b) then

$$\left.\frac{\partial \Phi}{\partial \eta_i}\right|_j = \left[\frac{\partial \underline{\varphi}}{\partial \underline{u}}\right]_j^T \frac{\partial j\underline{u}}{\partial \eta_i}$$

$$= s_j(\eta_{i,j}) = 0 \qquad (6.51)$$

The subscript j implies that $s_{i,j}$ is the jth estimate of the inner products obtained at the jth estimate of $\eta_{i,j-1}$, which is $\eta_{i,i}$.

In practical numerical computation, eq.(6.51) is too strict and it is preferable to satisfy this equation within some reasonable bounds, i. e.

$$| s_j(\eta_{i,j}) | < \alpha | s_0(\eta_{i,0}) | \qquad (6.52)$$

where $s_0(\eta_{i,0}) = \delta_i^T {}^i\varphi$, and

${}^i\varphi$ are the out-of-balance forces at end of ith iteration. Eq.(6.52) is illustrated in Fig.(6.10).

Numerical experience has indicated that a fairly slack tolerance is $\alpha = 0.6$. In such instances, many iterations will require no extra residual calculations since the first trial $\eta_{i,1}$ (normally unity unless acceleration is used) will immediately satisfy eq.(6.52). However, if eq.(6.52) is violated, a new scale $\eta_{i,2}$ must be tried as the second attempt to satisfy the equation. The second estimate $\eta_{i,2}$ can be computed in a number of ways[Wessels 1977, Batoz 1979 and Crisfield 1980]. For simplicity, a linear interpolation (or extrapolation) through the values $s_1(\eta_{i,1})$ and $s_0(\eta_{i,0})$ is usually adopted, i.e.

$$\frac{\eta_{i,2}}{\eta_{i,1}} = \frac{-s(\eta_{i,0})}{s(\eta_{i,1}) - s(\eta_{i,0})} = \frac{-s_0}{s_1 - s_0}$$

$$= \frac{-\delta_i^T \varphi_i}{\delta_i^T (\varphi_{i,1}(\eta_{i,1}) - \varphi_i)} \tag{6.53}$$

For further estimates, the concept is simply repeated:

$$\frac{\eta_{i,j+1}}{\eta_{i,j}} = \frac{-s_0}{s_j - s_0} \tag{6.54}$$

The following derivation extends the line search scheme for use with the arc–length method.

Substituting eq.(6.27a) for Δu_i and eq.(6.10) for φ_i into eq.(6.51) gives

$$\left.\frac{\partial \Phi}{\partial \eta_i}\right|_j = (\underline{\delta}_i + \Delta\lambda_i \underline{\delta}_T)^T ({}^j\lambda \underline{q}_0 - \underline{f}_j(\eta_j))$$

$$= s_j = 0 \tag{6.55}$$

However, as before, eq.(6.52) will be used as a practical substitute for eq.(6.51). The inner product s_j is then calculated at the jth estimate of $s_i(\eta_{i,j})$ using the internal force vector, $\underline{f}_j(\eta_j)$, i. e.

$$s_j = {}^j\lambda \underline{\delta}_i^T \underline{q}_0 - \underline{\delta}_i^T \underline{f}_{j,j} + \Delta\lambda_i {}^j\lambda \underline{\delta}_T^T \underline{q}_0 - \Delta\lambda_i \underline{\delta}_T^T \underline{f}_{j,j}$$

$$= d_1 {}^j\lambda - d_2 + d_3 \Delta\lambda_i {}^j\lambda - d_4 \Delta\lambda_i \tag{6.56}$$

Similarly, $s_0(\eta_{i,0})$ is given by

$$s_0 = (\underline{\delta}_i + \Delta\lambda_i \underline{\delta})^T ({}^j\lambda \underline{q}_0 - \underline{f}_i)$$

$$= {}^j\lambda \underline{\delta}_i^T \underline{q}_0 + \Delta\lambda_i {}^j\lambda \underline{\delta}_T^T \underline{q}_0 - \underline{\delta}_i^T \underline{f}_i - \Delta\lambda_i \underline{\delta}_T^T \underline{f}_i$$

$$= {}^{j}\lambda\ e_1 + \Delta\lambda_i\ {}^{j}\lambda\ e_3 - e_2 - \Delta\lambda_i\ e_4 \qquad (8.57)$$

Using the interpolation (or extrapolation) of eq.(6.54) a new scale $\eta_{i,j+1}$ is obtained. Substituting eqs.(6.56) and (6.57) into eq.(6.54) gives:

$$\frac{\eta_{i,j+1}}{\eta_{i,j}} = -\frac{e_1\ {}^{j}\lambda + \Delta\lambda_i\ {}^{j}\lambda\ e_3 - \Delta\lambda_i\ e_4 - e_2}{e_4\ \Delta\lambda_i - d_4\ \Delta\lambda_i + e_2 - d_2} \qquad (6.58)$$

Having obtained the secant–type interpolation of expression eq.(6.58), a straight forward application to the arc–length procedure can now be designed:

— Given $\eta_{i,1} = 1.0$, λ_i is found in the usual manner using either the quadratic equation or updated normal plane constraint.

— Update the displacements and internal forces;

— The inner products s_j and s_0 can then be calculated using equations (6.56) and (6.57). The adequacy of the first $\eta_{i,1} = 1.0$ is checked by eq.(6.52);

— If eq.(6.52) is not satisfied, this approach would involve the immediate application of eq(6.58) with $\eta_{i,1} = 1.0$ to interpolate for $\eta_{i,2}$. However, since the constraint equation used to calculate $\Delta\lambda_i$ was satisfied with $\eta_{i,1} = 1.0$, the constraint equation will be violated using the coefficients obtained with $\eta_{i,1} = 1.0$. In other words, the straight forward application of eq.(6.58) leads to a scalar $\eta_{i,2}$ that does not satisfy the constraint relationship unless the load level λ_i is also adjusted. Hence, eqs.(6.58) and the constraint equations, (6.35) or (6.42), must be solved simultaneously for $\Delta\lambda_i$ and $\eta_{i,j+1}$.

To combine the constraint equations with eq.(6.58), all equations are used. The scalars involving δ_T and q_0 are calculated once the tangential vector δ_T has been

computed. These are then kept fixed for the rest of the increment. The inner products involving $\underline{f}_i$, $\underline{\delta}_i$, q_0 and $\underline{\delta}_T$ are calculated when $\underline{\delta}_i$ has been computed. These remain fixed for the rest of the iteration for η. The scalars d_2 and d_4 involve the internal force vector at the end of the ith iteration, and are therefore re-computed each time when the new internal forces are calculated, which may be a number of times per iteration in adopting a line search.

The simultaneous solution of eq.(6.58) with the constraint equations is achieved using a simple direct substitution method. To start with, the procedure would use the original estimate for $\Delta\lambda_i$ obtained from the constraint equations with $\eta_{i,1} = 1.0$. The internal force vector vector $\underline{f}_{j,1}$ and appropriate inner products would then be computed and, if eq.(6.52) were violated, the calculation would follow the steps:

i). Solve eq(6.58) for $\eta i,2$;

ii). Replace $\eta_{i,1}$ with $\eta_{i,2}$ in the constraint equations and solve for a new $\Delta\lambda$

iii). go back to i) if there is a significant change in the two η_i.

However, it should be noted that eqs.(6.56) and (6.58) are not accurate unless ${}^j\lambda$ is the load level at which $f_{j,j}$ was computed, i. e. at the displacement level

$$ {}^ju = u_i + \eta_{i,j} \, (\underline{\delta}_i + \Delta\lambda_i \, \underline{\delta}_T) \qquad (6.59) $$

This approximation is due to the assumption that $f_{j,j}$ is independent from ${}^j\lambda$ and only depends on $\eta_{i,j}$. Fortunately, as Crisfield[Crisfield 1983] demonstrated, using eq.(6.58) gives very satisfactory results.

6.6 A Brief Description of Programming

Based on the modified Newton–Raphson method, the arc–length solution techniques, together with the line search scheme, have been incorporated into the program used in this study. This is described in the following flow chart. The following notation is used to denote inner products required in the procedure.

$$c_1 = \underline{\delta}_T^T \cdot \underline{\delta}_T \qquad c_2 = \underline{\delta}_T^T \cdot \underline{\delta}_i$$

$$c_3 = \underline{\delta}_T^T \cdot \underline{u}_i \qquad c_4 = \underline{\delta}_i^T \cdot \underline{u}_i$$

$$c_5 = \underline{\delta}_i^T \cdot \underline{\delta}_i$$

$$d_1 = \underline{\delta}_i^T \cdot \underline{q}_0 \qquad d_2 = \underline{\delta}_i^T \cdot \underline{f}_{j,j}$$

$$d_3 = \underline{\delta}_T^T \cdot \underline{q}_0 \qquad d_4 = \underline{\delta}_T^T \cdot \underline{f}_{j,j}$$

$$e_1 = d_1 \qquad e_2 = \underline{\delta}_i^T \cdot \underline{f}_i$$

$$e_3 = d_3 \qquad e_4 = \underline{\delta}_T^T \cdot \underline{f}_i$$

Flow Chart of Nonlinear Solution Scheme:

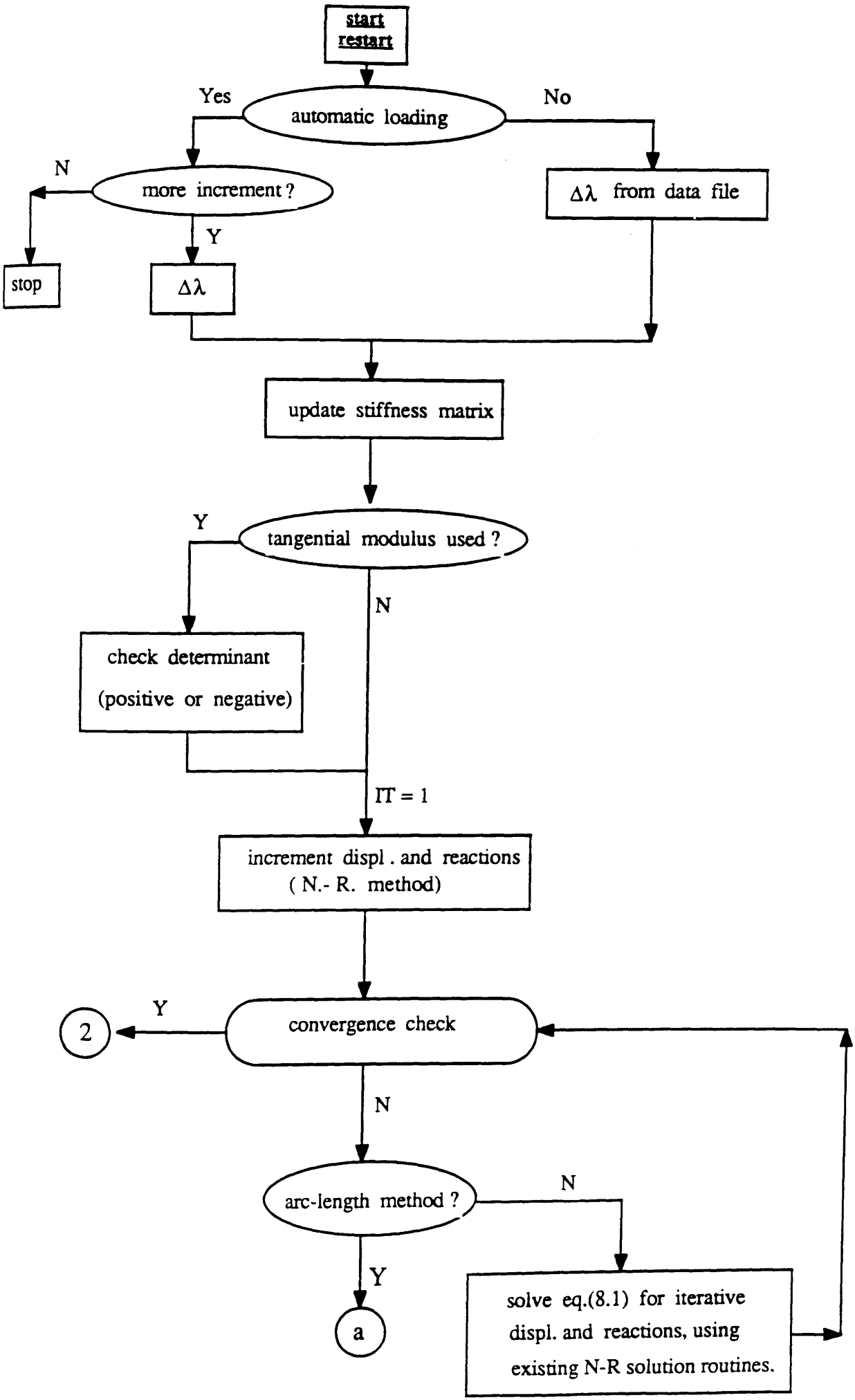
start
restart
Yes
automatic loading
No
N
more increment ?
Δλ from data file
Y
stop
Δλ
update stiffness matrix
Y
tangential modulus used ?
N
check determinant
(positive or negative)
IT = 1
increment displ . and reactions
(N.- R. method)
2
Y
convergence check
N
arc-length method ?
N
Y
a
solve eq.(8.1) for iterative
displ. and reactions, using
existing N-R solution routines.

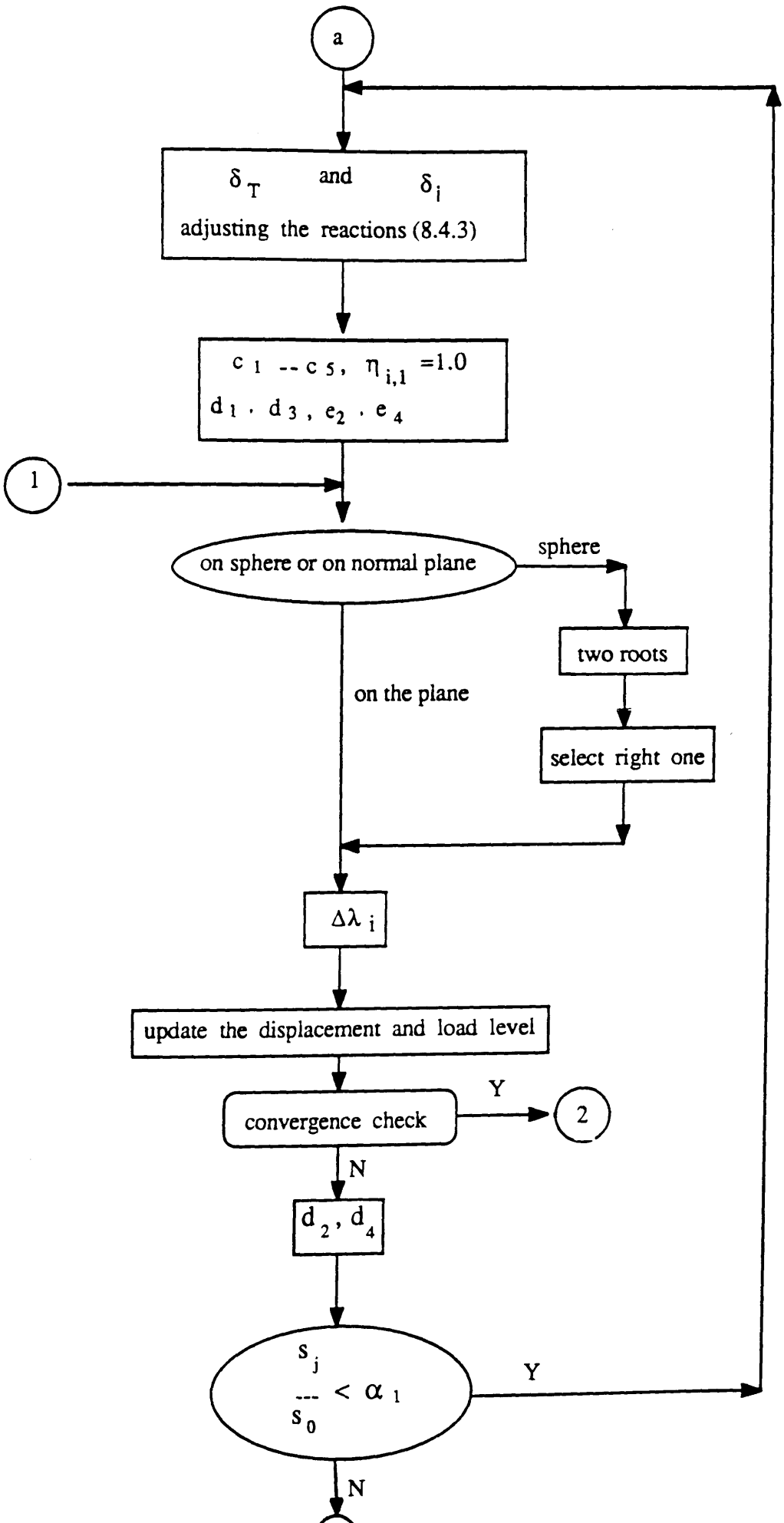
a
δ_T and δ_i
adjusting the reactions (8.4.3)
c_1 -- c_5, $\eta_{i,1}$ =1.0
d_1 . d_3 , e_2 . e_4
1
on sphere or on normal plane
sphere
two roots
select right one
on the plane
$\Delta\lambda_i$
update the displacement and load level
convergence check
Y
2
N
d_2, d_4
$\frac{s_j}{s_0} < \alpha_1$
Y
N

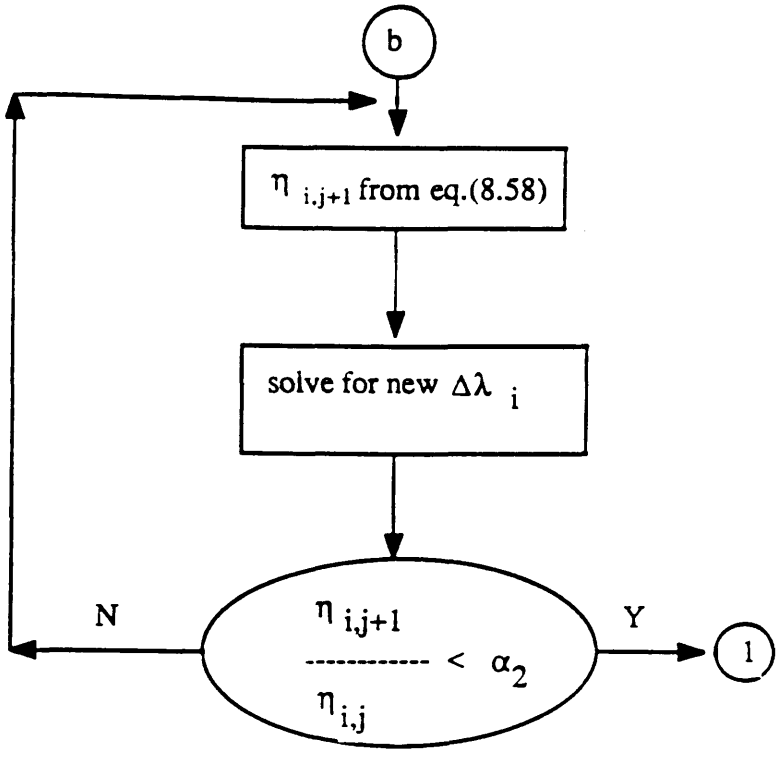
b
$\eta_{i,j+1}$ from eq.(8.58)
solve for new $\Delta\lambda_i$
N
$\frac{\eta_{i,j+1}}{\eta_{i,j}} < \alpha_2$
Y
1

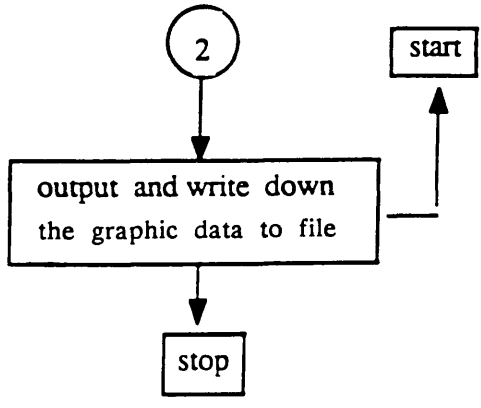
2
start
output and write down
the graphic data to file
stop

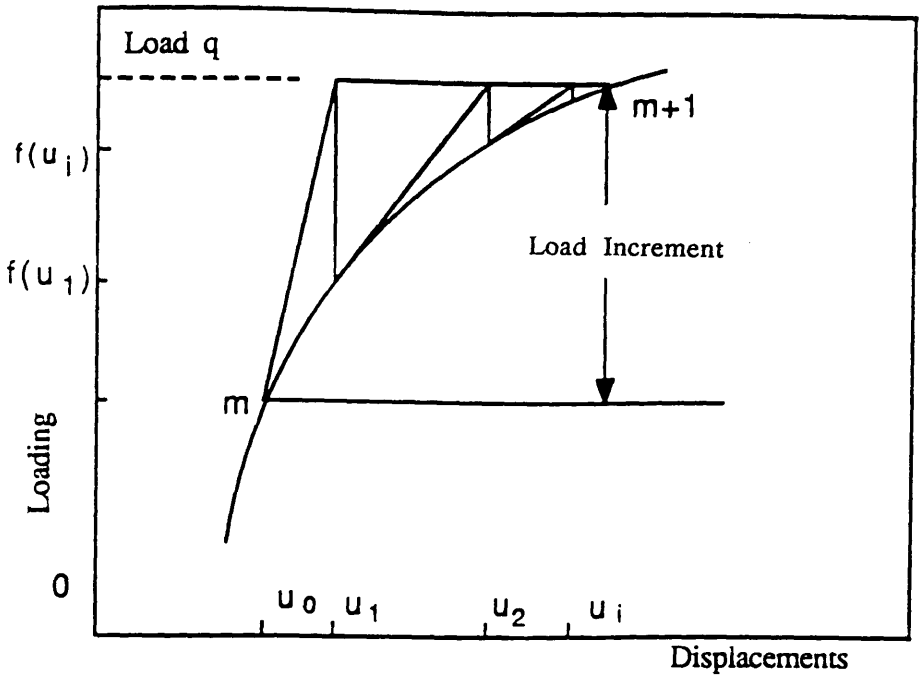

Fig.6.1 Newton– Raphson Iteration Procedure

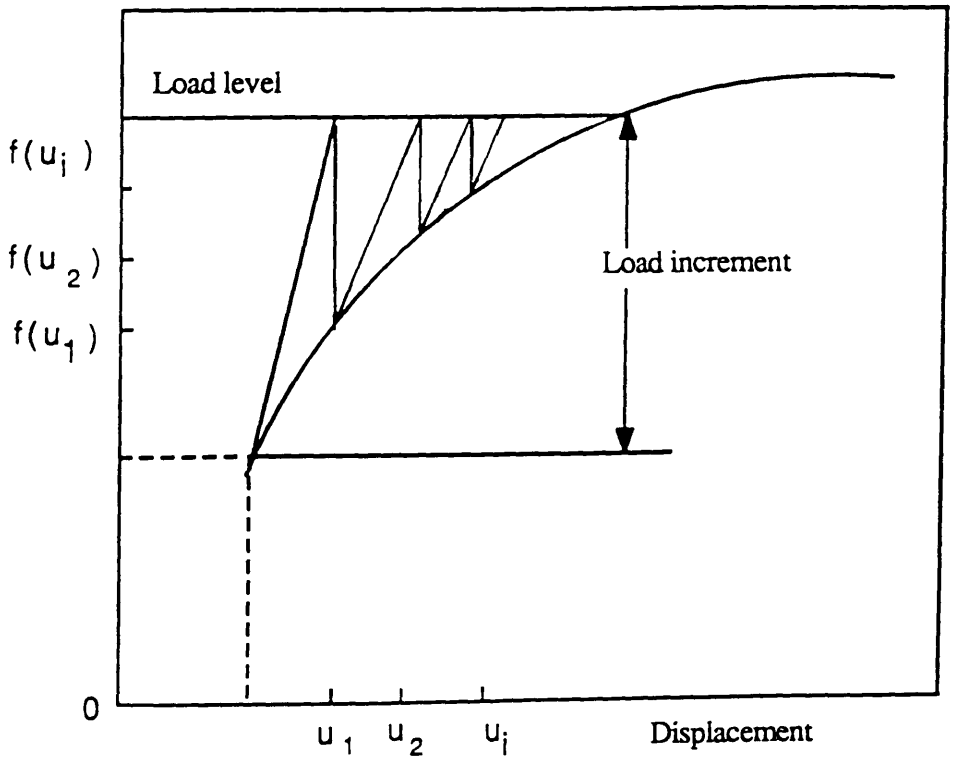

Fig.6.2 Modified Newton– Raphson Method

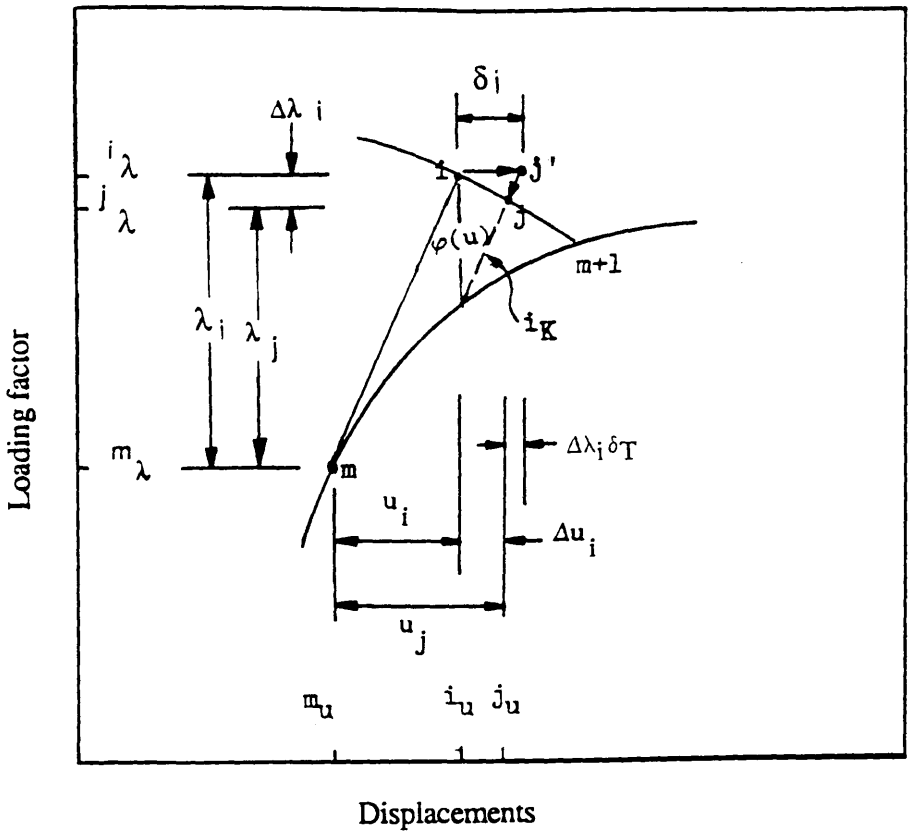

Fig.6.3 Notations

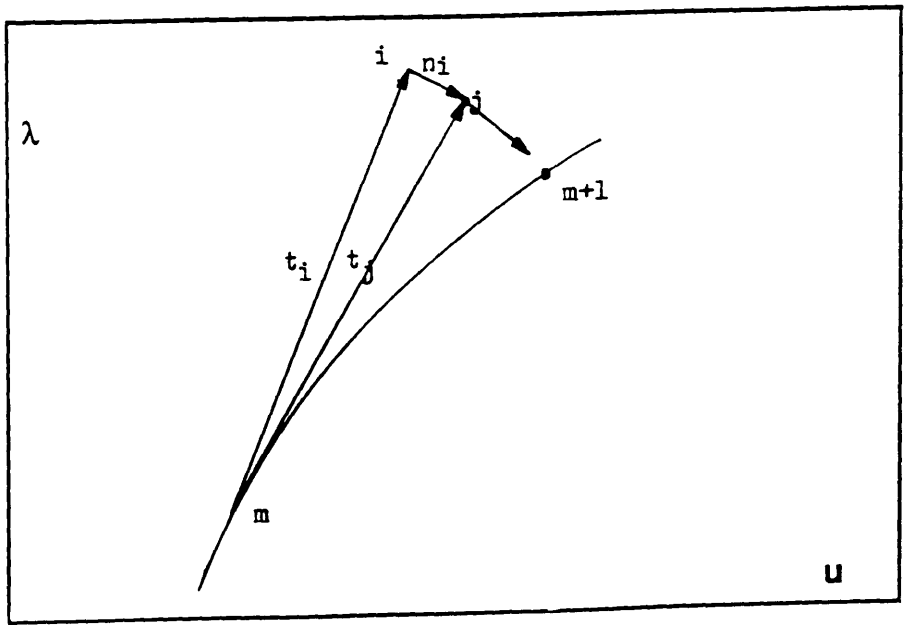

Fig.6.4 Arc– length Constraint

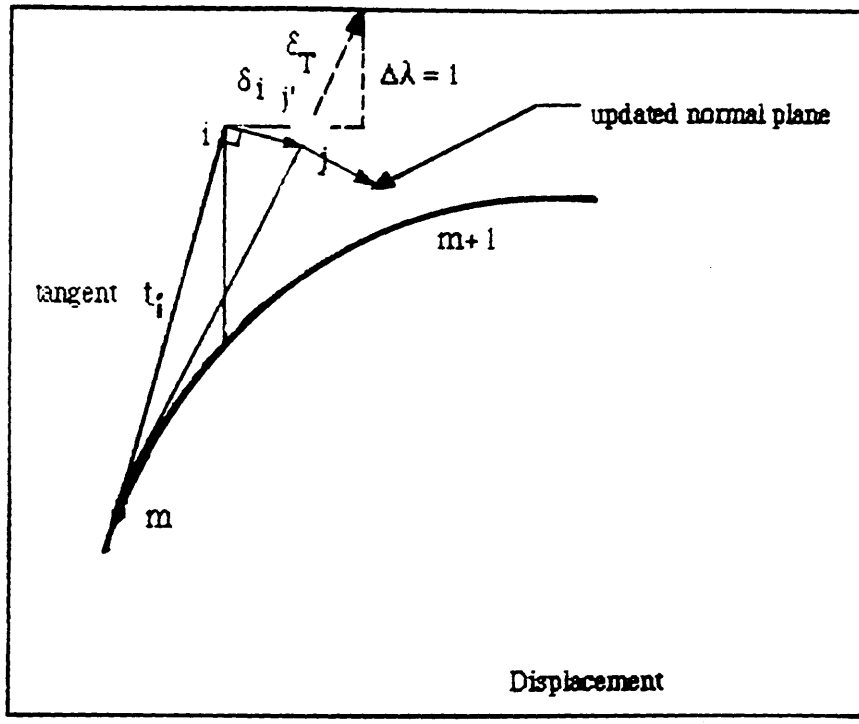

Fig.6.5 Iteration on Normal Plane

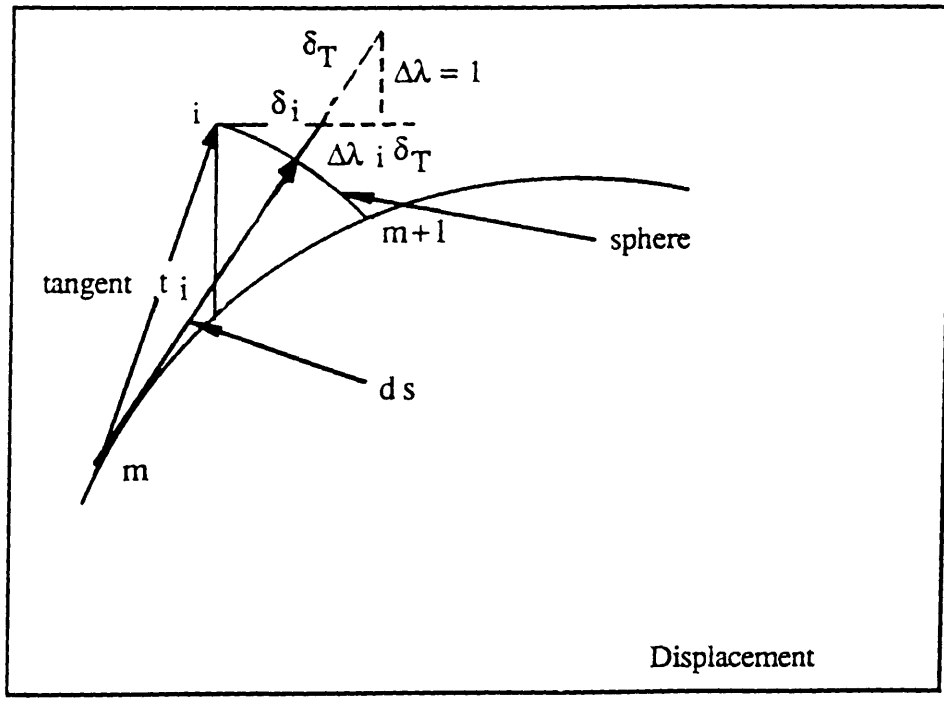

Fig.6.6 Iteration on 'Sphere'

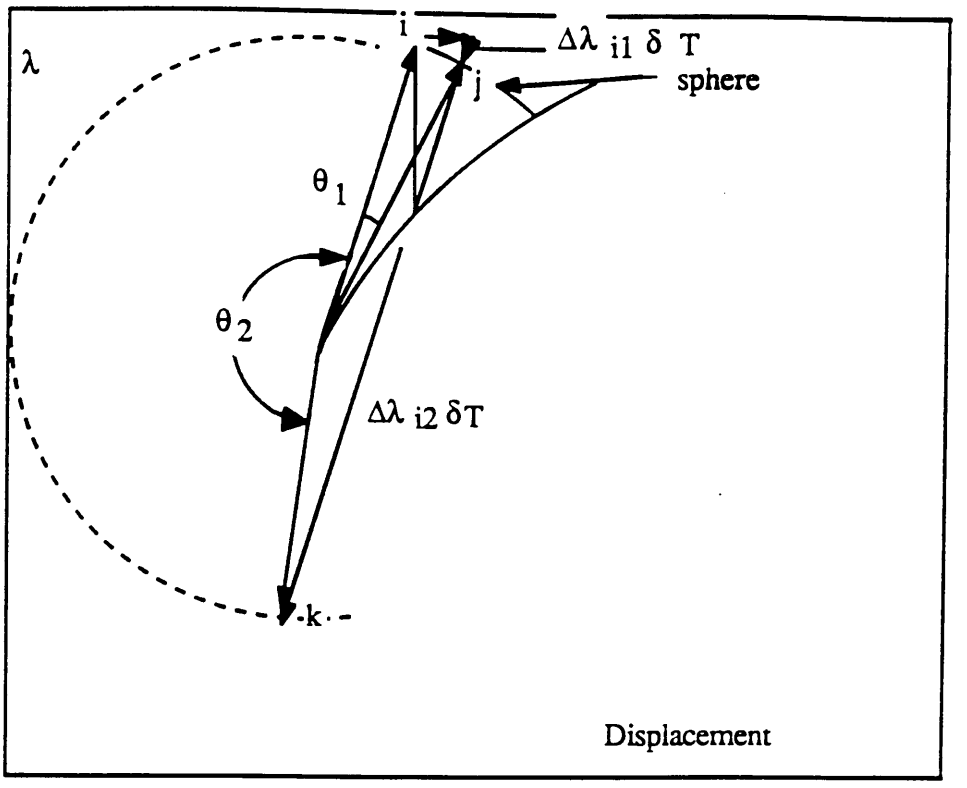

Fig.6.7 Selection of the Proper Root

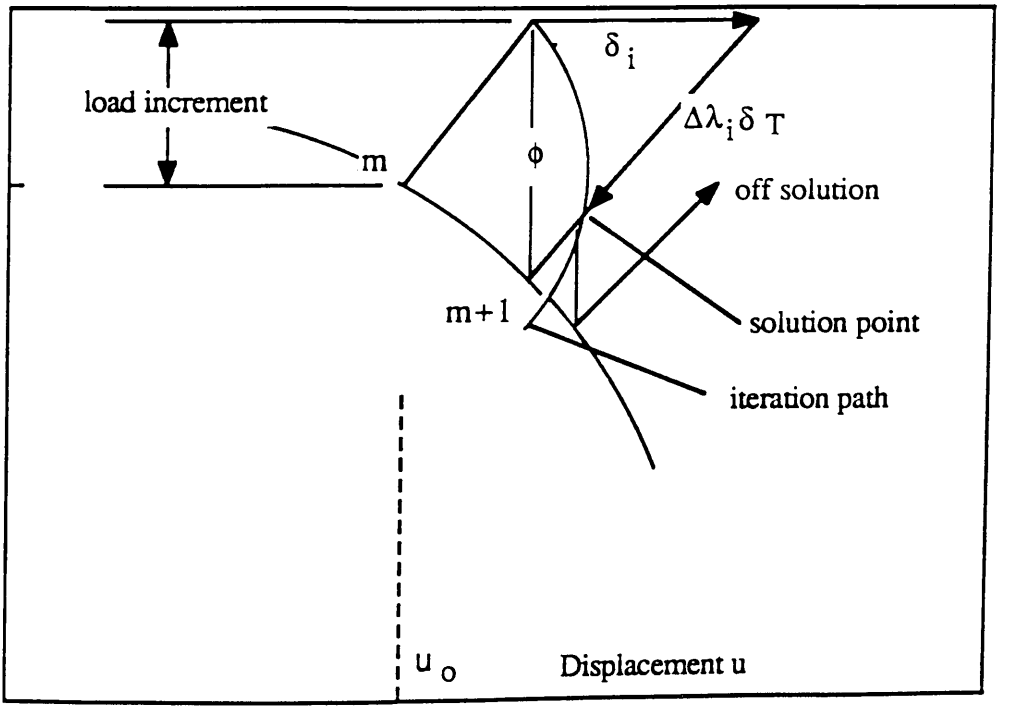

Fig.6.8 Tracing by Secant Stiffness Matrix

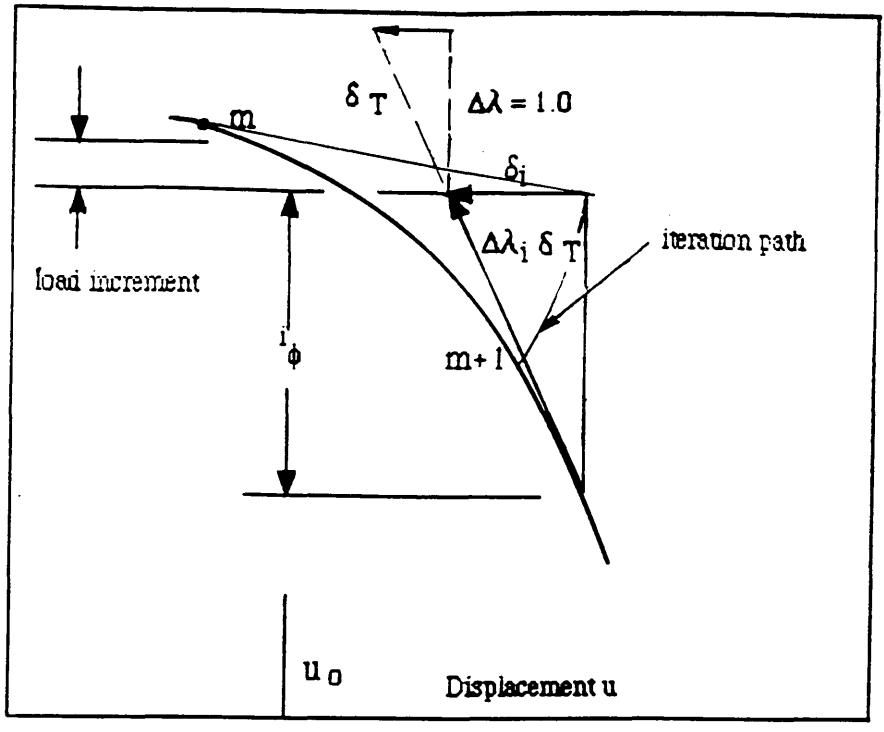

Fig.6.9 Tracing by Tangent Stiffness Matrix

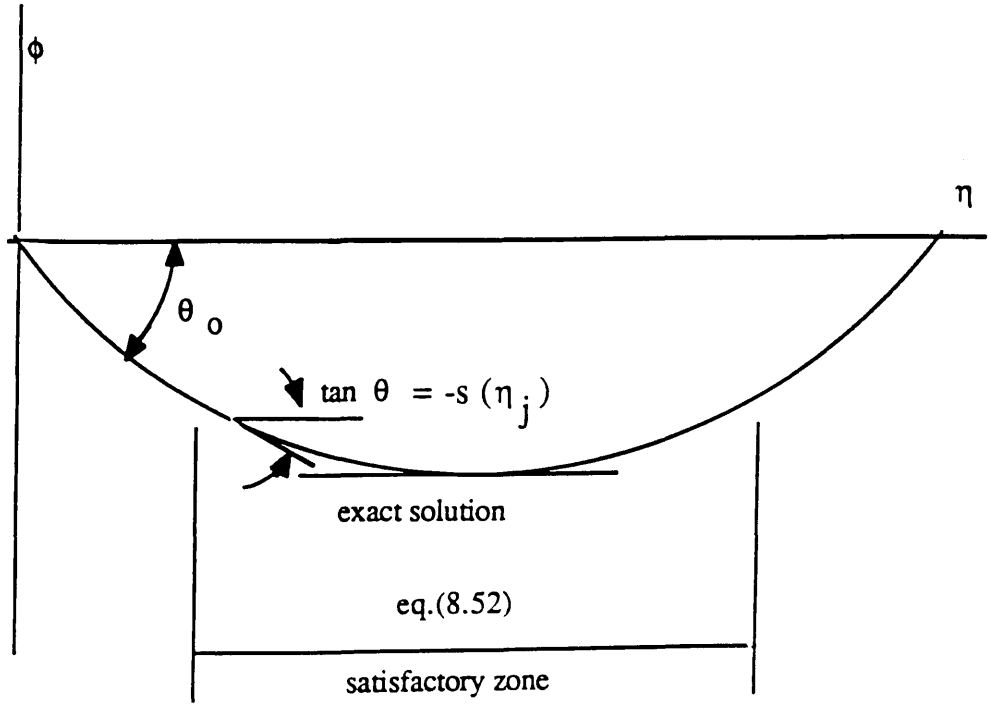

Fig.6.10 Line Search Restriction

CHAPTER SEVEN

FUNDAMENTAL NUMERICAL STUDIES

OF

MODELLING TECHNIQUES

7.1. Introduction

Having discussed and implemented the finite element computational representation of reinforced concrete structures, several examples are now presented to assess the methods developed. Fundamental numerical studies are carried out in this Chapter whilst the next Chapter presents applications to more realistic reinforced concrete structures.

The main purposes of this Chapter are:

1). To investigate the capability, effectiveness and reliability of the new proposed embedded reinforcement models, including curved bars.

2). To investigate the concrete crack rotation approach and strain–decomposed crack models for skew reinforced concrete panels to see how effective these are in tracing changing crack orientations.

3). To assess arc–length solution and line search techniques in reinforced concrete structure analysis, in particular when tracing post crack behaviour.

4). To investigate tension stiffening and shear retention laws. Although many relationships have been suggested to date, there is still no general agreement of the most appropriate relationships due to the complicated mechanism of such

effects.

5). To assess the capability of the implemented embedded bond–slip model and the adopted nonlinear bond–slip relationship, and to obtain a better insight into the fundamental behaviour of bond–slip.

These fundamental numerical studies have been undertaken on a stock of relatively simple reinforced concrete panels and specimens. They include: i) one–way reinforced concrete panels; ii) skew reinforced concrete panels; iii) biaxially loaded Bhide–Collins panels; and iv) pull–out tests and transfer tests.

The program used in these investigations is based on the original version of FECON 86[Phillips 1986]. This has been modified to include the new reinforcement modelling, bond modelling, tension stiffening, shear transfer, line search and arc–length solution techniques, and rotating and strain de–composed cracking simulation.

7.2 Comparison of Different Embedded Reinforcement Models

Introduction

The aim of this section is twofold. One is to assess the new formulations against the previous one of Phillips and Zienkiewicz. The capability and reliability of the latter formulation has been proven by quite a number of investigations on deep beams, prestressed concrete pressure vessels, etc. Therefore, it is worthwhile comparing the new models with the previous one by analysing some simple examples. The second aim is to show the potential use of the new models by comparing with the experimental results of a skew reinforced concrete panel.

7.2.1 One Way Reinforced Square Panels

Description of the Specimen

Two artificial specimens, 1000mm square with thickness of 100mm, reinforced in the x– direction, were analysed (see Fig.7.1). The two specimens have different location of reinforcement. In the first case, the bar distance d is 250mm from the boundary side while in the second one d equals 200mm. A uniformly distributed tensile load and a pure bending moment were applied as shown. The different locations of reinforcement were used because the first one can be analysed by all three models while the second one will show any variation in the steel stress due to the change of steel layout. Theoretically the stresses should be the same whatever the position of steel.

Parameters Studied

Variation of the steel stress will be investigated with reference to different meshes and the embedded models. Two meshes are used for the first case where d = 250mm while four meshes are used for the second case where d = 200mm, as shown in Fig.7.2(a) to (f), respectively. The numbers in each diagram indicate the different embedded models studied for each mesh, where I represents Phillips– Zienkiewicz formulation, II denotes the orientated embedded straight bar formulation, and III stands for the general embedded approach. A 3 by 3 Gauss integration rule was used. All analyses were linear– elastic.

Material Properties

The following concrete and steel properties were assumed.

Concrete: E_c = 20GPa, ν = 0.15

Steel: E_s = 210GPa, A_s = 300mm^2

Results

The steel stresses at the middle Gauss point in each bar are listed in Table 7.1(a) and 7.2(b) for the tensile load and bending load respectively. These show a very small but acceptable variation between rectangular elements and distorted elements. Likewise there is little difference between each formulation.

For the tensile loading, elements nearer to the boundary exhibit slightly higher steel stresses than those near to the loading. This is due to the fact that there is a displacement variation over the width of the panel corresponding to the uniformly distributed load. When an equal prescribed displacement is applied over the whole width, then all steel stresses were identical and equal to the theoretical value (see Table 7.1(a), mesh b). For mesh (f) which used 6 distorted elements leading to 4 bar elements along the length, the steel stress was much more evenly distributed along the bar, (see Table 7.1(a), mesh (f)).

Under bending load, similar observation can be made. In addition, the tensile and compressive steel stresses in the upper and lower bars respectively were identical at a given section, confirming the accuracy of each formulation.

Based on these results, it is concluded that all formulations perform satisfactorily and hence can be used and evaluated in more complex situations.

7.2.2 A Skew Reinforced Concrete Panel

Description of the Specimen

The next specimen presented is a real reinforced concrete panel selected from the experimental study conducted by Scanlon, Phillips and Green in 1988[Scanlon, Phillips and Green 1988]. The selected panel was 1000mm x 550mm x 100mm in size, reinforced with 10mm Φ torbar in the skew and transverse directions. Referring to shown in Fig.7.3, the reinforcement arrangement is defined by α = 71°, S_α = 33mm, and S_T = 100mm. The panel was subjected to one directional tension load under displacement control.

Parameters Studied

The intention of these analyses was to investigate the behaviour given by different mesh sizes and different embedded formulations. Two meshes were investigated, see Fig.7.4. The first one is a single element, 100mm x 35mm, reinforced with one skew bar and two transverse bars. The second mesh is also a single element but now representing the whole panel with the steel arrangement identical to the experimental specimen. The orientated embedded straight bar formulation (denoted Model I) and the general embedded bar formulation (Model II) were both studied. Although the analyses were nonlinear, other modelling aspects were kept as straightforward as possible in order to reduce the number of factors which might influence the comparisons. Thus cracking was modeled by the fixed crack approach with a constant shear retention factor of 0.5. Tension stiffening was neglected and full bond was assumed. Linear compressive behaviour was also assumed. The modified Newton–Raphson nonlinear solution procedure was used in all cases.

Material Properties

Concrete: E_c = 20GPa, ν = 0.15, f_t' = 2.63MPa, f_c' = 41.1MPa

Steel: E_s = 210GPa, f_s = 546MPa

Results

The results are shown in Figs.7.5 (a, b, c and d), in which the strains in the steel and concrete are compared with experimental results. General trends are similar in all cases. Before cracking occurred, all analyses were in close agreement with the experiment, indicating that both embedded formulations were performing satisfactorily and that there was little mesh sensitivity. After cracking, results started to change. There was a slight difference in the results of Model I and II for the same mesh (100mm x 35mm) but a significant difference in the results for the two meshes for Model II. This can be attributed to the bars being placed at their exact positions in the 1000mm x 550mm mesh, whereas in the 100mm x 35mm mesh the bars extended to the element edges.

The principal strains in the concrete (Fig.7.5(a)) and the principal strains angles in the concrete (Fig.7.5(b)) predict similar trends to experimental, especially the latter. The strains in the skew bars (Fig.7.5(c)) are in good agreement with experiment whilst those in the transverse bars (Fig.7.5(d)) are poor. All analyses overestimated the ultimate load.

The lack of close agreement with experiment after cracking is due to the adopted material laws rather than the performance of the embedded elements as such. In experiment, transverse cracks occurred first, followed by cracks inclined at about 35°. The fixed crack model used in the analysis would not be able to follow this behaviour and would produce a stiffer response and higher ultimate load.

7.3. Skew Reinforced Concrete Panels

Introduction

In this section, a full investigation of skew reinforced concrete panels is undertaken. The panels are specimens No.2, No.3 and No.9, again taken from the experimental study carried out in 1988[Scanlon, Phillips and Green 1988]. These panels are interesting in that they represent different types of fundamental behaviour of a reinforced concrete element under direct tension depending on the orientation of the skew reinforcement bars. Although all aspects of behaviour are of interest, special attention is paid to changing crack orientations and the post–crack response, i. e. the decreasing portion of the response curves after the initiation of cracks. In experiments, it has been seen that the crack orientations changed for different skew panels. After the first crack occurred the second crack may opens in an angle different from a right angle. It is therefore interesting to see if the strain–decomposed non–orthogonal crack model and rotating crack model can follow this behaviour properly.

Due to the inclination of the steel bar, the reinforcing bars can not effectively pick up the forces from concrete after crack formed. The structure hence exhibits high nonlinearity. A good solution technique in this type of structure analysis is therefore required.

Specimens No. 2 and No.3 were analysed under displacement control, whilst Specimen No.9 was analysed using arc–length and line search solution techniques.

Description of the Specimen

As shown in Fig.7.3, the panel was a rectangular plane of length L with width b and thickness t subjected to a tensile force T under displacement control. The

panels were uniformly reinforced with transverse bars placed perpendicular to the force T. The skew bars were placed at an angle α to the transverse bars. Bars were spaced at S_α and S_T in the skew and the transverse directions, respectively. Reinforcement consisted of 10mm Φ "Torbar", reinforcing in both the skew and transverse directions. Reinforcement details for each panel are given in Table 7.2.

Element Discretization

The whole panel for specimens No. 2 and 3 are analysed while only a part of specimen No.9 was taken for the analysis. The meshes for both concrete and reinforcement were generated automatically using the mesh generation routines, and they are shown in Fig.7.6 for Panel 2 and 3, and in Fig.7.7 for Panel 9.

Material Properties

The properties of the reinforcement and concrete are given in Table 7.3

Results

The results for specimens No.2, No.3 and No.9 are given in Figs.7.8 to Fig.7.10, respectively, along with experimental results. These include principal strains in the concrete, steel strains and the rotation of the principal strain angle. The initial and final crack patterns are given in Fig.7.11 (a), (b) and (c). For panel No.2, concrete principal strains are given in Fig.7.8(a) for different crack models whilst Fig.7.8(b) and (c) give the results for the strain decomposed model using 30° as the threshold angle. Panel No.3 was computed using the fixed crack model and the rotating crack model. The concrete principal strain and its strain angle are presented in Fig.7.9 (a) and (b). Fig.7.9(c) shows the steel strain versus load for the fixed crack model. Panel No.9 was analysed using both the fixed

and rotating crack models. The numerical results are given in Fig.7.10 for the principal strain in concrete and the strain in steel.

In the analysis of Panel 2, the orthogonal fixed crack, strain–decomposed crack and the rotating crack models are used. For the strain–decomposed concept, the chosen threshold angles are 30°, 45° and 60°. In the rotating crack model, the crack is allowed to rotate at every iteration. It is seen that while the fixed crack approach overestimates the loading capability the rotating crack model underestimates it. In the strain–decomposed crack model, the overestimation is reduced with a decrease in the threshold angle, see Fig.7.8(a). The results close to the experimental curve if the threshold angle is close to the crack inclination which occurred in the experiment. Therefore, it is suggested that if the crack inclination is known then the strain–decomposed crack model can be a useful tool to predict the ultimate load of the structure. If crack direction is not known, which is usually the case, then the fixed model can be used to give an upper bound whilst the rotating crack model will give a lower bound on the ultimate load.

The longitudinal and transverse steel strains as well as the principal strain angle of concrete are given in Fig.7.8(b) and (c) for the threshold angle of 30°. The results are in quite good agreement with those of the experimental ones.

Fig.7.10 show the results for specimen No.9 using both orthogonal fixed crack model and the rotating crack model, in which the crack is allowed to rotate once an increment. Consistent results were achieved including the behaviour of both concrete and steel. The solution convergence was obtained within five iterations after crack occurs, indicating that arc–length procedure with line search scheme is quite effective method in the nonlinear analysis of reinforced concrete structures.

The crack patterns presented in Fig.7.11(a), (b) and (c) are the results of the rotating crack approach. These have reasonably predicted the orientation of the second set of cracks.

7.4. Bhide– Collin's Panel

Inroduction

In this section, a one– way reinforced concrete panel subjected to combined tension and shear is examined. The panel was selected from the experimental work of Bhide– Collins[Bhide and Collins 1987], and designated PB20. This panel is interesting because it provides a good test of whether the various cracking models can properly allow for the detrimental effect of tensile cracking on the shear capacity. In reinforced concrete design, it is common practice to ignore the ability of concrete to resist tension. While this assumption is appropriate in design for bending and axial load, it is less so for shear. In addition, there are numerous practical situations in which reinforcement concrete structures are subjected to combined shear and tension stresses. The ability of cracked concrete to resist shear is even more important in such cases, especially if there is no shear reinforcement. It is, therefore, important to understand the behaviour of members without shear reinforcement subjected to combined tension and shear

In the following analyses, attention is focused on the tension stiffening and shear retention laws since these will have a crucial effect on post– cracking behaviour. The following tension stiffening laws were examined:

i) Sudden drop to zero on the initiation of the crack, i.e. no stiffening

ii) Yamaguchi and Nomura's bilinear strain– stress relationship, designated O– P

iii) Phillips and Zhang's trilinear strain–stress relation based on the fracture energy theory, designated P–Z with crack spacing l = 10mm and 15mm

iv) Bhide–Collins tension–stiffening law, used with assumed crack angles of 30°, 45°, 60° and 90° as well as the predicted angle.

v) Vecchio–Collins equation, designated V–C

All tension stiffening laws were used in conjunction with a constant shear retention factor of 0.5.

The shear retention laws examined are:

i) constant shear retention factors of 0.25, 0.5 and 0.7

ii) Melhorn's shear rule[Melhorn 1990], and

iii) bilinear relationships[Nilson 1985].

All various shear retention laws were used in conjunction with the Vecchio–Collins' tension stiffening law.

In all cases the fixed cracking model was used.

Description of the Specimen

The test panel was an 890 mm square reinforced concrete element with a thickness of 70 mm as shown in Fig.7.12. It was reinforced with 6mm diameter deformed reinforcement bars arranged in two layers parallel to the sides of the panel, and spaced at 44.5 mm centres as shown in Fig.7.13. A clear cover of 6 mm was provided between the faces of the panel and the outmost layer of reinforcing steel. The specimen was subjected to the combined tension and shear stresses under loading control, the proportion of tension to shear stress being 2.04

to 1.0 throughout the loading history

Element Discretization

Since the specimen was designed to be in a uniform state of stress only one eight-noded parabolic plane stress element was used, with nine integration points. The meshes for concrete and reinforcement are shown in Fig.7.14. The reinforcement was modelled as one-dimensional uniaxial members by the general embedded bar model. Perfect bond is assumed between reinforcement and concrete. Solutions were obtained using the modified Newton-Raphson scheme under load control.

Material Properties

The concrete properties are:

$f_c' = 21.7\text{MPa}$ $f_t = 2.56\text{MPa}$

$E_c = 20\text{GPa}$ $\nu = 0.15$

The reinforcement properties are:

$f_s = 424\text{MPa}$ $\rho_s = 0.02195$

$E_s = 210\text{GPa}$

Results

Tensile stress versus strain in the concrete, measured in the x-direction are plotted with the experimental curve in Fig.7.15(a), (b) and (c). It is clear from these curves that tension stiffening has more influence than shear retention on behaviour. The tension stiffening laws in Fig.7.15(a), all of which contained either sudden drops or very steep softening curves, did not follow the experimental curve very closely. The tension stiffening laws presented in Fig.7.15(b) all had

curved softening branches and gave a much closer prediction to experiment except when the assumed crack angle was at 90° to the reinforcement. From these curves, it would seem justified to recommend the use of either the Vecchio– Collins law, which is computationally less complex, or the Bhide– Collins law in conjunction with the crack angle predicted by cracking model. The latter suffers from the crack and the main reinforcement direction, which could be awkward in more general situations.

From Fig.7.15(c), it can be seen that there is very little practical difference between the different shear retention laws in this case, except that the small constant β factor = 0.25 is less stiff. In view of this, it would seem reasonable to recommend a constant β factor of 0.5 which is commonly used by other analysts, or the Melhorn law which takes into account the amount of reinforcement crossing a crack, which could be important in more general situations.

It would be emphasized, of course, that these conclusions are relevant only to the fixed crack model. A more comprehensive study is required if more general guidelines are to be drawn regarding other stress states or cracking models.

7.5 Bond– slip Modelling Techniques

Inroduction

In this section, the main purpose is to examine the embedded bond– slip formulation and study the fundamental bond– slip concepts. In addition, various bond– slip relationships will be investigated. A square one– way reinforced concrete panel as well as pull– out tests and a transfer test will be analysed. In these analyses, bond– slip was assumed for all the reinforcement bars of the

specimen.

7.5.1 Square Panel With One-Way Reinforcement

The square one-way reinforced panel studied previously in section 7.2.1 is used again here to study the bond-slip effects using the bond formulation in conjunction with general embedded bar formulation. The panel is shown in Fig.7.1, subjected to a uniformly distributed tensile load of 1.0 N/mm^2. It is recalled that the concrete modulus E_c was 20 GPa whilst for steel E_s was 210GPa.

The steel strain distribution is plotted in Fig.7.16(a), for different bond-slip modulii using mesh of Fig.7.2(a). The assumed bond modulii were 210.0GPa, 21.0GPa, 210.0MPa and 0.0MPa. The steel strain calculated without bond-slip is also given. It was shown that a change in bond modulus causes an change in steel strain. When the bond modulus is the same as the steel modulus (E_s=210GPa) the strain is identical to that given by the perfect bond formulation. When the bond modulus is small compared to the steel modulus (1/1000 of E_s) the steel strain decreases abruptly from the middle to the either side and the steel was therefore de-activated. For E_b=210.0MPa, the concrete deformation, bond-slip and steel deformation were also given in Fig.7.16(b), in which the steel was relatively moved back from concrete edge in a consistent manner as shown in Fig.7.16(a) for the same bond modulus.

Further study the variation of the steel strain distribution, mesh in Fig.7.16(c) were used. The results in Fig.7.16(d) were satisfactory.

Hence, the proposed bond formulation is capable of taking bond-slip phenomena into account in a consistent manner.

In addition, half of this panel (1000mm x 500mm) with loading on bond-slip degree of freedom was analysed using one element. Load and boundary conditions were shown in Fig.7.16(e and f). Numerical results were given as well. Due to the bond force, the concrete compresses from its original position while the reinforcement extends. The reaction forces were self-equilibrating along the boundary side, which is expected since the applied bond force is self-equilibrating. This analysis is somewhat artifical because it is not clear that such an extenal bond force system is physically possible. However, it would be a useful analytical 'device' for certain types of problems and should be investigated further in order to obtain a rational interpretation.

7.5.2 Pull-out Tests

Analyses of pull-out tests taken from the experimental work of Jiang, Shah and Andonian[Jiang, Shah and Andonian 1984] are presented in this section. The specimen consists of a rectangular concrete block and two reinforcement bars embedded in opposite sides of the cross-section, see Fig.7.17(a). The bars were standard 19mm diameter bars split into two halves. Tensile loads were applied directly to the bars. The purpose of the analyses was to compare different bond-slip laws against experimental data using the general embedded bar element formulation.

Two specimens A1 and A2, 127mm long, were analysed using a 6 element mesh (Fig.7.17(b)) for one quarter of the specimen. Table 7.4 lists other dimensions and material properties. The force is assumed to be transferred from reinforcing bar to concrete.

In all analyses, orthogonal fixed crack model was used with Vecchio-Collins

tension stiffening law and constant shear retention factor of 0.5. The solution were obtained using modified Newton-Raphson method.

Fig.7.18(a), (b) and (c) present steel strain distribution for specimen A1 using bond-slip relations i) constant E_b = 21000MPa, ii) Houde's equation, and iii) monotonic relationship. All exhibit good agreement with experimental results initially and up to the failure load. While the constant bond modulus underestimate the steel strain, ii) and iii) using bond stress-slip law are more consistent with the experimental strains except near the end of the specimen. In general, however, the comparison are good given the coarse mesh used. A finer mesh, especially near the specimen end would allow more concentrated cracking and hence decrease the force transfer from steel to concrete, increasing the steel strains. Crack formulation for specimen A1 is plotted in Fig.7.19

Fig.7.18(d) presents local slip along the bar for specimen A2 using Houde's bond law. Again good agreement is obtained at low load with greater discrepancy at higher loads near the specimen end.

7.5.3 Transfer Test

In this section, an anchorage transfer test was modelled using a specimen tested experimentally by Rehm et al[Rehm, Martin and Muller 1968]. The specimen was 2000mm x 2000mm x 2000mm and contained a curved reinforcement bar with a diameter of 12mm. The specimen was also analysed by Melhorn and Keuser in 1985 using contact elements to model the bond-slip effect. The dimensions and material properties are shown in Fig.7.20 along with the experimental and previous numerical strains in the reinforcing bar. This specimen was chosen as being particularly suitable for testing the embedded bond formulation when a curved bar was present.

The meshes for this study are shown in Fig.7.21 for both concrete and reinforcement. Houde's bond stress–slip law was adopted along with the fixed crack model and Vecchio–Collins tension stiffening with a constant shear retention factor of 0.5. A Newton–Raphson solution procedure was used under load control.

The analytical results for the steel strain distribution are given in Fig.7.22. The general trends are consistent with the results of the experiment and those of the previous analysis. However, due to a lack of detailed experimental and analytical information from the previous study, it is not possible to comment on the accuracy of the results. Nevertheless, the analysis indicates that the curved embedded bar formulation with bond slip effects performs satisfactorily.

Table 7.1(a) Reinforcement Stresses at the Second Gauss Point Load I†

Meshes	Model	Reinforcement Stress (N/mm²)			
		Bar One	Bar Two	Bar Three	Bar Four
a	I	0.989285E+01	0.976004E+01	similar to one	similar to two
	II	0.989285E+01	0.976004E+01	similar to one	similar to two
	III*	0.989290E+01	0.976007E+01	similar to one	similar to two
b	II**	0.168000E+02	0.168000E+02	0.168000E+02	0.168000E+02
c	II	0.989332E+01	0.979707E+01	similar to one	similar to two
d	II	0.988527E+01	0.977232E+01	0.988382E+01	0.978650E+01
	III	0.988460E+01	0.977837E+01	0.988454E+01	0.978240E+01
e	II	0.988379E+01	0.976346E+01	0.987507E+01	0.978022E+01
f	III***	0.986199E+01	0.988386E+01	0.988638E+01	0.986369E+01

† theoretical σ_s = 9.8777 N/mm².

* in doing this computation, the coordinate system was rotated 45°.

** mesh b was calculated under displacement control, δ= 0.08mm, theoretical stress σ_s = 16.8 N/mm².

*** the reinforcement stresses in bar five to eight are similar to those in bar one to four, respectively.

Table 7.1(b) Reinforcement Stresses at the Second Gauss Point Load II†

Meshes	Model	Reinforcement Stress (N/mm²)			
		Bar One	Bar Two	Bar Three	Bar Four
a	I	-0.502329E+01	-0.489087E+01	0.502329E+01	0.489087E+01
	II	-0.502329E+01	-0.489087E+01	0.502329E+01	0.489087E+01
	III*	-0.502207E+01	-0.488978E+01	0.502207E+01E	0.488978E+01
c	II	-0.590393E+01	-0.582288E+01	0.590393E+01	0.582288E+01
	III	-0.590522E+01	-0.582414E+01	0.590522E+01	0.582414E+01
d	II	-0.586691E+01	-0.579440E+01	0.585947E+01	0.577088E+01
	III	-0.590093E+01	-0.582810E+01	0.591027E+01	0.582115E+01
f	III**	-0.587095E+01	-0.588876E+01	-0.587299E+01	-0.583708E+01

† theoretical σ_s is 5.0131 N/mm² for (a) and 5.8987 N/mm² for (c), (d) and (f).

* in doing this computation, the coordinate system was rotated 45°.

** the reinforcement stresses in bar five to eight are similar to those in bar one to four but positive, respectively.

Table 7.2 Specimen Geometry of the Skew Reinforced Concrete Panels

Specimen No.	Reinforcement Angle (α deg.)	Reinforcement Spacing	
		Skew, S_α mm*	Transverse, S_T mm
2	71	66	200
3	71	33	200
9	30	33	100

* 1 in. = 25.4 mm

Table 7.3 Material Properties

concrete				
Specimen No.	Cube Strength (MPa*)	Splitting Tensile Strength (MPa)	Modulus of Rupture (MPa)	Modulus Elasticity (MPa)
2	39.6	2.85	3.29	20,000
3	41.1	2.63	4.79	20,000
9	63.0	3.63	4.98	20,000

Reinforcement:

0.2% Proof stress = 546.0 MPa

Ultimate stress =638.0 MPa

% Elongation = 7.9%

Young's Modulus = 210,000MPa

* 1 Mpa = 145 psi.

Table 7.4 Properties for Pull-out Specimens (D.H. Jiang 1984)

Spec. No.	b (mm)	h (mm)	f_c' (MPa)	f_t* (GPa)	E_c* (Gpa)	f_y (Mpa)	E_s (GPa)
A1	76	95	42.5	2.0	20.0	495	201.2
A2	95	95	43.5	2.0	20.0	495	201.2

* assumed for analysis

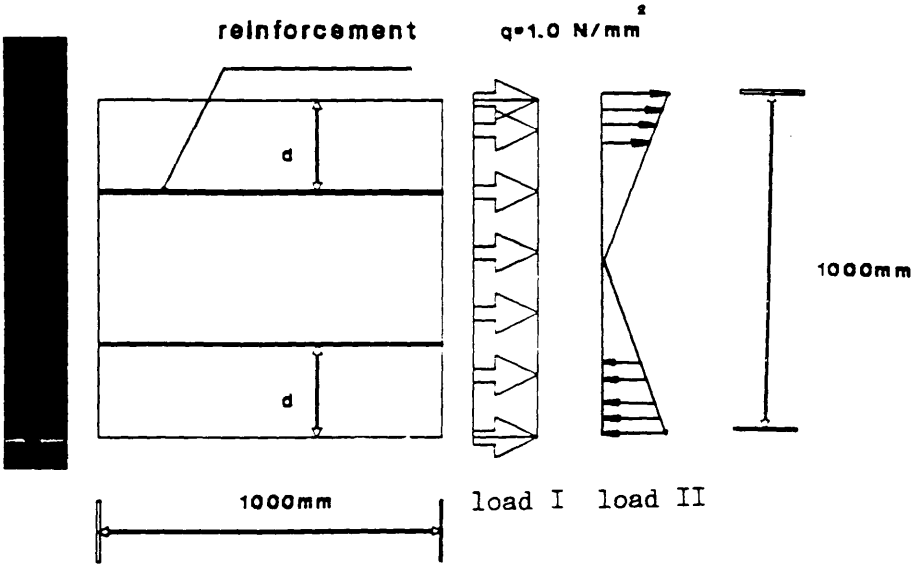

Fig.7.1 Dimensions and Loading Conditions

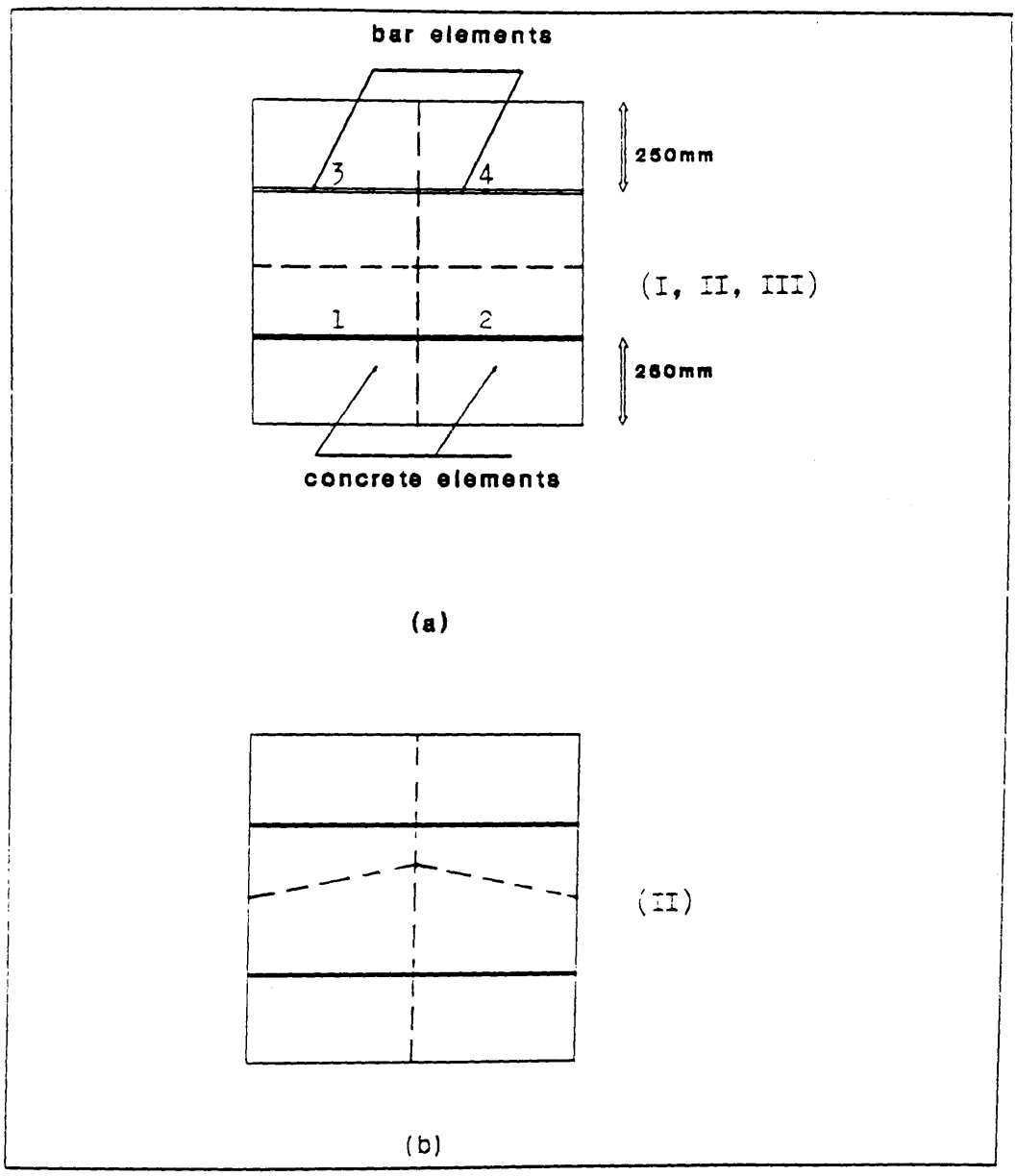

Fig.7.2 Meshes

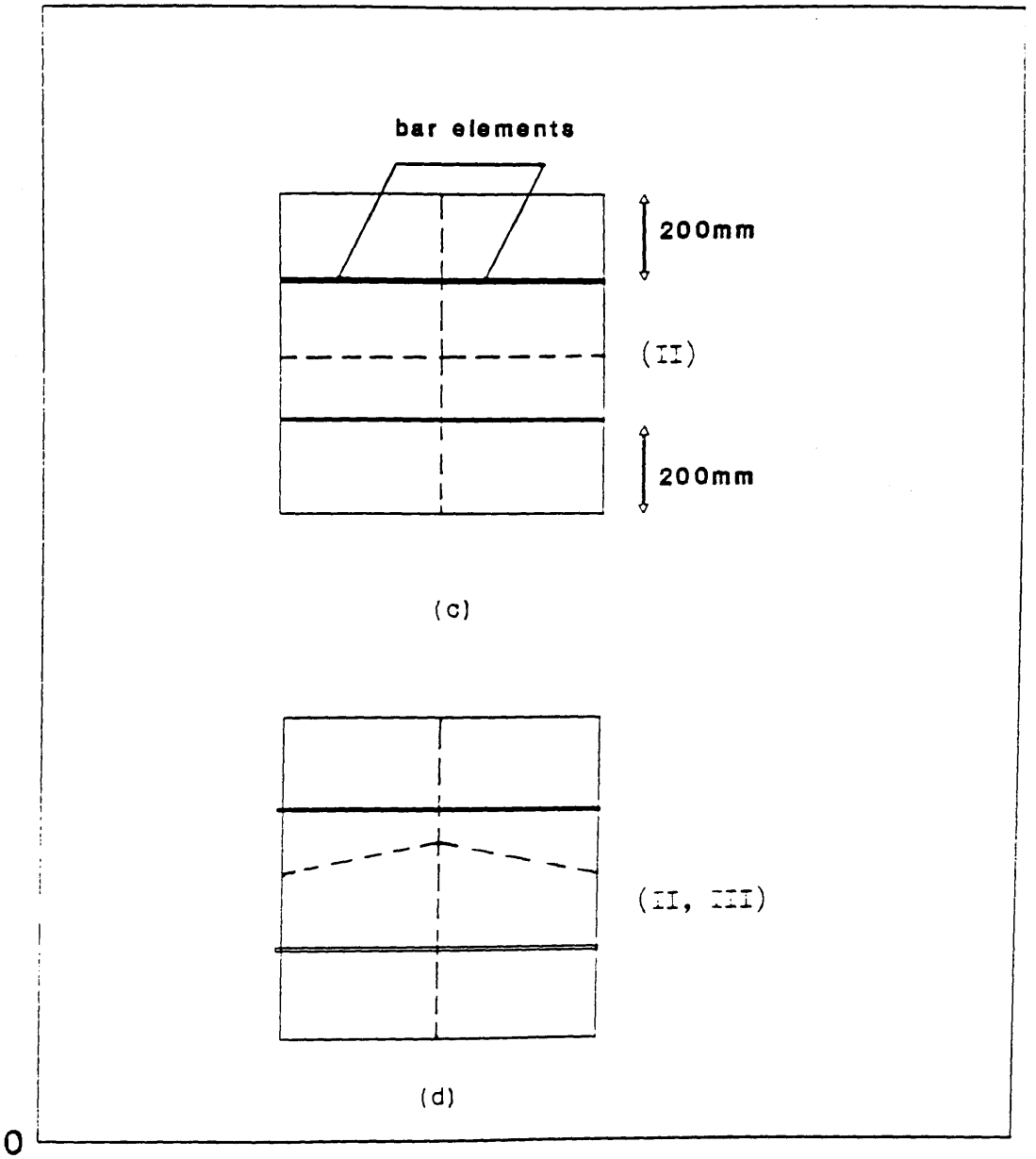

Fig.7.2 Meshes – – continued

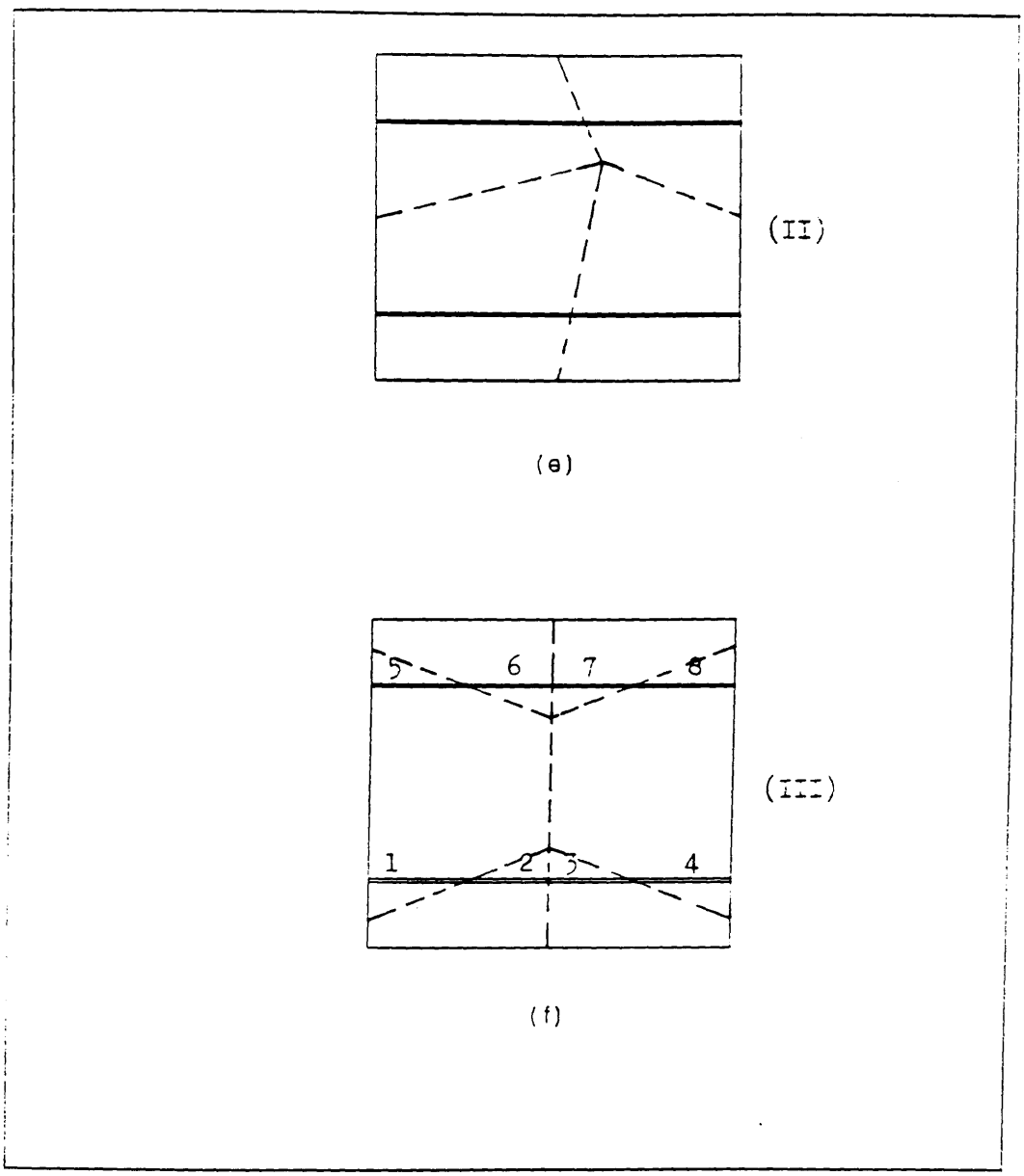

Fig.7.2 Meshes – – continued

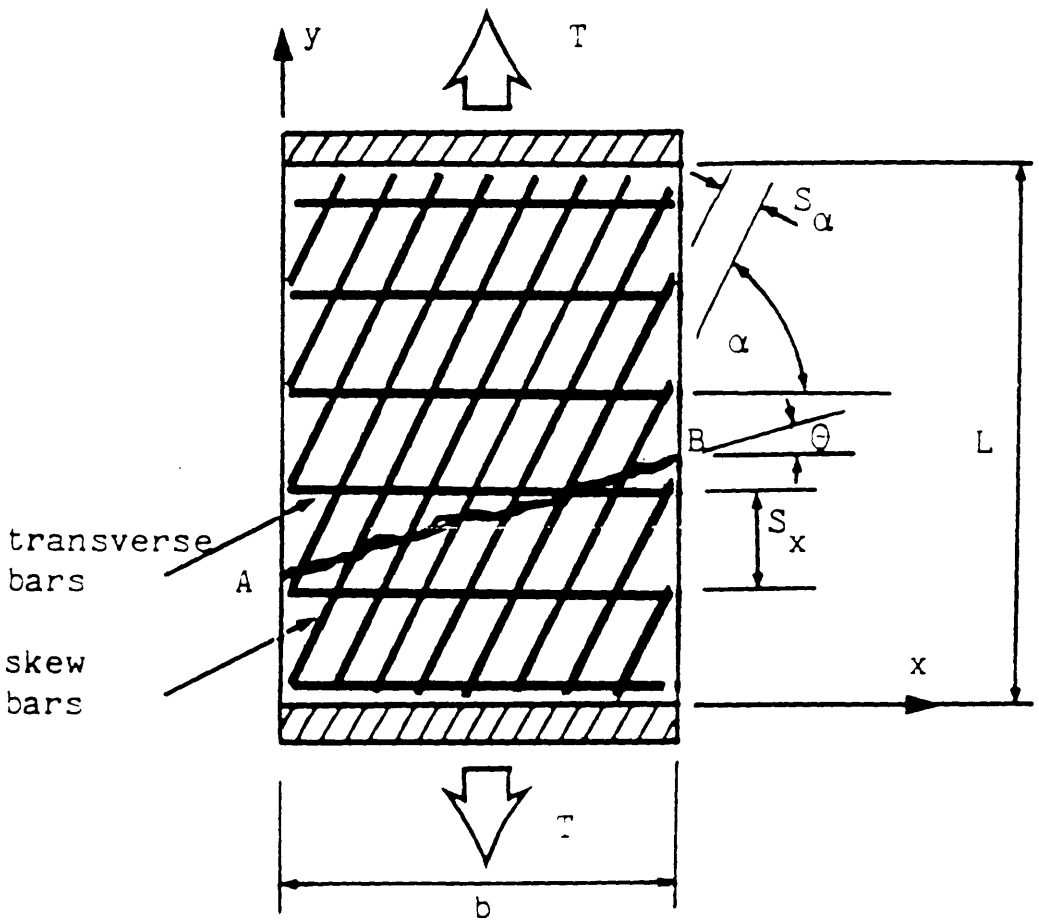

Fig.7.3 Dimensions and Loading Conditions

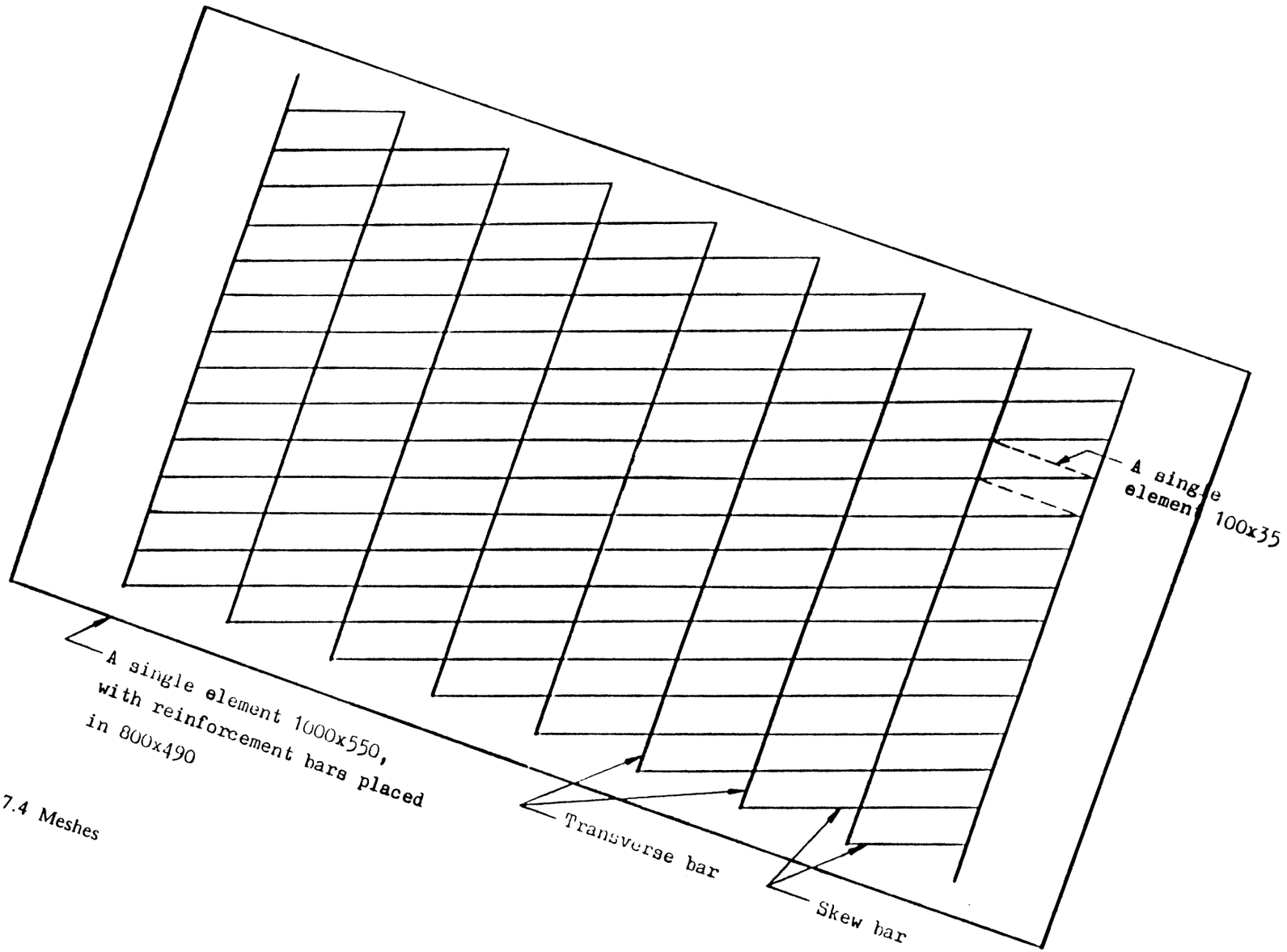

Fig.7.4 Meshes

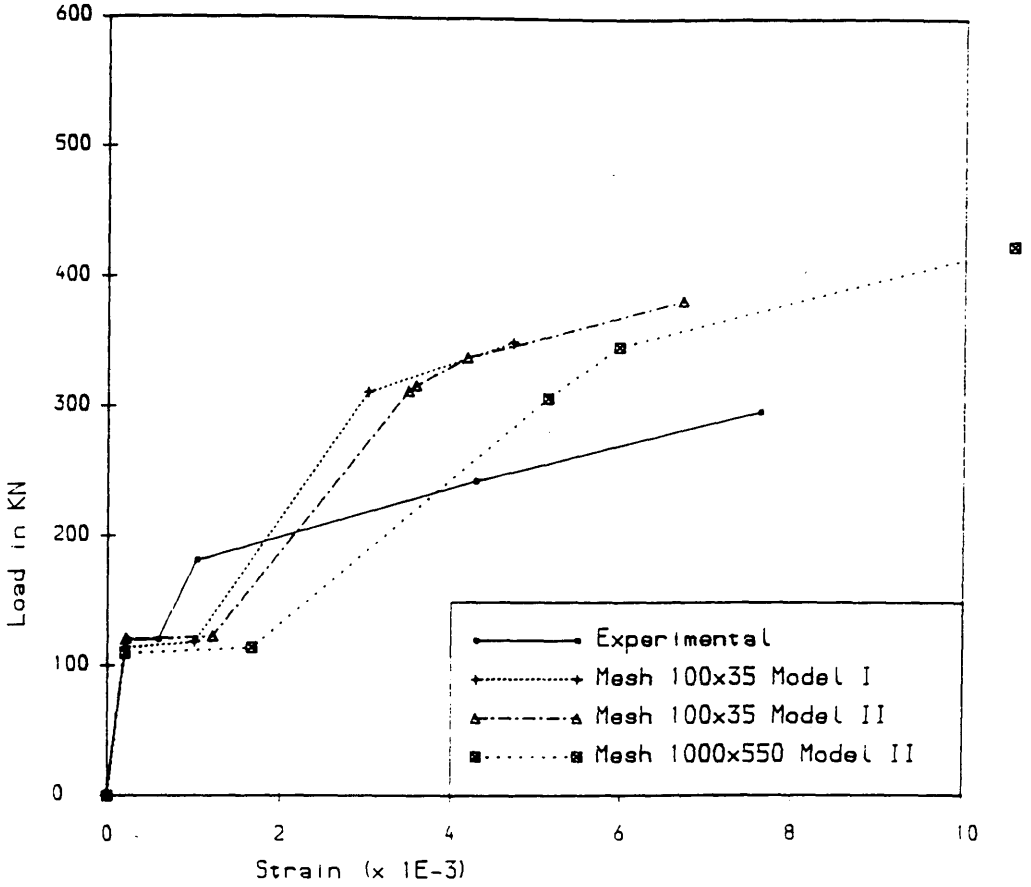

Fig.7.5(a) Load vs. Principal Strain

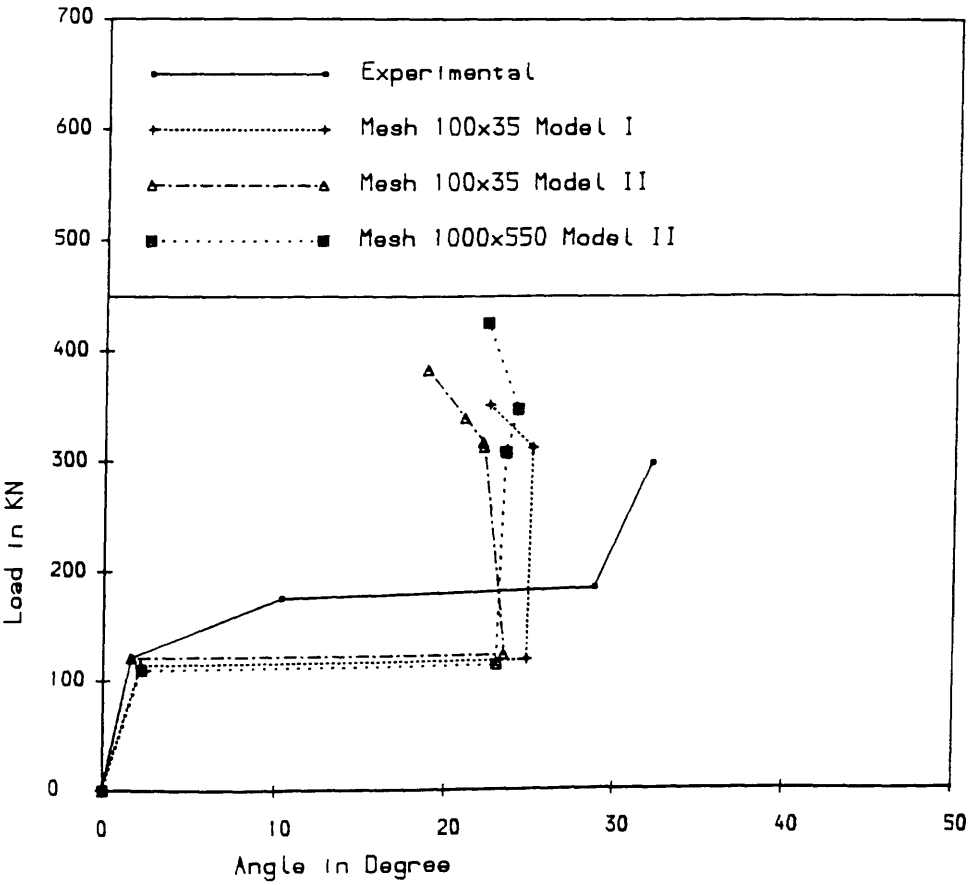

Fig.7.5(b) Load vs. Principal Strain Angle

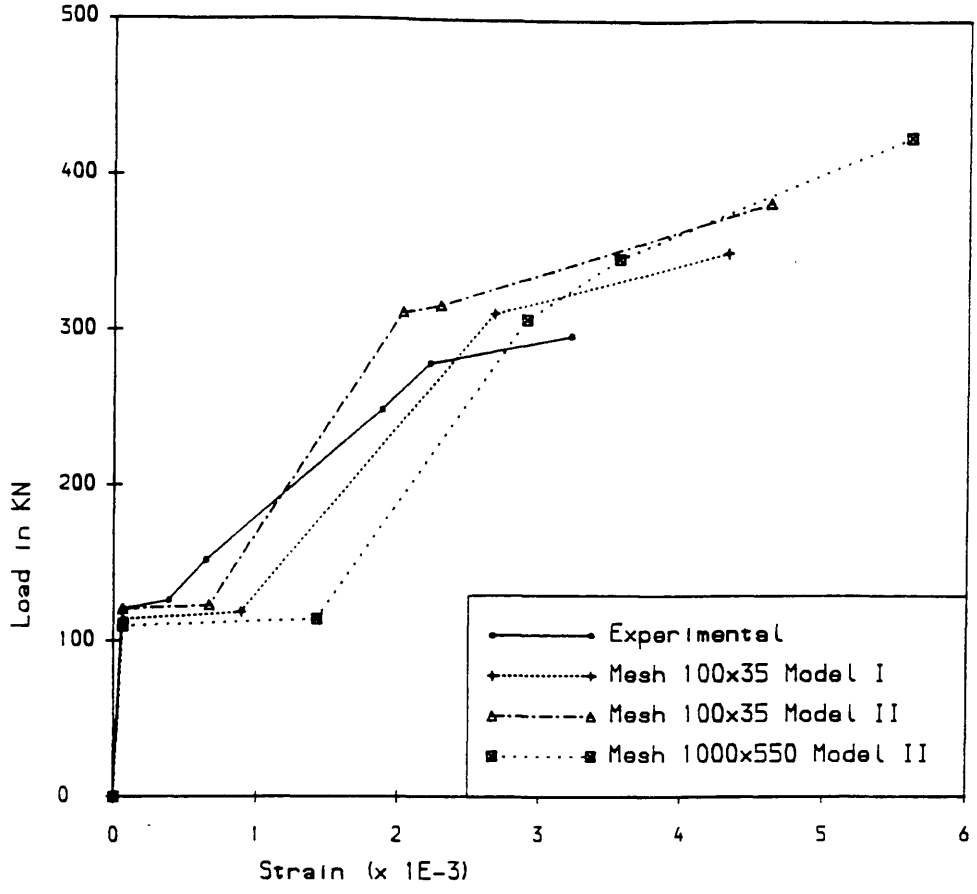

Fig.7.5(c) Load vs. Strain in Skew Bar

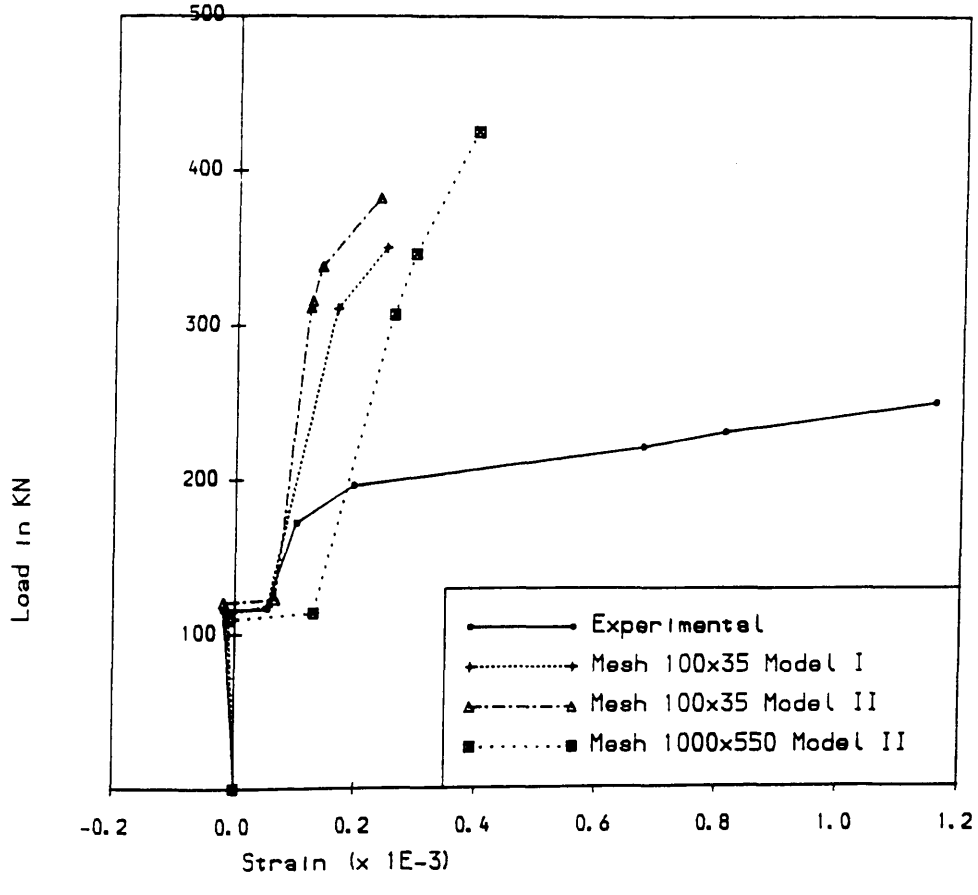

Fig.7.5(d) Load vs. Strain in Transverse Bar

CONCRETE MESH

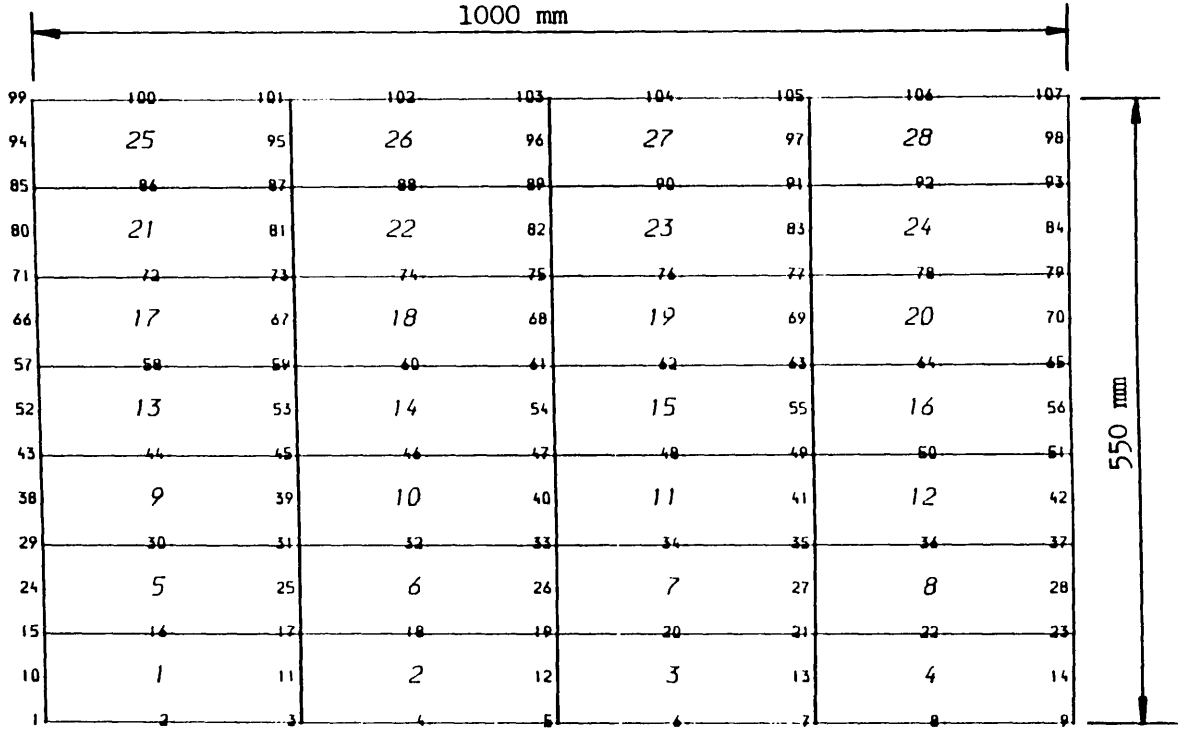

Fig.7.6 Meshes (No.2 and 3)

REINFORCEMENT MESH

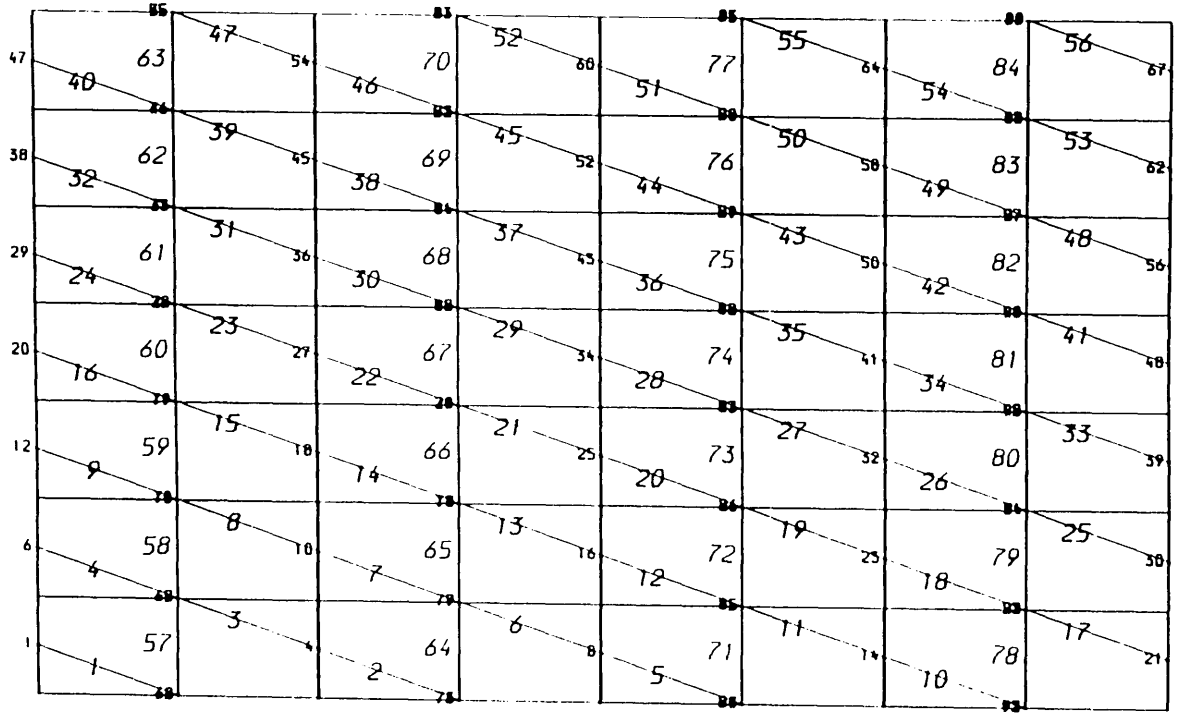

Fig.7.6 Meshes – – continued (No.2)

REINFORCEMENT MESH

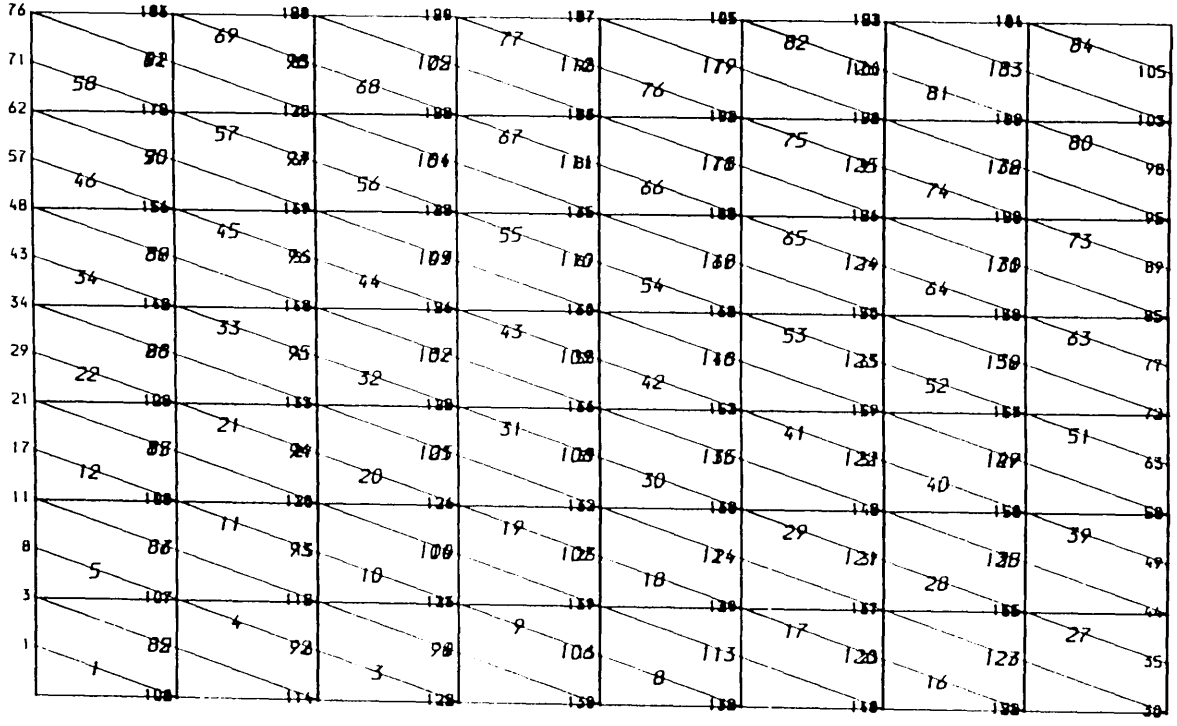

Fig.7.6 Meshes – – continued (No.3)

CONCRETE MESH

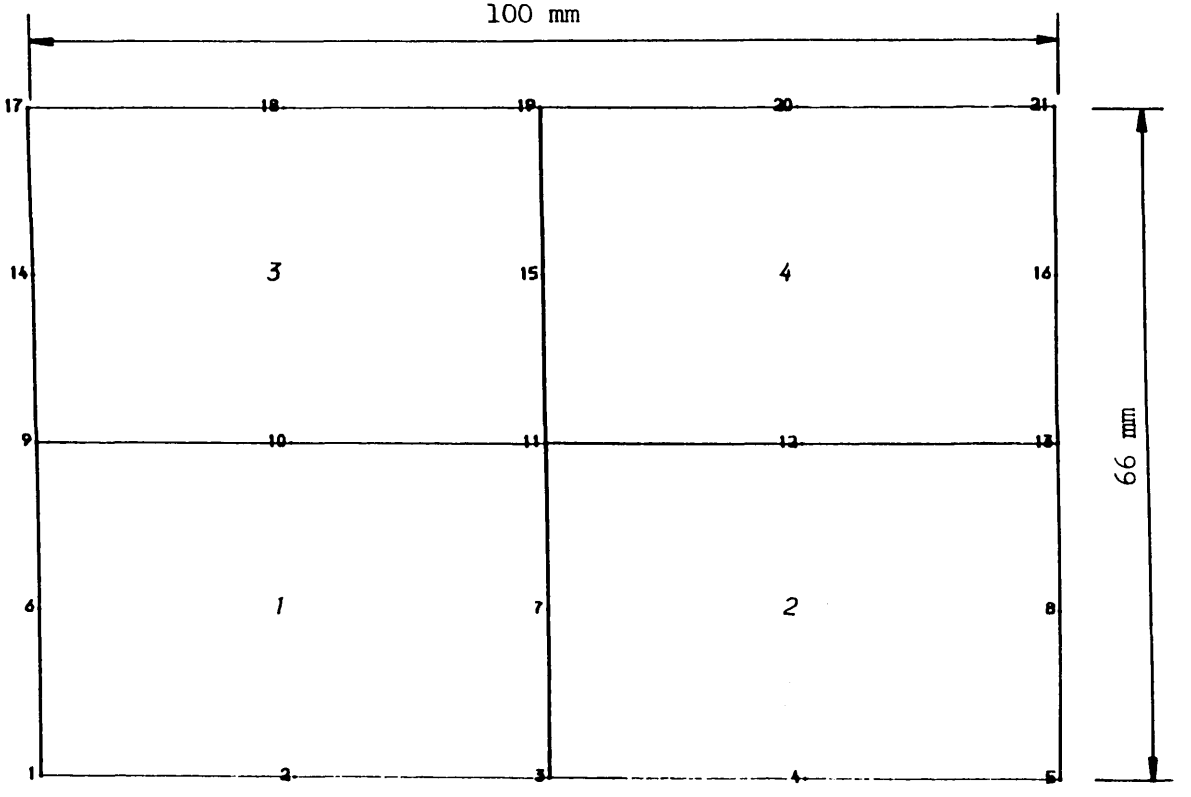

Fig.7.7 Meshes (No.9)

REINFORCEMENT MESH

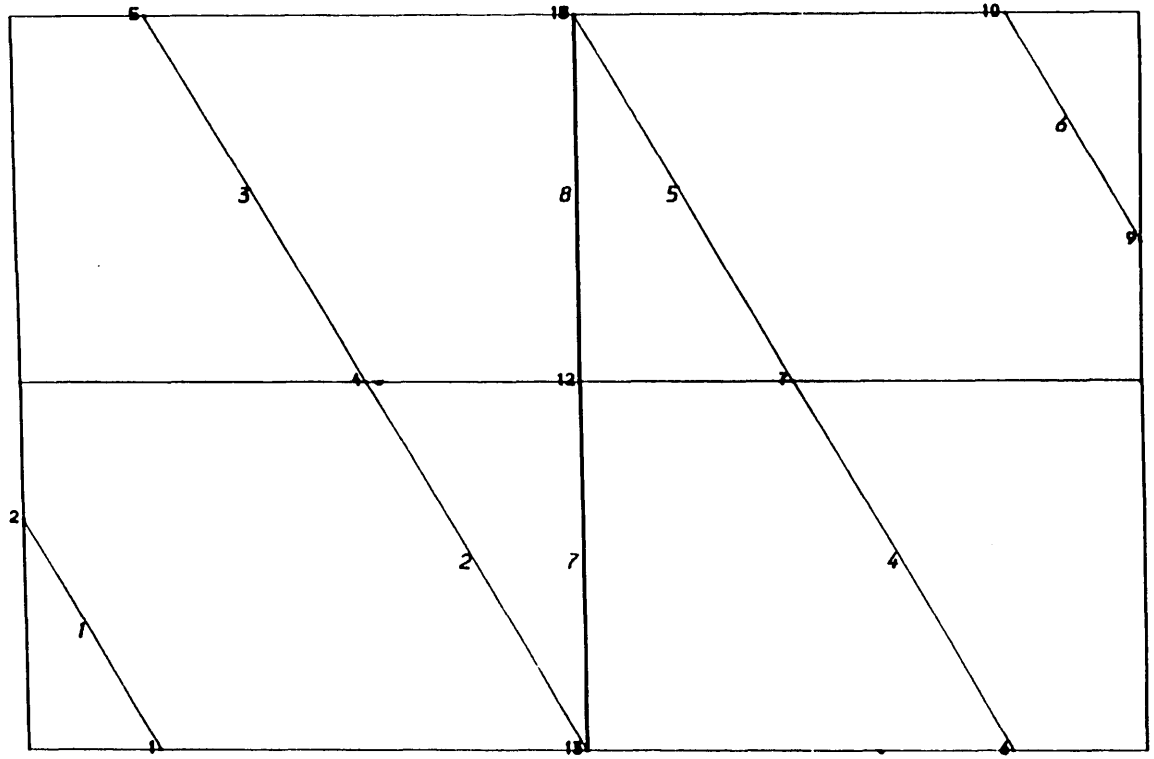

Fig.7.7 Meshes – – continued (No.9)

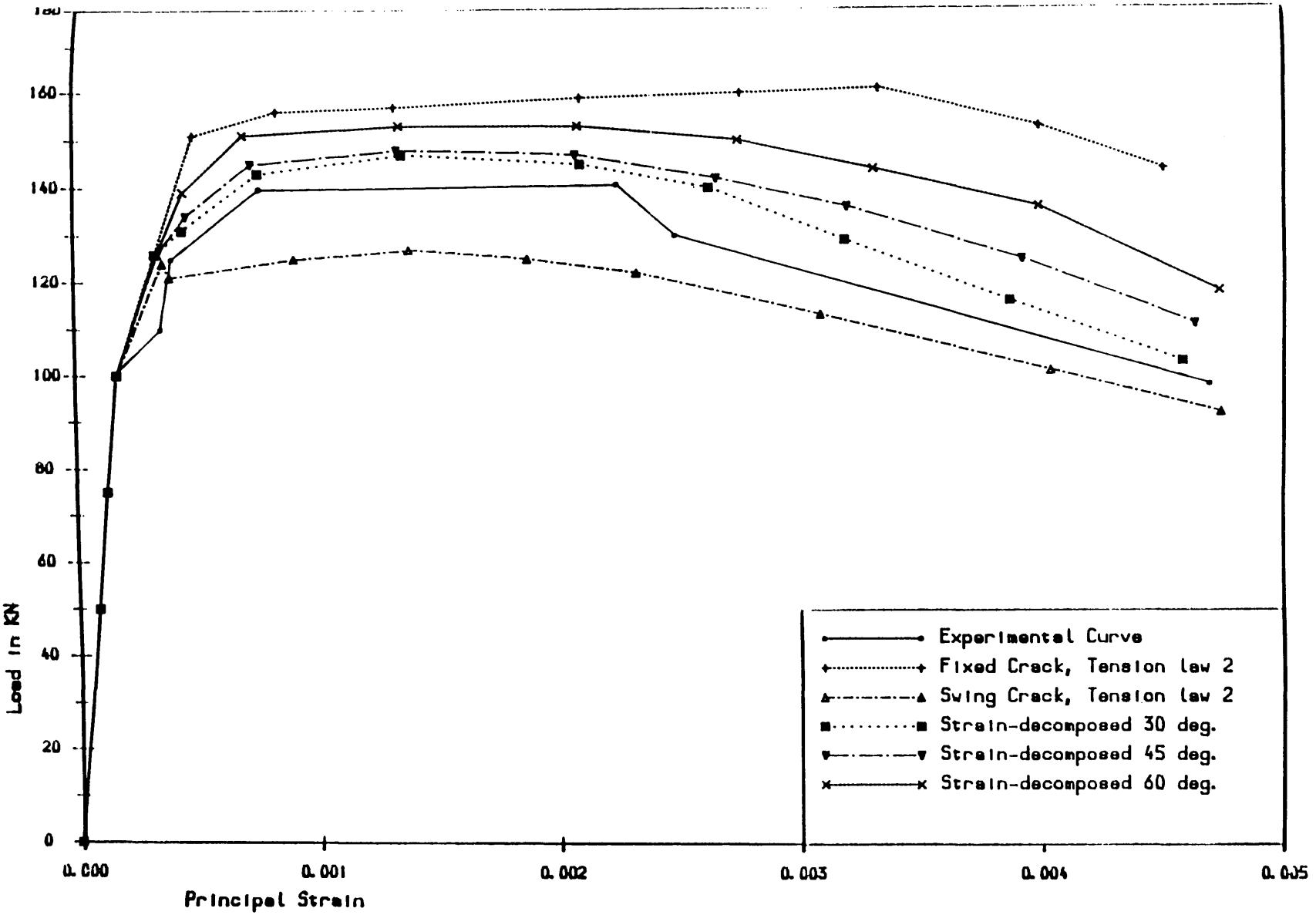

Fig.7.8(a) Load vs. Principal Strain (No.2)

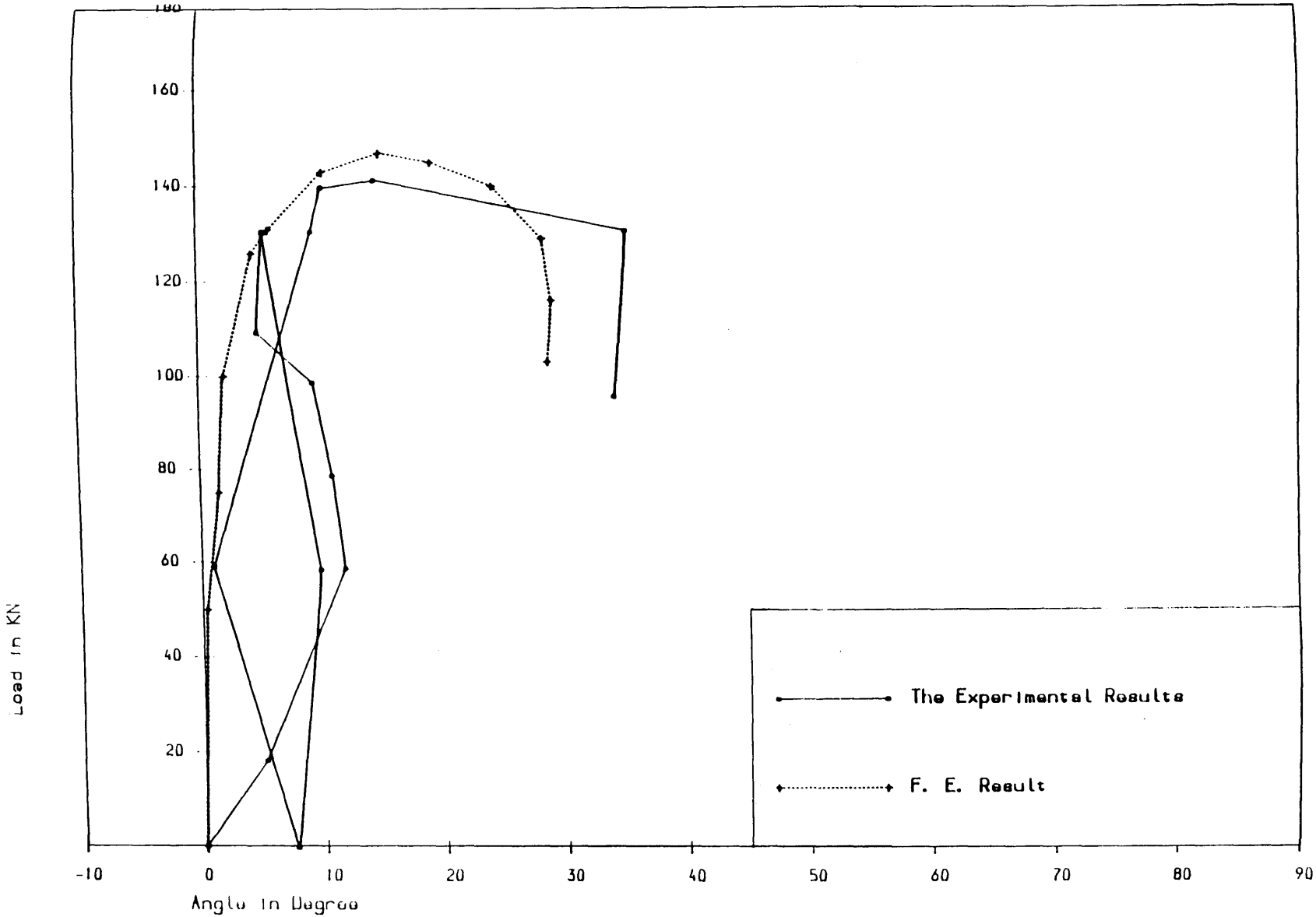

Fig.7.8(b) Load vs. Principal Strain Angle (No.2)

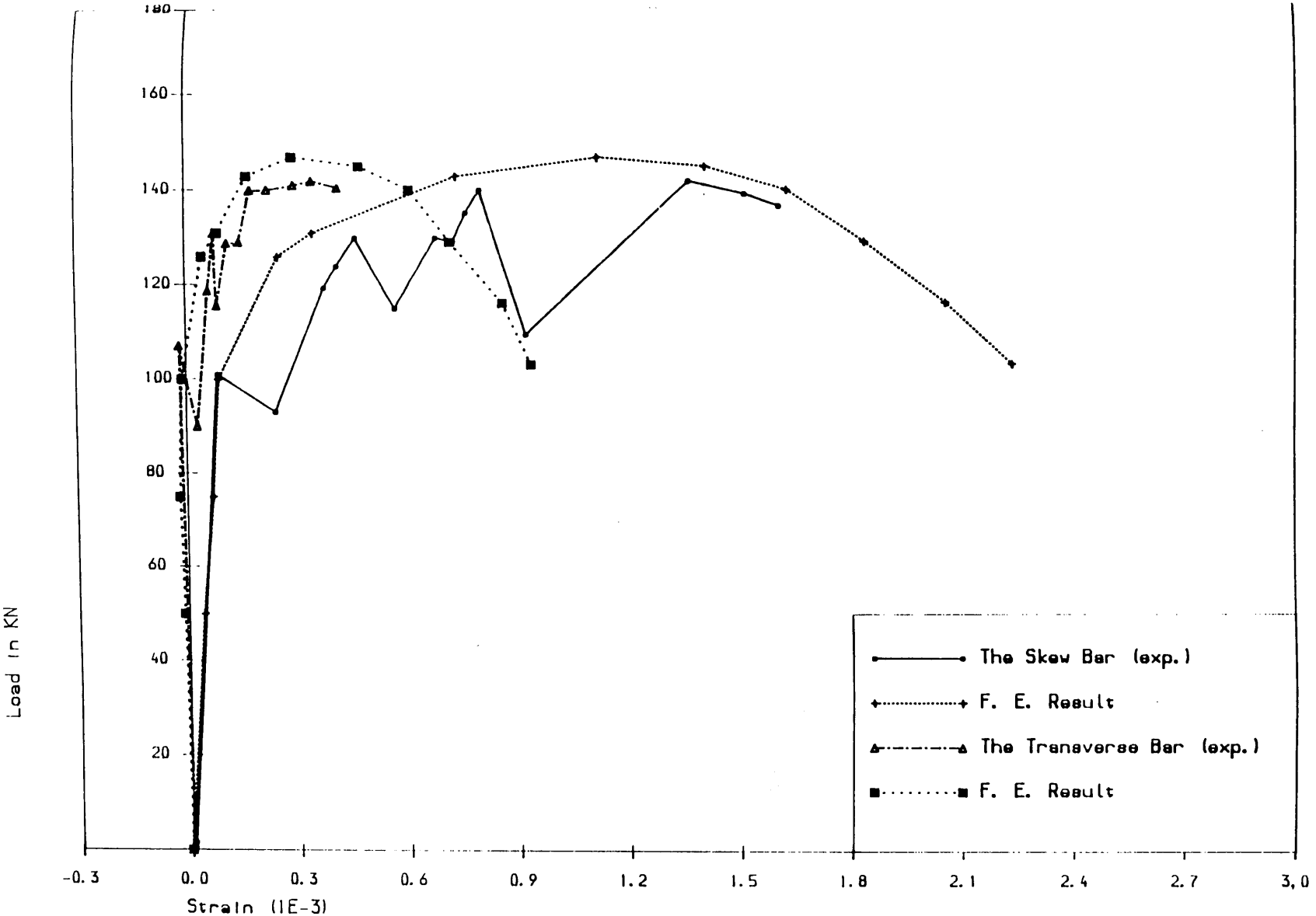

Fig.7.8(c) Load vs. Steel Strain (No.2)

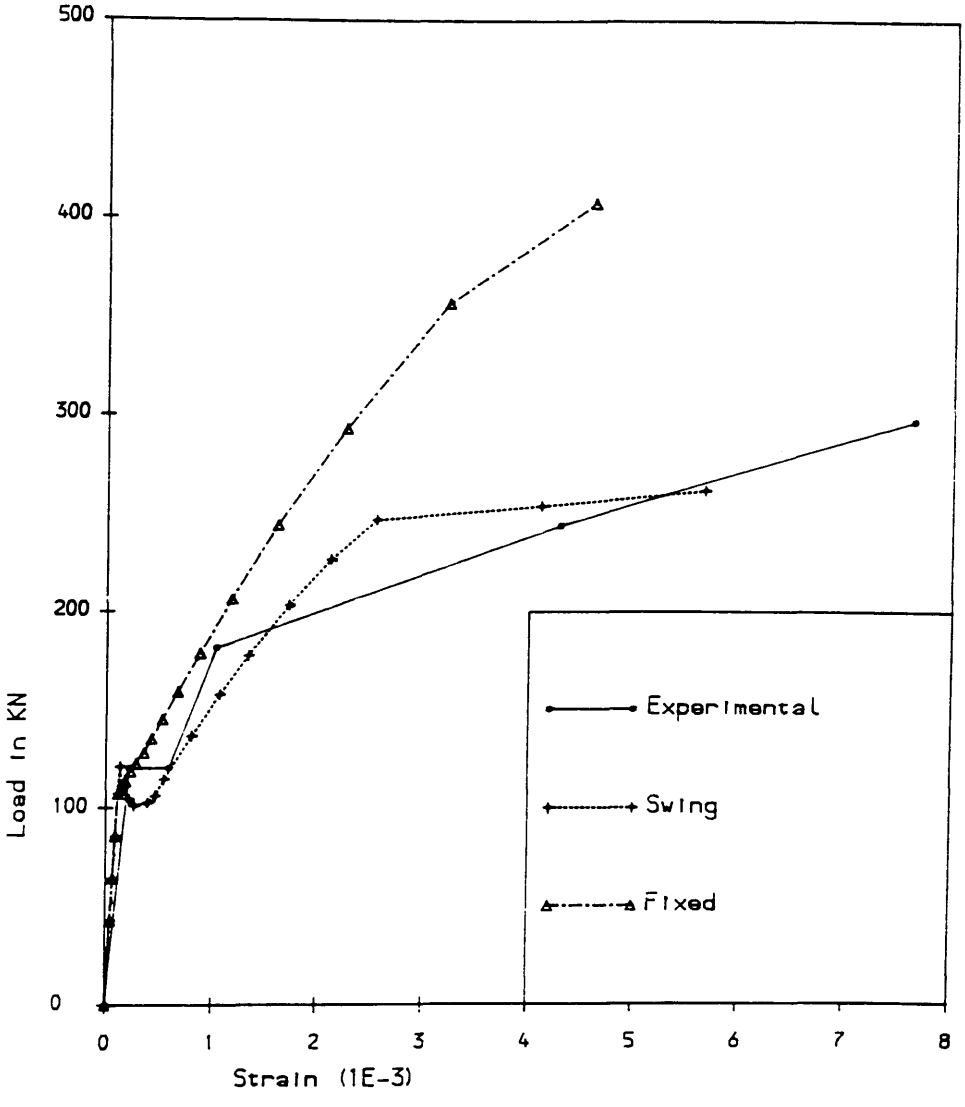

Fig.7.9(a) Load vs. Principal Strain (No.3)

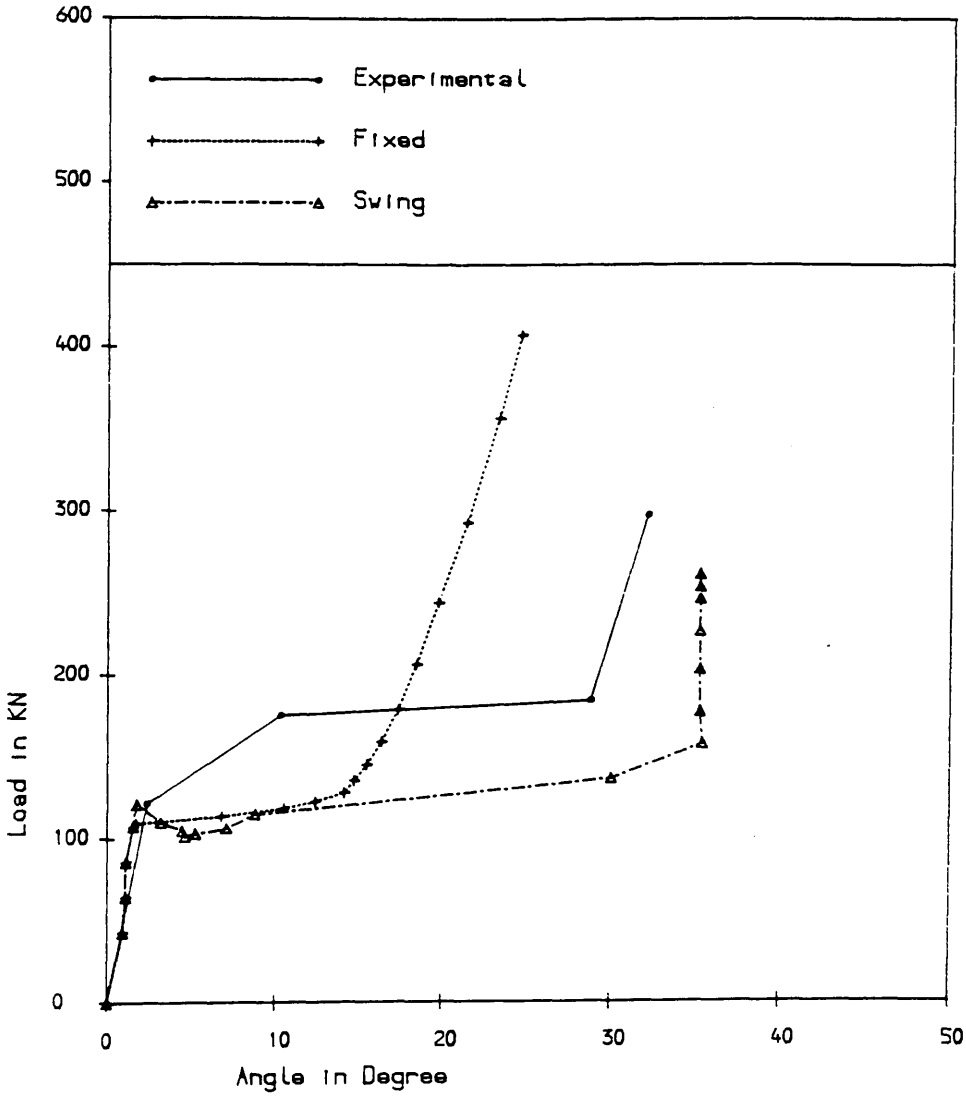

Fig.7.9(b) Load vs. Principal Strain Angle (No.3)

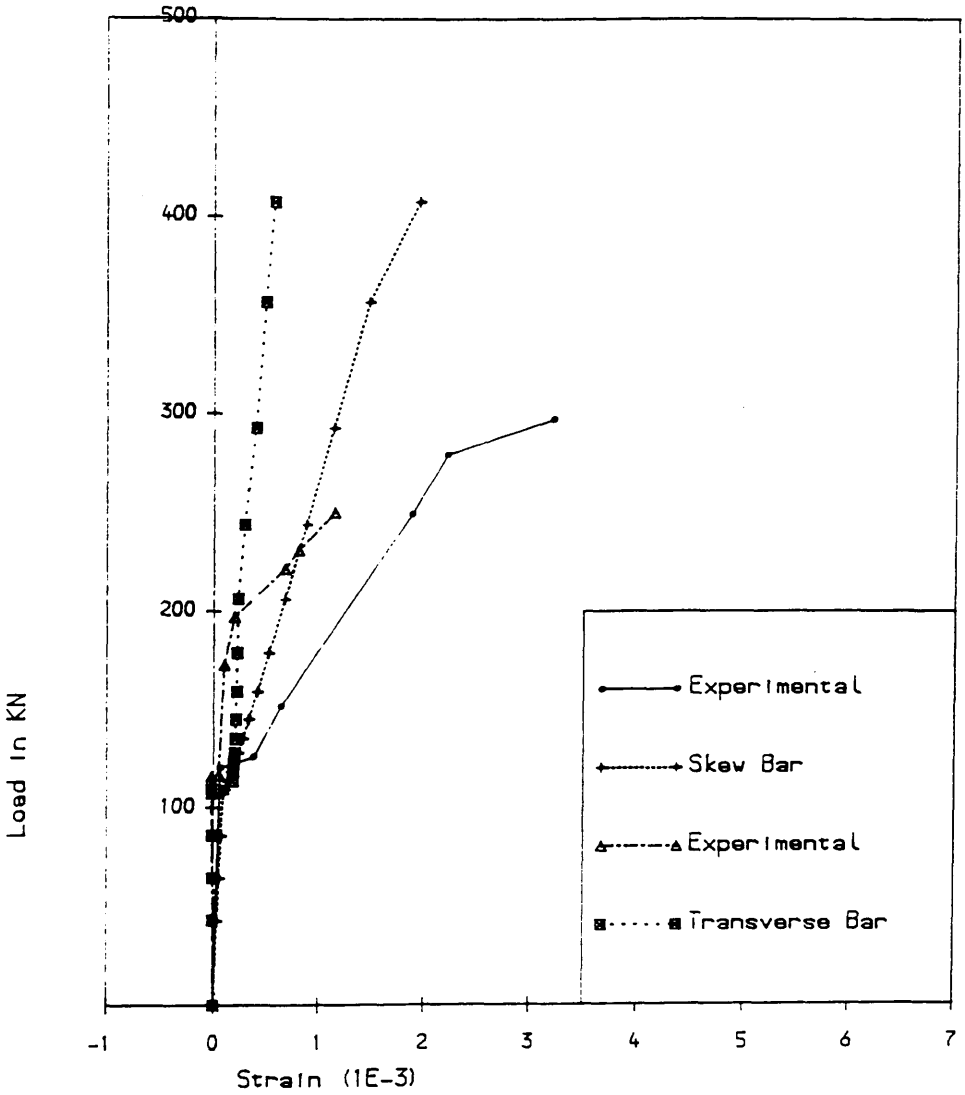

Fig.7.9(c) Load vs. Steel Strain (No.3)

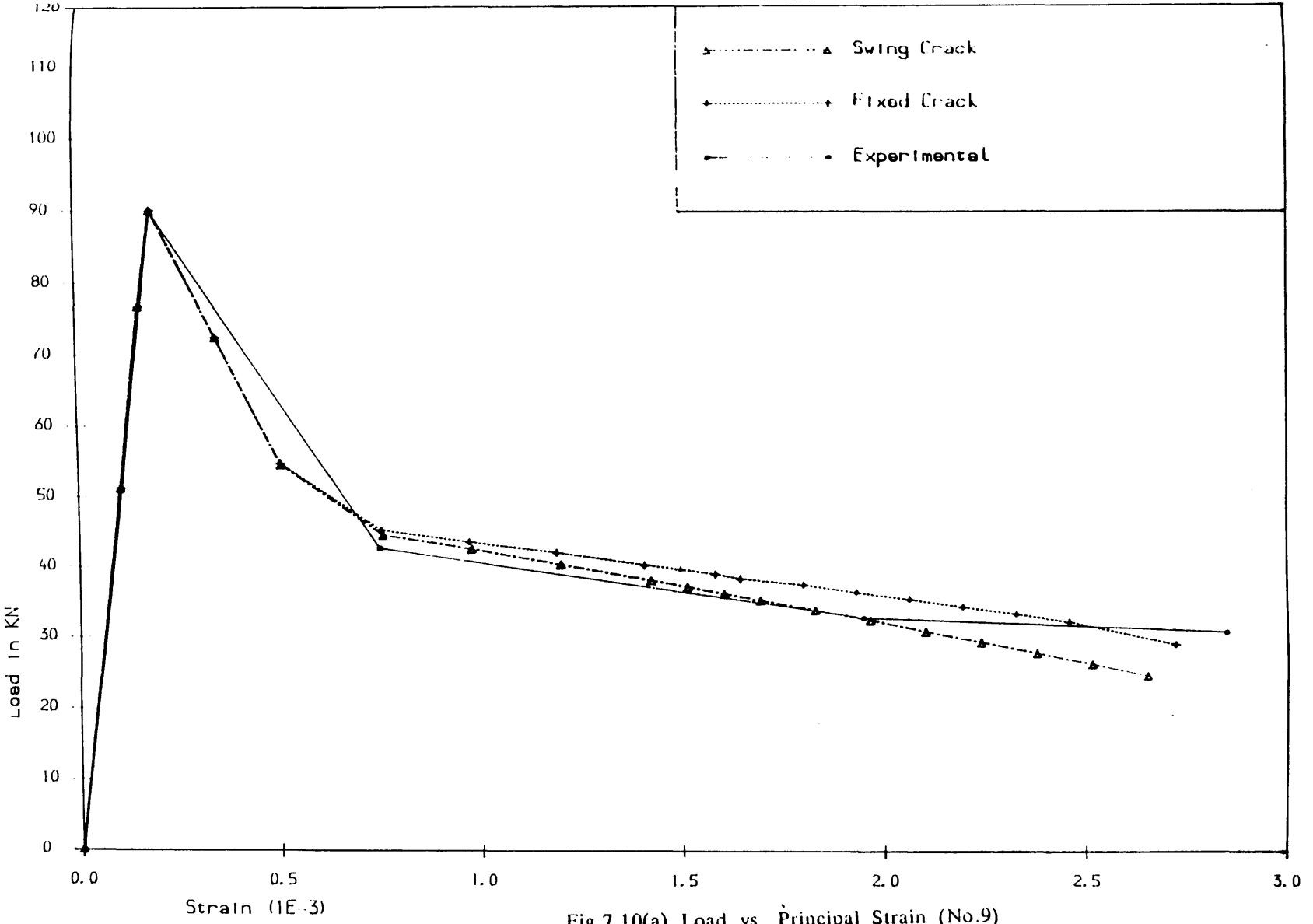

Fig.7.10(a) Load vs. Principal Strain (No.9)

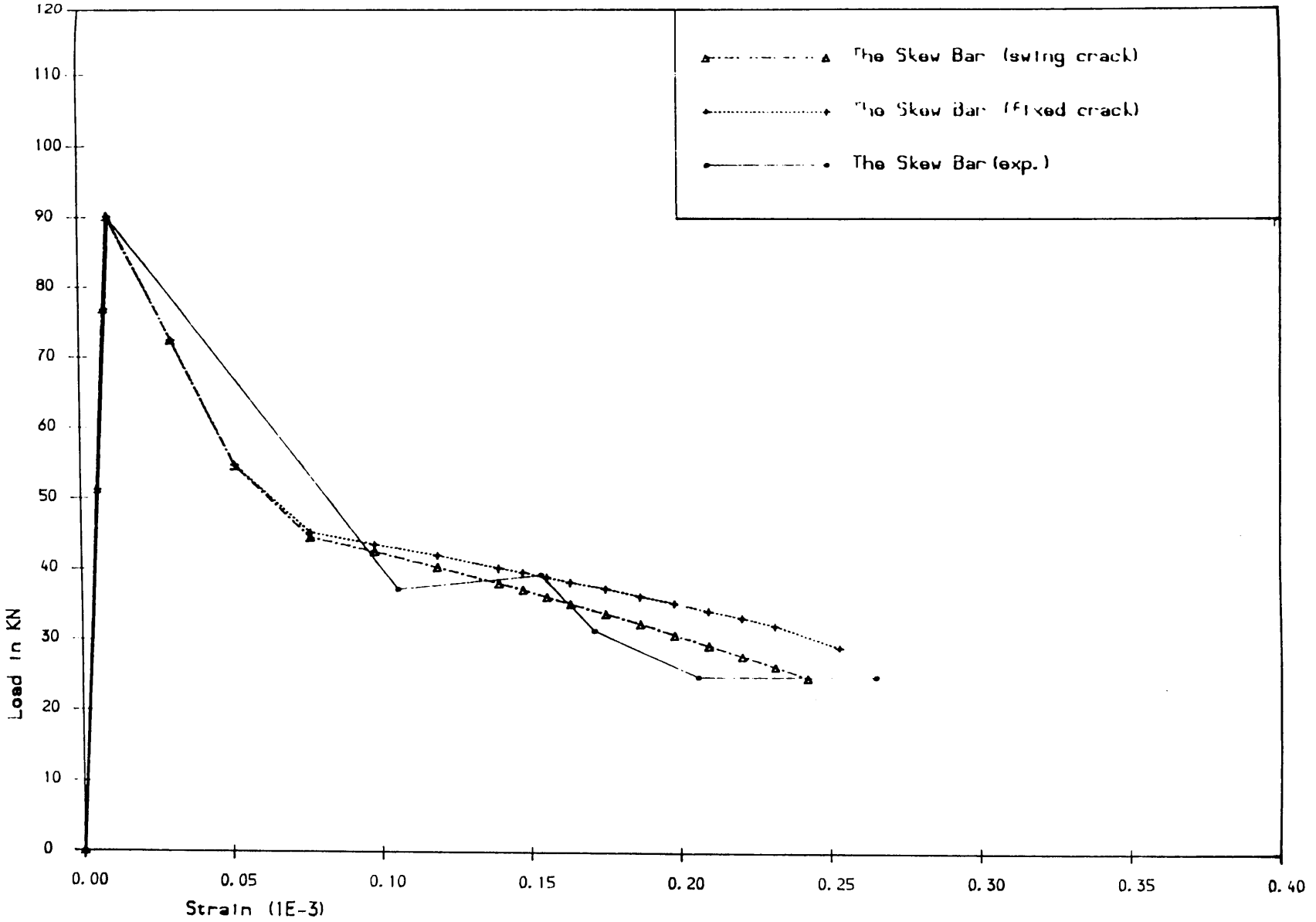

Fig.7.10(b) Load vs. Strain in Skew Bar (No.9)

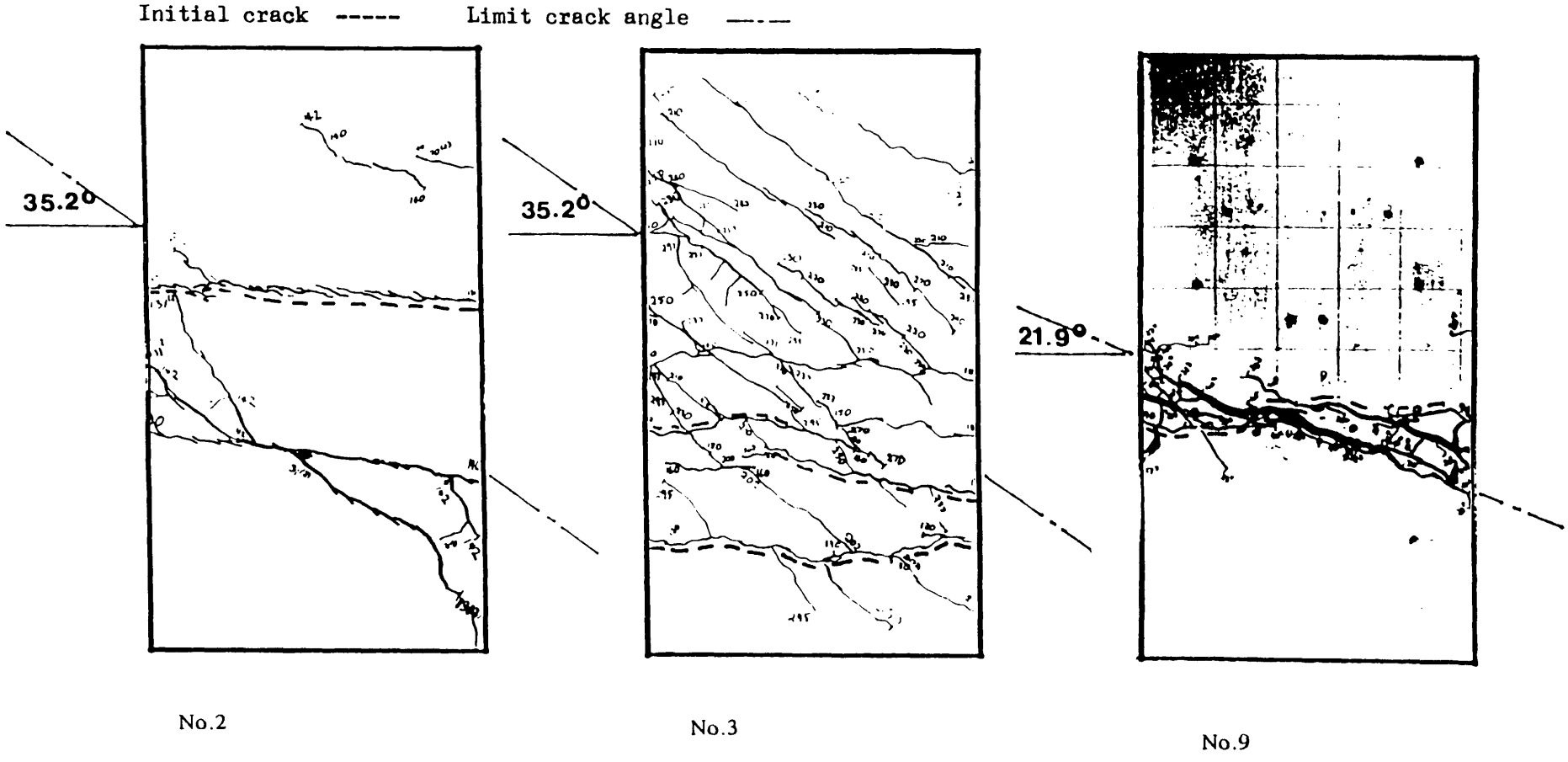

Fig.7.11(a) Experimental Crack Patterns

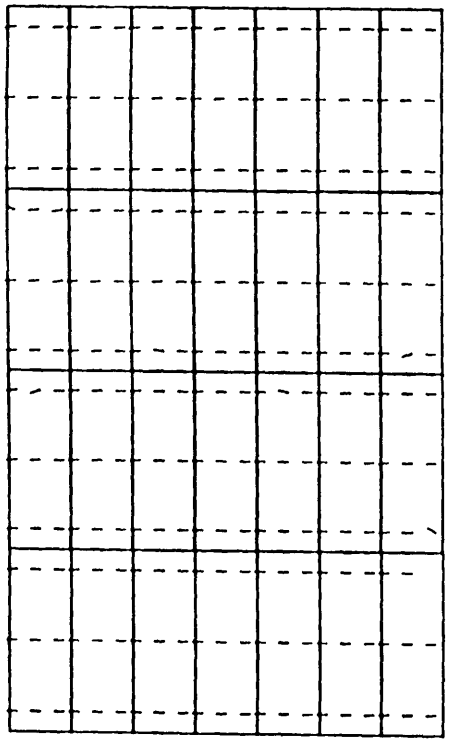

No.2

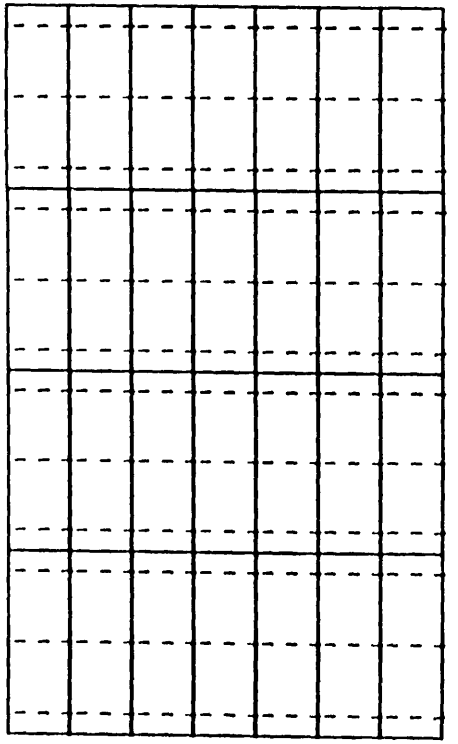

No.3

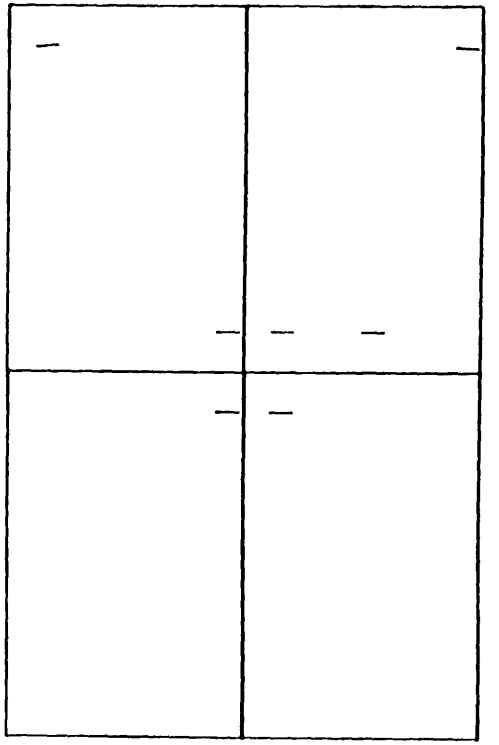

No.9

Fig.7.11(b) Numerical Crack Patterns (initial)

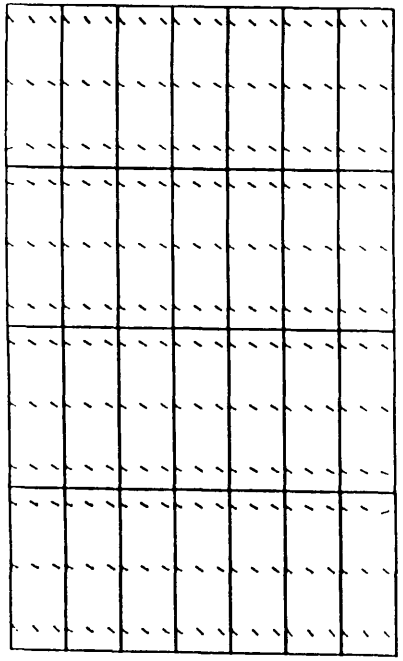

No.2

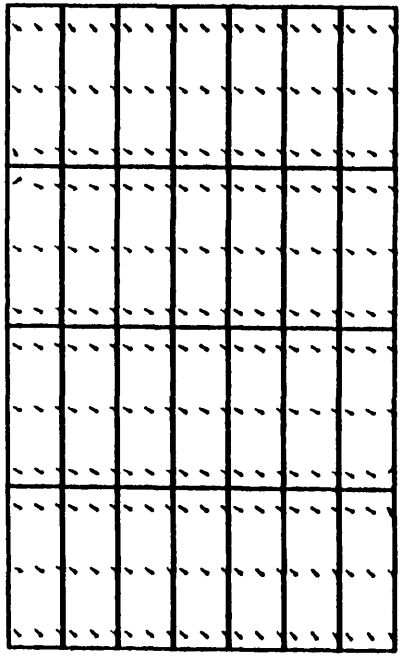

No.3

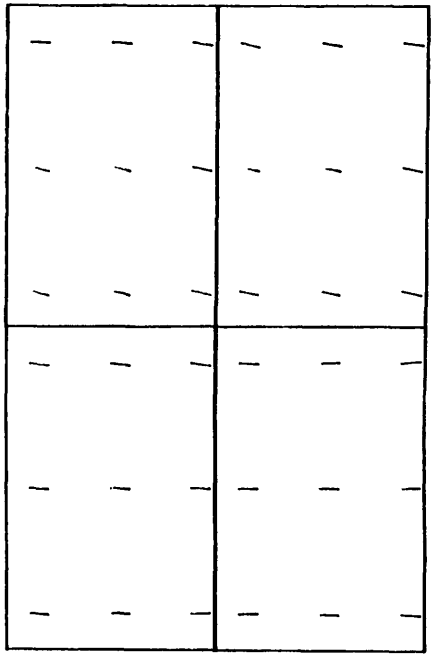

No.9

Fig.7.11(c) Numerical Crack Patterns (final)

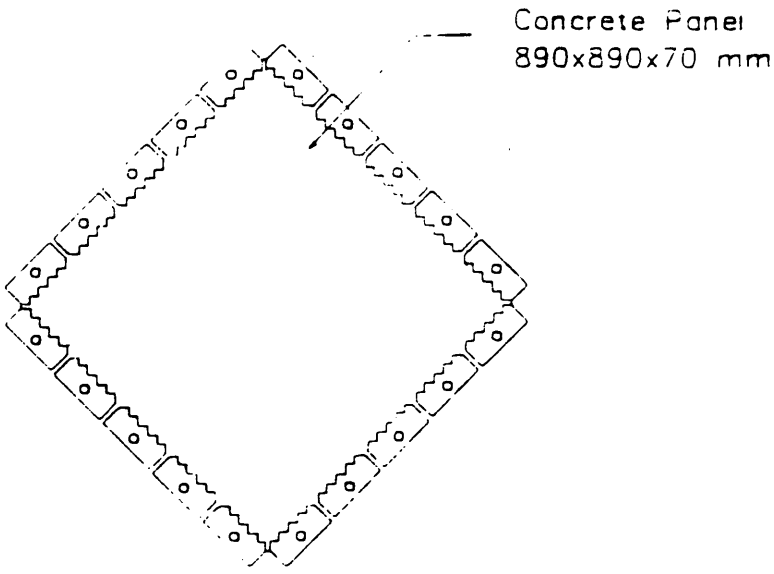

Fig.7.12 Collins' Panel

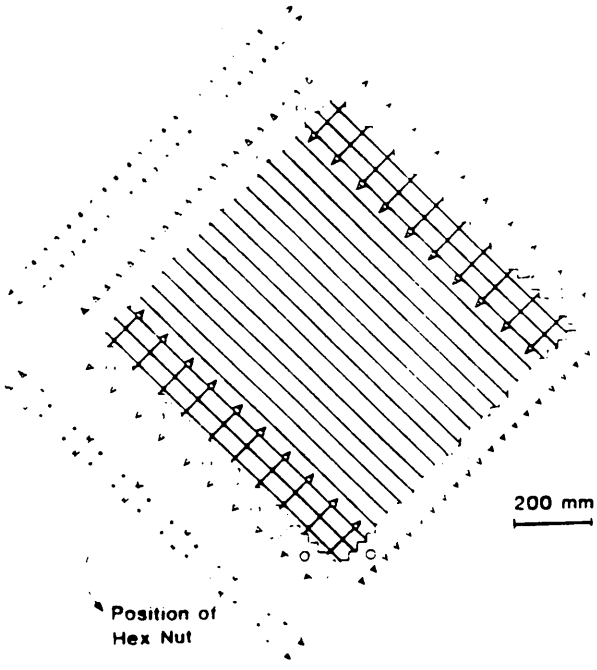

Fig.7.13 Reinforcement Layout

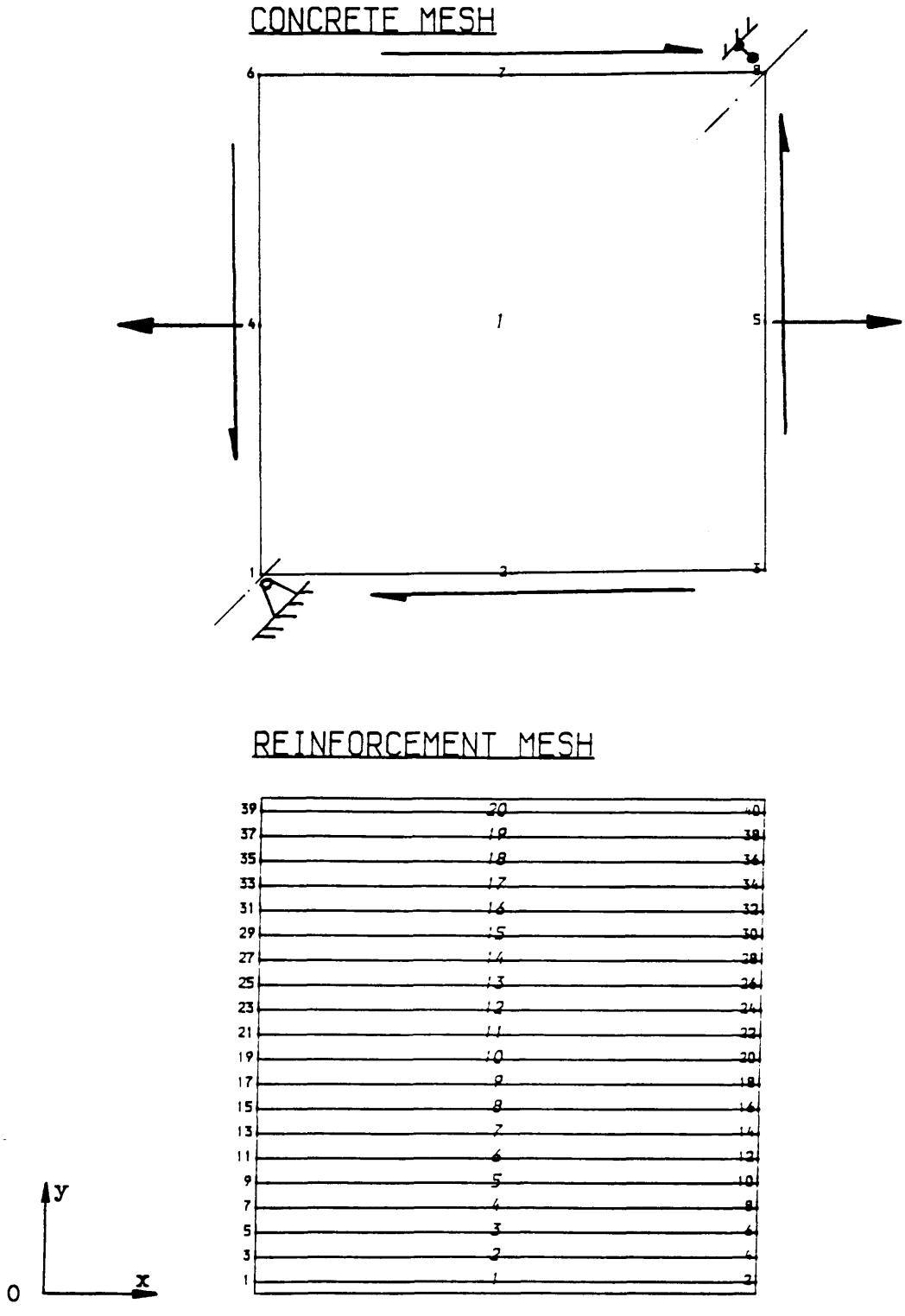

Fig.7.14 Meshes

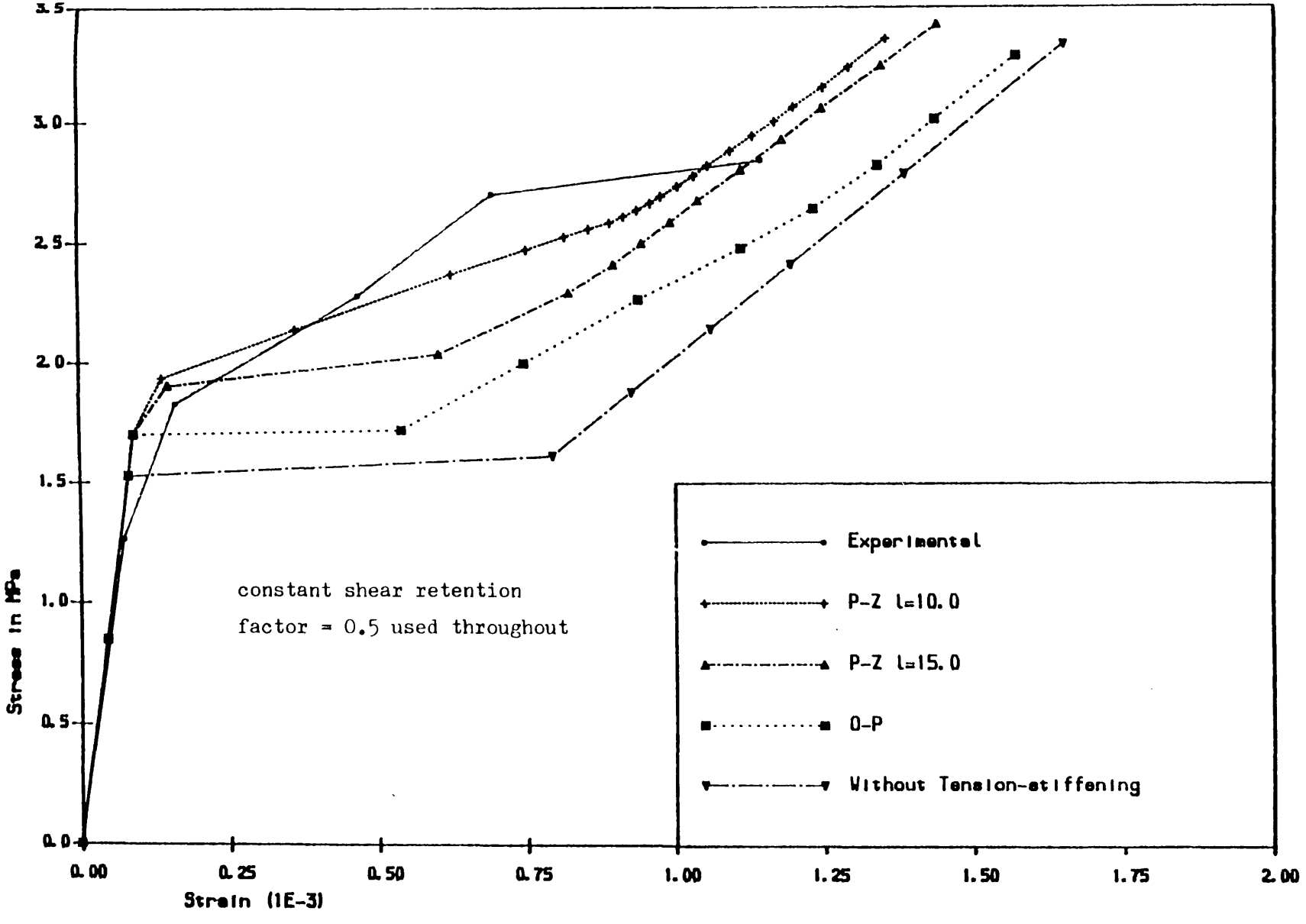

Fig.7.15(a) Tension Stress vs. Strain in x− Direction

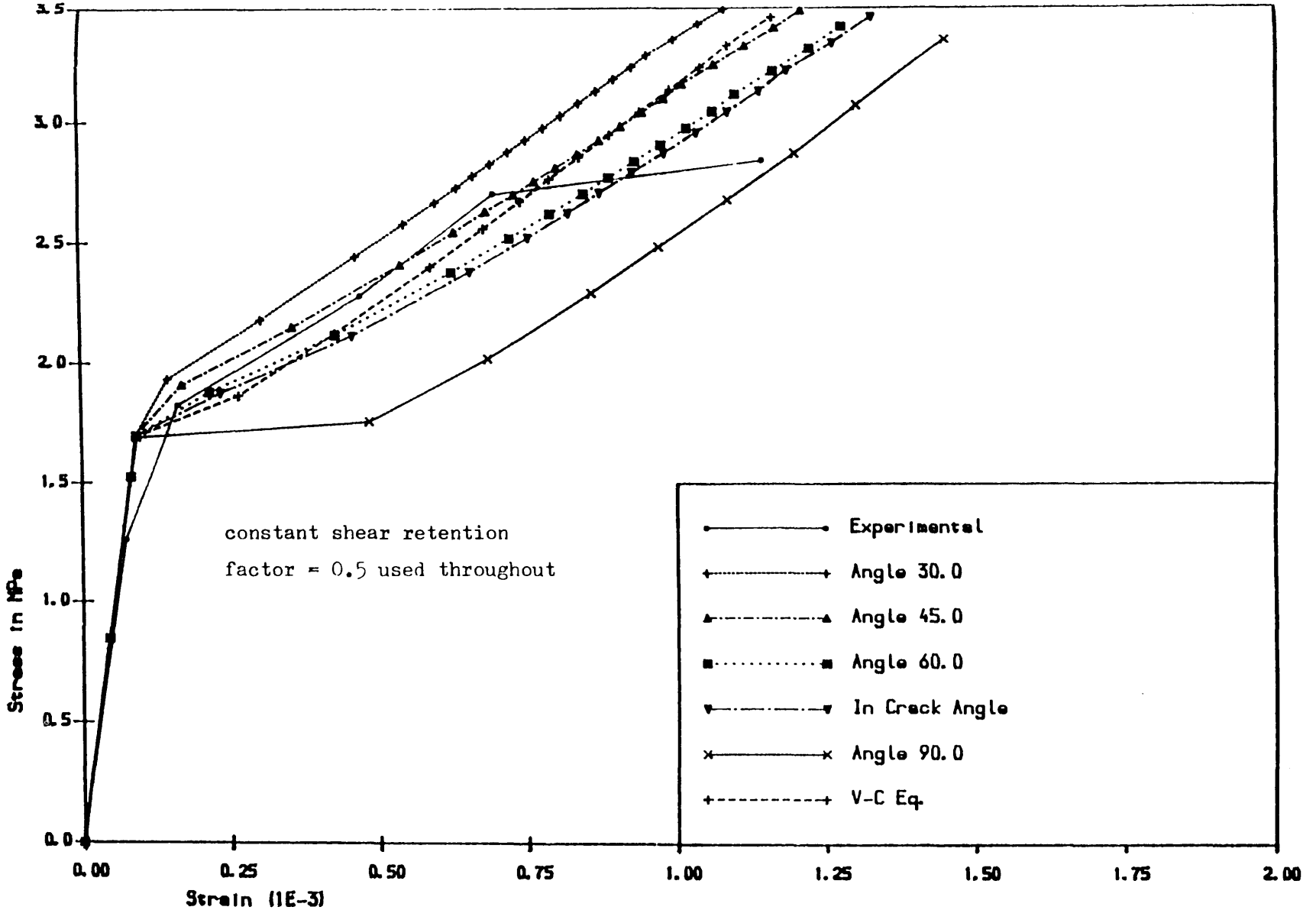

Fig.7.15(b) Tension Stress vs. Strain in x– Direction – – continued

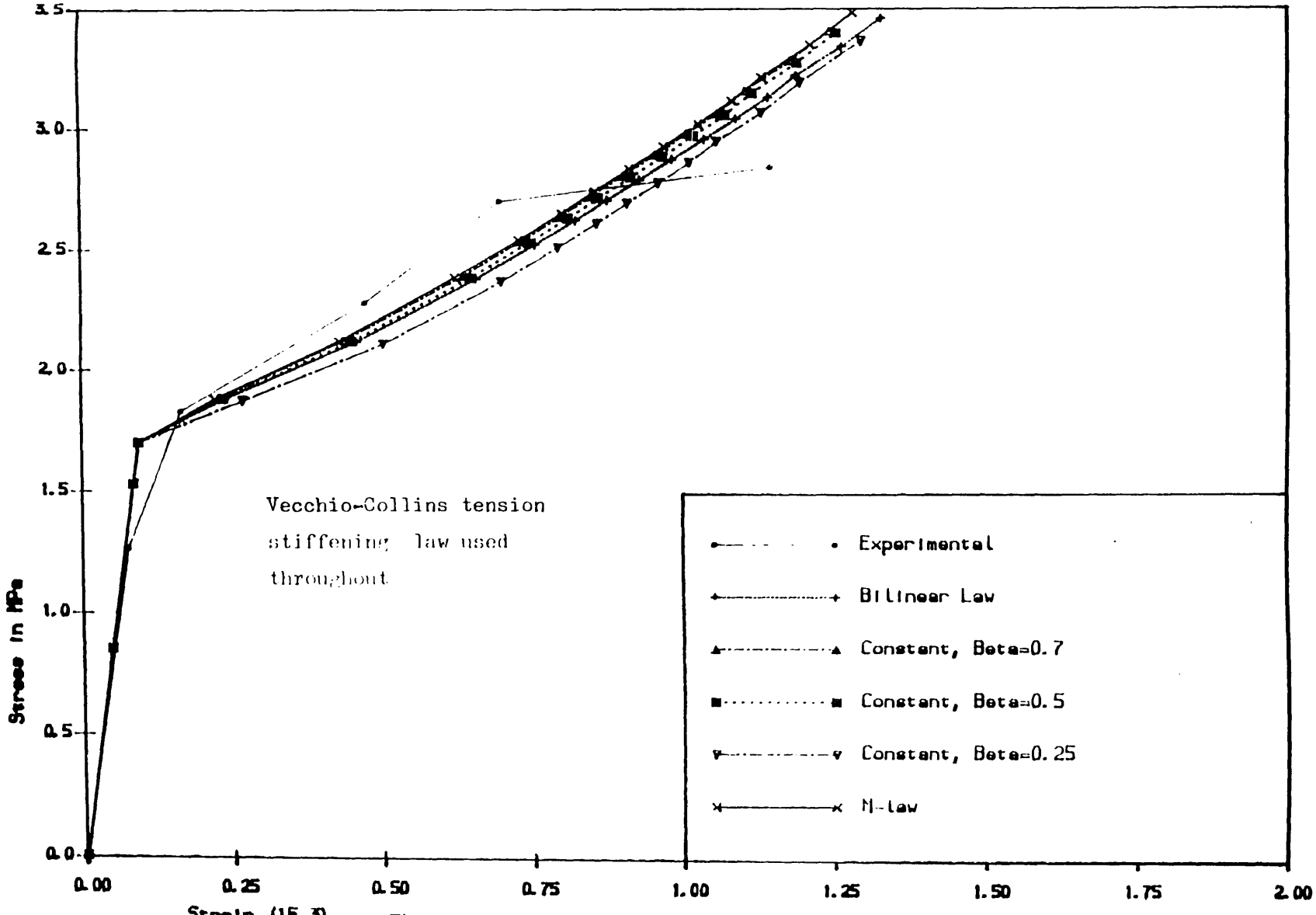

Fig.7.15(c) Tension Stress vs. Strain in x− Direction −− continued

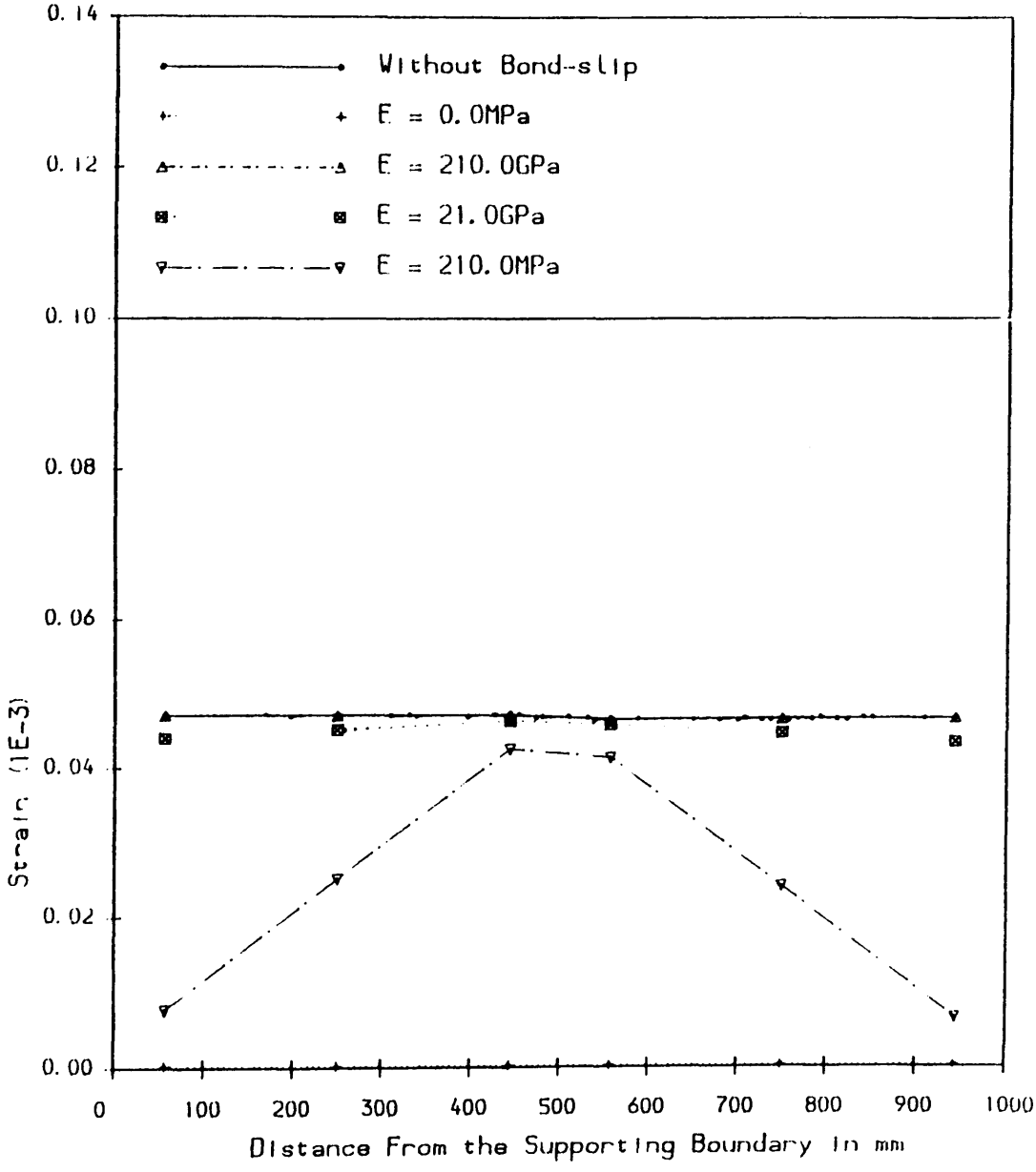

Fig.7.16(a) Steel Strain Variation

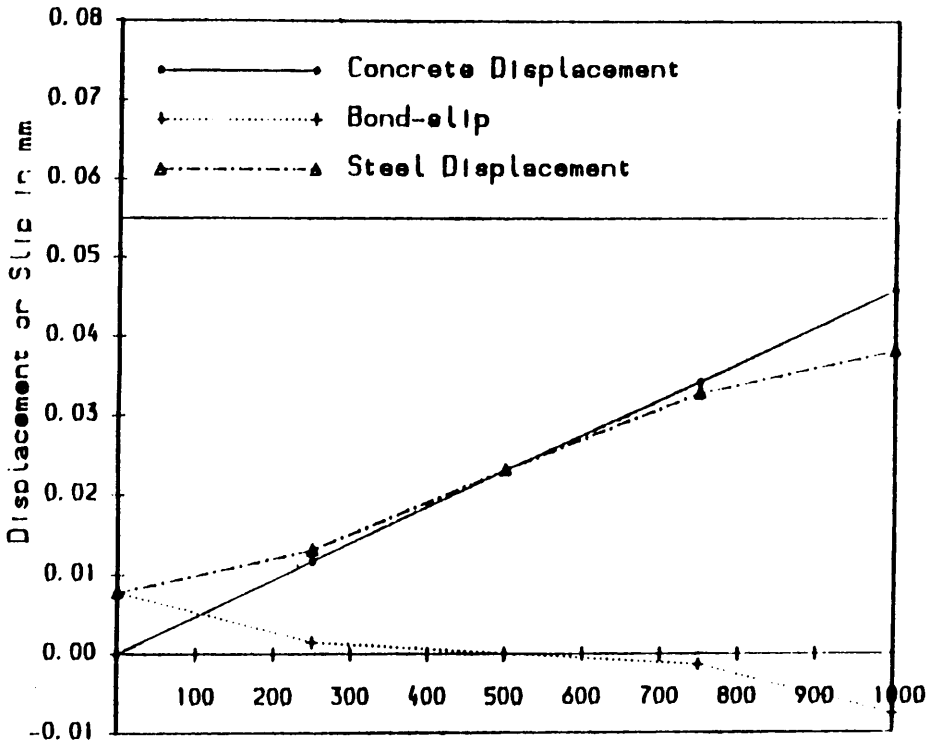

Fig. 7. 16 (b) Displacement and Slip Variation

Fig.7.16(b) Deformation And Slip

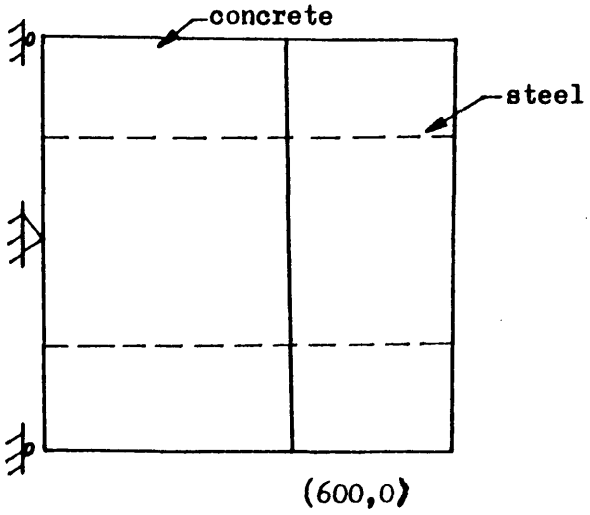

(a)

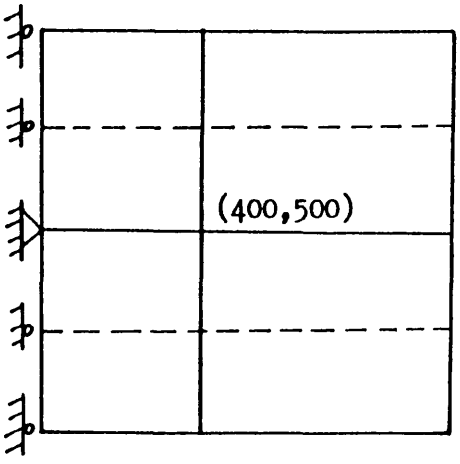

(b)

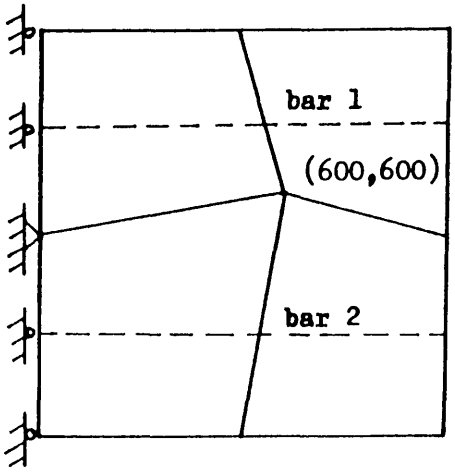

(c)

Fig.7.16(c) Meshes

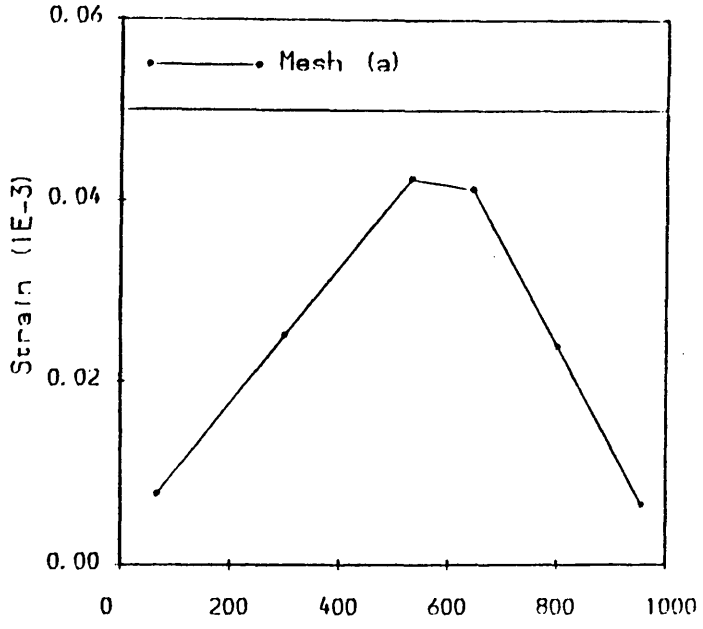

Distanoe From the Supporting Boundary in mm

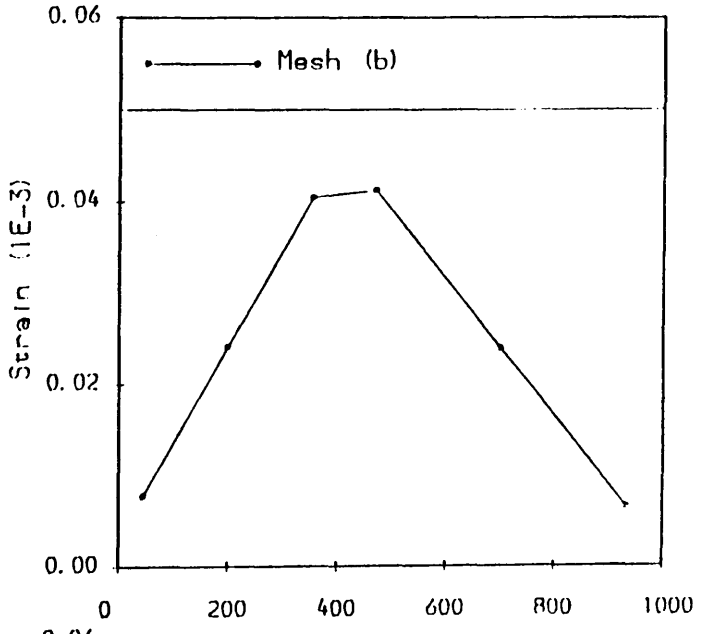

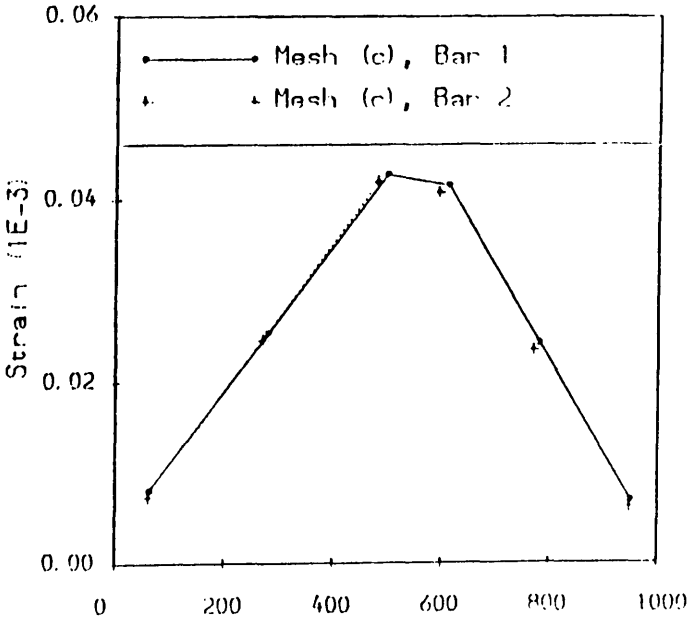

Fig.7.16(d) Steel Strain Distribution

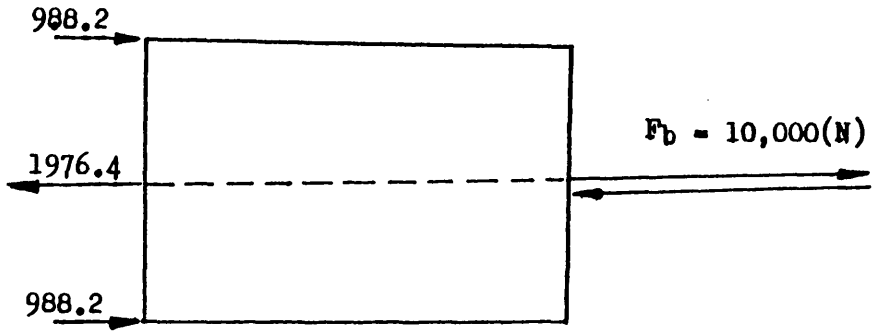

(i) Force and Reaction (N)

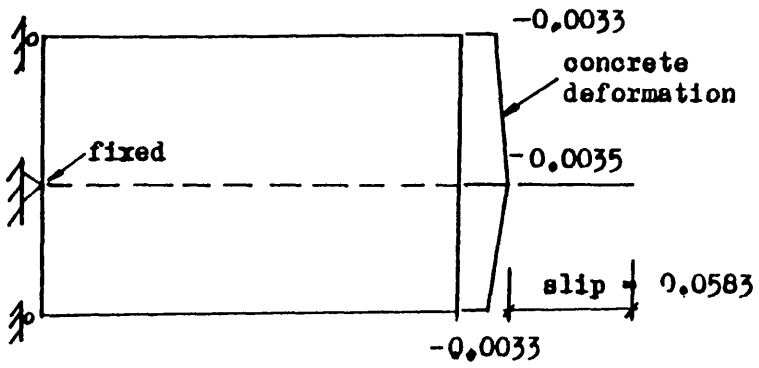

(ii) Deformation (mm)

Fig.7.16(e) Loaded Bond With fixed Steel End

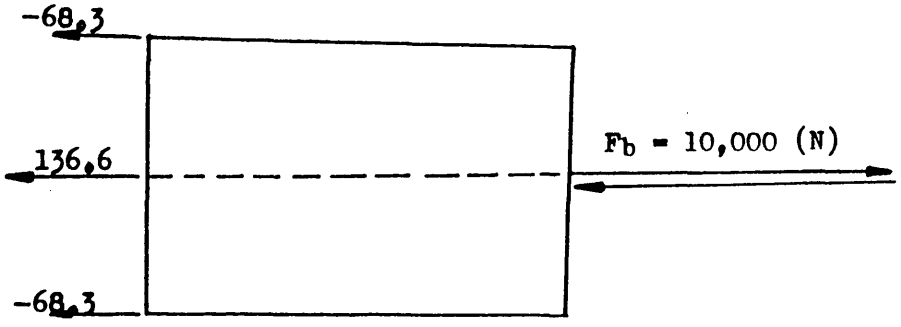

(i) Force and Reaction (N)

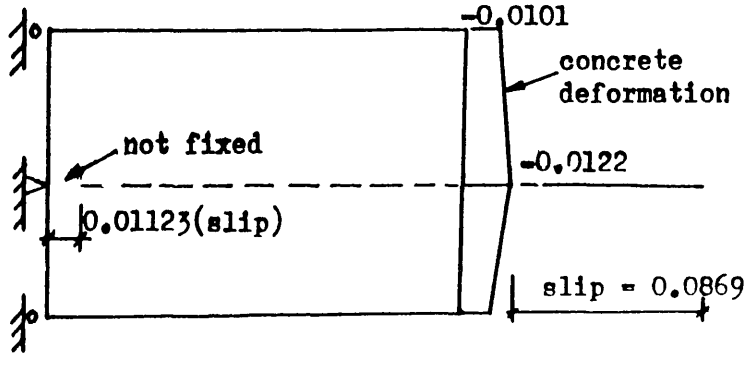

(ii) Deformation (mm)

Fig.7.16(f) Loaded Bond With Not Fixed Steel End

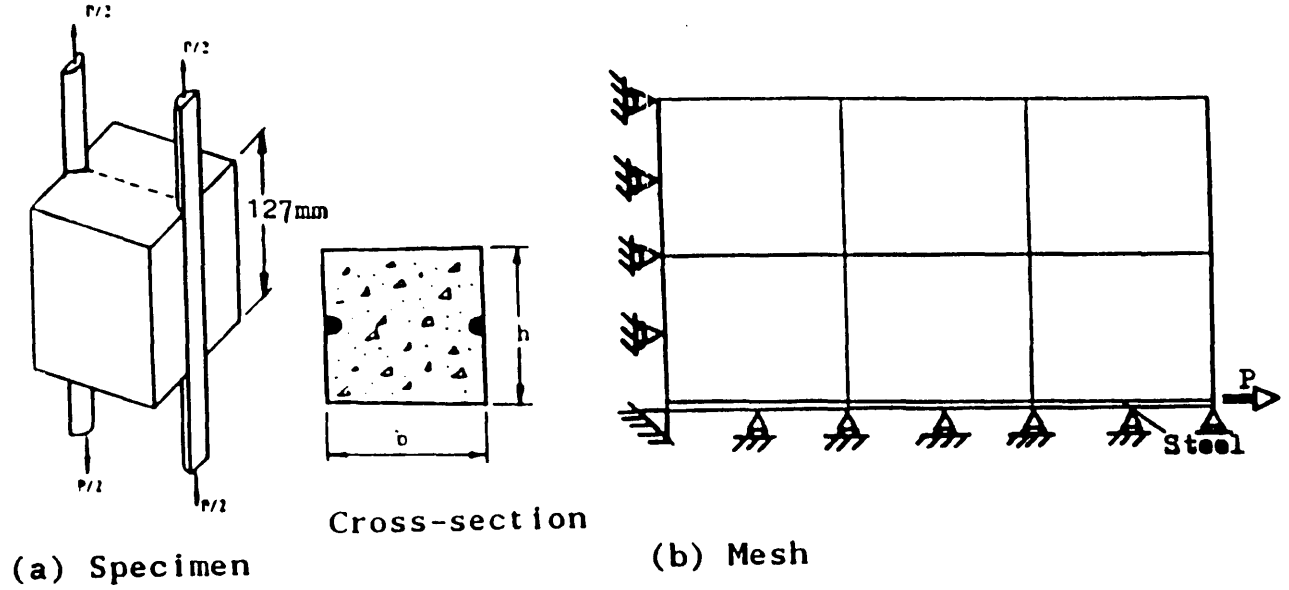

Fig.7.17 Details of Pull– out Test

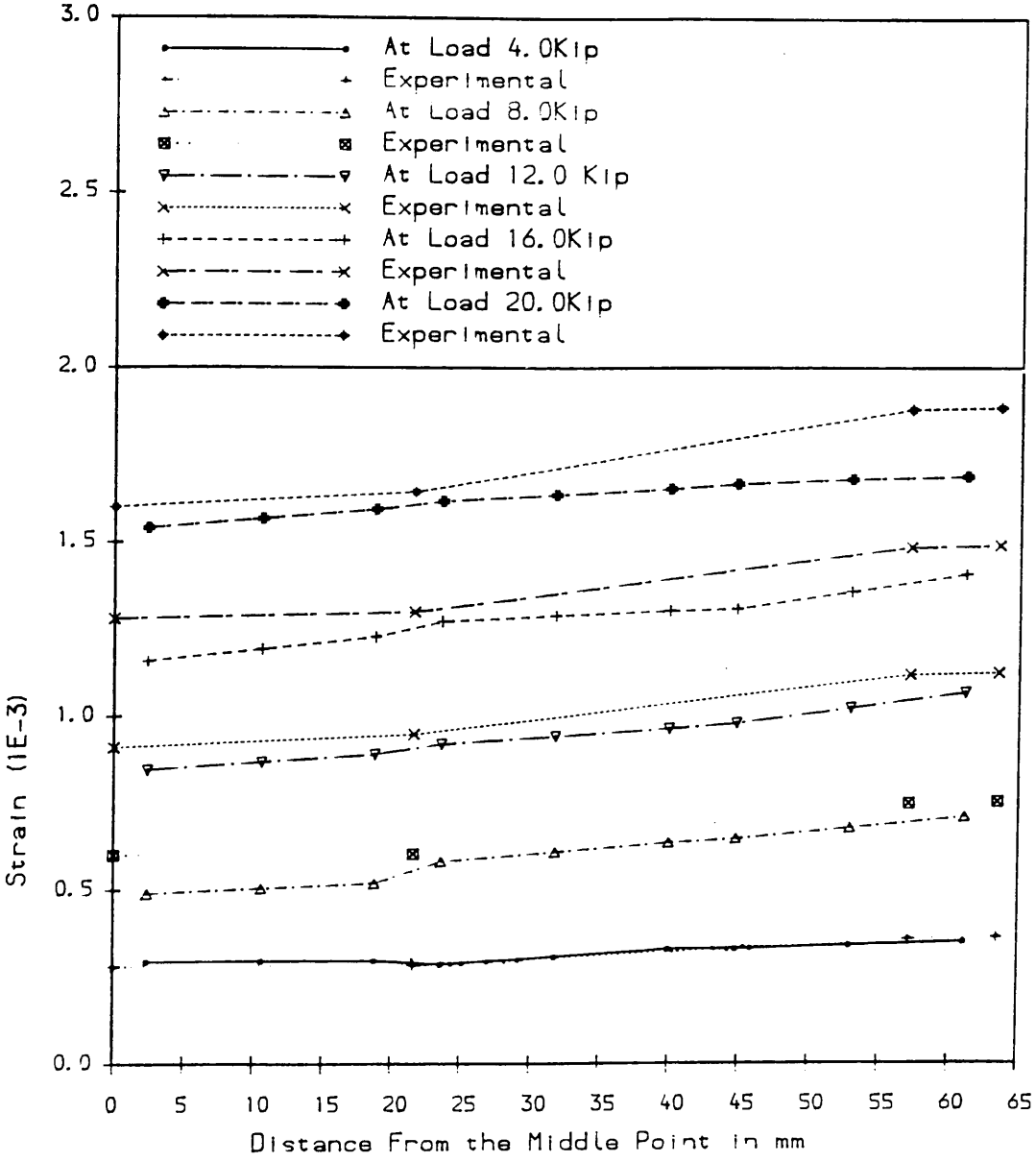

Fig.7.18(a) Steel Strain Distribution: E_b = 21,000.0(MPa)

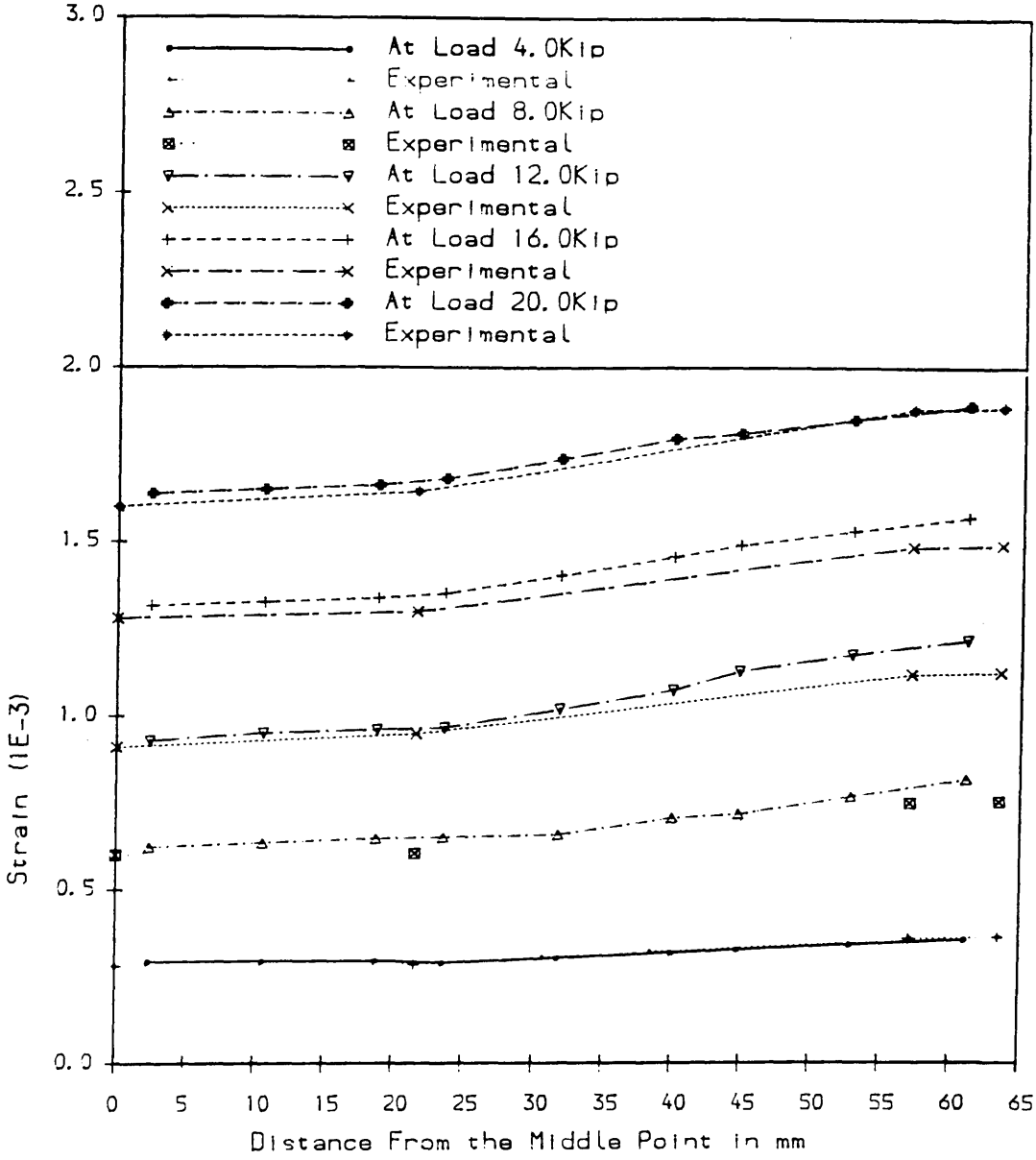

Fig.7.18(b) Steel Strain Distribution: Law One

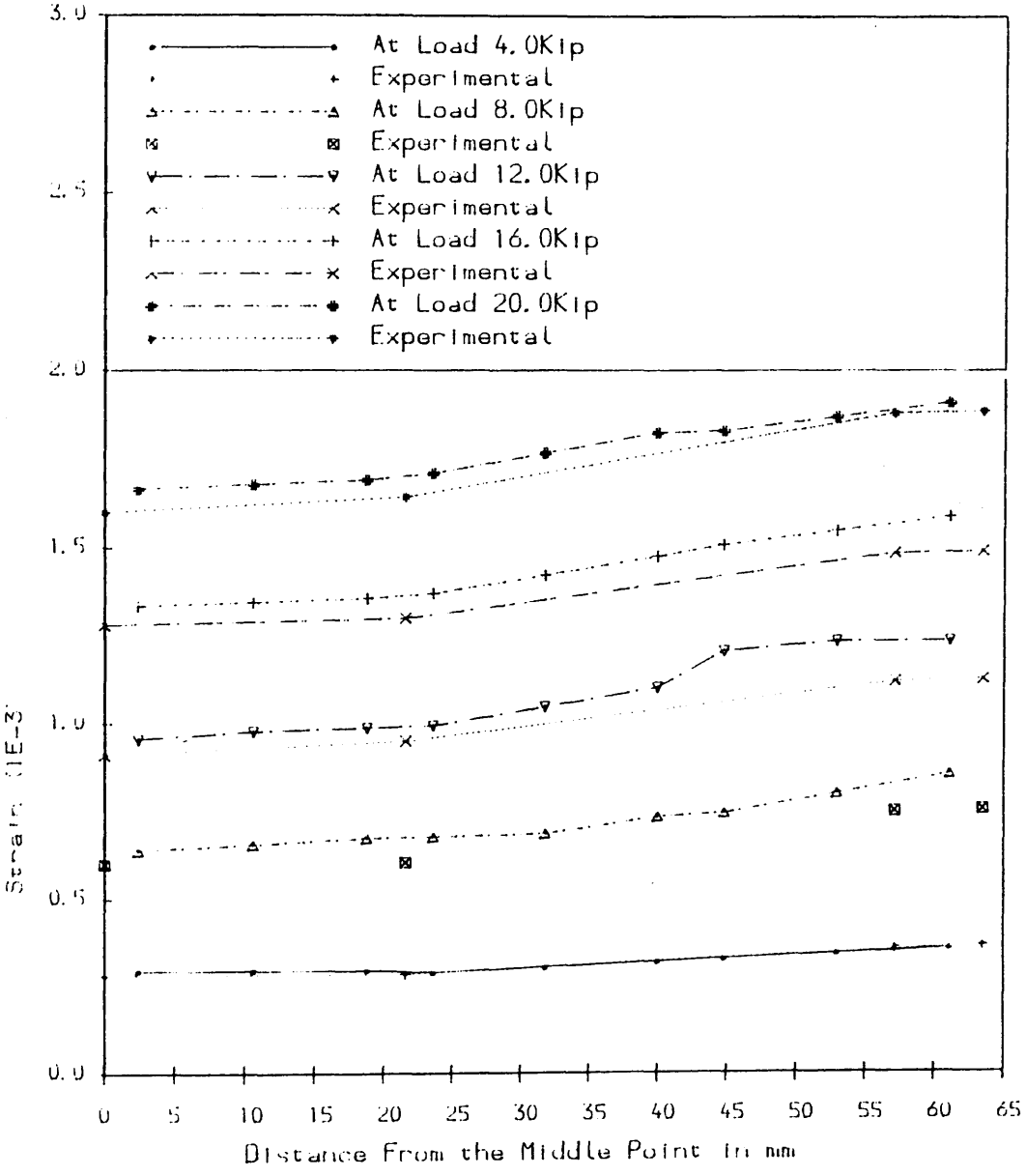

Fig.7.18(c) Steel Strain Distribution: Law Two

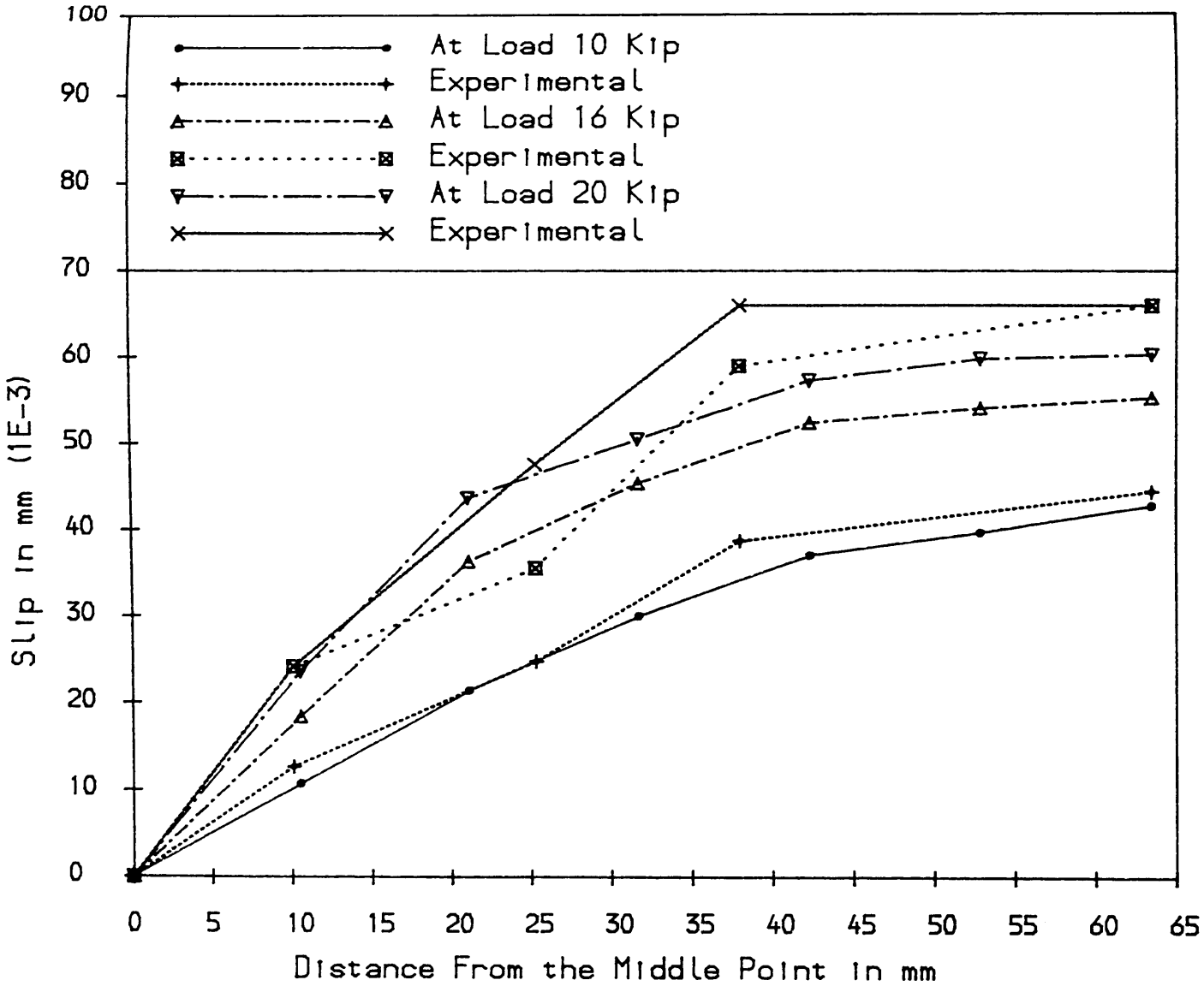

Fig. 7.18(d) Local Bond-slip (A2)

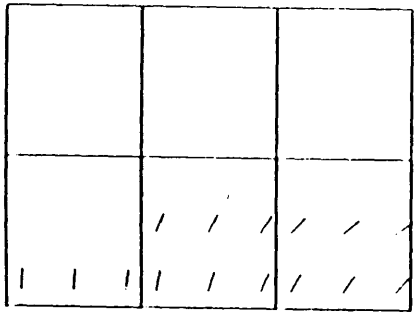

P = 8Kip

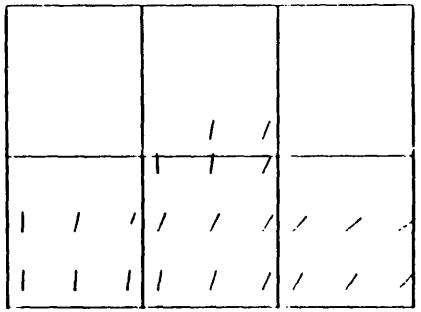

P = 12Kip

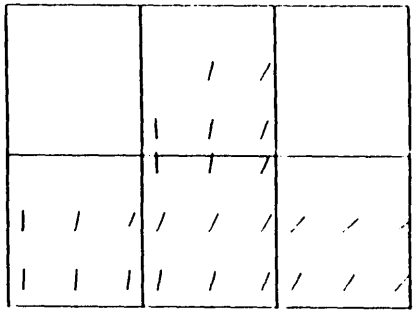

P= 16Kip

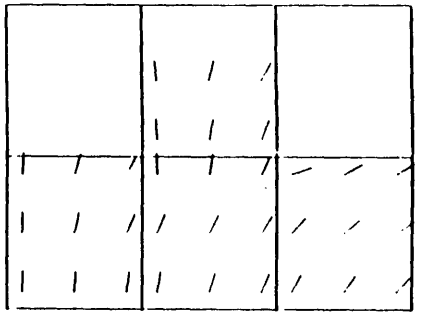

P= 20Kip

Fig.7.19 Crack Pattern

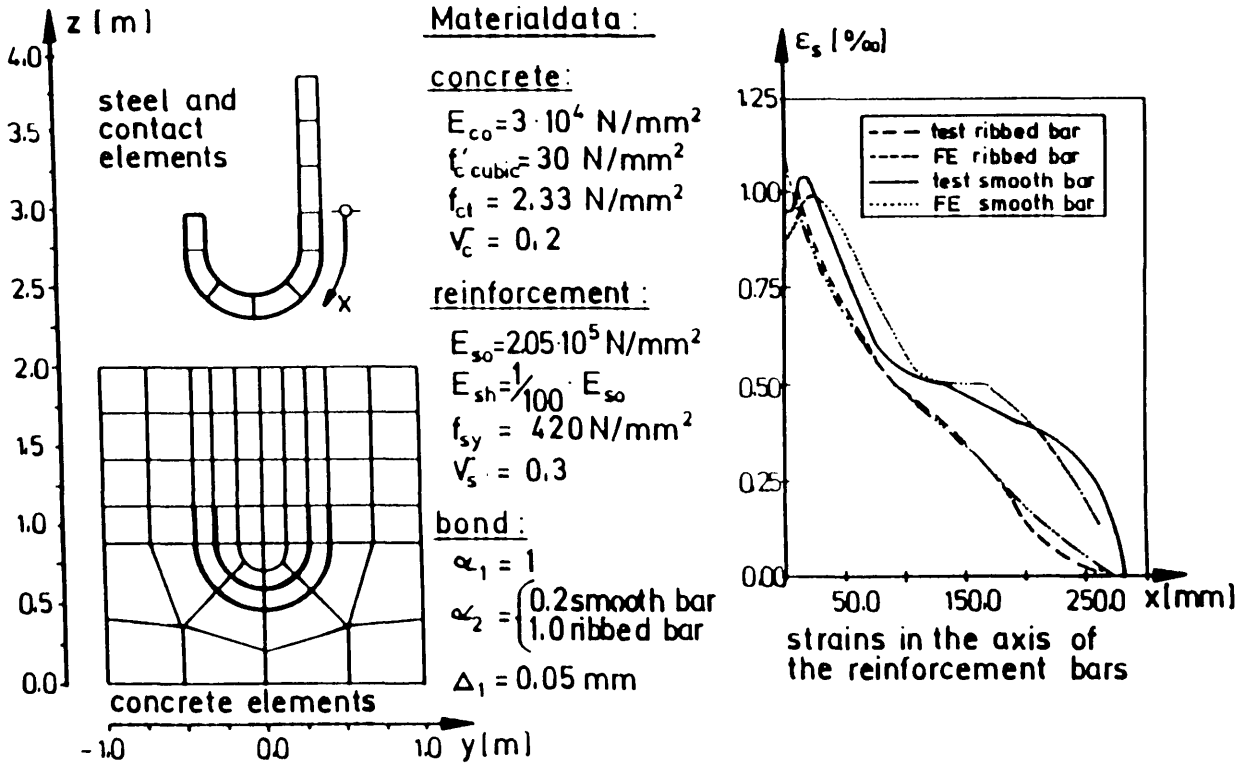

Fig.7.20 An Investigation on Transfer Test (Mehlhorn and Keuser 1985)

CONCRETE MESH

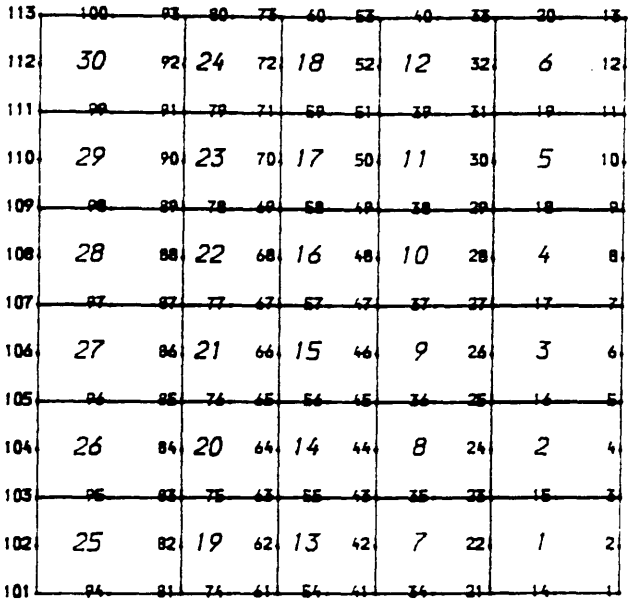

REINFORCEMENT MESH

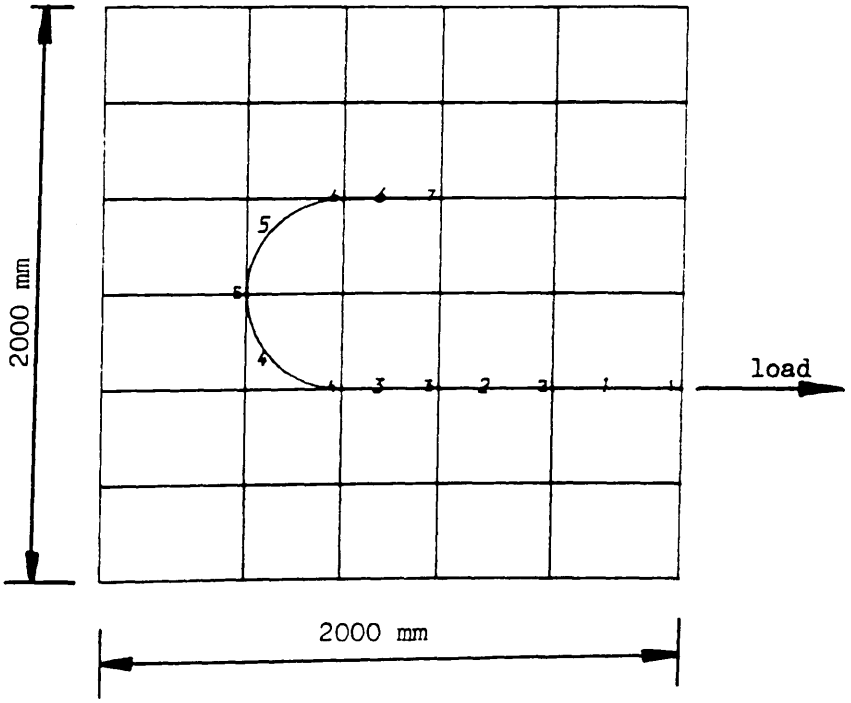

Fig.7.21 Meshes

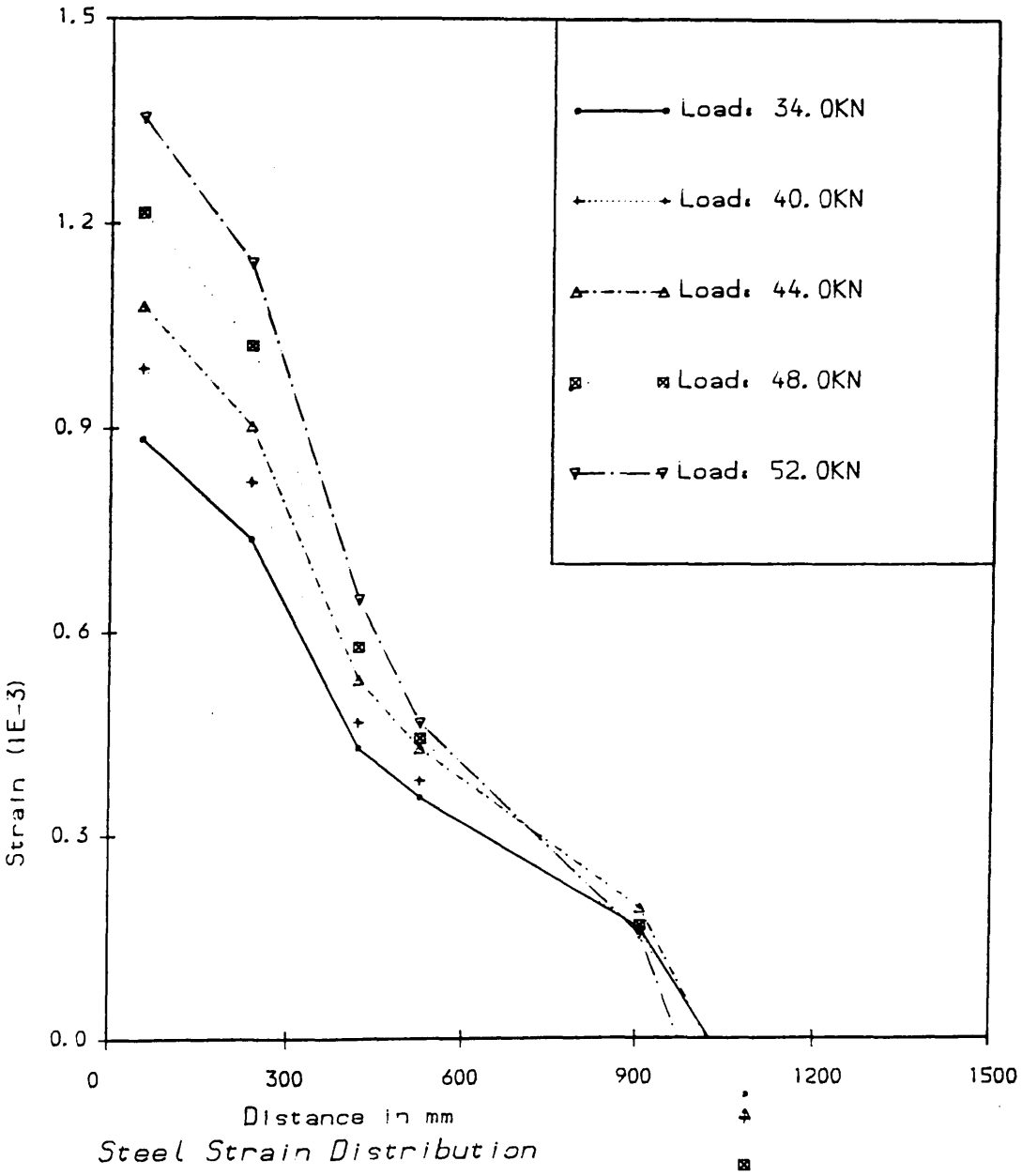

Fig.7.22 Transfer Test: F. E. Results

CHAPTER EIGHT

APPLICATIONS TO REINFORCED CONCRETE DEEP BEAMS AND BEAM–COLUMN JUNCTIONS

8.1 Introduction

In this Chapter, application to some reinforced concrete structures are made. In particular, two perforated deep beams and two beam–column junctions were analysed. These examples were selected because they exhibited various features which would test the potential and capability of the embedded reinforcement, bond models and crack models in more realistic situations. In all the following analyses, a uniaxial elastic–plastic law with linear work hardening was used for steel. Maximum principal stress criterion was employed for detecting initial crack formation.

8.2 Perforated Deep Beams

In this section, two deep beams with openings are presented. The numerical investigation was carried out for two reasons. Firstly, the deep beam is one of the most frequently employed members in modern construction having useful applications in a variety of structures, for instance, departmental stores, hotels, municipal buildings and so on. However, the behaviour of such members is still not fully understood, particularly if they contain web openings. Indeed, perforated deep beams are still not yet covered by major design codes of practice. It is well known that stress concentrations exist at the corner of openings, which obviously effect the loading–carrying capability. It is of interest to see if the behaviour can be improved by arranging skew reinforcement at the corner.

Secondly, in either experimental or engineering design, regions around the supports and loading points are usually provided with more dense reinforcement in order to contain the high load stresses and bursting stresses. These regions can be strengthened in finite element analysis by using a higher concrete compressive strength. However, the scale of the increase is usually made by assumption and by analytical experience. There is no rational approach to define how much the increase needs to be. The amount of increase for concrete compressive strength is crucial if the supports control the failure mode of the structure together with the yielding of steel. In this study, the general embedded bar model has been used to take the dense reinforcement into account.

8.2.1 Beam One

Specimen and Dimensions

The selected specimen was B3 taken from the experimental study conducted by Memon in 1982[G. H. Memon 1982]. The beam had an overall depth of 1000mm, thickness of 100mm and span length of 950mm, giving span to depth ratios of 0.95. It was perforated by a central rectangular opening. Two symmetrical increasing point loads were applied on the top surface until failure occurred. Details and dimensions of the beam are shown in Fig.8.1 in which

x_1 = 400 (mm) h_1 = 400 (mm)

x_2 = 625 (mm) h_2 = 300 (mm)

D = 1000 (mm) L = 950 (mm)

Shear span to depth ratio a/D = 0.32

Clear shear span to depth ratio x/D = 0.22

The arrangement of reinforcement is shown in Fig.8.2. $E_h = 0.1\ E_s$ is assumed.

Material Properties

Concrete:

$f_{cu} = 38.2\ N/mm^2$ $f_c' = 29.8\ N/mm^2$

$f_t = 2.85\ N/mm^2$ $E_c = 22.92\ kN/mm^2$

Steel properties are given in Table 8.1 and E_h is assumed $0.1E_s$.

The adopted solution scheme was Newton–Raphson method under displacement control. The rotating crack model was used with Bhide–Collins' tension stiffening law and Melhorn's shear retention model. Full bond was assumed.

Meshes for Concrete and Reinforcement

Due to the symmetry of the structure and loading, only half of the beam was analysed. For concrete, one mesh is used for all analyses but three different reinforcement meshes were considered shown in Fig.8.3. The first one simply models the longitudinal steel bars, local reinforcing at the loading and support points being ignored. The second one is exactly similar to the experimental layout of the bars. In the third mesh, two additional inclined 10mm Φ steel bars are included into the second reinforcement mesh at the corner of the opening. The three meshes are denoted by I, II and III.

Results

Numerical results are given in Fig.8.4 to Fig.8.7 along with experimental ones. For mesh II (i. e. reinforced supports), good correlation has been obtained for load–deflection, steel strains in the bars above the opening, as well as the crack patterns. Final failure was caused by crushing of concrete under the load, after yielding in the main reinforcement.

For the two other meshes (I and III) it can be seen that:

i) If the loading points and the supports are not reinforced with dense steel bars, failure is caused by crushing of concrete in this region. Also the steel strain increases at earlier stage (Fig.8.5) due to the more rapid deflection development (Fig.8.4). Therefore, un–reinforced supports can significantly effect the loading capacity of the structure and hence the local reinforcement needs to be taken into account in order to model the proper force transfer in this region. This is easily accomplished using the embedded formulation without having to resort to a finer concrete mesh in this region.

ii) For mesh III where a skew bar is located at each corner of the opening, at failure the concrete crushed at the loading points and also in the top corner of the hole. The top skew bar also prevented some cracking in this region. From the load–deflection curve and crack pattern, it can be seen the skew bars do not change overall structural behaviour very much, there being a small increase in strength of less than 4%. This is because the failure of the structure is not controlled by the stress concentrations around the corner of the opening. This is not too unexpected because the opening only slightly interrupts the primary load paths in the beam between the load points and supports.

8.2.2 Beam Two

Specimen and Dimensions

This example was taken from the experimental study of Khaskheli [Khaskheli 1989]. The dimensions and the reinforcement arrangement are shown in Fig.8.8 and Fig.8.9.

This beam was designed and tested to check the applicability of the "direct design" procedure[Khaskheli 1989] when web openings interrupt the load path in the shear spans. For the finite element analysis, it was the aim to examine the capability of the proposed modelling techniques in such engineering structures.

The specimen is a single–span perforated deep beam with two openings of 500mm x 500mm each in size. One was located below the mid–depth of the beam in one shear span, and another one was above the mid–depth of the girder in the other shear span. Two symmetrical point loads were applied on the top surface until failure occurred.

Span/depth ratio L/D = 1.40

Shear–span/depth ratio a/D = 0.40

Clear–shear span/depth ratio X/D = 0.35

Girder depth D = 2000.0 mm

Girder span L = 2800.0 mm

Girder thickness b = 100.0

Material Properties

Concrete:

f_{cu} = 57.0 N/mm^2 f_c' = 37.8 N/mm^2

f_t = 3.1 N/mm^2 E_c = 21.1 kN/mm^2

High yield deformed bars of 6mm, 8mm and 10mm diameter were used for the longitudinal and transverse reinforcement in the experiment. Their properties are given in Table 8.2.

Arc–length with line search scheme was used. Cracking was simulated by a fixed crack approach with Bhide–Collins' tension stiffening law, and Melhorn's shear retention method. Full bond was assumed.

Element Discretization

The whole specimen was discretized in the analysis. The concrete and reinforcement meshes are shown in Fig.8.10. Two reinforcement meshes were used, designated I and II. The first mesh is the same as the experimental layout, whilst the second included extra 10mm Φ diagonal bars in the corners of the openings.

Results

In Fig.8.11, the load–deflection curves are given for both experiment and computation. For mesh I the comparison is very satisfactory up to the failure stage. The numerical ultimate load is 1023 KN while the experimental one was just less than 1000 KN. The addition of skew bars increased the ultimate load by about 9%.

The comparison of the experimental and theoretical steel strain are shown in

Fig.8.12 for the first three longitudinal steel bars at the bottom of the span. The numerical results are satisfactory up to the development of cracking, after which it gives a stiffer response than the experiment. To a certain extent this can be attributed to the rather coarse mesh, which does not allow sufficient force transfer around the opening. Also, it may be due to the fact that full bond was assumed. The rather extensive cracking network would suggest that bond had deteriorated in certain regions. However, in general, the numerical prediction of steel strains follows the correct trends.

The crack patterns as well as the maximum stress contours are presented in Fig.8.13 for loading levels 400 KN, 700 KN and 1000 KN, in which the crack patterns are compared with the experimental ones. Apart from a few cracks occurring near the supports on either side of the beam, good agreement has been obtained. This slight difference is attributed to the simply supported boundary conditions being placed at the corner nodes of the corner element rather than spread over 200mm from the side as in the experiment.

The addition of skew bars in the corner of the openings had a greater influence on behaviour than in the previous beam. This is because the openings are in the shear span and will influence the force flow from the load point to support. Fig.8.12(a) shows that although the skew bars are contributing to the structural resistance, they are some way from yielding at failure. (The yield strain for 10mm Φ bar was 2350 microstrain). The results of these two analyses suggest that a parametric study of different reinforcement arrangements around the openings would help in identifying methods of strengthening beams with perforations.

8.3 Beam–Column Junction in Portal Frame

In this example, a single–bay portal frame is analysed. This structure was experimentally tested by Stroband and Kolpa[Stroband and Kolpa 1983] and has also been numerically analysed by van Mier[van Mier 1987]. Particular attention is given to the construction detail at the beam – column connection. The behaviour of this structural joint is interesting because in this kind of structure it is commonly assumed that the joint is as strong as the connected members. However, in certain cases, the strength of the joint may be lower. In addition, the curved corner reinforcement bar is difficult to model using conventional reinforcement modelling techniques. In this section, the effect of such a curved bar is investigated.

In the experimental investigation, it was found that the first crack in this kind of structure usually occurs in the mid–span region of the beam and in the column. Only at a more advanced stage does inclined flexible cracking occur in the corner. The development of the splitting cracks mainly depends on the radius of the curved reinforcement bar in the joint.

Description of the Problem

Dimensions and reinforcement of the portal frame are shown in Fig.8.14. There is no variation of the cross–section area of the beam and the column. The frame was loaded in accordance with the conditions of a four–point bending test under loading control as shown in Fig.8.15(a), which causes a negative bending moment in the joint between the beam and the column (see Fig.8.15(b)).

Material Properties

Concrete:

$f_c' = 37.8$ N/mm^2 $\nu = 0.15$

$f_t = 2.42$ N/mm^2 $E_c = 2.7$ KN/mm^2

Steel:

$E_s = 210.0$ KN/mm^2

$E_h = 0.1E_s$

$f_{sy} = 350.0$ KN/mm^2 (for Φ6)

$f_{sy} = 282.0$ KN/mm^2 (for Φ12)

$f_{sy} = 300.0$ KN/mm^2 (for Φ14)

The solution was obtained using the arc–length method with line search scheme. The rotating crack model was used with Vecchio–Collins' tension stiffening law and Melhorn's shear retention model. Full bond between concrete and reinforcement was assumed.

Element Discretization

As shown in Fig.8.16, one mesh is used for concrete while two meshes are examined for the reinforcement. The first has straight bars in the corner and the other has a curved bar in the corner.

Results

In Fig.8.17, load–deflection is compared with the numerical results of van Mier[van Mier 1987], where little significant difference is observed. For the

straight bar model, the ultimate load was 28KN whereas there was only a slight increase for the curved bar at 29KN. The experimental value was given as 28KN also. Unfortunately, no experimental load– deflection curve was reported.

Fig.8.18 examines the corner reinforcement in more detail by comparing the strain response of the curved approximation and the straight simplification.

For the straight bar, the steel stresses on either side of the corner diagonal are very similar until failure is approached, when the stress in the vertical bar increases more rapidly, reflecting the extra horizontal cracking that occurs in the column near the junction. For the curved bar the stresses at the same points have increased compared to the straight bar, but show a similar trend; however the point at the centre of the curve is now also carrying a substantial stress. This suggests that the junction is strengthened because the curved bar picks up the stresses released by the diagonal cracking in the concrete.

The maximum principal stress contour is shown along with van Mier's results in Fig.8.19 and 20 for linear stage and failure stage, respectively. The general trends are similar with some differences in stress occurring in the corner for the straight bar model and curved bar model, indicating that the curved bar is absorbing more tensile stress from the concrete.

Fig.8.21 compares the crack pattern with that of van Mier at loading level 8.0 KN while Fig.8.22 gives comparison of the results of present study, van Mier' study and Stroband– Kolpa's experimental results.

At loading level 8.0 KN, the cracking patterns agree quite well with the experimental crack pattern. At the final stage, satisfactory agreement has also been obtained. There is a slight difference of crack patterns between the curved

bar model and the straight bar model, indicating that the curved bar has slightly strengthened the corner and effected its local failure mode. The numerical results indicated crushing in the re-entrant corner of the junction, but that failure was actually caused by flexure in the main beam at a later load.

The final deformed mesh is given in Fig.8.23, where it can be seen that most deflection occurs in the middle of the beam, the beam being more flexible than the column. Also the crack development at the junction has allowed the beam to rotate more at its ends.

8.4 Beam-column Joint

A beam-column joint tested experimentally by Allwood[Allwood 1980], was selected to study the influence of bond-slip and its modelling. This type of structure is of interest because of the variation of stresses in the beam continuity bars as the bars pass through the columns, particularly wide columns, and how this is effected by bond-slip. Modern Codes of Practice allow the bending moment at the face of the column to be used for design calculations but, where the column width is large compared to the beam spans, such a bending moment can be substantially less than the value at the centre of the column.

Dimensions and Reinforcing Details

The analysis presented here investigated the stress distribution of the steel bars in the beam-column joint. Fig.8.24 shows the dimension and reinforcement details of the experimental specimen. Due to the symmetry of the structure, only one half has been analysed. Bond-slip was assumed for the longitudinal reinforcements of the beam. The concrete and reinforcement meshes are given in Fig.8.25.

Material Properties

Concrete compressive strength f_{cu} = 56.0MPa at 28 days. In this analysis, the following properties were assumed: E_c = 20GPa, f_t = 2.0MPa, ν = 0.15; and E_s = 210GPa, σ_y = 600MPa for high yield 4mm Φ bar, σ_y = 500MPa for 12mm Φ bar, $E_h = 0.1E_s$.

Houde's bond slip law was used in this analysis. The fixed crack model was used for concrete in conjunction with Vecchio–Collins' tension stiffening law and Melhorn's shear retention law. Solutions were obtained using the arc–length method with line search.

Results

Figs.8.26(a) and (b) show the computational results for steel stresses using perfect bond and bond–slip, respectively. For perfect bond the analysis underestimated the experimental steel stresses at all load levels whilst there was very close agreement when bond–slip was allowed for. The peak stress occurred more towards the beam in the numerical analysis, and were about 15% higher in magnitude near failure. The predicted ultimate loads were overestimated but within reasonable bounds: with full bond the failure load was 25.0KN, with bond–slip 22.5KN whereas the experimental load was reported to be 20KN.

8.5 Concluding Remarks

In this Chapter, applications of the modelling techniques to two perforated deep beams, a portal frame and symmetrical beam–column junction have been made. From the deflection curves, steel strain curves, crack patterns and stress contours,

it has been seen that the general embedded finite element reinforcement modelling procedure is reasonably accurate and potentially very useful. It also allows parametric studies to be conveniently undertaken to study the influence of reinforcement because additional bars can be included without the need for remeshing the analytical model. The bond modelling technique also proved useful in studying bond–slip effects and was able to demonstrate its influence very clearly.

Table 8.1 Properties of Reinforcement — Beam I (G. Memon 1982)

Normal Bar Diameter mm	Young's Modulus KN/mm^2	0.2% Proof Stress f_y N/mm^2	Strain at 0.2% Proof Stress ϵ_y	Ultimate Stress N/mm^2
6	215.5	503.0	0.45	566.0
8	252.0	531.0	0.41	542.0
10	252.0	504.0	0.42	679.0

Table 8.2 Properties of Reinforcement — Beam II (G. Khaskheli 1989)

Bar Size mm	Area KN/mm^2	Young's Modulus KN/mm^2	0.2% Proof Stress N/mm^2
6	28.0	199.0	513.0
8	50.0	195.0	520.0
10	79 .0	200.0	471.0

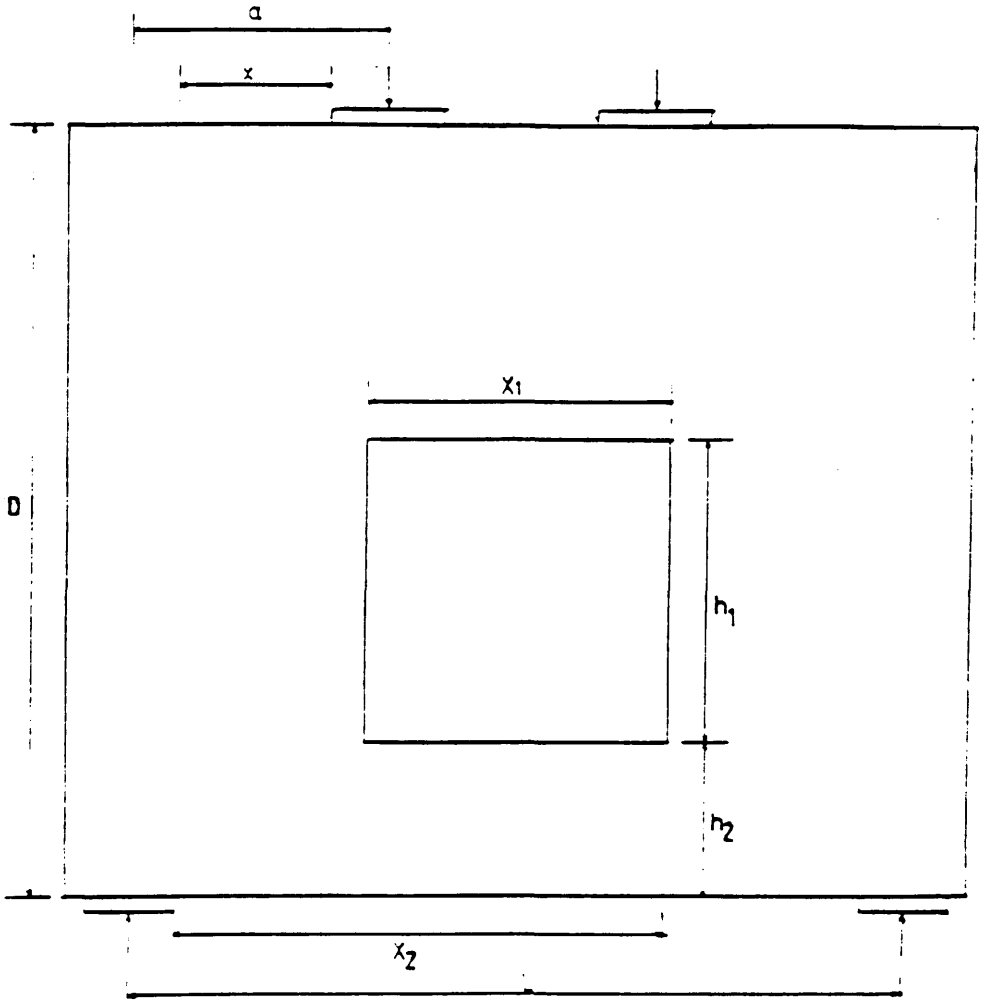

Fig.8.1 Details of Dimensions (B3)

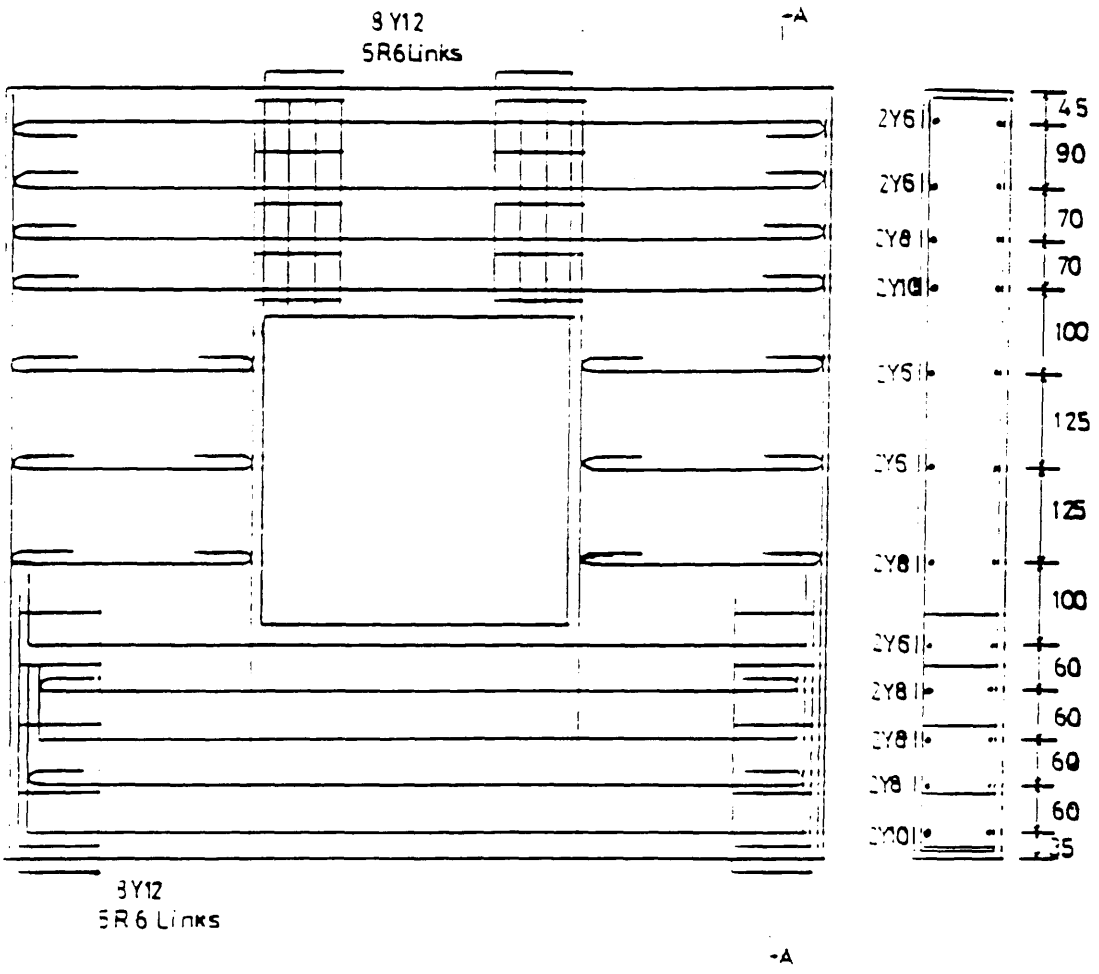

Fig.8.2 Arrangement of Reinforcement Section A-A

CONCRETE MESH

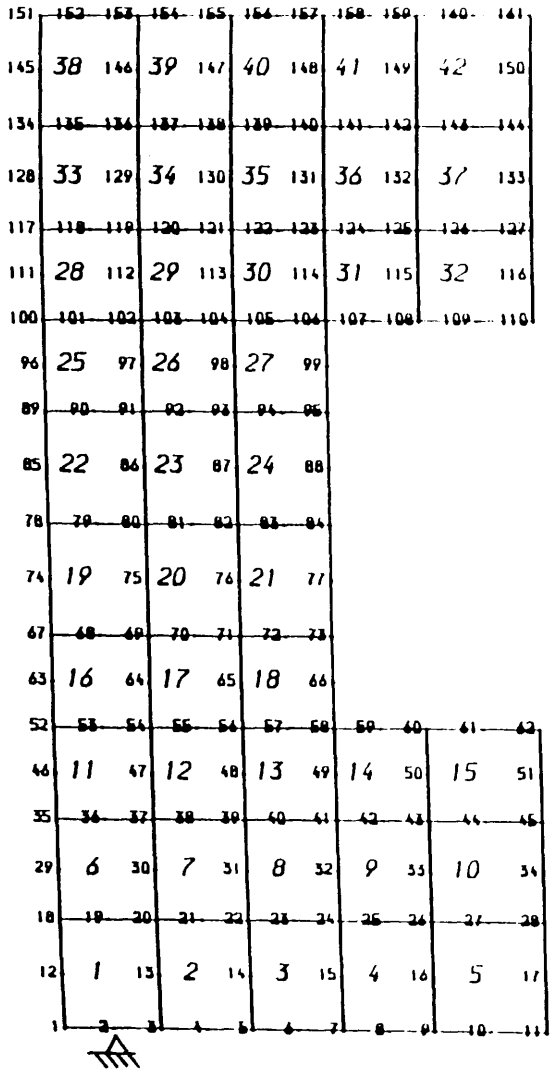

REINFORCEMENT MESH 1

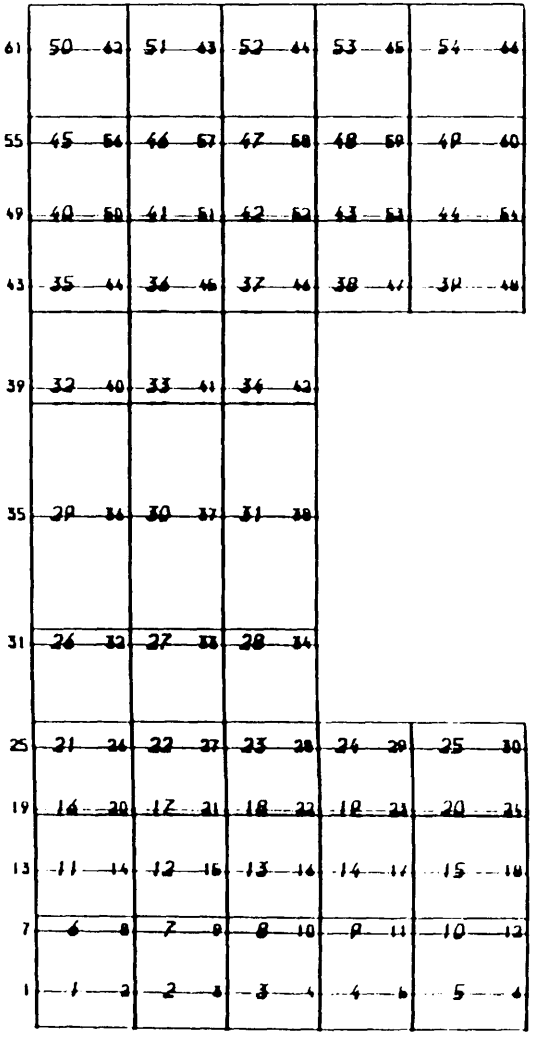

Fig.8.3 Meshes

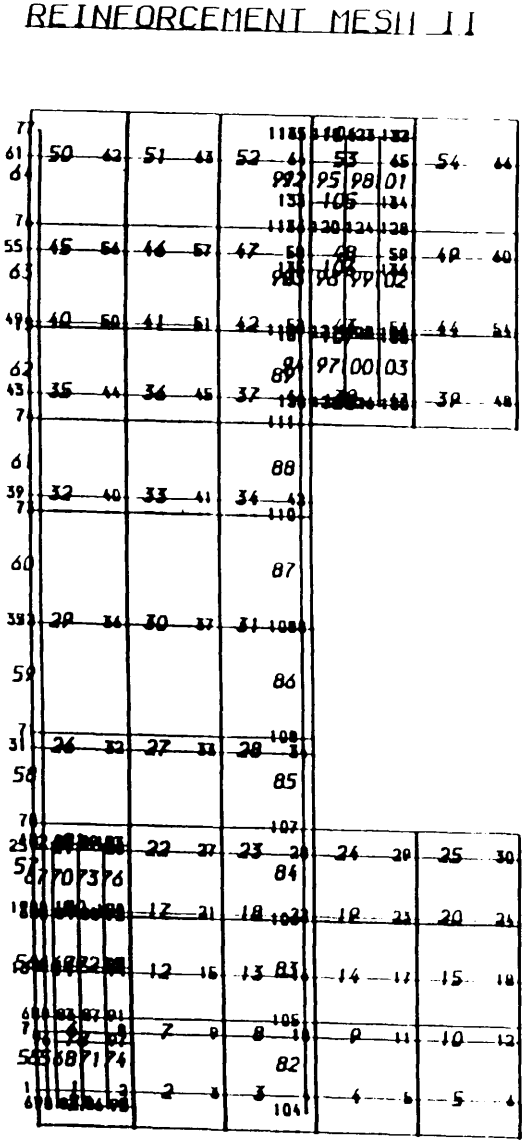

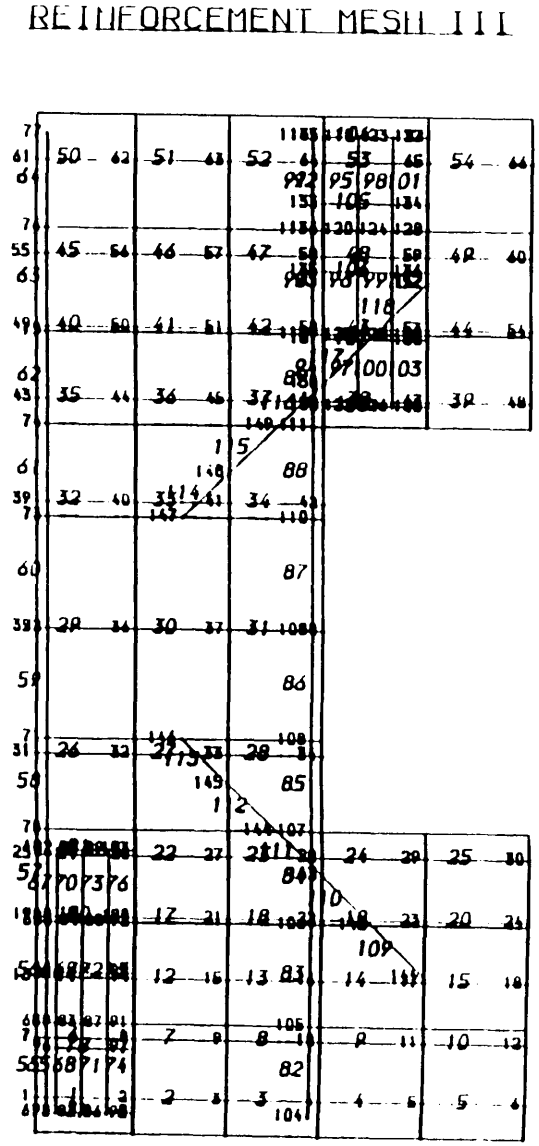

Fig.8.3 Meshes —continued

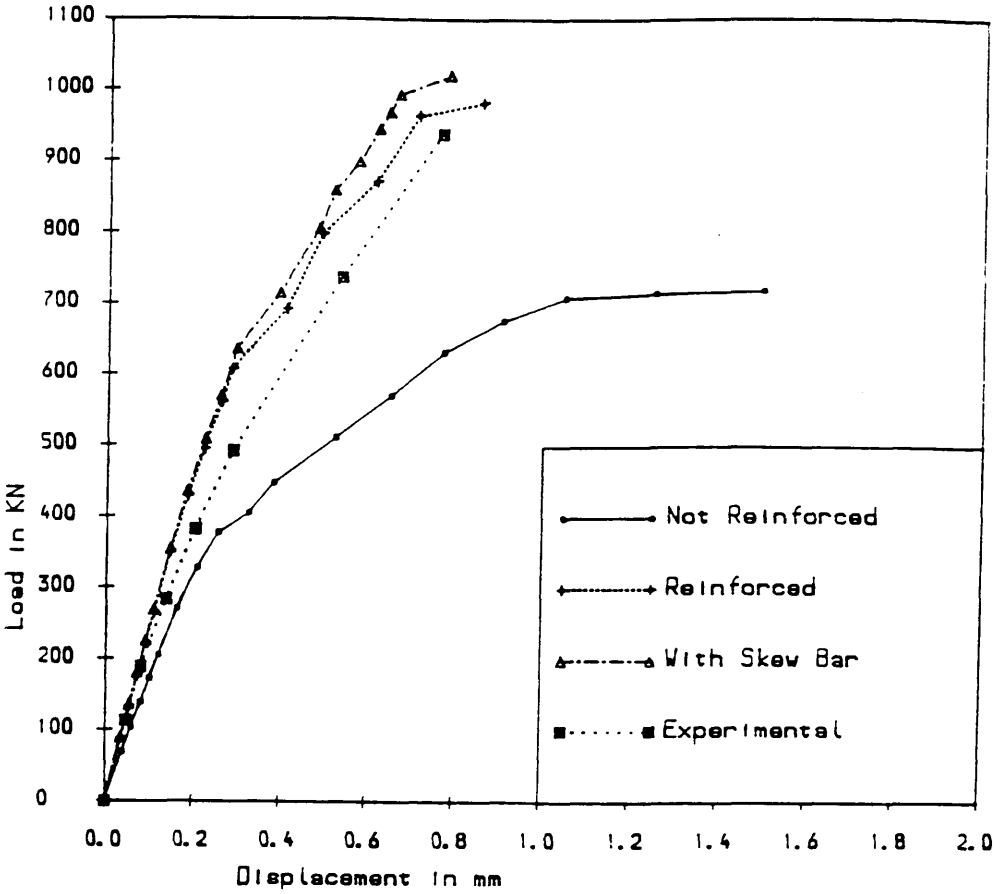

Fig.8.4 Load vs. Deflection

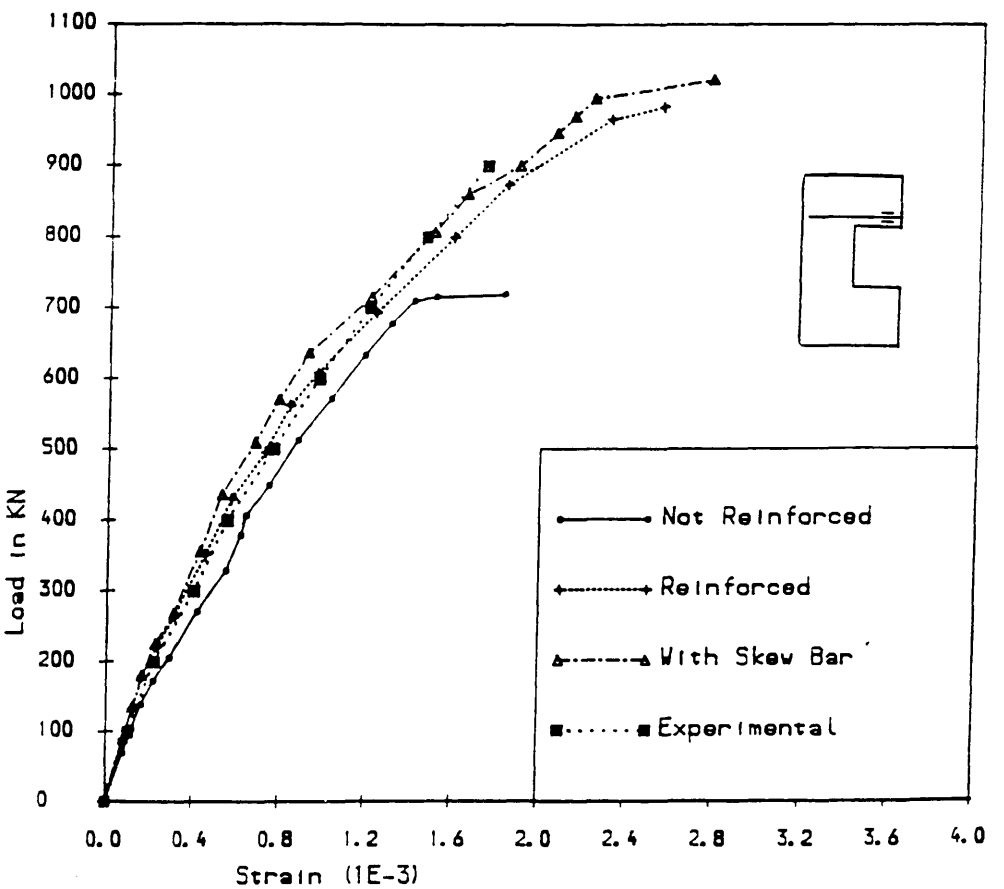

Fig.8.5 Load vs. Steel Strain

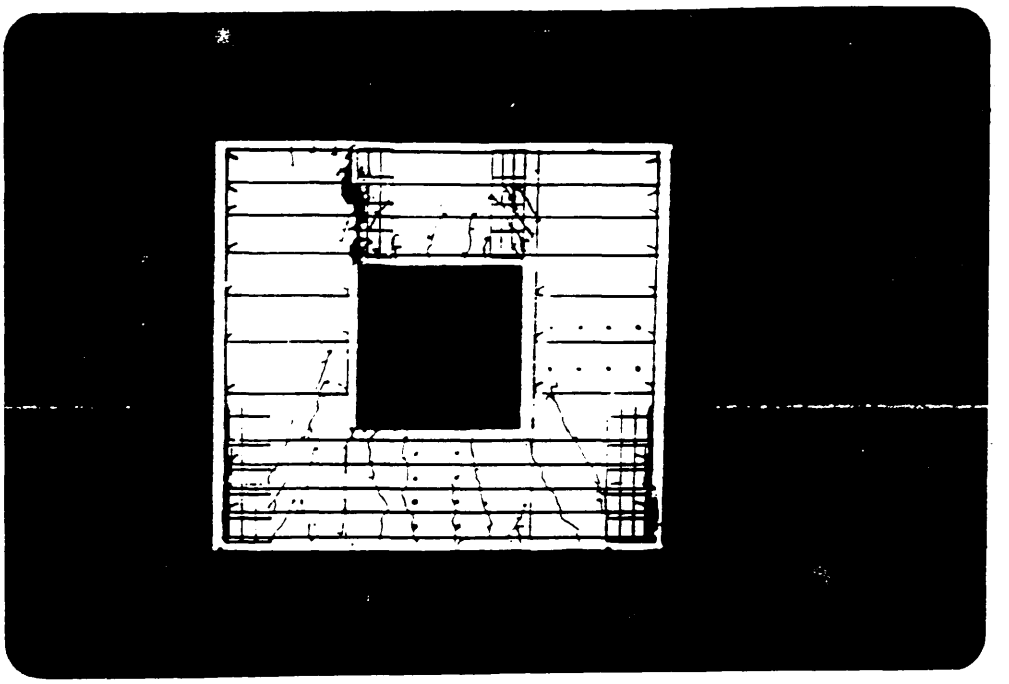

Fig.8.6 Experimental Crack Pattern

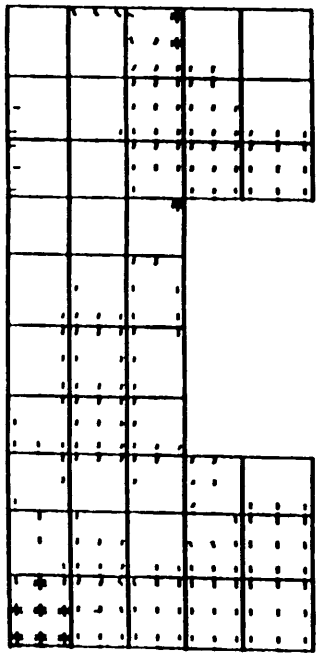

Not Reinforced

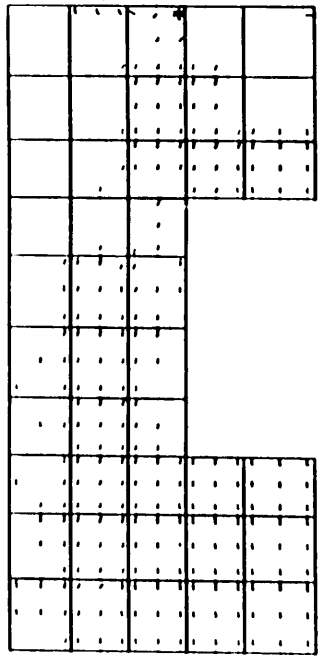

Reinforced

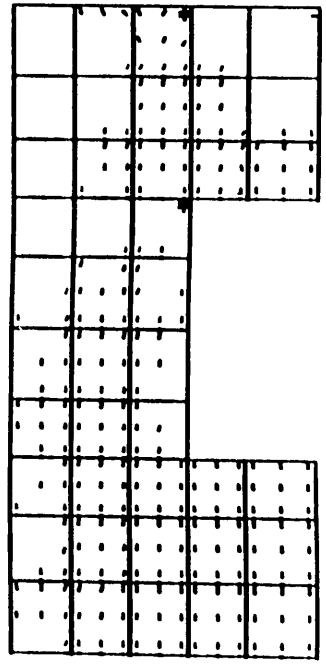

With Skew Bars

Fig.8.7 Final Crack Pattern

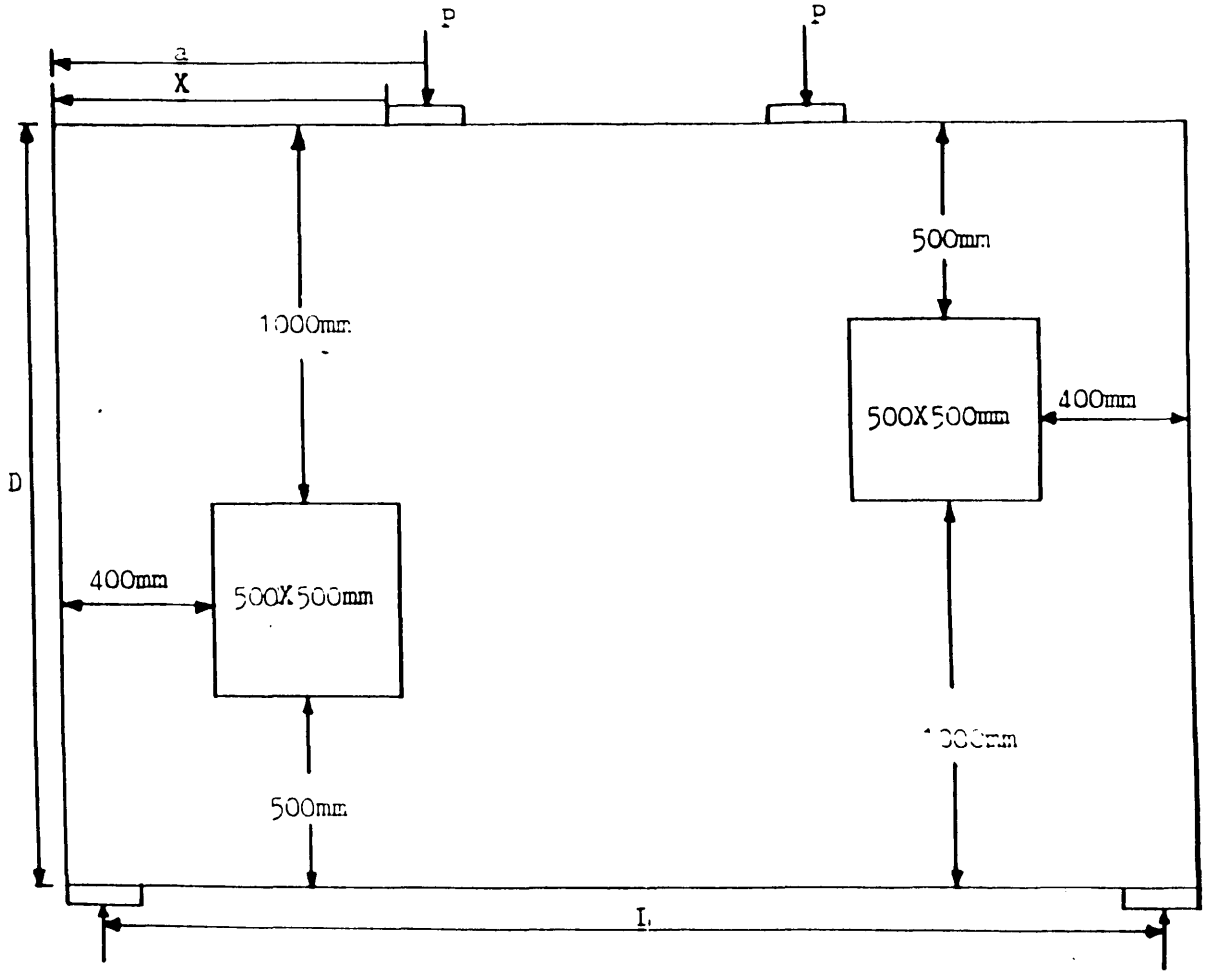

Fig.8.8 General Dimensions of the Specimen (TRGRAS 9)

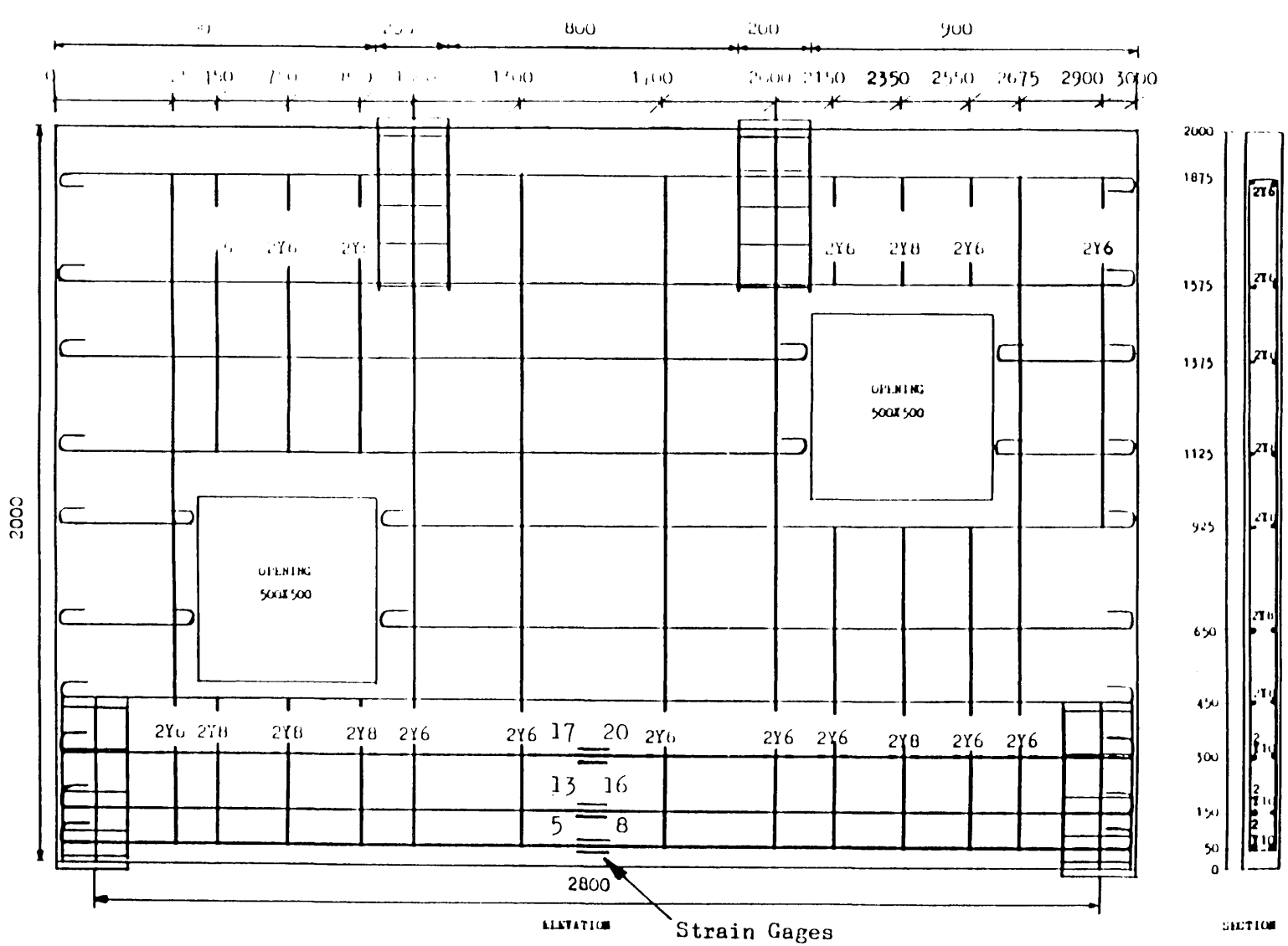

Fig.8.9 Dimensions and Reinforcing Details

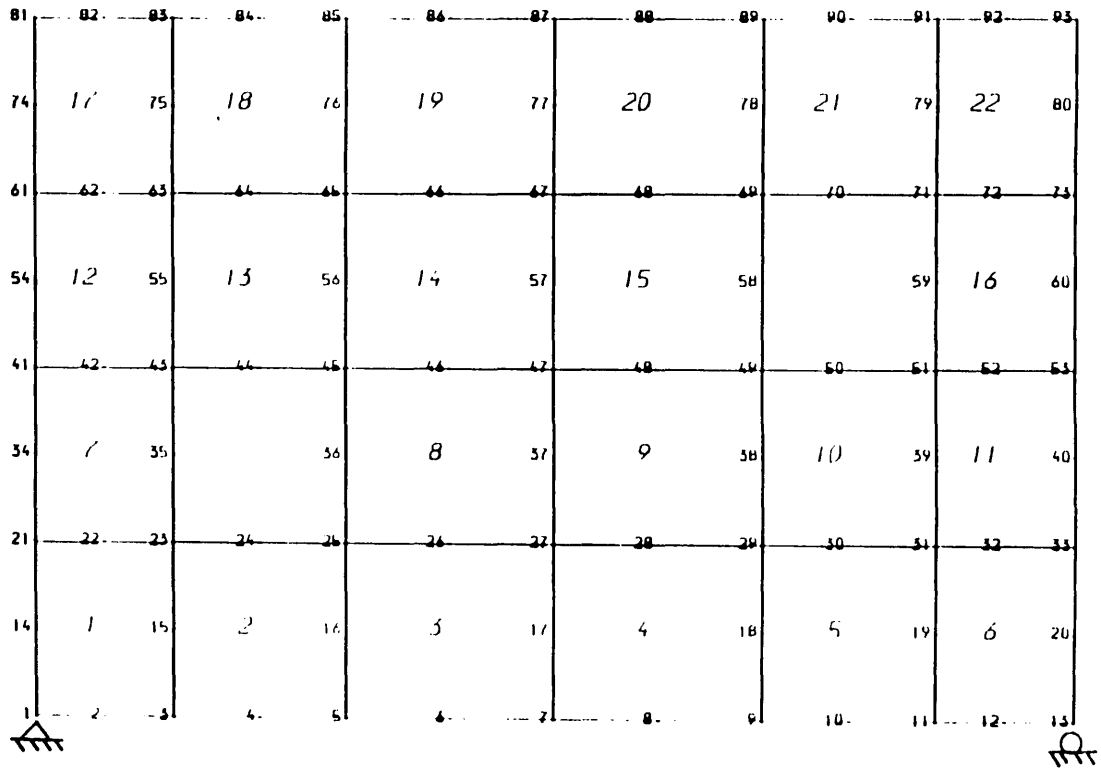

Fig.8.10 Meshes

REINFORCEMENT MESH --I

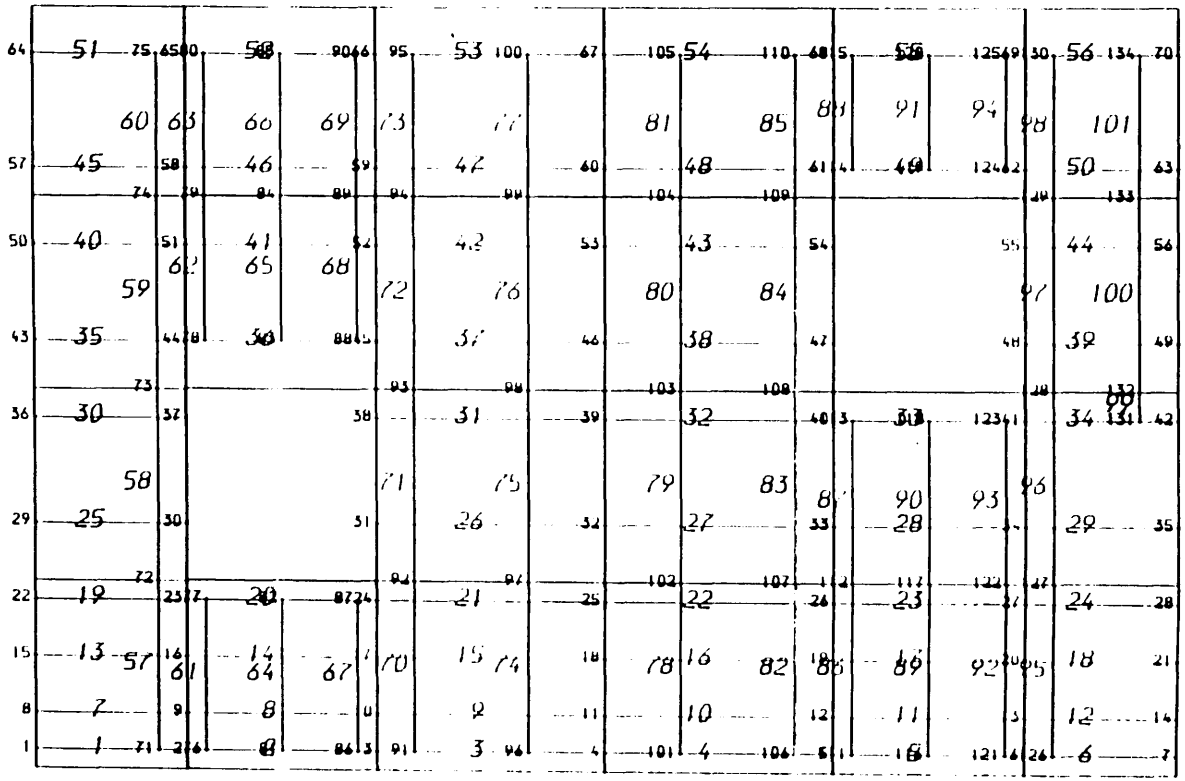

Fig.8.10 Meshes —continued

REINFORCEMENT MESH --II

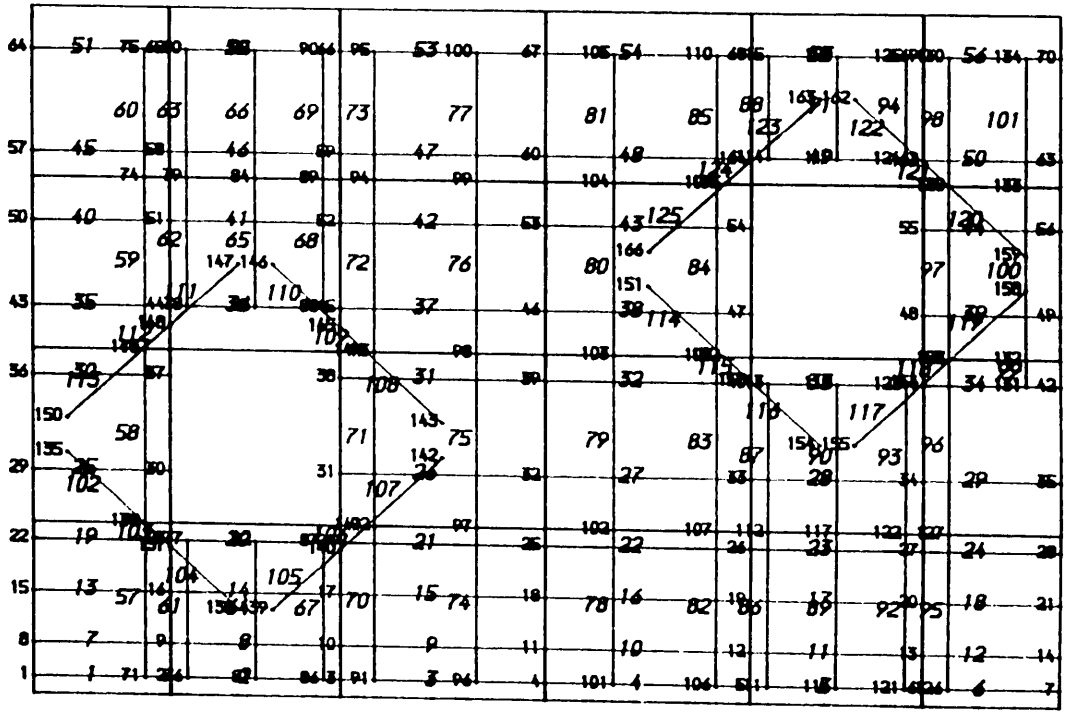

Fig.8.10 Meshes --continued

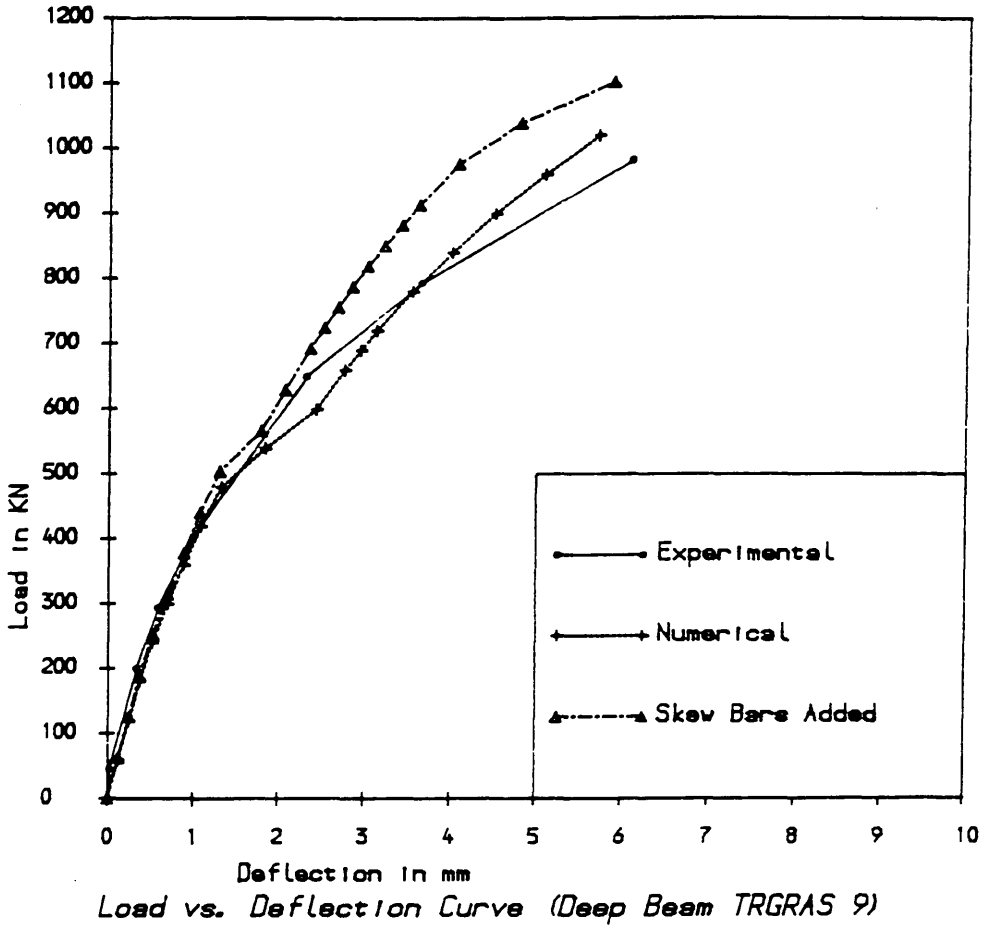

Fig.8.11 Load vs. Deflection

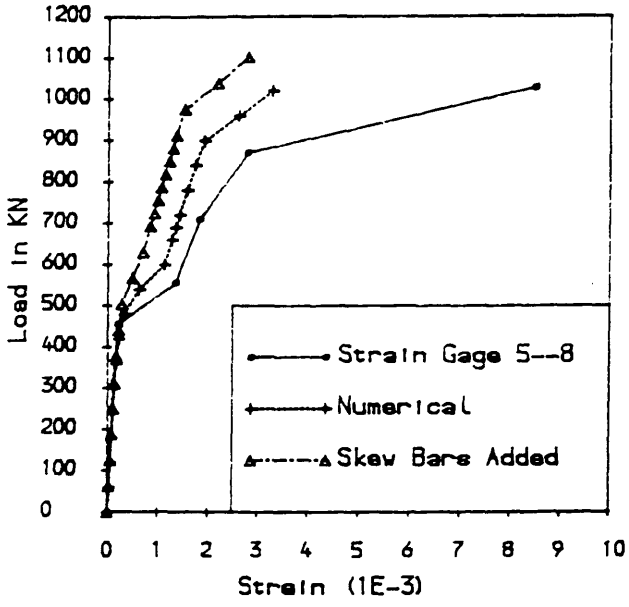

(a)

Fig.8.12 Load vs. Steel Strain (ref. to Fig.8.9)

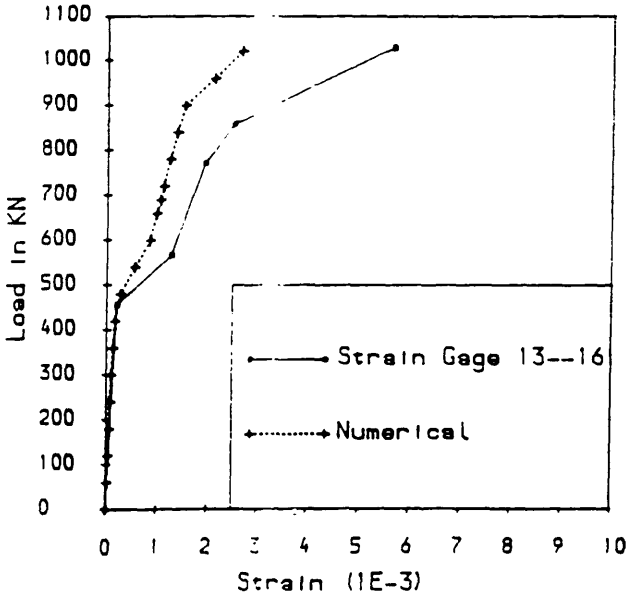

(b)

Fig.8.12 Load vs. Steel Strain —continued

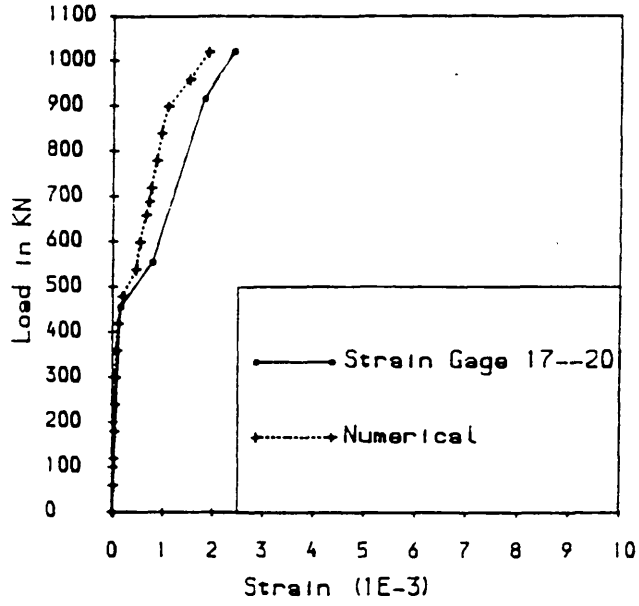

(c)

Fig.8.12 Load vs. Steel Strain —continued

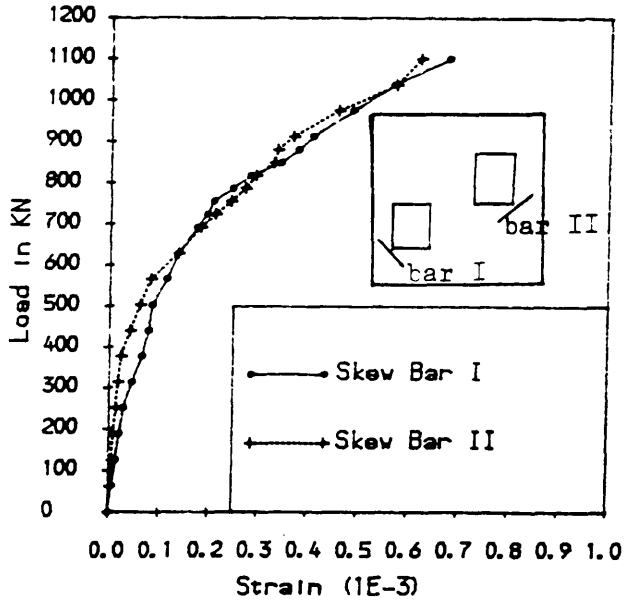

(d)

Fig.8.12 Load vs. Steel Strain —continued

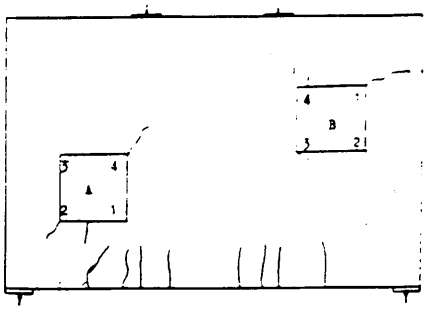

(a) Experimental Crack Pattern at 400KN

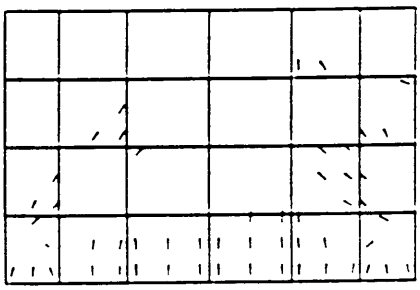

(b) Numerical Crack Pattern at 420KN

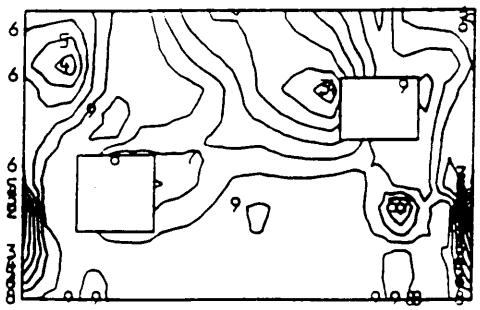

(c) Maximum Principal Stresses at 420KN

Fig.8.13 Loading Configuration

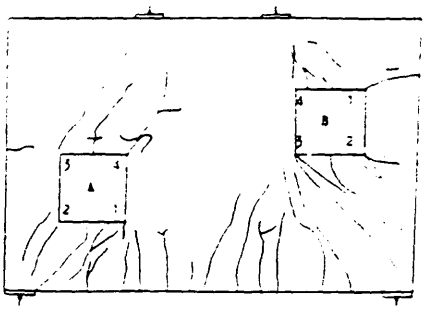

(d) Experimental Crack Pattern at 700KN

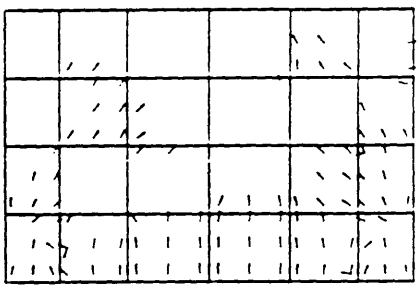

(e) Numerical Crack Pattern at 700KN

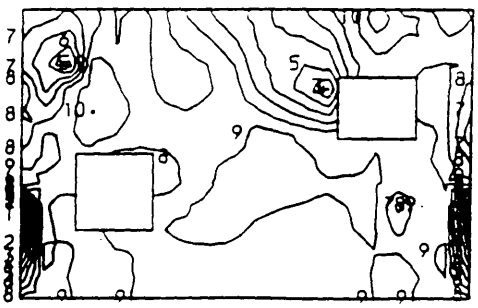

(f) Maximum Principal Stresses at 700KN

Fig.8.13 Loading Configuration —continued

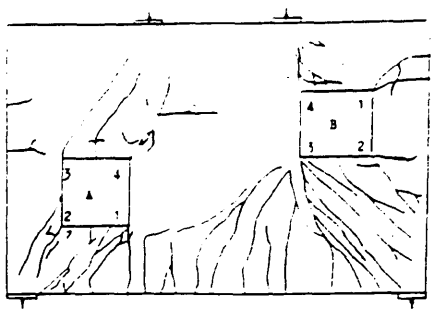

(g) Experimental Crack Pattern at 1000KN

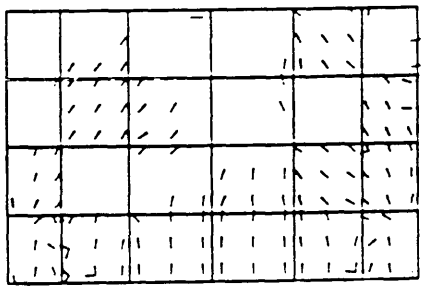

(h) Numerical Crack Pattern at Failure

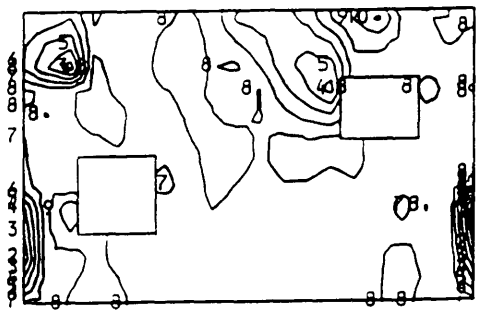

(i) Maximum Principal Stresses at Failure

Fig.8.13 Loading Configuration —continued

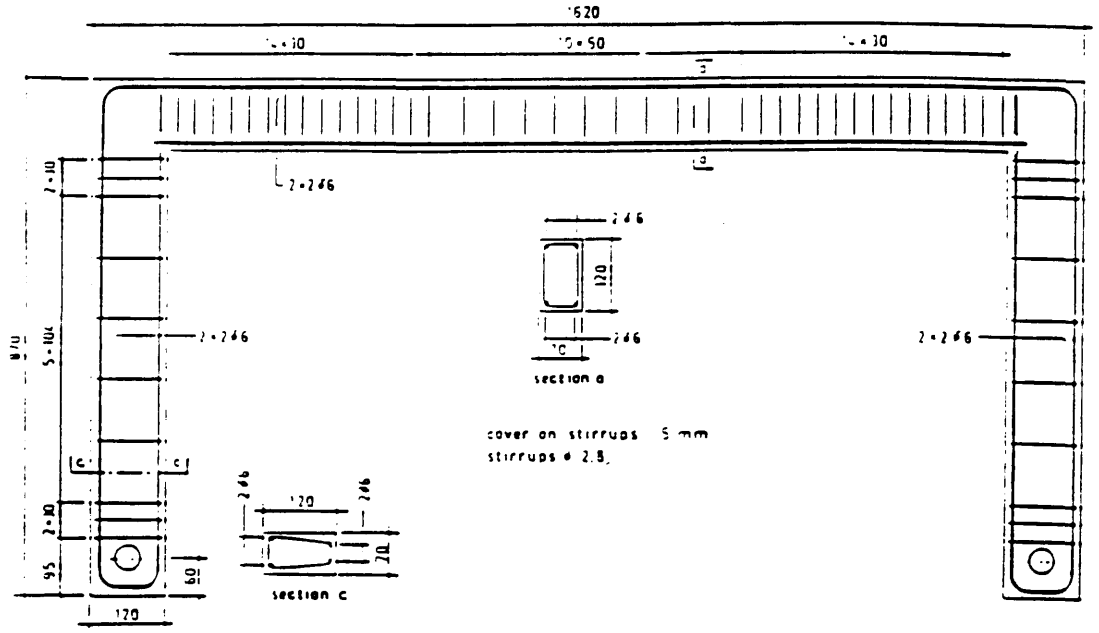

Fig.8.14 Portal Frame: dimensions and reinforcement details

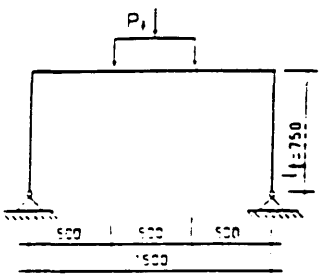

(a) Loading of the Frame

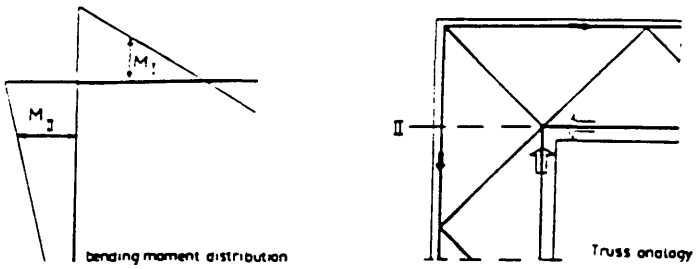

(b) Location of Critical Sections

Fig.8.15 Loading Conditions

CONCRETE MESH

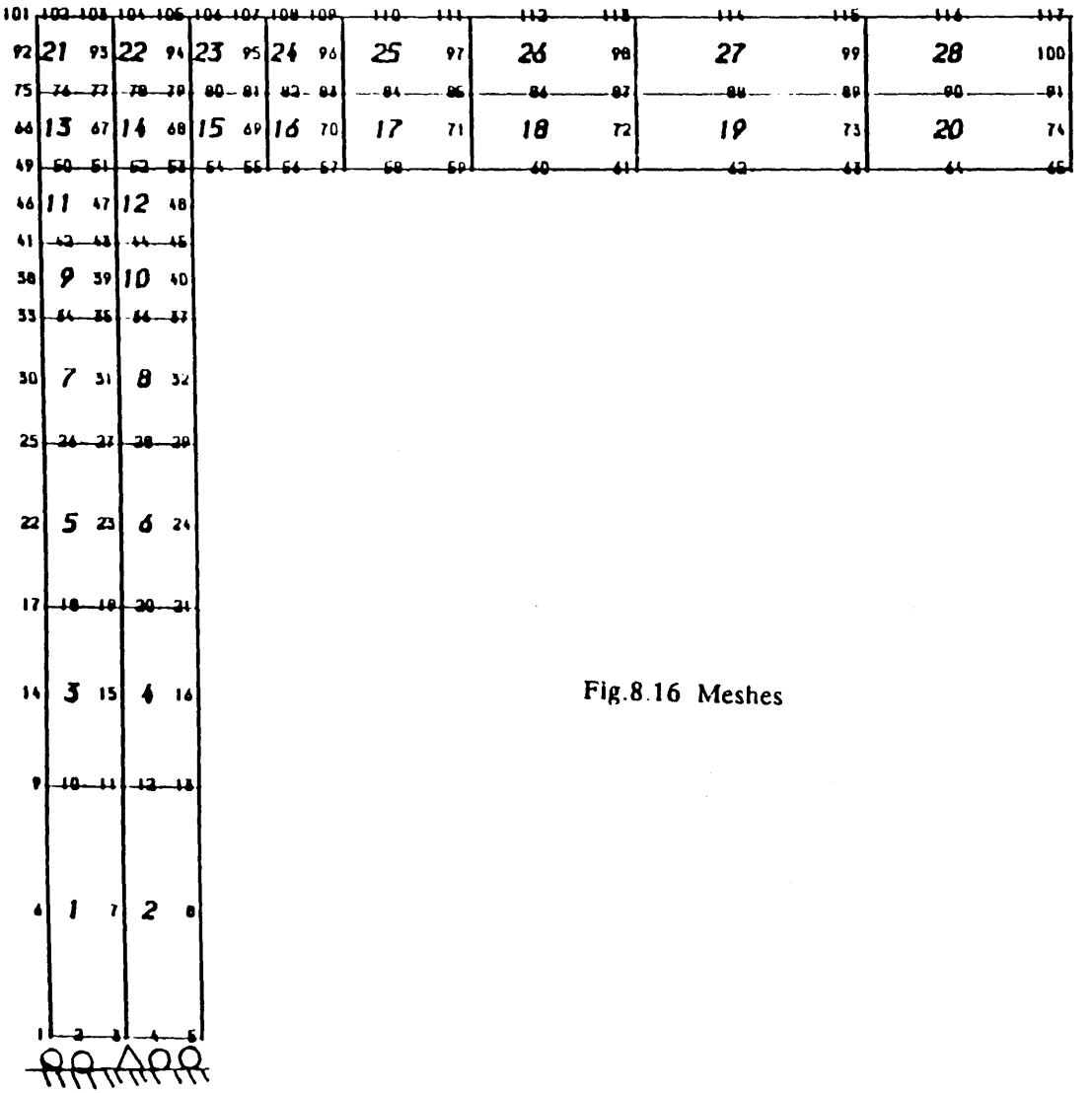

Fig.8.16 Meshes

REINFORCEMENT MESH

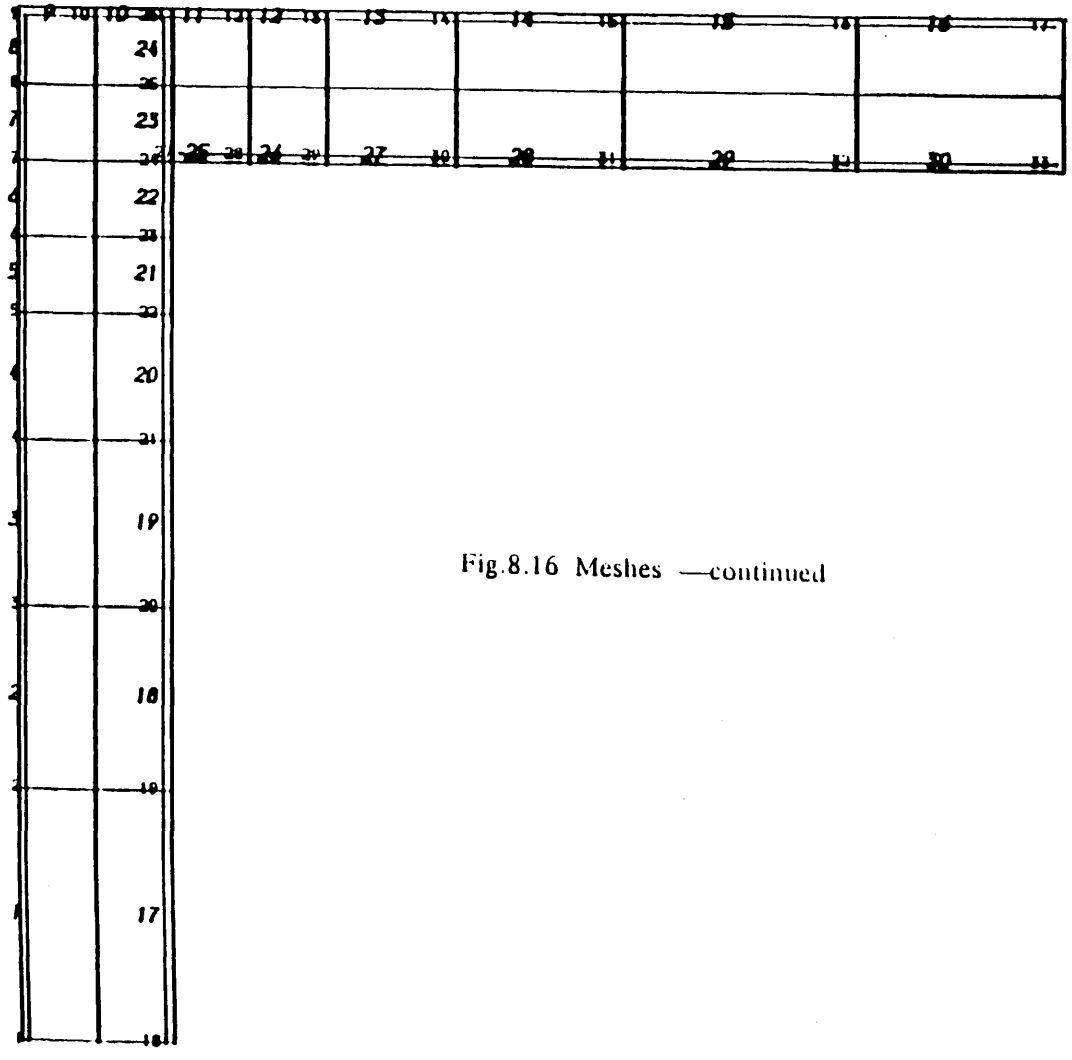

Fig.8.16 Meshes —continued

REINFORCEMENT MESH

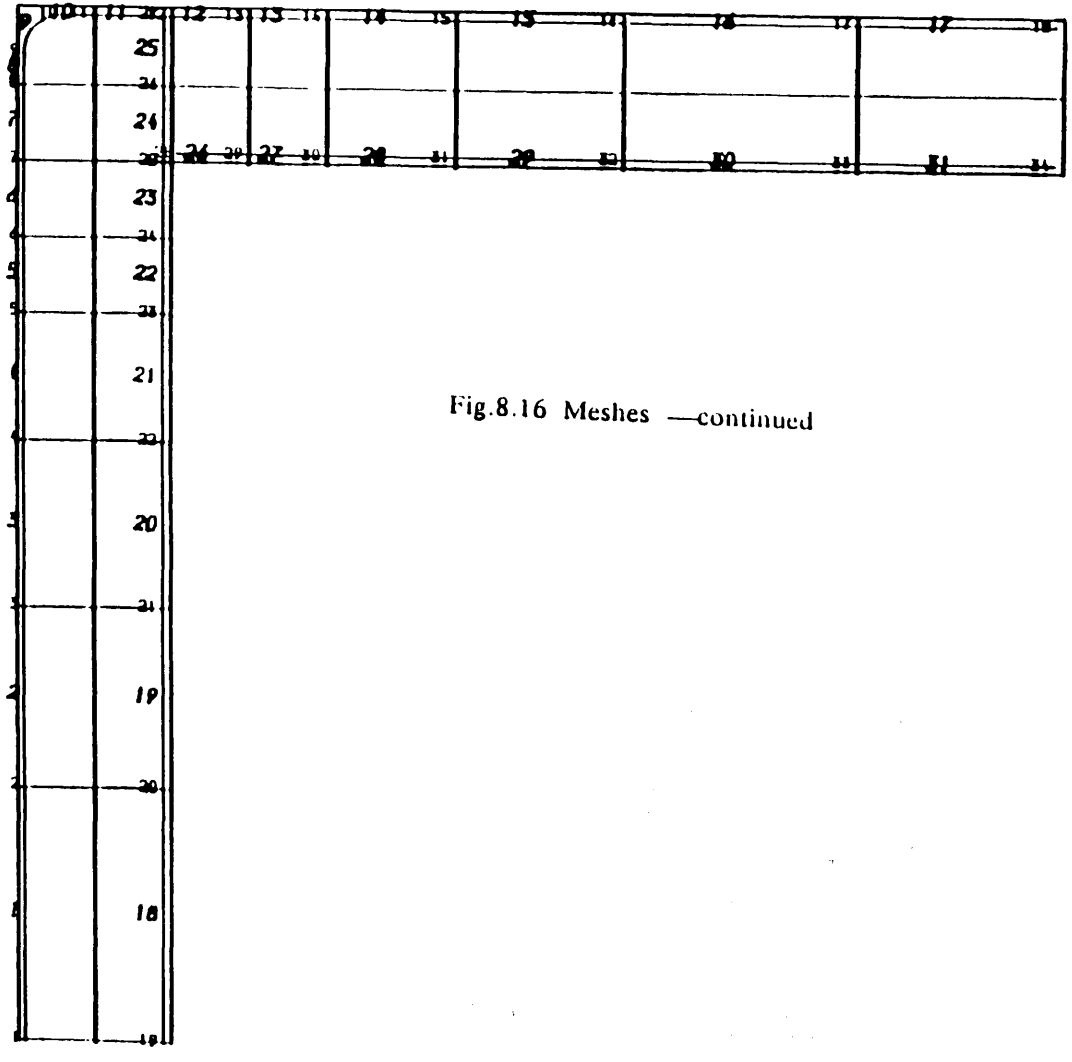

Fig.8.16 Meshes —continued

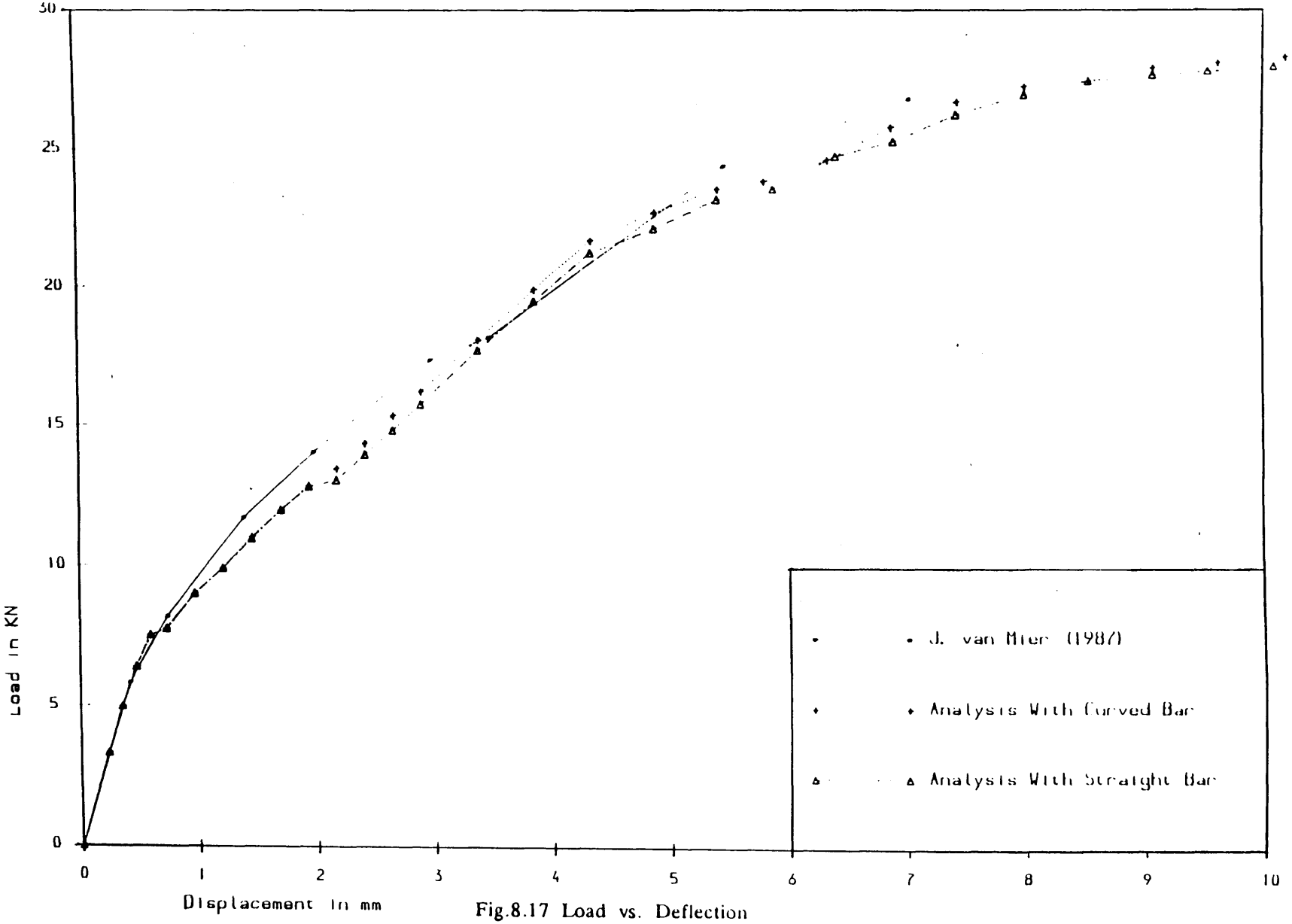

Fig.8.17 Load vs. Deflection

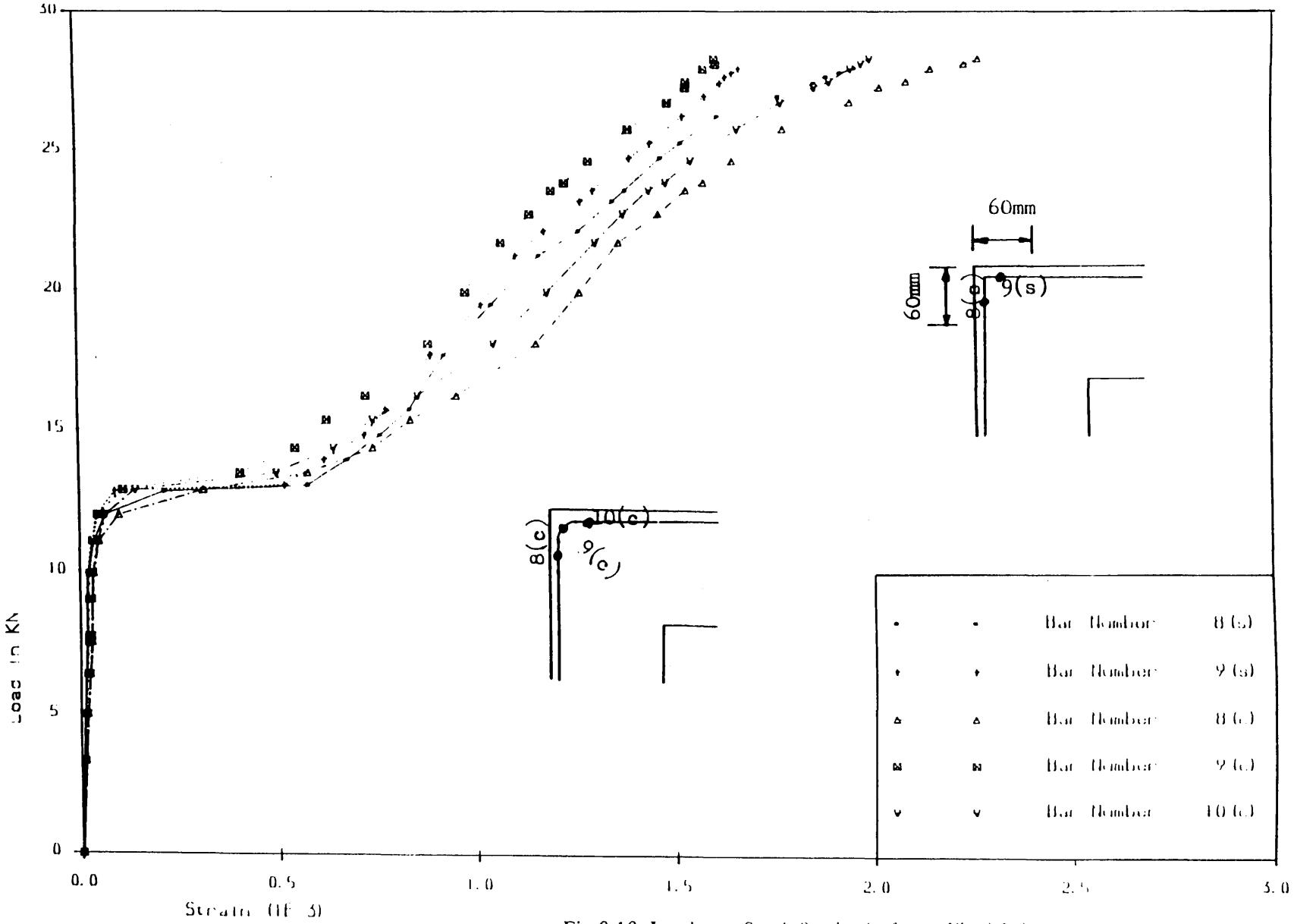

Fig.8.18 Load vs. Steel Strain (ref. to Fig.8.16)

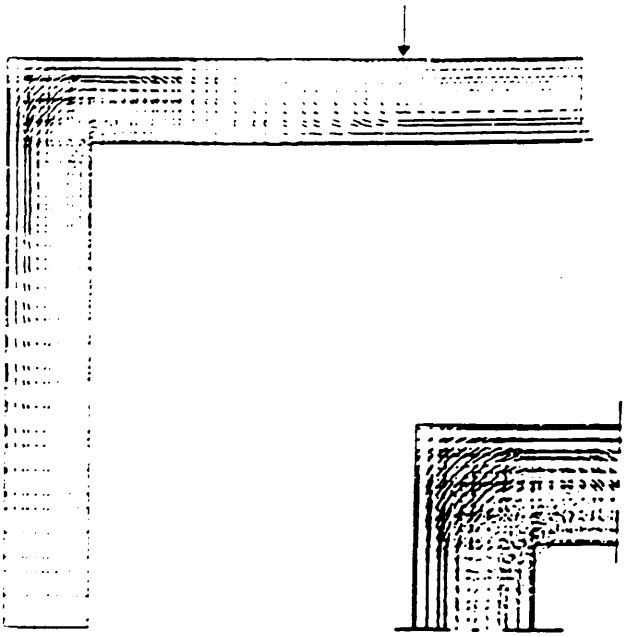

the overall view detail of the corner

(a) J. van Mier (1987)

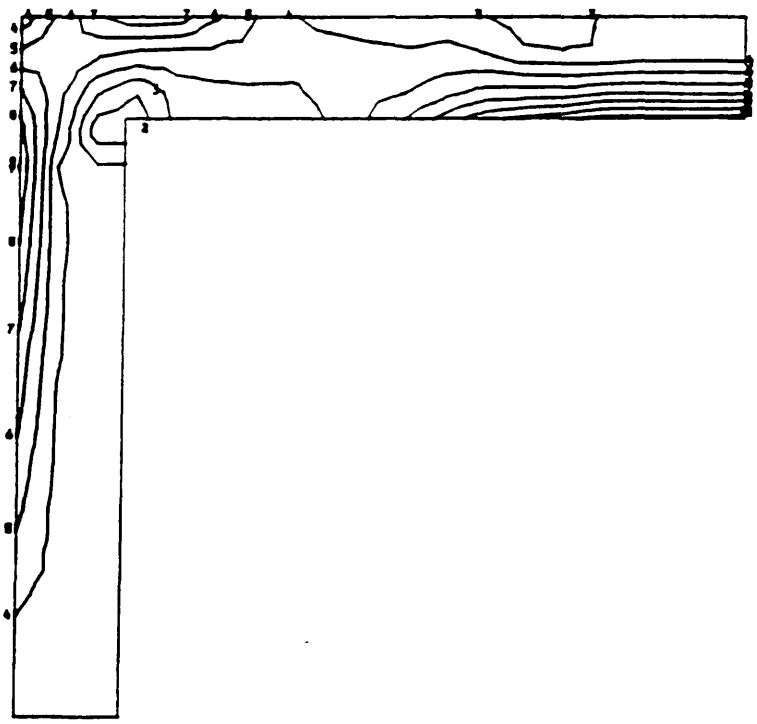

(b) Finite element results

Fig.8.19 Maximum Principal Stresses —linear stage

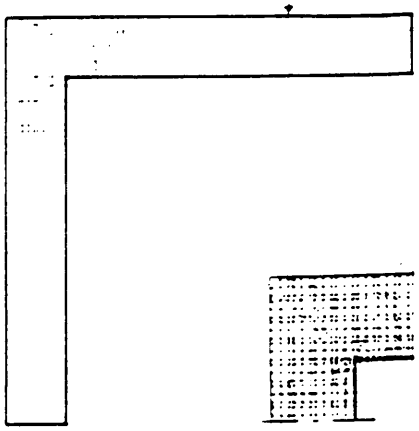

overall view　　detail of the corner

(a) J. van Mier (1987)

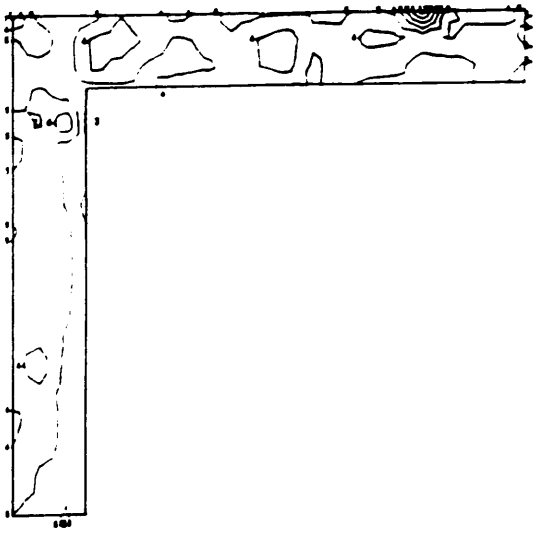

c) Finite Element Results (curved bar model)

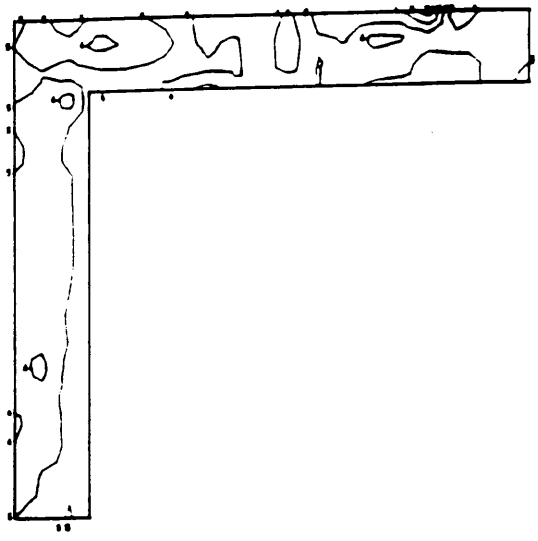

(b) Finite Element Results (straight bar model)

Fig.8.20 Maximum Principal Stresses —failure

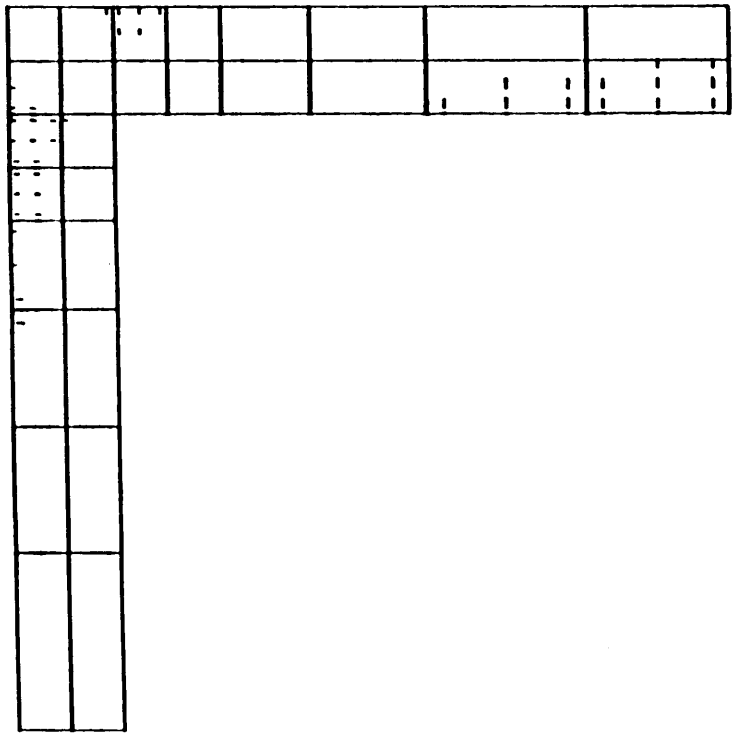

(a) Finite Element Results at 8.2KN

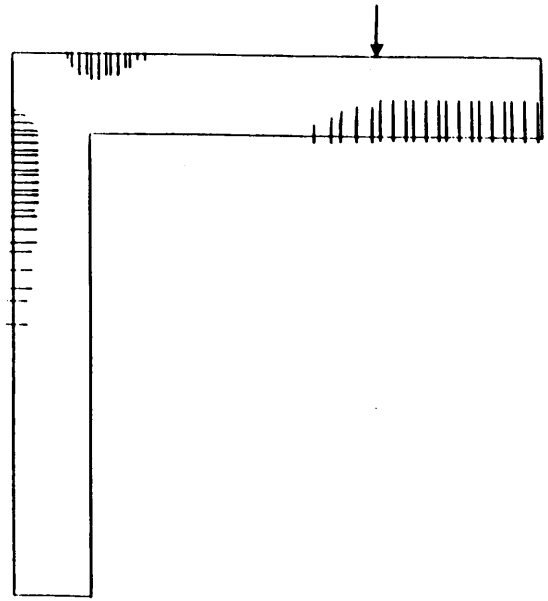

(b) J. van Mier's Results at 8.0KN

Fig.8.21 Crack Patterns

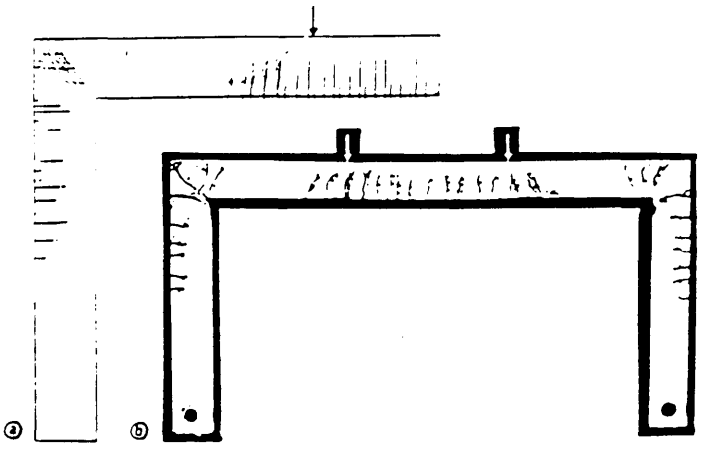

(a) J. van Mier (1987)

(b) Experimental (Stroband and Kolpa 1983)

Fig.8.22 Crack Patterns at Failure

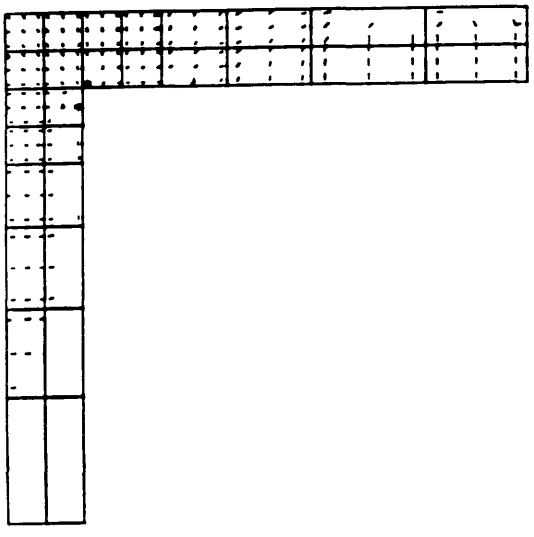

(a) Straight Bar Model

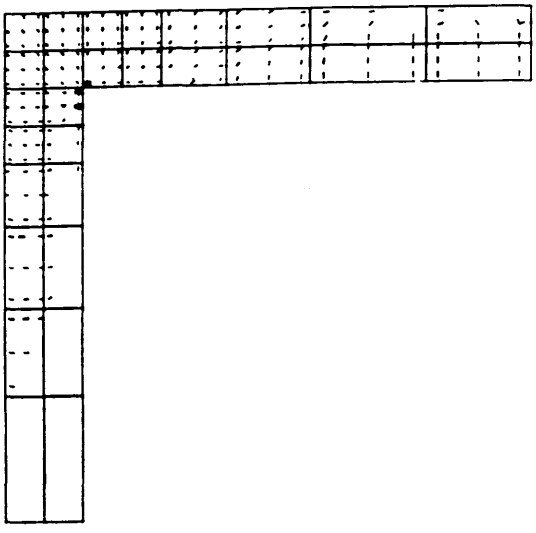

(b) Curved Bar Model

Fig.8.22 Crack Patterns at Failure —continued

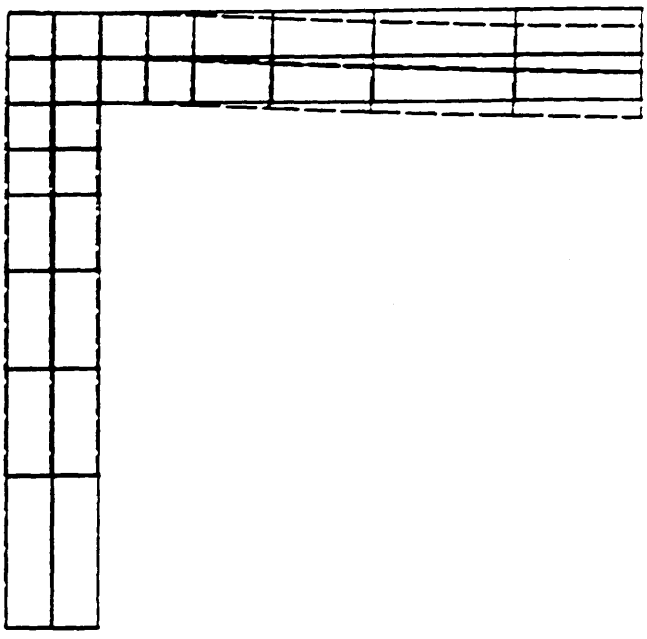

Fig. 8.23 Final Deformed Mesh

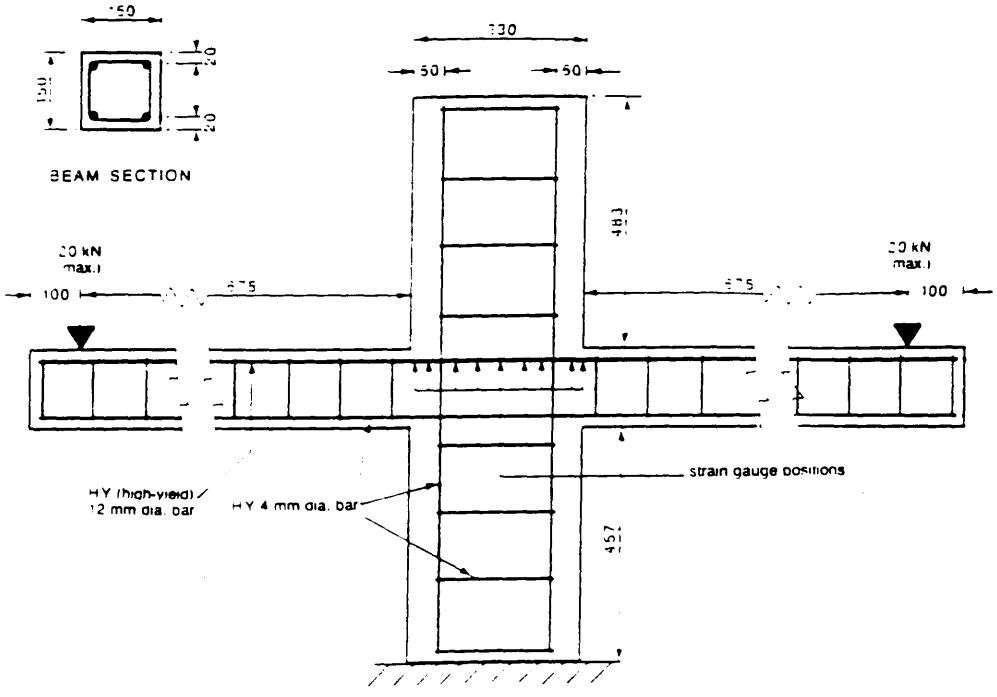

Fig.8.24 Dimensions and Reinforcement Layout

CONCRETE MESH

REINFORCEMENT MESH

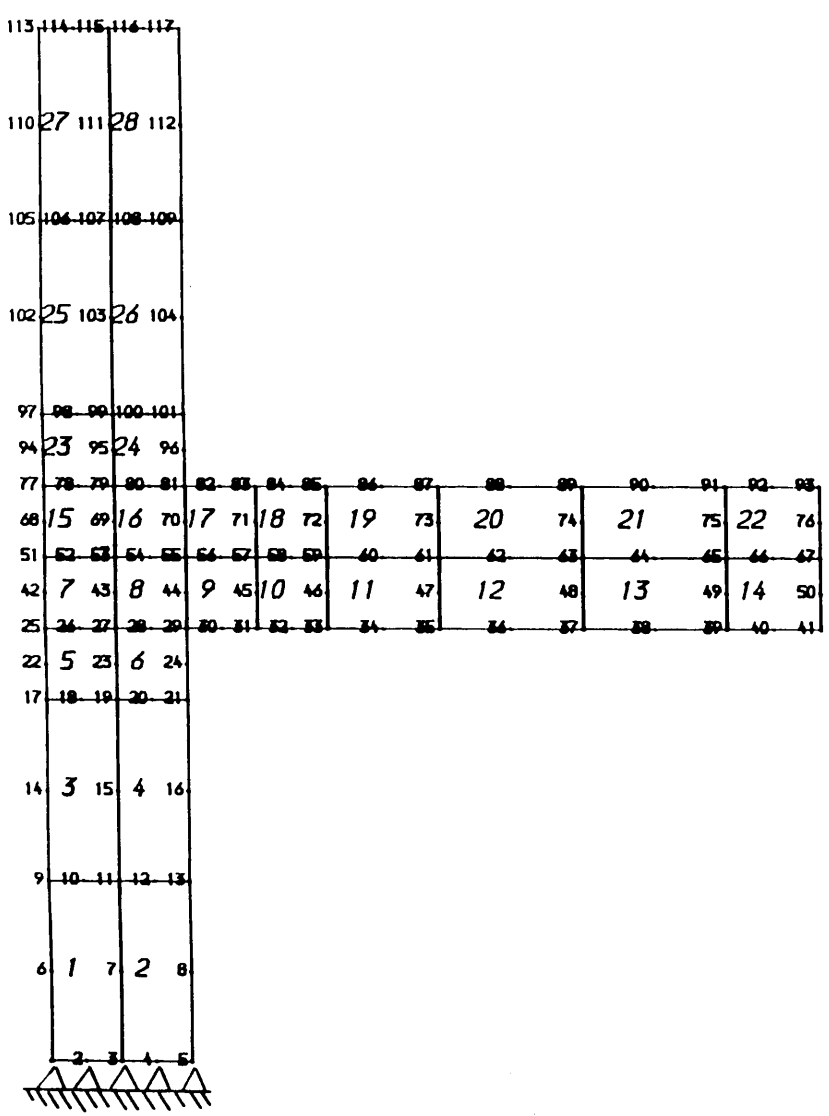

Fig.8.25 Meshes

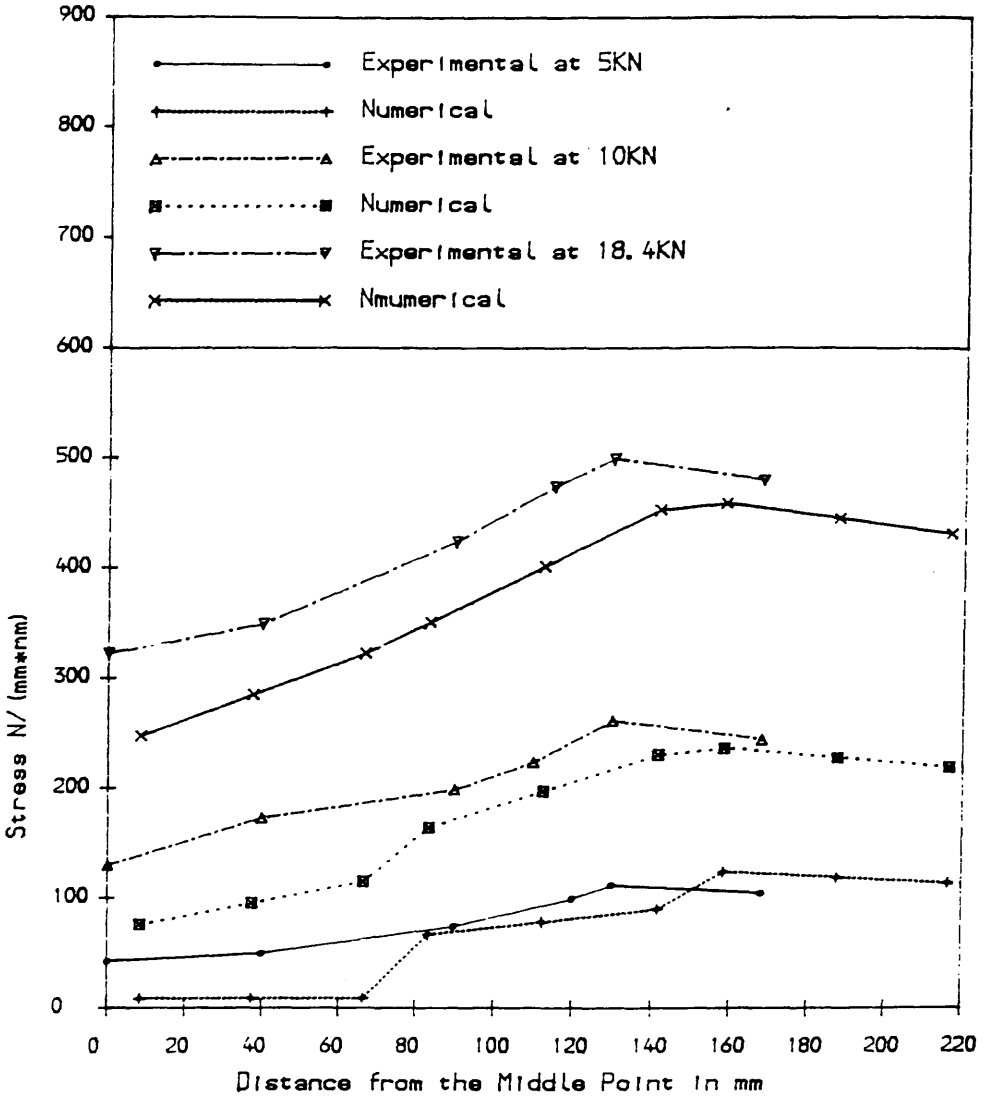

Fig.8.26(a) Steel Stress Distribution —perfect bond

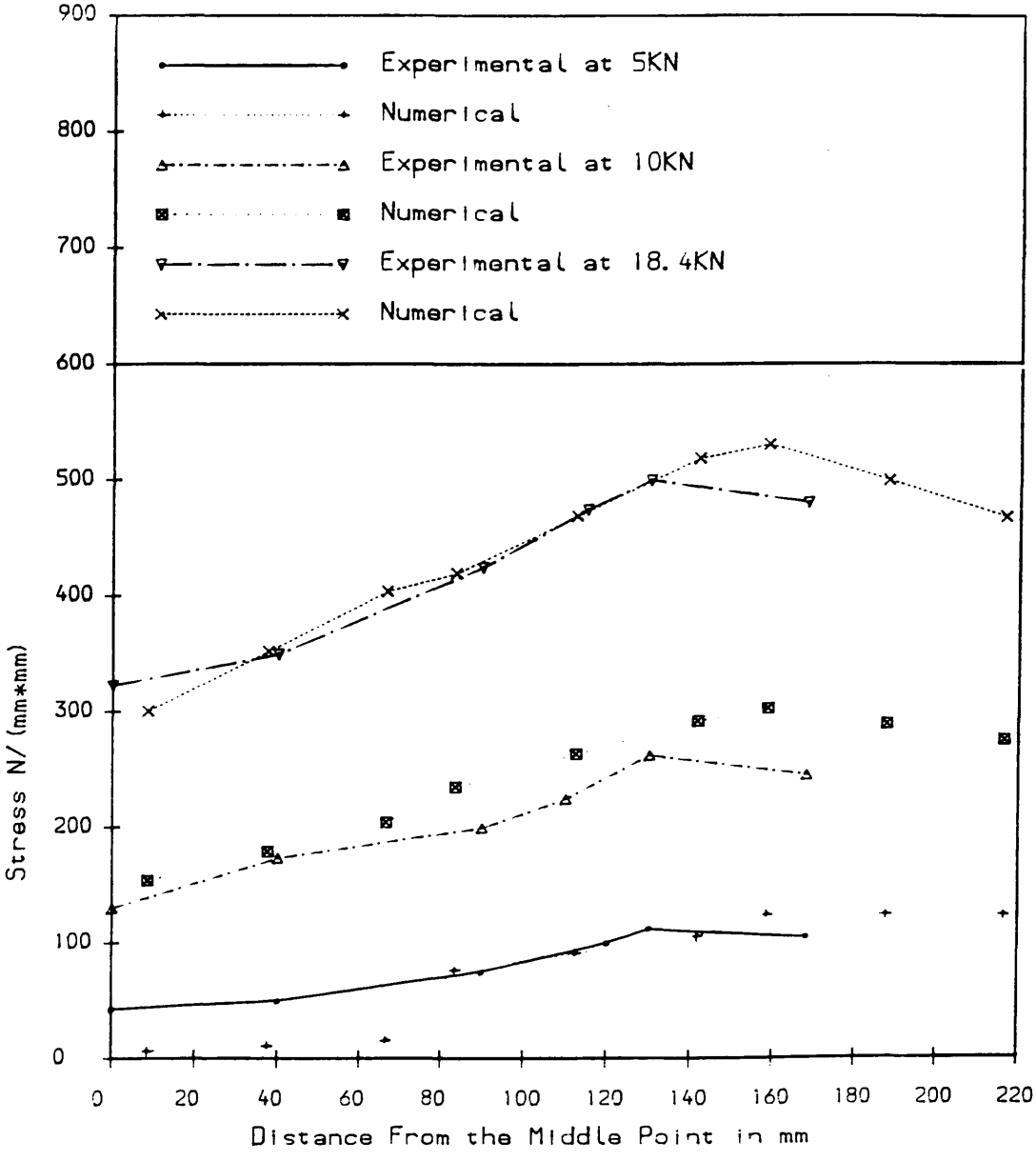

Fig.8.26(b) Steel Stress Distribution —bond— slip

CHAPTER NINE

CONCLUSIONS

9.1 General Points

This study has been concerned with the nonlinear finite element modelling of reinforced concrete structures. Three primary aspects of numerical approximation have been studied: reinforcement modelling techniques, material behaviour and nonlinear solution techniques. In particular, the following areas have been examined in detail: crack modelling, including shear retention and tension stiffening, embedded reinforcement modelling, bond slip modelling, bond stress–slip relationships and arc–length and line search solution schemes. Attention was limited to 2–dimension idealizations.

A stock of numerical examples has been analysed, including both those examining fundamental behaviour as well as applications to more realistic engineering structures. For the fundamental investigations, the selected specimens were mainly reinforced concrete panels under well–defined states of stress and bond specimens. The engineering structures included perforated deep beams and beam–column junctions.

For these classes of problem, the results of the developed numerical procedures were satisfactory, most being in good agreement with experimental data.

9.2 Fundamental Study

1. Two embedded reinforcement formulations and one embedded bond–slip model have been developed and implemented, leading to a general model for embedded

reinforcement with bond–slip effects. All these models have performed well in application. The general reinforcement model is particularly useful because it allows the main concrete finite element mesh and the reinforcement mesh to be developed quite independently.

2. For the bond–slip bond modelling, a general formulation was developed and studied. The model is effective in taking bond–slip effects into account. The bond stress–slip relationships used in this study are good enough to obtain results consistent with experimental ones. For many structures, a constant bond modulus is sufficient to approximate general bond–slip effects. If the constant modulus is of the same magnitude scale as the elastic modulus of steel, the bond is almost perfect.

3. Cracking behaviour was modeled using a smeared approximation. In particular, fixed cracking model, strain–decomposed cracking model and rotating cracking models were examined and compared.

The rotating crack model allows the crack to rotate continuously whilst in the fixed crack models the new crack direction can only appear in the direction of predefined threshold angles.

If cracks form at different orientations during the loading process, the swinging approach gives a lower bound on the loading capacity of the structure whilst the fixed orthogonal model gives an upper bound. The strain decomposed approach predicts a value between these two bounds, depending on the threshold angles adopted. For structures where crack directions do not change very much, the fixed crack model is sufficiently accurate for predicting loading behaviour.

The strain decomposed and swinging crack models require substantially more computational effort than the fixed orthogonal crack model, and should only be selected when the circumstances justify a more accurate approach.

4. A number of shear retention and tension stiffening post–cracking models were examined. On the basis of the examples analysed in this study, the Vecchio–Collins[Vecchio and Collins 1985] and Bhide–Collins[Bhide and Collins 1987] equations are recommended for tension stiffening while Mehlhorn's formulation[Mehlhorn 1990] is recommended for shear retention.

5. Solution schemes examined in this study were the Newton–Raphson method and arc–length and line search schemes. All these were effective under load control up to peak loads. However, the arc–length and line search, being the most sophisticated, was particularly effective in tracing post–cracking behaviour.

9.3 Application to Reinforced Concrete Structures

In this study, the modelling techniques have been used to analyse perforated deep beams and beam–column junctions. In all analyses, the deflection curves, steel strain curves, maximum stress contours as well as crack patterns generally showed satisfactory agreement with either experimental results, or the numerical predictions of other researchers. The general embedded reinforcement modelling procedure proved very useful in discretising structures in which the reinforcement layout was complex. It made the inclusion of extra reinforcement bars into an existing mesh very convenient. It has also been shown that bond–slip effect can be taken into account in application without great difficulty.

1. The analysis of perforated deep beams indicates that the addition of skew bars around an opening influenced behaviour if the opening was in the load path, by

restraining local failure in the vicinity of the opening and hence improving the ultimate capacity. The importance of properly modelling the reinforcement near load and support points, in order to prevent premature local failure, was also demonstrated.

2. Analysis of the beam–column junction demonstrated that in certain situations where bond–slip effects are significant, the steel stresses are significantly influenced by the bond slip simulation. Assuming perfect bond underestimated the steel stress, whilst allowing for bond–slip produced better agreement with experimental results, and reduced the predicted load carrying capacity of the junction.

9.4 Suggestion for Further Research

1. Since reinforcement in cracked concrete structures is usually subjected to dowel action, further research is needed to incorporate this effect into the embedded representation of the steel bar. In such situations, the reinforcing steel will no longer be regarded as a slender uniaxial element but as a beam element.

2. The embedded reinforcement formulation should be investigated for use in predicting the behaviour of prestressed concrete structures. The fact that curved bars or cables can be readily accommodated makes the embedded formulation potentially powerful for these structures.

3. The cracking models and reinforcement models should be examined under repeated and cyclic loading regimes. The mechanisms involved are substantially more complicated and would provide a severe test of the proposed models.

4. An obvious development is to extend the formulations proposed in this study to three dimensional structures.

REFERENCE

Ahmad, M. and Bangash, Y. 'A Three Dimensional Bond Analysis Using Finite Element', Computers and Structures vol.25 No.2 pp.281-296 (1987)

Allwood, R.J. 'Reinforcement Stresses in a Reinforced Concrete Beam Column Connection', Mag. of Concrete Research, Vol.32 pp.143-146, Sept. (1980)

Allwood, R.J. and Bajarwan, A.A. 'A New Method for Modelling Reinforcement and Bond in Finite Element Analysis of Reinforced Concrete', Int. J. Num. Meth. in Eng., Vol.28, 833-844 (1989)

Al-Mahaidi, R.S.H. 'Nonlinear Finite Element Analysis of Reinforced Concrete Deep Members', Report 79-1, Dept. of Structural Engineering, Conell University, Jan. (1979)

Al-Mahaidi, R.S.H. and Nilson, A.H. 'Nonlinear Finite Element Analysis of Reinforced Concrete Deep Members' Report No.79-1, Dept. of Structural Engineering. Cornell University, Ithaca, N.Y. Jan. (1979)

Andenaes, E., Gerstle, K. and Ko, H.Y. 'Response of Mortar and Concrete to Biaxial Compression', J. of Eng. Mech. Div, Proc. of ASCE, Vol.103, pp.515-525, August (1977)

Balakrishnan, S. and Murray, M.W. 'Prediction of Response of Concrete Beams and Panels by Nonlinear Finite Element Analysis', Coll. on 'Computational Mechanics of Concrete Structures', IABSE, Delft, The Netherlands, 393-404 (1987)

Baldwin K. (ed.) 'Modern Methods for Automating Finite Element Mesh Generation', Proc. of Session Sponsored by the Engng., Mech. Div. of ASCE in Conjunction With the ASCE National Convention

in Boston, Massachusetts, Published by ASCE, N.Y. (1986)

Bathe, K. J. 'Finite Element Procedures in Engineering Analysis' Englewood, Cliffs, N.J. (1982)

Batoz, J.L. and Dhatt, G. 'Incremental Displacement Algorithms for Nonlinear Problems' Int. J. Num. Meth. Eng. Vol.14, pp.1262-1267 (1979)

Bazant, Z.P. 'Endochronic Inelasticity and Incremental Plasticity', Int. J. of Solids and Structures, Vol.14, pp.691-714 (1978)

Bazant, Z.P. 'Work Inequalities for Plastic-Fracturing Materials', Int. J. of Solids and Structures, Vol.16, pp.873-901 (1980)

Bazant, Z.P. 'Comment on Orthotropic Models for Concrete and Geomaterials' J. Eng. Mech., ASCE, Vol.109(3), pp.849-865 (1983)

Bazant, Z.P. and Bhat, P.D. 'Endochronic Theory of Inelasticity and Failure of Concrete', J. Eng. Mech. Div, ASCE, Vol.102, pp.701-722, August (1976)

Bazant, Z.P. and Gamburova, P. 'Rough Cracks in Reinforced Concrete' J. of Struct. Div., Proc. of ASCE, Vol.106, April (1980)

Bazant, Z.P. and Kim S.S. 'Plastic-Fracturing Theory for Concrete', J. of the Eng. Mech. Div., Proc. of ASCE, Vol.105, pp407-428, With Errata in Vol.106, June (1979)

Bazant, Z.P. and Oh, B. 'Crack Band Theory for Fracture of Concrete' RILEM, Mat. Struct. 16, pp.155-177 (1983)

Bazant, Z.P. and Shieh, C.C. 'Hysteretic Fracturing Endochronic Theory for Concrete', J. of Eng. Mech. Div, ASCE, Vol.106, pp.929-950, Oct. (1980)

Bhide, S.B. and Collins, M.P. 'Reinforced Concrete Element in Shear and Tension' Research Report No.87-02, Dept. of Civil Eng., University of Toronto, 308pp. (1987)

Blaauwendraad J. 'Realisation and Restrictions-Application of Numer-

ical Models to Concrete Structures', Finite Element Analysis of Reinforced Concrete Structures, ASCE Publication, Edited by Meyer C. andOkamura H., pp.557-578 (1985)

Blaauwenfraad J. and Grootenboer, H.J. 'Essential of Discrete Crack Analysis', IABSE Reports, 34, Coll. Advanced Mech. of Reinforced Concrete, Delft University Press, pp.263-272 (1981)

de Borst R. 'Nonlinear Analysis of Frictional Material', Dissertation, Delft University of Technology, The Netherlands (1986)

de Borst, R. and Nauta, P. 'Smeared Crack Analysis of Reinforced Concrete Beams and Slabs Failing in Shear', in Proc. Int. Conf. Computer Aided Analysis and Design of Concrete Structures', Edited by Damjanic et al, Swansea, Part 1, pp.261-273 (1984)

de Borst R. and Nauta, P. 'Non-orthogonal Cracks in a Smeared Finite Element Model' Eng. Computation 2, pp.35-46 (1985)

Bresler, B. and Bertero, V.V. 'Behaviour of Reinforced Concrete Under Repeated Load', Trans ASCE Journal, Struct. Div. Vol.94, No.ST6. pp.1567-1590, June (1968)

Bresler, B. and Pister, K.S. 'Strength of Concrete Under Combined Stresses', J. Am. Concr. Inst. Vol.55, pp.321-345, Sept.(1958)

Bresler, B. and Pister, K.S. 'Failure of Plain Concrete Under Combined Stresses', Trans, ASCE Vol.122, 1957, pp.1049-1068, June (1967)

'Bridge Input Program (Type 1) FESS', Centre for Numerical Methods in Engineering, Swansea, CPR7 (1968)

Broms, B.B. 'Crack Width and Crack Spacing in Reinforced Concrete Members', ACI Journal, Vol.62(10), pp.1237-1255, Oct. (1965)

Bruggeling A.S.G. " Structural Concrete: Science into Practice " , HERON 32(2), pp.1-67 (1987)

BS 4449 'British Standard Specification for Carbon Steel Bars for

the Reinforcement of Concrete', British Standards Institutions (1988)

Buyukoztur, K.O. 'Nonlinear Analysis of Reinforced Concrete Structures', Comp. and Strct., Vol.70 pp.149-156 (1977)

Cedolin, L. and Dei Poli, S. 'Finite Element Studies of Shear-Critical Beams' J. of the Eng. Mech. Div., ASCE, Vol.103, June (1977)

Cervenka, V. 'Inelastic Finite Element Analysis of Reinforced Concrete Panels Under In-plane Loads', Dissertation, University of Colorado, Boulder (1970)

Cervenka, V. and Gerstle, K.H. 'Inelastic Analyses of Reinforced Concrete Panels', I: Theory, Int. Assoc. Bridge Struct. Eng. Publis h, Vol.31-II, pp.31-45, II: Experimental Verification and Application, ibid, Vol.32-II, pp.25-39 (1971 and 1972)

Chen, W.F. 'Plasticity in Reinforced Concrete', Published by McGraw-Hill Book Company, New York (1982)

Chen, W.F. and Yamahuchi E. 'On Constitutive Modelling of Concrete Materials' in 'Finite Element Analysis of Reinforced Concrete Structures', ASCE Publication, Tokyo, Japan, Meyer C. and Okamura H.(Eds), May 21-24 (1985)

Cowan, H.J. 'The Strength of Plain Reinforced and Prestressed Concrete Under the Action of Combined Stresses', Mag. Concr. Research. Vol.5, No.14, pp.75-86, Dec. (1953)

Cope, R.J. and Rao, P.V. 'Nonlinear Finite Element Analysis of Concrete Slab Structures', Proceedings of the Institution of Civil Engineers, Vol.63, Part 2, pp.159-179 (1977)

Cope, R.J., Rao, P.V., Clark, L.A. and Norris, P. 'Modelling of Reinforced Concrete Behaviour for Finite Element Analysis of Bridge Slabs', Numerical Methods for Nonlinear Problems 1,

Taylor C. et al(eds), Pineridge Press, Swansea, pp.457-470 (1980)

Cowan, H.J. 'The Strength of Plain, Reinforced and Prestressed Concrete Under the Action of Combined Stresses', Mag. Concrete Research, Vol.5, No.14, pp.75-86, Dec. (1953)

Crisfield, M.A. 'A Fast Incremental/Iterative Solution Procedure That Handles 'Snap-Through'', Proc. Symp. on 'Computational Methods in Nonlinear Structural and Solid Mech.' Washington, Oct. (1980)

Crisfield, M.A. 'An Arc-length Method Including Linear Search and Accelerations', Int. J. for Num. Meth. in Eng. Vol.19, pp.1269-1289 (1983)

Crisfield, M.A. and Wills, J. 'Numerical Comparisons Involving Different 'Concrete Models'', IABSE Reports 54, Coll. Comp. Mech of Reinforced Concrete, Delft University Press, pp.177-187 (1987)

Doerr, K. 'Bond Behaviour of Ribbed Reinforcement Under Transversal Pressure', Proccedings of IASS Symposium, Darmstadt, Germany, July (1978)

Dougill, J.W. 'Some Remarks on Path Independence in the Small Plasticity', J. of Applied Math. Vol.32, Oct. pp.233-243 (1975)

Dougill J.W. 'On Stable Progressively Fracturing Solids', Zeitschriftfuer Angewandte Nathematik und Physik (ZAMP). Vol.27, pp.423-437 (1976)

Durocher, L.L. and Garsper, A. 'A Versatile Two-dimensional Mesh Generator with Automatic Bandwidth Reduction'. Computers and Structures, Vol.10, pp.561-575 (1979)

Edwards, A.D. and Yannopoulos, P.J. 'Local Bond Stress-slip Relation ships Under Repeated Loading', Magazine of Concrete Research,

Vol.30 No.103, pp.62-72 June (1978)

Edwards, A.D. and Yannopoulos, P.J. 'Local Bond-Stress to Slip Relationships for Hot Rolled Deformed Bar and Mild Steel Plain Bars', ACI Journal, Vol.76, pp.405-420, March (1979)

Elwi, A.E. and Hrudey, T.M. 'Finite Element Model for Curved Embedded Reinforcement', J. Eng. Mech., Vol.115(4), pp.740-754 (1989)

Famiyesin O.O. 'Modelling and Computational Aspects of the Nonlinear Finite Element Analysis of General Concrete Structures', PhD Thesis, University College of Swansea, Wales, U. K. (1990)

Fenwick, R.C. 'The Shear Strength of Reinforced Concrete Beams' PhD Thesis, University of Canterbury, New Zealand (1966)

Gerstle, K.H. and Cinse et al, D. H. 'Strength of Concrete Under Multi-axial Stress States', Proc. McHenry Symp. Concr. Struct. (Mexico City 1976), Am. Concr. Inst. Publ. SP55, pp.103-131 (1978)

Gijsber F.B.J. and Hehemann, A.A., 'Some Tensile Tests on Reinforced Concrete, Report BI-77-61, TNO Inst. for Building Mat. and Struct. Delft (1979).

Goode, C.D. and Helmy, M.A. 'The Strength of Concrete Under Combined Shear and Direct Stress', Mag. Concrete Research, Vol.19, No.59, pp.105-112, June (1967)

Goodman R.E., Taylor, R.L. and Brekke, T.L. 'A Model for the Mechanics of Jointed Rock' J. Soil Mech, and Foundation Div., ASCE, Vol.94(3) pp.637-659 (1968)

Gopalaratnam, V.S. and Shah, S.P. 'Softening Response of Plain concrete in Direct Tension', J. of ACI, Vol.82, pp.310-323, May-June (1985)

de Groot A.K., Kusters G.M.A. and Monnier Th., ' Numerical Modelling of 10: Gijsber F. B. J. and Hehemann, A.A., ' Some Tensile Tests

on Reinforced Concrete, Report BI-77-61, TNO Inst. for Building Mat. and Struct. Delft(1979).

de Groot A.K., Kusters G.M.A. and Monnier Th., " Numerical Modelling of Bond-slip Behaviour " HERON 26 (1B), pp. 1-90 (1981)

de Groot A.K., Kusters G.M.A. and Monnier Th., " Numerical Modelling of 9: J. G. Rots Chapter 4: Issues of Finite Element Approximation, and Chapter 7 Fracture and Bond in Reinforced Concrete', Thesis report, the Civil Dept. Delft Uni. of Tech. (1988)

Grootenboer H.J. 'Finite Element Analysis of Two-dimensional Reinforced Concrete, Taking Account of Nonlinear Physical Behaviour and Development of Discrete Cracks', Dissertation, Delft Uni. of Tech., The Netherlands (1979)

Gupta, A.K. and Akbar, H. 'Cracking in Reinforced Concrete Analysis' J. Struct. Eng. Vol.110(8), ASCE, pp.1735-1746 (1984)

Han, D.J. and Chen, W.F. 'Constitutive Modelling in Analysis of Concrete Structures' J. Eng. Mech. Div. ASCE, Vol.112 (1986)

Hayashi, S. and Kokusho, S. 'Bond behaviour in the Neighbourhood of the Crack', in 'Finite Element Analysis of Reinforced Concrete Structures', ASCE Publication, Meyer, C. and Okamura H.(Eds), pp. 374-383 (1985)

Hoshuno, M. 'Ein Beitrag Zur Unterschung des Spannungszstandesan Arbeitsfugen mit Spanngliedkopplungen Von Abschnittsweise in Ortbet on Hergestellten Spambetonbrucken', Dissertation, Darmstadt, (1974)

Houde, J. 'Study of Force-displacement Relationships for the Finite Element Analysis of Reinforced Concrete', Report No.73-2, Dept. of Civil Engineering and Applied Mechanics, McGill University, Montreal, Dec. (1973)

Hsieh, S.S., Ting, E.C. and Chen, W. F. 'An Elastic-Fracture Model

for Concrete, Proc. of Eng. Mech. Div. Spec. Conf. Austin, Tex pp.437-440 (1979)

Hungspreug, S. 'The Local Interaction Between Reinforcing Bars and Concrete Under High-level Reversed Cyclic Loading', PhD Thesis, Civil Engineering Dept., Cornell University of Ithaca, N. Y. (1981)

Jiang, D.H., Shah, S.P. and Andonian, A.T. 'Study of the Transfer of Tensile Forces by Bond', ACI Journal, Vol.81, 251-259 (1984)

Johnarry, T. 'Elasto-plastic Analysis of Concrete Structures Using Finite Element', PhD Thesis, University of Strathclyde, U. K., May (1979)

Joseph, M. and Gerstle, H. 'Bond Deterioration in Concrete Panels Under Load Cycles', ACI J., Vol.76, No.2, pp.311-325, Feb. (1979)

Keuser, M., Mehlhorn G. and Cornelius, V. 'Bond Between Prestressed Steel and Concrete — computer analysis using ADINA', Computers and Structures Vol.17, No.5-6 pp.669-676 (1983)

Khaskheli, G.B. 'The Direct Design of Reinforced Concrete Transfer Girders', PhD Thesis, University of Glasgow, Scotland, U. K. (1989)

Khouzam, M. 'A Finite Element Investigation of Reinforced Concrete Beams', McGill University, Montreal, Canada, Oct. (1977)

King I.P., 'Triangular Mesh Generation Program'. Centre for Numerical Methods in Engineering, Swansea, CPR 2 (1967)

Kollegger, J. and Gunther, G. and Mehlhorn, G. 'Zug-und Zug-Drukversuche an Stahlbeton Scheiben (Tensionand Tension-Compression Tests on Reinforced Concrete Panels)', Nr.1, Forschungsberichte aus dem Fachgebiet Massivbau, Gesamthochschule, Kassel (1986)

Kotsovos, M.D. 'Effect of Stress Path on the Behaviour of Concrete

Under Triaxial Stress States', J. Am. Concr. Int. Vol.76(2) pp.213-223, Feb. (1979)

Kotsovos, M.D. and Newman, J.B. 'Behaviour of Concrete Under Multiaxial Stress', J. Am. Concr. Inst. Vol.74(9), pp.443 -446 (1977)

Kupfer, H. 'Das Verhalten des Betons Unter Zweiachsiger Bean Spruchung', Techn. Hochsch. Munchen, Cehrstuhl Massivbau, ber.18 (1968)

Leibengood, L.D., Darwin, D. and Dodds, R.H. 'Parameters Affecting Finite Element Analysis of Concrete Structures', J. Struct. Eng. Vol.112(2), pp.326-341 (1986)

Litton, R.W. 'A Contribution to the Analysis of Concrete Structures Under Cyclic Loading', Dissertation, University of California, Berkeley (1974)

Luts, L.A. and Gergely, P. 'Mechanics of Bond and Slip of Deformed Bars in Concrete', ACI Journal, Vol.64, pp.771-791 (1968)

Mains, R.M. 'Measurement of Distribution of Tensile and Bond Stresses Along Reinforcing Bar', ACI Journal, Vol.48, pp.335-352, Nov. (1951)

Malvern, C.E. 'Introduction to the Mechanics of a Continuous Medium' Prentice-Hall, Inc. Englewood, Cliffs, N. Y. (1969)

Mehlhorn, G. 'Some Developments for Finite Element Analysis of Reinforced Concrete Structures', Proceedings of 2nd Int. Conf. on Computer Aided Analysis and Design of Concrete Structures, Edited by Bicanic, N. and Mang, H., Held in Zell am See, Austria 4th-6th, April (1990)

Mehlhorn, G. and Keuser, M. 'Isoparametric Contact Element for Analysis of Reinforced Concrete Structures', in 'Finite Element Analysis of Reinforced Concrete Structures', ASCE Publiction,

Meyer, C. and Okamura, H.(Eds), Tokyo, 329-347 (1986)

Memon, G.H. 'Ultimate Strength Design of Perforated Deep Beams', Msc. Thesis, Civil Eng. Dept., University of Glasgow, Scotland, U.K. (1982)

Mier, J.G.M. 'Examples of Nonlinear Analysis of Reinforced Concrete Structures With DIANA', HERON, Vol.32(3) (1987)

Millard, S.G. and Johnson, R.P. 'Shear Transfer in Cracked Reinforced Concrete', Mag. of Concrete Research, Vol.37, No.130, pp.3-15, March (1985)

Mills, G.M. 'A Partial Kinking Yielding Criterion For Reinforced Concrete Slabs', Mag. of Concrete Research, Vol.27, No.90, pp.13-22, March (1975)

Mills, L.L. and Zimmerman, R.E. 'Compressive Strength of Plain Concrete Under Multiaxial Loading Conditions', J. ACI, Vol.67, pp.802-807, Oct. (1970)

Mirza, M.S. and Houde, J. 'Study of Bond-slip Relationships in Reinforced Concrete', ACI Journal, Vol.76, pp.19-46 (1979)

Mirza, S.A. and MacGregor, J.G. 'Variability of Mechanical Properties of Reinforcing Bars', ASCE, Vol.105, ST5, pp.921-937, May (1979)

Morita, S. and Kaku, T. 'Local Bond Stress-slip Relationship Under Repeated Loading', Prel. Report, IABSE Symposium, Lisbon, pp.221-227 (1973)

Mufti, A.A., Mirza, M.S., McCutcheon, J.O. and Houde, J. 'A Study of the Behaviour of Reinforced Concrete Elements', Structural Concrete Series, No.70-5, McGill University (1970)

Mufti, A.A., Mirza, M.S., McCutcheon, J.O. and Houde, J. 'A Study of the Nonlinear Behaviour of Structural Concrete Elements', Proc. of the Special Conf. of Finite Element Method in Civil Eng.,

Montreal, Canada, June (1972)

Nammur, J.G. and Naaman, A.E. 'Bond Stress Model for Fiber Reinforced Concrete Based on Bond-slip Relationship', ACI Journal, Vol. 86, Jan-Feb (1989)

Neilissen, L.J.M. 'Biaxial Testing of Normal Concrete', Heron (Delft), Vol.18, No.1 (1982)

Nelson, I. Baron, M.L. and Sandler, I. 'Mathematical Models for Geological Materials for wave Propagation Studies', Shock Waves and the Mechanical properties of Solids, Syracuse Uni. Press Syracuse, N.Y. (1971)

Newman, K. and Newman, J.B. 'Failure Theories and Design Criteria for Plain Concrete', Eng. Design., Civ. Eng. Material, pap.83 Southampton (1969)

Ngo, D. and Scordelis, A.C. 'Finite Element Analysis of Reinforced Concrete Beams', ACI Journal, Vol.64, pp.152-163 (1967)

Nies, W. 'A New Method for the Measurement of Local Slip Between Steel and Concrete', PhD. Thesis, Technical University, Darmstadt (1979)

Nilson, A.H. 'Nonlinear Analysis of Reinforced Concrete by Finite Element Method', ACI Journal Vol.65, pp.757-766, Sept. (1968)

Nilson, A.H. 'Internal Measurement of Bond-slip', ACI Journal, Vol. 69, pp.439-441 (1972)

Nilson A.H. et al (eds.) 'State-of-the-Art Report, Finite Element Analysis of Reinforced Concrete', ASCE Publication, New York, 544pp. (1982)

Noakowski, P. " Die Bewehrung Von Stahlbetonbauteilen Bei Zwangbeanspruchung in Folge Temperatur " Deutscher Ausschuss Fur Stahlbeton 296 (1978)

Ottosen, N.S. 'A Failure Criterion for Concrete' J. of the Engng.

Mech. Div., ASCE, Vol.103, No.EM4, pp.527-535, Aug. (1977)

Ottosen, N.S. 'Constitutive Model for Short-time Loading of Concrete', J. of the Engng. Mech. Div., ASCE, Vol.105, No.EM1 pp.127-141, Feb. (1979)

Ottosen, N.S. 'Nonlinear Finite Element Analysis of Pull-out Test', J. of Struct. Div., ASCE, Vol.107, No.ST4, pp.591-603 April (1981)

Park, R. and Panlay, T. 'Reinforced Concrete Structures' John Wiley and Sons, 769pp (1975)

Phillips, D.V. 'Nonlinear Analysis of Structural Concrete by Finite Element Methods', PhD Thesis, University College of Swansea, Wales, U. K. (1972)

Phillips, D.V. 'Fecon: Nonlinear Finite Element Software for Structural Concrete', FECON Manual, University of Glasgow (1986)

Phillips, D.V. and Wu, Z.P. 'An Orientated Embedded Bar Fomulation With Bond-slip', Proc. of Int. Cof. on Numerical Methods in Eng.: theory and Applications, Swansea, pp.320-328 (1990)

Phillips, D.V. and Zienkiewicz, O.C. ' Finite Element Nonlinear Analysis of Reinforced Concrete Structures' Proc.Inst.Civ.Engrs, Vol.61, Part2, pp.59-88 (1976)

Pochanart, S. and Harmon, T. 'Bond-slip Model for Generalized Excitations Including Fatigue', ACI Journal, Vol.86, pp.464-474, Spet-Oct. (1989)

Rahman, A., Hinton, E. and Zienkiewicz, O.C. 'Computational Models for Reinforced Concrete Systems in Advanced Mechanics of Reinforced Concrete —Final Report, IABSE Colloquium, Delft, pp.303-313 (1981)

Ramm, E. 'Strategies for Tracing the Nonlinear Response Near Limit Points' in 'Nonlinear Finite Element Analysis in Structural

Mechanics', Proceeding of the Europe-U. S. Workshop, Ruhr-Universitat Bochum, Germany, Edited by Wunderlich, W., Stein, E. and Bathe, K. J., pp.28-31, July (1980)

Rashid, Y.R. 'Analysis of Prestressed Concrete Pressure Vessels', Nuclear Eng. and Design, Vol.7(4), pp.334-344 (1968)

Rhem G. 'On the Essentials of Bond Between Concrete and Reinforcement', Deutscher Asschuss fur Stahlbeton, 138 (1961)

Rhem, G. and Eligehausen, R. 'Bond of Ribbed Bars Under Cycle Repeated Loads' ACI Journal, Vol.76, No.2, pp.297-309, Feb (1979)

Rhem G., Martin, H. and Muller, H.H. 'Ausziehversuche mit Betonstahlhaken', Materialprufungsamt fur das Bauwesen der TU Munchen, Bericht, Nr.1975 08, April (1968)

Richart, F.E., Brandtzag, A. and Brown, R.L. 'A Study of the Failure of Concrete Under Combined Compressive STresses', Uni. Ill. Eng. Exp. ST. Bull. 185 (1928)

Richart, F.E., Brandtzag, A. and Brown, R.L. 'The Failure of Plain and Spirally Reinforced Concrete in Compression', Uni. Ill. Eng Exp. ST. Bull 190, April (1929)

Riggs, H.R. and Powell, G.H. 'Rough Crack Model for Analysis of Concrete', J. Eng. Mech., ASCE, Vol.112(5), pp.448-464 (1986)

Riks, E. 'The Application of Newton's Method to the Problem of Elastic Stability', J. Appl. Mech. 39 pp1060-1066 (1972)

Riks, E. 'An Incremental Approach to the Solution of Snapping and Buckling Problems', Int. J. Solids Struct. Vol.15 pp529-551 (1979)

Rots, J.G. 'Strain-softening Analysis of Concrete Fracture Specimens', in 'Fracture Toughness and Fracture Energy of Concrete', Wittman F. H. (Ed), Elsevier Science Publcation, Amsterdam

pp.137-148 (1986)

Rots, J.G. 'Computational Modelling of Concrete Fracture', Dessertation, Technical University of Delft, Delft, The Netherlands (1988)

Rots, J.G., Nauta, P., Rusters, G.M.A. and Blaauwendraad J. 'Smeared Crack Approach and Fracture Localization in Concrete', Heron 30(1), pp.1-48 (1985)

Saouma, V.E. and Ingraffea, A.R. 'Fracture Mechanics Analysis of Discrete Cracking' in Final Report IABSE Coll., Advanced Mech. Reinforced Concrete, Delft University Press, Delft, pp.413-436 (1981)

Scanlon, A. 'Time Dependent Deflections of Reinforced Concrete Slabs', PhD. Thesis, Uni. of Alberta, Edmonta, Canda (1971)

Scanlon, A., Phillips, D.V. and Green, D.R. 'Direct Tension Tests on Panels with Skew Reinforcement', Structural Research Report ST 1/88, University of Glasgow, 227pp. (1988)

Schafer, H. 'A Contribution to the Solution of Contact Problems With the Aid of Bond Elements', Comp. Meth. Appl. Mech. Eng. Vol.6, pp.335-354 (1975)

Schapery, R.A. 'On A Thermodynamic Constitutive Theory and Its Applications to Various Nonlinear Materials', Proceedings, IUTAM Symposium, Kilbride, B.A. Boley (Ed), New York June (1968)

Schnobrich, W.C. 'Discussion of 'Nonlinear Stress Analysis of Reinforced Concrete' by Iiapan S. and Doo Lan T.F.', J. Struct. Div., ASCE, Vol.98(10), pp.2237-2328 (1972)

Scordelis, A.C. 'Finite Element Analysis of Reinforced Concrete Structures' Proceeding of the McGill, Engineering Institute of Canada Specialty Conference on Finite Element Methods in Civil Engineering, McGill University, Montreal, pp71-114, June (1972)

Scordelis, A.C. 'Past, Present and Future Developments', in Finite Element Analysis of Reinforced Concrete Structures' ASCE Pub. Meyer, C. and Okamura, K. (eds), pp.656-666 (1985)

Shipman, J.M. and Gerstle, K.H. 'Bond Deterioration in Concrete Panels Under Load Cycles', ACI Journal, Vol.76, No.2, pp.331-325 (1979)

Sinha, B.P. Gerstler, K.H. and Tulin L.G. 'Stress-strain Relations for Concrete Under Cyclic Loading', J. Am. Conc. Inst. Vol.61 (2), pp.195-211, Feb. (1964)

Sinisalo, H.S. Tuomala, M.T.E. and Mikkola M.J. 'Nonlinear Finite Element Analysis of Reinforced Concrete Slabs Subjected to Transient Inpulsive Loading', in 'Advances in Concrete Slab Technology, Proc. of Int. Conference on Concrete Slabs, Dundee University, Pergamon Press, Edited by Dhir and Munday, pp.140-148, April (1979)

Somayaji, S. and Shah, S.P. 'Bond Stress Versus Slip Relationship and Cracking Response of Tension Members', ACI Journal, Vol.78, No.3, pp.217-225, May-June (1981)

Stroband, J. and Kolpa, J.J. 'The Behaviour of Reinforced Concrete Column-to-Beam Joints-Part 1: Corner Joints Subjected to Negative Moments, Research Reports 5-83-9, Dept. of Civil Engineering, University of Technology, Delft, The Netherlands (1983)

Suidan, M. and Schnorich W.C. 'Finite Element Analysis of Reinforced Concrete', J. Struct. Div., ASCE, Vol.99(10), pp.2109-2122 (1973)

Tanner, J.A. 'An Experimental Determination of Bond Slip in Reinforced Concrete', MSc thesis, Cornell University, Ithaca, N. Y. Nov (1971)

Tasuji, M.E., Slate, F.O. and Nilson, A.H. 'Stress-strain Response

and Fracture of Concrete in Biaxial Loading', Proc. Am. Concr. Inst., Vol.75(7), pp.306-312, July (1978)

Taylor, M.A. Jain, A.K. and Ramey M.R.O. 'Path Dependent Biaxial Compressive Testing of All-lightweight Aggregate concrete' J. Am. Concr. Inst. Vol.69(12), pp.758-764, Dec. (1972)

Tepfers R. 'Cracking of Concrete cover Along Anchored Deforming Reinforcing Bars' Mag. of Concrete Res. 31(106), pp3-12(1979)

Timoshenko, S. and Goodier, J. N. 'Theory of Elasticity', McGraw-Hill, New York (1951)

Valanis, K.C. 'A Theory of Viscoplasticity Without a Yield Surface', Archiwum Mechaniki Stossowanej (Archives of Mechanics, Warsaw, Vol.23, pp.517-551 (1971)

Valliappan, S. and Doolan, T.F. 'Nonlinear Stress Analysis of Reinforced Concrete', J. Struct. Div., ASCE, Vol.98(4), pp.885-897 (1972)

Vecchio, F.J. and Collins, M.P. 'The Modified Compression-Field Theory for Reinforced Concrete Elements Subjected to Shear', J. of the ACI, Vol.83(2), pp.219-231 (1986)

Vermeer, P.A. and de Borst, R. 'Non-Associated Plasticity for Soils' Concrete and Rock, Heron, Vol.29, No.3 (1984)

Viwathanatepa, S., Popov, E.P. and Bertero, V.V. 'Effects of Generalized Loadings on Bond of Reinforcing Bars Embedded in Confined Concrete Blocks', Report No.VCB/EErc-79/22, Earthquake Engineering Research Centre, University of California, Berkeley, 304pp. Aug. (1979)

Walraven, J.C. 'Aggregate Interlock-A Theoretical and Experimental Analysis' Dissertation, Technical University of Delft, Delft, the Netherlands (1980)

Watstein, D. 'Bond Stress in Concrete Pull-out Specimens', ACI J.

Vol.38, pp.35-50, Sept. (1941)

Wegmuller, A.W. 'Elasto-plastic Finite Element Analysis of Plates', Techniques Note TN99, Proceedings of the Institute of Civil Engineering, Vol.57(2), pp.535-543, Sept. (1974)

Wempner, G.A. 'Discrete Approximations Related to Nonlinear Theories of Solids', Int. J. Solids Struct. Vol.7 pp.1581-1599 (1971)

Wessels, M. 'Das Statische Und Dynamische Durchschlags Problem der Imperfekten Flachen Kugelschale bei Elastischer Rotationssymmetrischer Verformung', Dissertation, TU Hannover, Mitteil, Nr.23 des Instituts Fur Statik (1977)

Willam, K., Pramono, E. and Sture, S. 'Fundamental Issues of Smeared Crack Models', Proc. SEM-RILEM, Int. Conf. on Fracture of Concrete and Rock, Edited by Shah S.P. and Swartz S.E., SEM, Bethel pp.192-207 (1987)

Willam, K.J. and Warnke, E. P. 'Constitutive Models for the Triaxial Behaviour of Concrete', Int. Assoc. Bridge Struct. Eng Sem. Concr. Struct. Subjected Triaxial Stresses (Bergamo, Italy 1974), Int. Assoc. Bridge Struct. Eng. Proc. Vol.19 pp.1-30

Wu, E.R. 'Some Findings in Using The Program, 'A Versatile Two-Dimensional Mesh Generator With Automatic Bandwith Reducation'' Computers and Structures, vol.12 pp.181-183 (1980)

Wu, E.R. 'Techniques to Avoid Duplicate Nodes and Relax Restrictions on The Superelement Numbering in A Mesh Generator', Computers and Structures Vol.15, pp.419-422 (1982)

Yamaguchi, H. and Nomura, S. 'Analysis of Reinforced Concrete Walls By Plastic-fracturing Theory', in 'Finite Element Analysis of Reinforced Concrete Structures', ASCE Publication, Meyer, C. and Okamura, H.(Eds), pp.204-213 (1985)

Zienkiewicz, O.C. 'Finite Element Method', McGraw-Hill Ltd. London

(1979)

Zienkiewicz, O.C. and Phillips, D.V. 'An Automatic Mesh Generation Scheme for Plate and Curved Surfaces by 'Isoparametric' Coordinates'. Int. J. for Num. Meth. in Engineering, Vol.3, pp.519-528 (1971)

APPENDICES

Appendix I

Basic Procedure of Finite Element Method

Based on homogeneous, continuous and isotropic assumptions, the element stiffness matrix for an individual finite element can be determined using an energy principle, such as the principle of virtual work or total potential energy. The general procedure is given by

i) For any structure or an element, the internal displacements $\{\delta\}$ at any point within the system can be expressed in terms of the nodal displacements $\{\delta^e\}$ by means of assumed displacement functions $[N]$, i. e.

$$\{\delta\} = [N]\{\delta^e\} \qquad (I.1)$$

in which $[N]$ is a set of interpolation function termed "shape functions". It is used to approximate the true displacement behaviour of the element in the continuum, based on Laplace interpolation.

ii) Taking proper derivatives of eq.(I.1), the strain–displacement relationship is then established as

$$\{\epsilon\} = [B]\{\delta^e\} \qquad (I.2)$$

where $[B]$ is the so–called strain matrix. It is generally composed of derivatives of the shape functions.

iii) Select an appropriate stress– strain relationship for the element material, i.e.

$$\{\sigma\} = [D]\{\epsilon\} \tag{I.3}$$

where $[D]$ is the constitutive relationship matrix of the element.

iv) Substitute eq.(I.2) into eq.(I.3) to obtain the stress– displacement relation. i. e.

$$\{\sigma\} = [D][B]\{\delta^e\} \tag{I.4}$$

v) Provided that the element shape functions have been interpolated properly so that no singularities exist in the integrands of the functions, the total potential energy of the continuum will be the sum of the energy contributions of the individual elements, i. e.

$$\pi = \sum_e \pi_e \tag{I.5}$$

where π_e represents the total potential energy of element e, which can be rewritten as

$$\pi_e = \frac{1}{2}[\delta^e]^T \int_{ve} [B]^T [D][B][\delta^e]\, dv$$

$$- [\delta^e]^T \int_{ve} [N]^T \{p\}\, dv - [\delta^e]^T \int_{se} [N]^T \{q\}\, ds \tag{I.6}$$

where ve is the element volume; se is the loaded element surface; p is the body forces per unit volume and q is the applied surface forces.

vi) Performing the minimization for element e with respect to the nodal displacements $\{\delta^e\}$ for the element, gives

$$\frac{\partial \pi_e}{\partial [\delta^e]} = \int_{ve} [B]^T [D] [B] \{\delta\}^e \, dv$$

$$- \left\{ \int_{ve} [N]^T \{p\} \, dv + \int_{se} [N]^T \{q\} \, ds \right\}$$

$$= K^e \{\delta^e\} - F^e \qquad (I.7)$$

where

$K^e = \int_{ve} [B]^T [D] [B] \, dv$ is the stiffness matrix of the element, and

$F^e = \int_{ve} [N]^T \{p\} \, dv + \int_{se} [N]^T \{q\} \, ds$ is the equivalent nodal forces for the element.

Generally, the integration indicated in K^e must be carried out numerically within the element.

vii) Once the element stiffness matrices have been calculated and transformed from local to global coordinate system, the structural stiffness matrix K can then be formed by the systematic addition of element stiffness matrices, i. e.

$$[K] \{\delta\} = \{F\} \qquad (I.8)$$

where $\{F\}$ is the known external nodal forces and $\{\delta\}$ is the unknown nodal displacements obtained by solving eq.(I.8).

viii) Having worked out the nodal displacements, the element stresses within each element are given by

$$\{\sigma\} = [D] [B] \{\delta^e\} \qquad (I.9)$$

ix) Other subsidiary element quantities can also be obtained in a similar manner.

In finite element analysis, the isoparametric element is commonly adopted, i. e. the shape function used to define the variation of displacements are the same as those functions used to define the mapping relationship between global Cartesian coordinates and the local curvilinear co-ordinates. This study makes use of the eight node isoparametric elements for two dimensional problem and the [N] matrix of such an element is given by

$$[N] = \begin{bmatrix} N_i & 0 \\ 0 & N_i \end{bmatrix} \quad (i = 1 \text{ to } 8) \qquad (I.10)$$

where N_i is a parabolic shape function. For corner nodes

$$N_i = \frac{1}{4}(1 + \xi_o)(1 + \eta_o)(\xi_o + \eta_o - 1) \qquad (I.11a)$$

where $\xi_o = \xi\ \xi_i$ and $\eta_o = \eta\ \eta_i$.

For middle nodes

$$N_i = \frac{1}{2}(1 - \xi^2)(1 + \eta_o) \quad (\text{if } \xi_i = 0.0) \qquad (I.11b)$$

and

$$N_i = \frac{1}{2}(1 + \xi_o)(1 - \eta^2) \quad (\text{if } \eta_i = 0.0) \qquad (I.11c)$$

Then, the displacements within an element is defined by

$$\begin{bmatrix} u \\ v \end{bmatrix} = [N] \begin{bmatrix} u_i \\ v_i \end{bmatrix} \quad (i = 1 \text{ to } 8) \qquad (I.12)$$

where u_i and v_i are the nodal coordinates.

The geometry is defined by

$$\begin{bmatrix} x \\ y \end{bmatrix} = [N] \begin{bmatrix} x_i \\ y_i \end{bmatrix} \quad (i = 1 \text{ to } 8) \qquad (I.13)$$

where x_i and y_i are the nodal coordinates of the element.

The strain at a point in an element is given by

$$\{ \epsilon \} = \begin{Bmatrix} \epsilon_x \\ \epsilon_y \\ \gamma_{xy} \end{Bmatrix} = \begin{Bmatrix} \partial u/\partial x \\ \partial v/\partial y \\ \partial u/\partial y + \partial v/\partial x \end{Bmatrix} = [B]\{\delta^e\} \qquad (I.14)$$

where $[B] = [B_1, \cdots, B_8]$ and

$$[\ B_i\ (\xi, \eta)\ ] = \begin{bmatrix} \partial N_i/\partial x & 0 \\ 0 & \partial N_i/\partial y \\ \partial N_i/\partial y & \partial N_i/\partial x \end{bmatrix} \qquad (I.15)$$

Since the shape function is expressed in a local curvilinear system, a transformation is required from local to global. This is a well-known relation between cartesian and curvilinear derivatives, given by

$$\begin{Bmatrix} \partial/\partial x \\ \partial/\partial_y \end{Bmatrix} = [J]^{-1} \begin{Bmatrix} \partial/\partial \xi \\ \partial/\partial \eta \end{Bmatrix} \qquad (I.16)$$

where $[J]$ is the Jacobian matrix given by

$$[J] = \begin{bmatrix} \partial x/\partial \xi & \partial y/\xi \\ \partial x/\partial \eta & \partial y/\partial \eta \end{bmatrix} \qquad (I.17a)$$

In the local system, this [J] matrix is given by

$$[J] = \begin{bmatrix} \partial N/\partial \xi \\ \partial N/\partial \eta \end{bmatrix} \begin{bmatrix} x \\ y \end{bmatrix} \qquad (I.17b)$$

Having obtained the [B] matrix and [J] matrix, the stiffness matrix in eq.(I.7) can be worked out over the element volume in the local coordinate system, in which

$$\int_{ve} dv = \int_{-1}^{1} \int_{-1}^{1} \det|J| \, d\xi d\eta \qquad (I.18)$$

In this study, the Gauss–Legendre quadrature rules have been used to carried out this integration.

Appendix II

Stress Invariants

The three principal stress invariants I_1, J_2 and J_3 are often used in formulating various criteria of failure for concrete material. These are given by

$$I_1 = \sigma_1 + \sigma_2 + \sigma_3 \qquad (II.1a)$$

$$J_2 = \frac{1}{6}\left[(\sigma_1 - \sigma_2)^2 + (\sigma_2 - \sigma_3)^2 + (\sigma_3 - \sigma_1)^2\right] \qquad (II.1b)$$

$$J_3 = s_1 s_2 s_3 \qquad (II.1c)$$

where I_1, J_2 and J_3 are the first, second and third stress invariants;

σ_i is the principal stress;

s_i is the deviatoric stress, representing a state of pure shear,

$s_i = \sigma_i - \sigma_{oct}$ and $\sigma_{oct} = I_1/3$ are the mean normal stress or octahedral normal stress.

The octahedral normal stress acts on a plane which has equal angles with each of the principal stress directions. The plane is defined as an octahedral plane. Its corresponding normal strain is given by

$$\epsilon_{oct} = \frac{1}{3} (\epsilon_1 + \epsilon_2 + \epsilon_3) \qquad (II.2)$$

The shear stress on the octahedral plane is given by

$$\tau_{oct} = \sqrt{(2J_2/3)} \qquad (II.3)$$

where τ_{oct} is the octahedral shear stress.

The corresponding octahedral shear strain reads

$$\gamma = \frac{2}{3} [(\epsilon_1 - \epsilon_2)^2 + (\epsilon_2 - \epsilon_3) + (\epsilon_3 - \epsilon_1)]^{\frac{1}{2}} \qquad (II.4)$$

Detailed derivations are given in [Chen 1982].

Appendix III

Damage Rule

Under monotonic loading, the bond resistance of a deformed bar depends primarily on the strength of the "concrete key", i.e. the concrete between the steel lugs. After the damaged area exceeds the lug spacing, there is only friction to provide bond resistance. The frictional resistance must be developed as the

concrete key is being damaged. As shown in Fig.III.1, it is assumed that the damage occurs in a linear fashion and is divided into a "strength component" and a "frictional component".

The strength component depends on the total damage and the loss of the strength does not depend on whether the damage is all in one direction or is composed of slip components in each direction. The deterioration of the frictional bond stress can be determined by assuming that the frictional bond stress reduces from the frictional bond stress of the previous cycle (suggested to be about 18%[Pochanart and Harmon 1989]), assuming no new frictional resistance developed during the cycle under the slip control.

Appendix IV

Equilibrium Between Concrete and Reinforcement

As shown in Fig.IV.1, the force acting on the bond by reinforcement F_{sb} is the same in magnitude as the force F_{bs} acting on the reinforcement by the bond at an arbitrary point P, i. e.

$$F_{sb} = F_{bs} \tag{IV.1}$$

where

$$F_{sb} = \int_{v_e} \left[\frac{dH_b}{dr} \right] [\sigma_s] \, dv_s \begin{bmatrix} \delta^e \\ U_b \end{bmatrix}$$

$$= \int_{v_s} [B_b]^T [D_s] [B_s \quad B_b] \, dv_s \begin{bmatrix} \delta^e \\ U_b \end{bmatrix} \tag{IV.2}$$

$$F_{bs} = \int_{\substack{bond \\ surface}} [H_{bj}]^T [D_b] [H_{bj}] \, dv_b [u_{bj}]$$

(IV.3)

where l is the length of the bar.

Substituting eqs.(IV.2) and (IV.3) into eq.(IV.1) gives

$$K_{bs1}^{T} \cdot \delta^{e} + (K_{bs} - K_{b}) \cdot U_{b} = 0 \qquad (IV.4)$$

where

$K_{bs} = \int_{vs} [B_{bs}]^{T}[D_s][B_{bs}]\, dv_s$, and

$K_{bs1} = \int_{vs} [B_{cs}]^{T} [D_s][B_{bs}]\, dv_s$ are stiffness matrices due to bond effects;

$K_b = \int_{bond} [H_b]^{T} [D_b] [H_b]\, dv_b$ is the bond stiffness matrix.

Appendix V

Explicit Force Equilibrium Condition of Reinforcement with Bond-slip

In embedded reinforcement model with bond-slip, the equivalent reinforcement force is given by

$$\begin{bmatrix} F_{sc} \\ F_{sb} \end{bmatrix} = \int_{vs} [B_{cs} \quad B_{bs}]^{T} [D_s] [B_{cs} \quad B_{bs}] \begin{Bmatrix} \delta^{e} \\ U_b \end{Bmatrix} dv \qquad (V.1)$$

where $[B_{cs} \quad B_{bs}]$ is the strain matrix of steel given by eq(5.36),

$[D_s]$ is the constitutive relationship matrix.

This equivalent force consists of two parts F_{sc} and F_{sb}. The former is the

embedded reinforcement force produced by its movement together with concrete. The latter is due to bond-slip. In other words, F_{sb} should by equilibrated by bond force F_b:

$$F_b = K_b U_b \tag{V.2}$$

Therefore

$$F_{sb} = \int_{vs} B^T_{bs} D_s B_{cs} \delta^e dv + \int_{vs} B^T_{bs} D_s B_{bs} U_b dv$$

$$= K_b U_b \tag{V.3}$$

i.e.

$$\begin{bmatrix} K^T_{bs1} & K_{bs} \end{bmatrix} \begin{bmatrix} \delta^e \\ U_b \end{bmatrix} = K_b U_b \tag{V.4}$$

where K_b, K_{bs1} and K_{bs} are defined in eq.(5.41)

For the whole element, it hence gives

$$\begin{bmatrix} K_c + K_s & K_{bs1} \\ K^T_{bs1} & K_{bs} \end{bmatrix} = \begin{bmatrix} F^e \\ K_b U_b \end{bmatrix} = \begin{bmatrix} F^e \\ F_b \end{bmatrix} \tag{V.5}$$

As mentioned above, F_b is a bond force rather than an applied external force of structure, and hence can not be increased/decreased incrementally in computation. It is only dependent on the particular mechanical state at a given region.

In compuation, F_b can be kept at right hand side of the equilibrium equation. But this makes calculation tedious and invalidates the standard finite element solution procedure. In order to overcome this difficulty, F_b was shifted to left hand side of the equation while maintaining the equilibrium condition of the

structure through the assembly strategy of the element stiffness matrix at structural level, which leads to eq.(5.41) and (5.42).

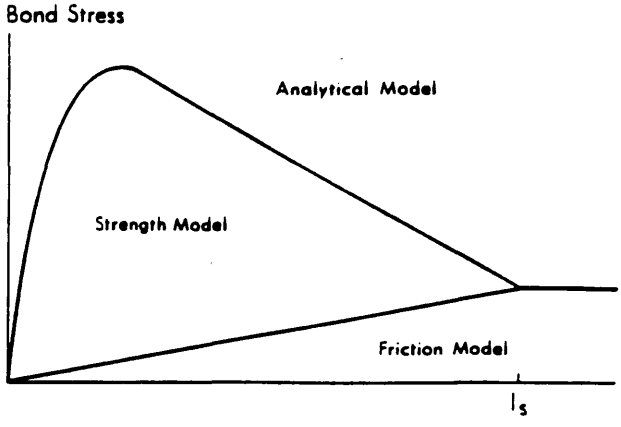

Fig.III.1 Strength Model and Frictional Model

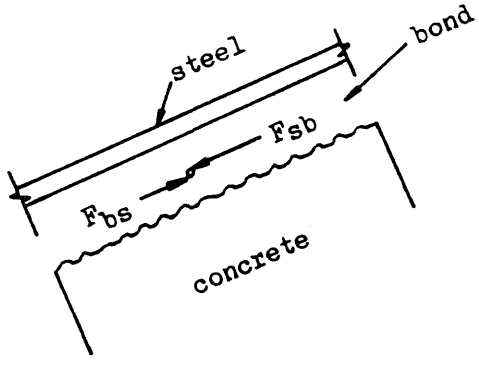

Fig.IV.1 Equilibrium Between Reinforcement and Concrete